



HAL
open science

Elaboration de films de perovskites hybrides par coévaporation pour des applications photovoltaïques.

Chloe Dindault

► **To cite this version:**

Chloe Dindault. Elaboration de films de perovskites hybrides par coévaporation pour des applications photovoltaïques.. Material chemistry. Université Paris Saclay (COmUE), 2019. English. NNT : 2019SACLX079 . tel-02441820

HAL Id: tel-02441820

<https://theses.hal.science/tel-02441820>

Submitted on 16 Jan 2020

HAL is a multi-disciplinary open access archive for the deposit and dissemination of scientific research documents, whether they are published or not. The documents may come from teaching and research institutions in France or abroad, or from public or private research centers.

L'archive ouverte pluridisciplinaire **HAL**, est destinée au dépôt et à la diffusion de documents scientifiques de niveau recherche, publiés ou non, émanant des établissements d'enseignement et de recherche français ou étrangers, des laboratoires publics ou privés.

Development of coevaporated perovskite thin films for tandem solar cells applications.

Thèse de doctorat de l'Université Paris-Saclay
préparée à l'École Polytechnique

École doctorale n°573 Interfaces :
approches interdisciplinaires,
fondements, applications et innovation (Interfaces)
Spécialité de doctorat: Physique

Thèse présentée et soutenue à Palaiseau, le 8 octobre 2019, par

Chloé DINDAULT

Composition du Jury :

Mme Nadine Witkowski Professeure, Sorbonne Université, Institut des NanoSciences de Paris (CNRS)	Présidente
Mme Mireille Richard-Plouet Directeure de Recherche, Université de Nantes, Institut des Matériaux Jean Rouxel (CNRS)	Rapporteuse
Mr Benoit Lessard Maître de Conférences, Université d'Ottawa	Examineur
Mr Matthieu Manceau Ingénieur de Recherche, Institut National pour l'Energie Solaire (CEA-LITEN)	Examineur
Mr Rachid Belkhou Chercheur, Responsable de ligne de lumière, Synchrotron SOLEIL (CNRS/CEA), Université Paris-Saclay	Examineur
Mr Yvan Bonnassieux Professeur, Ecole Polytechnique, Laboratoire de Physique des Interfaces et des Couches Minces (Ecole Polytechnique/CNRS), IP Paris	Directeur de thèse
Mr Denis Tondelier Ingénieur de recherche, Laboratoire de Physique des Interfaces et des Couches Minces (Ecole Polytechnique/CNRS), IP Paris	Co-Directeur de thèse

To my family and friends.

Acknowledgments

For this part, I will switch to French.

Je voudrais tout d'abord naturellement remercier mon encadrement : Yvan, Denis et Bernard (même si tu n'apparais pas officiellement tu as toujours été là, pas loin, et toujours pertinent). Vous avez cru en moi dès le début, dès mon stage de M2 en février 2016 et vous vous êtes battus pour me garder. Vous avez appris à travailler avec moi et mon (fort) caractère. Cela n'a pas toujours été facile mais vous avez su être là dans les moments clefs. Je vous remercie sincèrement de la confiance que vous m'avez faite très tôt et de l'indépendance que vous m'avez offerte, essentielle pour moi.

Tout naturellement je passe ensuite à ceux sans qui ce travail n'aurait pas pu être mené : l'IPVF avec particulièrement Bruno Carlotti puis Roch Drozdowski-Strehl et Christophe Bonelli et le LPICM avec Pere Roca i Cabarrocas. Vous m'avez offert un environnement de travail dans lequel j'ai pu m'épanouir pleinement. Dans la continuité, je tiens à remercier les équipes supports de l'IPVF avec notamment Sonia Haouka, Bérengère Larue, Ariana Salemi puis Viviane Bastiao. Même si je ne passais dans les locaux de l'IPVF qu'une fois par mois pour récupérer mon bulletin de salaire, vous m'avez toujours tous accueillie avec le sourire. Je tiens ensuite à remercier tout particulièrement Alexis Denis pour son aide pendant le déménagement de l'équipement du LPICM vers l'IPVF puis pendant la phase de remise en service. Je remercie aussi l'équipe du projet F, porté par Jean Rousset, notamment Amelle Rebai, Javier Ramos et Florian Hilt avec qui j'ai le plus interagi mais aussi tous les autres. Enfin, je remercie tous les chercheurs IPVF, nos effectifs ont bien grandi depuis mon arrivée dans la structure, continuez les efforts menés afin de réaliser les objectifs que l'IPVF s'est fixé.

Je souhaite ensuite adresser de sincères remerciements à la totalité du laboratoire LPICM dans lequel j'ai passé le plus clair de mes journées ces trois dernières années. Je pense particulièrement à Gabie, Jérôme, Eric, Marc, Guillaume, Rafaël, Mengkoing, Alaric, Nicolas, Tiphaine, Ghewa et Romain avec qui j'ai passé d'agréables moments autour d'un café, d'une raclette ou de bières. Merci à l'ensemble de l'équipe OLAE (Organic Large Area Electronics) et plus particulièrement à notre équipe réduite perovskites et ces différents membres : Warda, Heejae, Arthur, Alexandre, Eric, Jonas, Tiphaine, Hindia, Minjin, Corentin, Khaoula et Hae-Yeon (doctorants, post-doctorants et stagiaires par ordre chronologique) ainsi que Yvan, Bernard, Denis et Jean-Eric pour les discussions et échanges, toujours riches.

Je tiens maintenant à remercier les différents collaborateurs rencontrés dans le cadre de notre étude en Synchrotron. Maxime, c'est avec toi que tout a commencé entre le LPICM et la ligne de lumière HERMES à SOLEIL. Je me rappellerai longtemps de quelques nuits à travailler jusqu'à 2h du matin, à supporter ton humour (de 2h du matin lui aussi...) et croiser les doigts que le faisceau ne coupe pas. Sufal, grâce à toi j'ai pu prendre les rênes de cette collaboration sereinement à la suite de Maxime. Tu as été d'une grande aide au travers des différentes campagnes de mesures mais encore plus en dehors de celles-ci, lors du traitement des données. Philip ton arrivée ne pouvait pas mieux tomber, ton expertise et ton énergie ont su donner un nouvel élan à notre petite équipe STXM/Perovskites. C'est un réel plaisir (et une certaine fierté) de voir que les choses se pérennisent et qu'une thèse en collaboration entre le LPICM et HERMES est sur le point de commencer.

Je passe maintenant aux remerciements plus personnels. Ce manuscrit n'existerait sûrement pas sans le soutien sans faille des quelques personnes suivantes : Fabienne, Marlinka, Hindia, Anna, Tanguy, Ronan, Patxi et Cyril. Vous m'avez tous supportée pendant ces longs mois de rédaction (et bien avant aussi, mais j'étais encore relativement supportable à l'époque).

Fabienne, je crois que mon épanouissement personnel dans ce laboratoire a commencé avec toi. J'ai très vite été épanouie professionnellement dans ce cadre de travail mais il m'a fallu du temps pour sortir de ma bulle, enlever ces écouteurs constamment vissés sur mes oreilles, prendre le temps de faire des pauses dans mon travail et prendre du recul. Tout ça est venu avec toi, avec ton amitié, avec ta folie et avec ton énergie. Tu rayannes tout simplement. J'ai trouvé en toi une amie avec qui parler, chanter, danser, pleurer mais surtout rire et sourire. On a du mal à se rappeler le moment exact depuis lequel on se parle, je crois que c'est parce que j'ai l'impression de t'avoir toujours eu à mes côtés dans cette folle aventure. Tu n'as pas idée de ce que je te dois, je n'aurai pas pu réaliser la moitié de ce que j'ai fait sans toi. Cette thèse existe grâce à ton amitié et ton soutien. Je suis heureuse de t'avoir à mes côtés dans la vie, pour de longues années.

Malinka, il aura fallu que le préfabriqué 404 de l'équipe Total ferme pour que tu migres vers nos locaux et que notre amitié commence. Depuis, on a rattrapé le temps perdu je crois. J'ai très vite trouvé en toi bien plus qu'une simple camarade de repas et de virées à la boulangerie ou à la piscine, j'ai trouvé en toi une véritable amie. Tu as été d'une aide précieuse ces derniers mois, bien plus que je ne saurai le retranscrire ici. C'est à ton tour maintenant de te lancer dans la rédaction. Vas-y, tu verras c'est super ! ... Tu as tout ce qu'il faut pour le faire. Je "t'abandonne" au pire moment. Je ne pourrai malheureusement pas être là (physiquement) pour te soutenir, t'accompagner dans cette aventure mais tu sais que tu peux compter sur moi, comme j'ai pu compter sur toi, pour t'écrire des messages de motivation, te remonter le moral quand ça n'ira pas, te gronder quand tu baisseras les bras, te féliciter quand tu auras fini des chapitres, t'aider à relativiser (la 'sagesse' de ceux qui y sont passés), te rappeler que même si c'est dur tu vas y arriver. Mais je serai là aussi (et surtout !) pour parler de tout sauf de la thèse. À tout moment, n'hésite pas. On se donne rendez-vous à Lyon, pour partager des restos, des spectacles et des apéros, à nos années d'amitié à venir !

Hindia, Anna et Tanguy je vous regroupe car vous avez été mes co-bureaux pendant cette thèse mais vous êtes devenus bien plus que cela... de vrais et chers amis. Vous avez été les plus exposés à mon humeur (souvent mauvaise) lors de la rédaction de ce manuscrit, à mes inquiétudes, à mes sautes d'humeur, à mes larmes de joie et de stress, à mes capacités vocales (mauvaises), à mes moyens (débiles) de décompresser (faire des bulles, me coller des gobelets sur le front ou essayer d'éteindre la lumière du bureau en tirant sur l'interrupteur avec un pistolet NERF...) et à mes périodes d'euphorie à la fin d'un chapitre et de doutes au début du suivant. Pour certains, notre bureau est le plus bruyant du bâtiment, pour moi c'est... effectivement le plus bruyant mais c'est aussi un bureau rempli de bonnes ondes, de mots (plus ou moins scientifiques) écrits au tableau, de bonbons, de madeleines, de compotes et de plantes (dédicace Bob et RIP ton orchidée trop tôt lâchement assassinée Tanguy...). Bref, le meilleur bureau (même si j'ai toujours eu la pire des chaises et le plus petit des bureaux...). Prenez en soin !

Ronan, il t'aura suffi de 2h pour me donner le déclic après 2 semaines à être bloquée sur ce chapitre 3. La sagesse du post-doc sûrement... Avec toi et Malinka on a formé un sacré trio, à se retrouver bien souvent après 18h30 dans la cafétéria pour débriefer de la journée ou de nos week-ends/vacances, autour d'un encas (voire d'un repas complet pour toi...). Merci pour ta patience, ton soutien et ton amitié.

Patxi, ton insupportable bonne humeur aura plus d'une fois eue raison de mon humeur grincheuse. Je ne vais pas dire que c'est un succès total mais je crois qu'à force d'acharnement tu as un peu réussi à me faire relativiser les choses. Merci pour tes encouragements chaque fois que tu passais devant le bureau ces derniers mois. Tu as été un soutien indéfectible, parfois dur dans tes mots (quand il le fallait) tu as toujours été juste et honnête à mon égard. Ton soutien a été d'une importance cruciale, plus que tu ne peux le réaliser. Enfin, je tiens à t'adresser un merci tout sauf anecdotique d'avoir rendu réel un objet que j'ai pensé dès mon arrivée au laboratoire.

Cyril, tu as toujours pris le temps de dépanner mes différents équipements tout en m'expliquant chaque fois (quitte à parfois te répéter) les opérations menées. Grâce à toi j'ai étendu mon lexique avec des mots comme 'tombac, Fomblin, colliers, jauge, vanne, etc...'. Mais tu ne t'es pas arrêté au seul soutien technique, tu as aussi (souvent) pris le temps de me remonter le moral et de m'aider à voir les choses différemment. Tu diras certainement que l'accompagnement des doctorants fait partie de ton travail (et c'est là toute la modestie qui te caractérise), mais j'aime à penser que tu l'as fait parce tu as sincèrement cru en moi, dès le début, pas seulement parce que tu es professionnellement consciencieux. Merci pour ton soutien et ta patience mais aussi (et surtout) ta gentillesse.

Je conclurai en remerciant ma famille : mes parents Sylvaine et François, ma sœur Estelle, mon frère Cédric, ma tante Marie-Luce, mon beau-frère Geoffrey, mon neveu Léandre et toi petit bébé qui n'est pas encore là mais qui fait déjà de moi une tante doublement heureuse, et mes amis : Elodie, Adeline, Clémence, Ophélie, Sébastien et Valentin. Merci à chacun d'entre vous pour votre amour inconditionnel. Dans les moments difficiles je n'ai pas lâché, me disant que cette thèse si je ne la faisais pas pour moi, au moins je la faisais pour vous, pour vous rendre fiers. Je ne vais pas plus m'épancher ici, sachez juste que tant que vous êtes tous à mes côtés, je sais que je suis sur le bon chemin.

List of abbreviations

2/3/4T: 2/3/4-terminal
a-Si: amorphous Silicon
ALS: Advanced Light Source
APS: Advanced Photon Source
ARPES: Angle-Resolved PhotoEmission Spectroscopy
BCP: 1-(1,3-Benzodioxol-5-ylCarbonyl) Piperidine
c-Si: crystalline Silicon
CB: ChloroBenzene
CIGS: Copper Indium Gallium Selenide
CLS: Canadian Light Source
DMF: N,N-DiMethylFormamide
DMSO: DiMethylSulfOxide
DSSC: Dye-Sensitized Solar Cell
EELS: Electron Energy Loss Spectroscopy
ESRF: European Synchrotron Facility
ETL: Electron Transporting Layer
EXAFS: Extended X-ray Absorption Fine Structure
FAI: Formamidinium Iodide
FET: Field-Effect Transistor
FIB: Focused Ion Beam
FTIR: Fourier Transform InfraRed
FZP: Fresnel Zone Plate
GI-WAXD: Grazing-Incidence Wide Angle X-ray Diffraction
GI-WAXS: Grazing Incidence Wide Angle X-ray Scattering
GI-XRD: Grazing Incidence X-ray Diffraction
HERMES: High Efficiency and Resolution beamline for X-ray Microscopy and Electron Spectroscopy
HTL: Hole Transporting Layer
ICL: InterConnecting Layer
ITO: Indium Tin Oxide
LED: Light Emitting Diode
LINAC: LINear ACcelerator
MAI: MethylAmmonium Iodide
NEXAFS: Near-Edge X-ray Absorption Fine Structure
NSLS: National Synchrotron Light Source
NSRRC: National Synchrotron Radiation Research Center
OD: Optical Density
OLED: Organic Light Emitting Diode
OSA: Order Sorting Aperture
PCBM: Phenyl-C₆₁-Butyric acid Methyl ester
PEA(I): PhenylEthylAmmonium (Iodide)
PEDOT:PSS: Poly(3,4-EthyleneDioxyThiophene) PolyStyrene Sulfonate
PF: Photon Factory
PLS: Pohang Light Source
polyTPD: Poly(bis-4-butylphenyl-N,N-bisphenyl)benzidine

PV: PhotoVoltaics
QCM: Quartz Crystal Microbalance
SAT: Site Acceptance Tests
SEM: Scanning Electron Microscopy
SLS: Synchrotron LightSource
SOLEIL: Source Optimisée de Lumière d'Energie Intermédiaire du LURE
SPEM: Scanning PhotoEmission Microscopy
SR: Synchrotron Radiation
SRPES: Synchrotron Radiation PhotoEmission Spectroscopy
SSRF: Shanghai Synchrotron Radiation Facility
SSRL: Stanford Synchrotron Radiation Lightsource
STXM: Scanning Transmission X-ray Microscopy
TEM: Transmission Electron Microscopy
TEY: Total Electron Yield
UVSOR: UltraViolet Synchrotron Orbital Radiation
WAXS: Wide Angle X-ray Scattering
XANES: X-ray Absorption
XAS: X-ray Absorption Spectroscopy
XPS: X-ray Photoelectron Spectroscopy
XRD: X-Ray Diffraction
XRF: X-ray Fluorescence

Table of content

Acknowledgments	i
List of abbreviations	v
Emerging photovoltaics: the key to photovoltaics democratization?	1
Thesis aim and outline	3
Chapter 1.	5
A glimpse of hybrid perovskites for photovoltaic applications: focus on the deposition methods.	5
Introduction	7
I. Perovskites	8
II. Photovoltaic effect and solar cells	10
III. Perovskites in PV	13
i. New perovskite compositions	15
ii. New types of cells	16
iii. New manufacturing processes	18
IV. 'Simple' CH ₃ NH ₃ PbI ₃ thin films fabrication by coevaporation	22
Conclusion	27
Chapter 2.	29
Design and engineering of a reactor for perovskite coevaporation.	29
Introduction	31
I. Coevaporation process for perovskites using a proof-of-concept reactor	32
i. Initial developments and identification of missing features	32
ii. Proof-of-concept assessment results	37
II. Comparison of the specifically designed reactor with the proof-of-concept one	41
III. Implementation of the new reactor designed for perovskite coevaporation	43
i. Site Acceptance Tests	43
ii. Transfer knowledge between equipments	46
iii. Single compound depositions	49
iv. Toward coevaporation	53
Conclusion	56

Chapter 3.	57
Fabrication of perovskite thin films using coevaporation.	57
Introduction	59
I. Coevaporation process for perovskite thin films	60
i. Focus on the process repeatability	60
ii. Focus on the material properties	67
II. Open discussions	76
i. Process-related aspects	76
ii. Material-related aspects	76
Conclusion	78
Chapter 4.	79
Nanoscale characterisation of perovskite films using Synchrotron-based technique.	79
Introduction	81
I. X-ray radiation	82
II. X-ray Absorption Spectroscopy	83
III. Synchrotron lightsource	85
i. Synchrotron radiation	85
ii. Synchrotron facility	86
IV. Scanning Transmission X-ray Microscopy	88
i. History and development	88
ii. STXM instrumentation	91
iii. STXM measurements	92
V. Synchrotron-based studies of perovskite films	95
VI. LPICM perovskite team STXM studies	96
VII. Homogeneity of wet- and dry-perovskite films assessed by Synchrotron STXM	98
i. Samples preparation	98
ii. STXM Measurements	100
iii. Post-processing methodology	105
iv. Ratio calculations results	109
v. Open discussion	113
Conclusion	114

Conclusion and Perspectives	115
List of references	a
Annexes	
Fabrication of perovskite solar cells at LPICM	A
Résumé en français	E

Emerging photovoltaics: the key to photovoltaics democratization?

In the current climate crisis context, more and more citizens are looking for ways to contribute to the fight against global warming at their own humble level. People are trying to limit their negative impact on the planet: decreasing their meat consumption, avoiding plastics, limiting their carbon footprint, recycling, embracing a zero waste philosophy lifestyle. In the present digital era, rethinking our electricity consumption appears equally relevant. Indeed, electricity is becoming “the fuel of choice” accounting for 20% of the global final consumption according to IEA’s 2018 World Energy Outlook report ¹.

Based on abundant, sustainable and available resources, solar photovoltaic (PV) and wind power stand as the most obvious choices, among renewables, to generate green electricity. Although well adapted for large scale facilities, wind power cannot be easily implemented at the local level by climate-concerned citizens. Indeed, wind turbines are rarely installed in the backyard of a suburban house while, on the other hand, solar panels are widely deployed on their rooftops. Solar PV then stands as the most convenient technology for small-scale green electricity production.

Although the photovoltaic market is dominated by Silicon, historical actor of the field and the current most efficient technology, there is indubitably room for parallel niche markets where the so called emerging technologies, such as organic and perovskite PV, would perfectly fit. In the optics of democratizing photovoltaics, chosen technologies should be cheap, easy to implement and adaptive. Manufactured from low cost materials, using low cost processes, organic and perovskite PV are cheaper than Silicon. Based on thinner absorbing layers, they offer a flexibility and a lightness that Silicon fails to provide. In addition, their colourfulness brings an aesthetical feature into the matter that would further broaden the range of possibilities.

Being older than its perovskite counterpart, organic PV can already claim (despite its relatively low efficiencies) several successful implementations and realisations among which: OPVIUS’s solar trees implemented at the entrance of Merck headquarters in Germany², Heliatek’s flexible organic solar films installed on canopies at the Roland Garros French Open³ and ARMOR’s OPV film ‘ASCA’ installed on horticultural greenhouses⁴.

Possessing all the features that make OPV appealing while reaching higher efficiencies, perovskites seem to be the perfect material for market penetration. Despite their youthfulness in the photovoltaic field, perovskites transfer from the laboratory to the industry is already initiated with companies such as Saule Technologies and Oxford PV.

In November 2016, Oxford PV took a huge step toward commercialization of perovskite solar cells, securing the acquisition of a former Bosch Solar CISTech GmbH production site⁵, equipped with 17,000 m² of pilot line facilities. In July 2019, ‘The perovskite

¹ [International Energy Agency 2018 World Energy Outlook report](#)

² [Merckgroup.com](#)

³ [Heliatek.com](#)

⁴ [Asca.com](#)

⁵ [OxfordPV.com / news 14 Nov. 2016](#)

company' secured a £65 million funding⁶ to push further the development of their vacuum-processed perovskite based tandem approach. At the end of 2018, the Polish start up Saule Technologies announced the installation of their inkjet-printed perovskite solar modules at Henn-na hotel in Japan⁷. Few months later, they were launching a pilot installation on Skanska's offices in Warsaw⁸. Although no products are yet available, both Saule technologies and Oxford PV are unquestionable driving forces in the race of perovskite PV toward the market.

⁶ [OxfordPV.com / news](http://OxfordPV.com/news) 3rd July 2019

⁷ Sauletech.com

⁸ Skanska.pl

Thesis aim and outline

This thesis was carried out in the framework of the Project F “Perovskite solar cells” of the Institut Photovoltaïque d’Île-de-France (IPVF) in close collaboration with the Laboratoire de Physique des Interfaces et des Couches Minces (LPICM) from CNRS (UMR 7647) and Ecole Polytechnique. IPVF’s project F addresses three major aspects of the perovskite photovoltaics field: device stability, large surface deposition and tandem applications.

The present thesis covers the last two topics of IPVF project F as the objective is to develop, using a semi-industrial reactor, the coevaporation process for perovskite thin films fabrication with the target of tandem applications.

The first chapter of the manuscript will introduce the reader to the perovskite materials, their characteristics and properties to eventually direct the interest toward their use as light absorber in solar cells. Navigating through the progress made in the field of perovskite photovoltaics we will ultimately focus on the processing methods. Following an overview of the different methods for perovskite thin films fabrication, we will narrow down the scope to the coevaporation process. Finally, discussing a literature review of the topic will provide some basic insights on the method used in the follow-up chapters.

The second part of the manuscript will take the reader through the early stages of our development of the coevaporation process for perovskite thin films fabrication. Starting off on a proof-of-concept reactor, our initial developments will drive us to design a second reactor, dedicated to perovskite coevaporation. The implementation and initial trials on this new reactor will be detailed, setting the ground for the next chapter.

The third part of the manuscript will be dedicated to the development of the coevaporation process using the specifically designed reactor. In the hope of taming the deposition technique the focus will be first given to process-related considerations. Eventually properties of the fabricated materials will be studied, discussed and correlated to the deposition conditions. From these results, various aspects will be debated, paving the way for future developments.

The last part of the manuscript will take the reader to new horizons, away from the perovskite thin films fabrication toward their characterization using a Synchrotron-based technique. After a thorough introduction to the lightsource world, we will eventually introduce the X-ray based spectromicroscopy technique used to study our perovskite films. Results of our study will then be disclosed and discussed.

Ultimately, general conclusions from the previous four parts will be drawn and ideas for future research will be provided.

Chapter 1.

A glimpse of hybrid perovskites for photovoltaic applications: focus on the deposition methods.

Michael Saliba: - “New world record for perovskite solar cells at 25.2% KRICT/MIT. [...]”

Aron Huckaba: - “Wow! Can’t wait to see how they did it.”

Michael Saliba: - “Will be very exciting. Although not even the previous record is published yet haha”

Twitter @miliba01, August 3rd 2019

Introduction

The present chapter aims at setting the scene for the rest of the manuscript. Following a brief synopsis on the perovskite family and their outstanding optoelectronic properties, we will address key concepts of photovoltaics through its history, theory and applications, these latter being our interest in the framework of this thesis.

We will eventually resume to the history of perovskites in the photovoltaic field. The first use of perovskites as light absorber goes back to only a decade ago. It then quickly became a trending topic, such that perovskites are now directly challenging the historical actors of the field. Along the way, tremendous progresses were achieved on the levels of: composition, cell types and deposition processes. We will provide insights on each of these topics with a particular focus on these latter.

Achieving high efficiencies at low cost, perovskites have all it takes for a great industrial future. We will eventually direct our interest towards the coevaporation process for perovskite solar cells. This vacuum-based technique, already widely implemented in the OLED industry for example, stands as a viable candidate for the manufacturing of large area perovskite thin films.

I. Perovskites

In 1839, German mineralogist Gustav Rose discovered a calcium titanate mineral of chemical formula CaTiO_3 . The crystal structure consists of a TiO_6 octahedron inside a Ca_8 cube, in 3D it can be seen as a network of corner-sharing octahedra with Calcium-filled cavities (Figure 1). The arrangement can be reduced to its unit cell formula ABX_3 , A being the corner atoms in the cubic lattice, B the centre atom and X the face centred ones. As a tribute to the Russian mineralogist Lev Alexeïevitch Perovski the structure was named 'perovskite'. Depending on the nature of the X-site atom, subfamilies can be defined: oxide ($\text{X} = \text{O}^{2-}$)^{9,10,11,12,13} and halide ($\text{X} = \text{I}^-$, Cl^- or Br^-) perovskites.

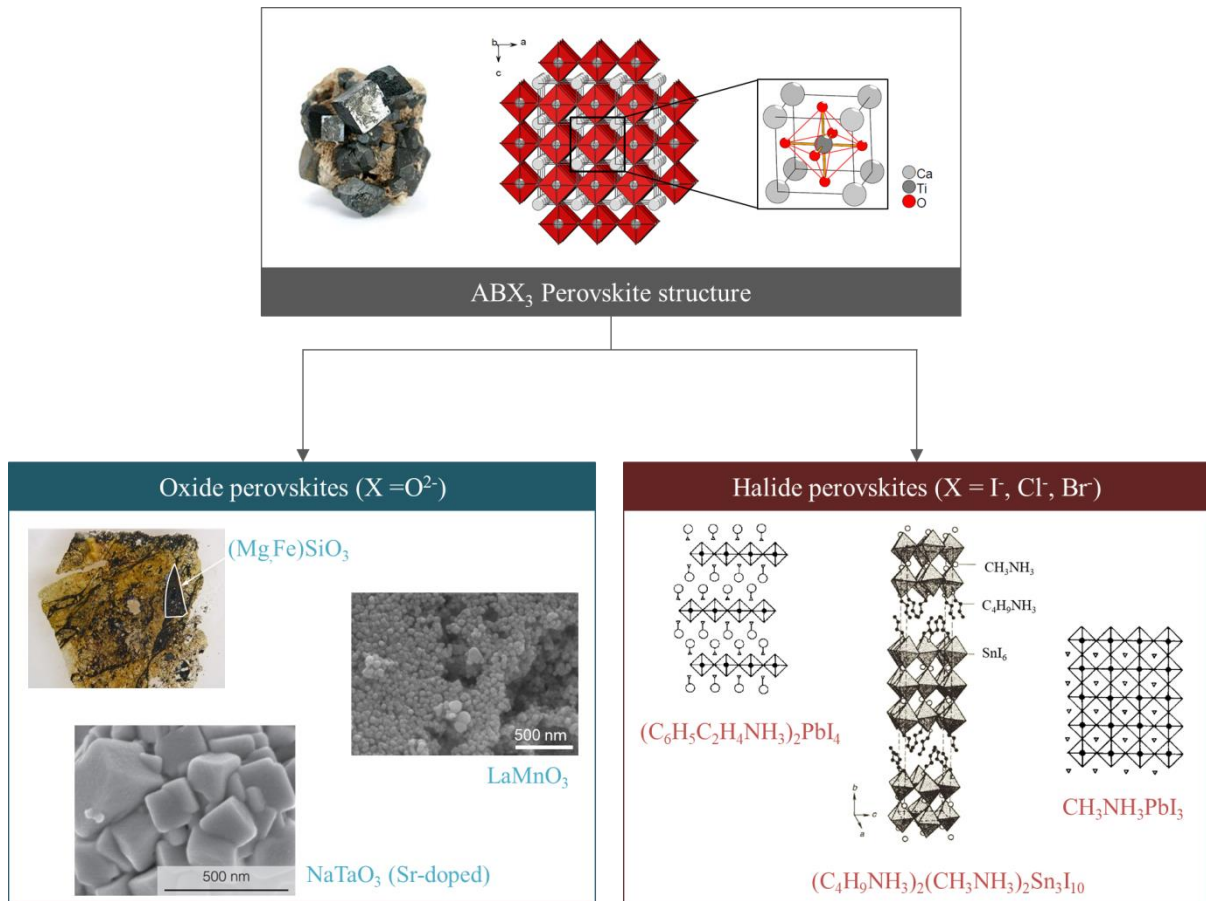


Figure 1. Perovskite family tree: from the parent general ABX_3 crystal structure¹⁴ (with CaTiO_3 mineral¹⁵) to the oxide subfamily with $(\text{Mg,Fe})\text{SiO}_3$ bridgmanite from Earth lower mantle¹⁶, catalytic LaMnO_3 ¹³ and Sr-doped NaTaO_3 ¹⁷ and halide subfamily with $(\text{C}_6\text{H}_5\text{C}_2\text{H}_4\text{NH}_3)_2\text{PbI}_4$ ¹⁸, $(\text{C}_4\text{H}_9\text{NH}_3)_2(\text{CH}_3\text{NH}_3)_2\text{Sn}_3\text{I}_{10}$ ¹⁹ and $\text{CH}_3\text{NH}_3\text{PbI}_3$ ¹⁸.

⁹ E. Knittle and R. Jeanloz, (1987) *Science* 235, 668

¹⁰ F. Nestola *et al.*, (2018) *Nature*, 555, 237-41

¹¹ M. F. M. Zwickels *et al.*, (1999) *Catalysis Today*, 47, 73-82

¹² H. Huang *et al.*, (2019) *Diamond & Related Materials*, 91, 199-206

¹³ Q. Wang and L. Ma, (2019) *New J. Chem.*, 43, 2974-80

¹⁴ adapted from N. Louvain's thesis manuscript « *Relations Structures-Propriétés dans des matériaux hybrides multifonctionnels : Investigations structurales et théoriques.* » (2008) <tel-00450691>

¹⁵ Wikipedia

¹⁶ Earth-Building Bridgmanite: Caltech (2014)

¹⁷ L. An and H. Onishi, (2015) *ACS Catal.*, 5, 3196-206

¹⁸ T. Ishihara, (1994) *J. of Luminescence*, 60 & 61, 269-74

¹⁹ D. B. Mitzi *et al.*, (1994) *Nature*, 369, 467-9

Considering halide perovskites, B-site is occupied by a dication like Pb^{2+} , Sn^{2+20} , Bi^{2+21} or Ge^{2+22} (either pure or mixed^{23,24}) and A-site can be occupied by a large variety of univalent cations (organic or not). If the A-cation is too big, the 3D network is shattered, leading to layered perovskites with a dimensionality of 2. By fine molecular engineering, intermediate 2 to 3D phases can even be obtained²⁵. Although, strictly speaking ‘perovskite’ refers to the 3D arrangement, lower dimension materials also fall under the perovskite banner, as derived from the parent structure, making this family a rather complex and wide one.

Whatever their dimensionality, halide perovskites have quite outstanding properties of photoconductivity as reported in 1958 by Møller for Caesium halide perovskite CsPbX_3 ²⁶ and later on in 1978 by Weber for the hybrid organic-inorganic lead halide perovskites $\text{CH}_3\text{NH}_3\text{SnBr}_x\text{I}_{3-x}$ ²⁷ and $\text{CH}_3\text{NH}_3\text{PbX}_3$ ²⁸ (a non-exhaustive yet very complete review can be found in Mitzi²⁹). Therefore, halide perovskites can be integrated in a variety of optoelectronic devices such as Light Emitting Diodes (LED)³⁰, Field Effect Transistors (FET)³¹ or Solar Cells³² (Figure 2). Throughout this document, focus is given to the solar cell applications.

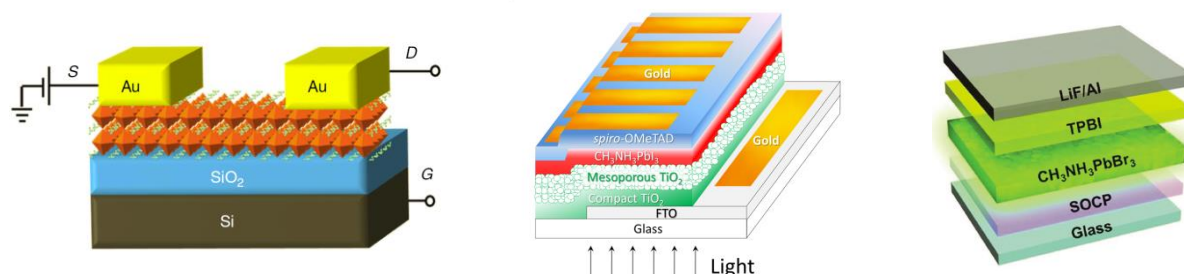


Figure 2. Examples of halide perovskite-based optoelectronic devices: $\text{CH}_3\text{NH}_3\text{PbX}_3$ Field-Effect Transistor³¹ (S, D and G being Source, Drain and Gate), $\text{CH}_3\text{NH}_3\text{PbI}_3$ Solar cell³³ and $\text{CH}_3\text{NH}_3\text{PbBr}_3$ Light Emitting Diode³⁴.

The love story between perovskites and photovoltaics is quite recent, being only ten years old. In 2009, Kojima *et al.*³⁵ used $\text{CH}_3\text{NH}_3\text{PbI}_3$ in Dye-Sensitized Solar Cells (DSSC) yielding 3.8% efficiency. Since then, perovskite photovoltaics has taken off as its own technology: new cells were developed and higher efficiencies have been achieved. Before going any deeper into this story, let us take a step aside to focus on photovoltaics: its history and theory.

²⁰ F. Hao *et al.*, (2014) *Nat. Photon.*, 8, 489-94

²¹ B-W. Park *et al.*, (2015) *Adv. Mater.*, 27, 6806-13

²² G. Stoumpos *et al.*, (2015) *J. Am. Chem. Soc.*, 137, 21, 6804-19

²³ S. Lee *et al.*, (2018) 227, 311-4

²⁴ N. Ito *et al.*, (2018) *J. Phys. Chem. Lett.*, 97, 1682-8

²⁵ A. Leblanc *et al.*, (2017) *Angew. Chem. Int. Ed.*, 56, 16067-72

²⁶ C. K. Møller, (1958) *Nature*, 182, 1436

²⁷ D. Weber, (1978) *Zeitschrift für Naturforschung B*, 33, 8, 862-5

²⁸ D. Weber, (1978) *Zeitschrift für Naturforschung B*, 33, 12, 1443-5

²⁹ D. B. Mitzi ‘Synthesis, Structure, and Properties of Organic-Inorganic Perovskites and Related Materials’ in *Progress in Inorganic Chemistry*, K. D. Karlin (1999)

³⁰ Y. H. Kim *et al.*, (2015) *Adv. Mater.*, 27, 1248

³¹ W. Yu *et al.*, (2018) *Nature Communications*, 9, 354

³² M. Grätzel, (2014) *Nature Materials*, 13, 838–42

³³ O. Almora *et al.*, *Rev. Cub. Fis.* (2017), 34, 1, 58-68

³⁴ H. Cho *et al.*, (2015) *Science*, 4, 350, 6265, 1222-5

³⁵ A. Kojima *et al.*, (2009) *J. Am. Chem. Soc.*, 131, 17, 6050-1

II. Photovoltaic effect and solar cells

Discovered in 1839 by the French physicist Alexandre Edmond Becquerel³⁶, the photovoltaic effect depicts the conversion of light into electricity by a material. Photovoltaic active materials are empirically sorted out in three generations: Silicon (poly- and mono-crystalline), thin films (CIGS, CdTe, amorphous Si) and the so-called “emerging PV” that gathers organic and quantum dots among other technologies. If each generation has its own specificities, solar cells all basically operate in the same way.

At the heart of the solar cell is the semi-conductor absorbing layer (Figure 3). Semi-conductor materials are defined by a non-zero conduction-to-valence bandgap (E_g), typically of a few eV (above tens of eV the material can be considered as insulating). Their illumination promotes one conduction band electron to the valence band, creating an electron/hole pair in the absorber. Due to the energy difference between the carrier-selective layers, generated charges are separated and finally collected at the electrodes. The overall process creates an electrical current in the device and its efficiency is estimated by the produced to incident power ratio, *i. e.* the electricity to light ratio.

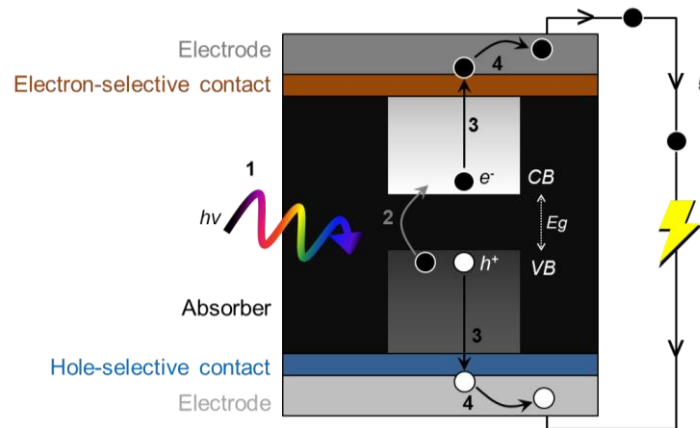
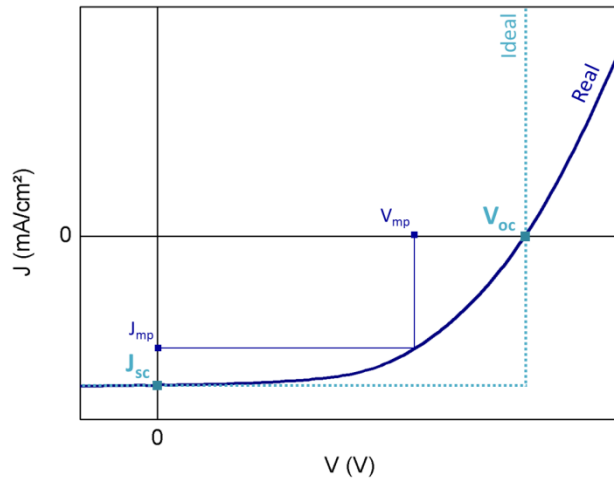


Figure 3. Photoconversion process steps: 1. Photon ($h\nu$) absorption; 2. electron/hole (e^-/h^+) pair creation; 3. charges separation; 4. charges collection and 5. current generation (VB and CB: Valence and Conduction Bands and E_g the bandgap).

Experimentally, solar cells are characterized by current-voltage measurements: a voltage bias (V) is applied to a device under illumination and the current (I) delivered is measured. From the obtained J-V curve (very often, the current density J is preferred to the current I), one can extract three important values: the open circuit voltage (V_{oc}), the short-circuit current density (J_{sc}) and the Fill Factor (FF) and calculate a fourth one: the photoconversion efficiency (PCE). This set of parameters defines the device. As depicted on the J-V curve in Figure 4, V_{oc} and J_{sc} are defined as the voltage value for a zero current density and the current density value for a zero voltage respectively. The Fill Factor is calculated as the ratio of the maximal power (mp) actually delivered by the cell over the power if the cell was ideal (equation [1]). It depicts the device ideality gap, *i. e.* the closer it gets to 1, the more optimized the device is. Finally, the PCE is calculated as the ratio of the produced power over the incident power (equation [2]).

³⁶ E. Becquerel, (1839) Comptes rendus des séances de l'Académie des sciences, 9, 561



$$FF = \frac{V_{mp} \times J_{mp}}{V_{oc} \times J_{sc}} \quad [1]$$

$$PCE = \frac{P_{prod}}{P_{inc}} \quad [2]$$

$$PCE = \frac{V_{oc} \times J_{sc} \times FF}{P_{inc}}$$

Figure 4. Example of ideal (dotted line) and real (solid line) current density-voltage (J-V) curve with V_{oc} and J_{sc} points and formula for calculated FF [1] ('mp' maximal power) and PCE [2] parameters.

When the PV device consists of only one absorbing layer it is said to be “single-junction”. This type of cells has the intrinsic limitation of being unable to convert more than 30% of the incoming solar spectrum. Streamlined in 1961 by Shockley and Queisser³⁷ this theoretical limit can be overcome by combining several junctions. The basic idea of such configuration is to stack cells on top of each other in order to expand the spectral window collected by the device and increase its efficiency. As depicted Figure 5, highest energy photons are absorbed by the top cell, the remaining unabsorbed ones reach the lower cell where they are then absorbed. The point of this multijunction configuration being the maximization of light collection, absorption windows of the different cells should be complementary, without overlaying too much.

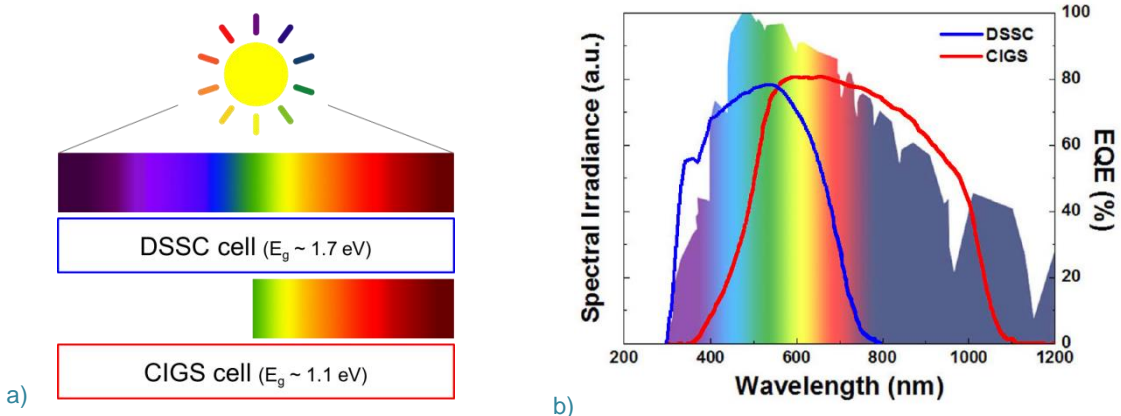


Figure 5. a) Light absorption in a DSSC-CIGS tandem device and b) Spectral irradiance of solar light and External Quantum Efficiencies (EQE) spectra of separated DSSC (blue curve) and CIGS (red curve) single-junction solar cells³⁸.

As the current single junction PV technologies are getting closer and closer to the 30% limit, the multijunction approach unquestionably represents the future of PV. Reviews on multijunctions can be found in Lu *et al.*³⁹ for organics, in Colter *et al.*⁴⁰ for III-V materials

³⁷ W. Shockley and H. J. Queisser, (1961) *J. Appl. Phys.* 32, 510

³⁸ S.H. Moon *et al.*, (2015) *Sci. Rep.* 5, 8970

³⁹ S. Lu *et al.*, (2017) *Sc. China Chem.*, 60, 4, 460-71

⁴⁰ P. Colter *et al.*, (2018) *Crystals*, 8, 445

and in Yamaguchi *et al.*⁴¹ for Si. This multijunction configuration; although very attractive; involves important device engineering.

Considering a tandem device (two junctions) several configurations are possible: two, three and four-terminal (Figure 6), each of them having its advantages and drawbacks.

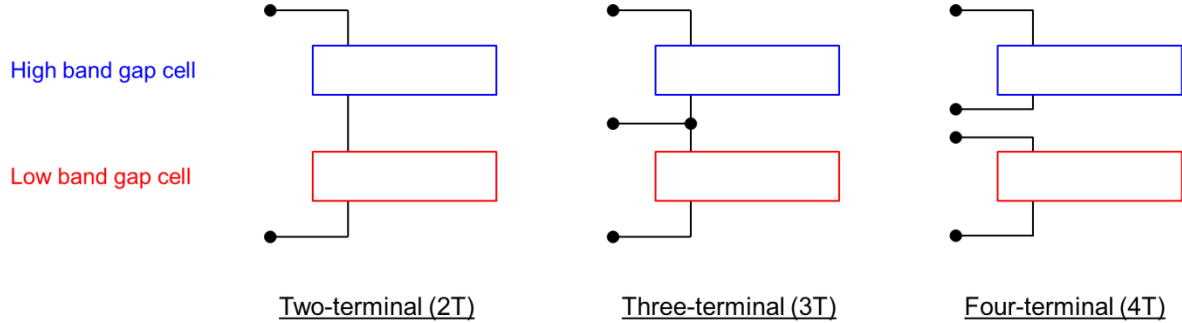
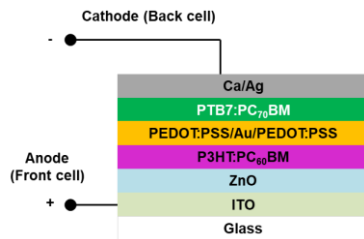


Figure 6. Schematic views of the different configurations possible for a tandem cell.

From an electrical point of view, tandems can be connected either in series or parallel and depending on the type of connection, limitations on the V_{oc} and J_{sc} values arise (Figure 7). For a series-connected tandem (typically the 2T configuration), the tandem's J_{sc} is limited by the lowest J_{sc} of the two subcells (equation [3]). The 2T configuration then requires a current matching between the two subcells in order to minimize current loss. For a parallel-connected tandem (typically the 3T configuration), the tandem's J_{sc} is the sum of the two subcells' J_{sc} (equation [4]). For this configuration, no current matching is needed. The 4T configuration is the most electrically compliant as it can be connected either in series or parallel.

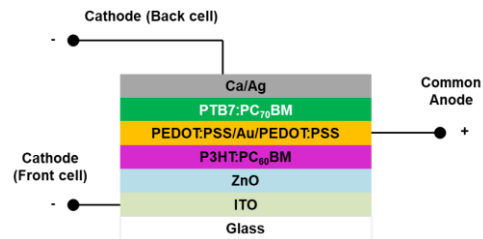
Series-connected tandem:



$$J_{sc_tandem} = \min(J_{sc_top}; J_{sc_bottom}) \quad [3]$$

$$V_{oc_tandem} = V_{oc_top} + V_{oc_bottom} \quad [5]$$

Parallel-connected tandem:



$$J_{sc_tandem} = J_{sc_top} + J_{sc_bottom} \quad [4]$$

$$V_{oc_tandem} = \min(V_{oc_top}; V_{oc_bottom}) \quad [6]$$

Figure 7. Series and parallel connections for a tandem device: illustrating scheme of an OPV tandem device⁴² and corresponding equations for both J_{sc} and V_{oc} values.

The 4T is also the simplest configuration in terms of manufacturing, each of the subcells being processed on its own and then simply mechanically stacked together. The 2T and 3T configurations are more challenging as they involve monolithic processing, the top cell substrate being the entire bottom cell. The $N+1^{th}$ layer deposition should be compatible with the N^{th} lower layer. As the cell stack goes up, the process temperatures should go down. For a wet on dry deposition, lower layer wettability to the upper layer solvent is essential. For

⁴¹ M. Yamaguchi *et al.*, (2018) *J. Phys. D: Appl. Phys.*, 51, 133002

⁴² adapted from I. Etxebarria *et al.*, (2014) *Solar Energy Materials & Solar Cells*, 130, 495–504

wet on wet deposition, N+1th layer solvent must be orthogonal to the lower Nth layer solvent to prevent its dissolving.

Aside from these technical considerations, tandem structure also implies a fine material engineering, regarding both the interconnecting layer (ICL) between the two subcells and the absorbing material of each of these cells. To mitigate photon loss, ICL's absorption in the range of interest should be minor. To minimize parasitic resistive effects, ICL should ensure a good ohmic contact between the cells. To minimize energy losses, ICL energy levels should fit into the overall device energy band diagram. As far as absorbers choice goes, although a large variety of materials combination is possible, with the goal of industrialization, multijunction cells should meet the PV market. Representing 95%⁴³ of this latter, crystalline Silicon (c-Si) appears as the obvious choice for the bottom cell material. Simulations show the optimum top cell bandgap for a c-Si-based tandem device to be 1.72 eV for a 2T configuration and 1.8 eV for a 4T configuration⁴⁴ (respectively red and green plot on Figure 8).

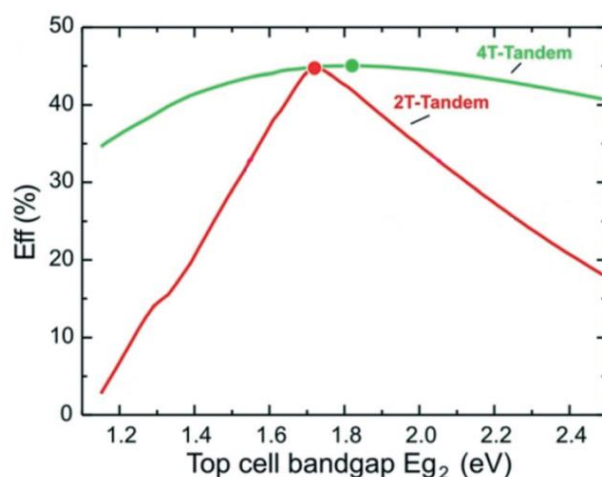


Figure 8. 2T and 4T tandem cell efficiency as a function of the top cell bandgap for a c-Si bottom cell with a 1.1 eV bandgap⁴⁵.

Owing to their tunable optical properties, their outstanding PV performances and their low cost manufacturing, perovskites stand out as very promising candidates for tandem applications. Their rise in the field of photovoltaics did not happen by accident and is supported by the numerous developments the perovskite technology underwent since its emergence, only ten years ago.

III. Perovskites in PV

While the first steps of perovskite in the field of photovoltaics were through the already existing Dye-Sensitized Solar Cells technology³⁵, perovskite PV eventually emerged as its own technology in 2012⁴⁶. The following year perovskites were nominated in *Science's* Top 10 breakthrough of the year as the “newcomer [that] juices up the race to harness sunlight”⁴⁷. Efficiencies went up very quickly to reach the symbolic 20% by 2015. Such rise in efficiency is unprecedented in the field of photovoltaics. As a matter of fact, it took only 6

⁴³ Franhofer Photovoltaics Report, March 2019

⁴⁴ T. Todorov *et al.*, (2016) *Mol. Syst. Des. Eng.*, 1, 370-6

⁴⁵ adapted from reference 44

⁴⁶ H-S. Kim *et al.*, (2012) *Sci Rep*, 2, 591

⁴⁷ *Sciences' top 10 breakthroughs 2013*

years for perovskites to go from 14 to 24% efficiency when it took 18 years for crystalline Silicon to do the same (Figure 9).

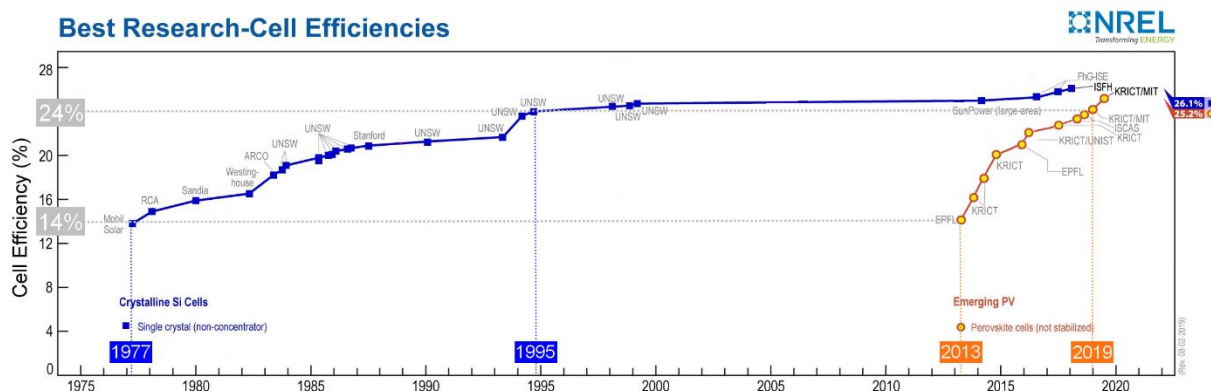


Figure 9. Simplified NREL chart for Best Research cell efficiencies with a focus on c-Si and perovskite technologies⁴⁸.

Due to this unprecedented rise in efficiency, perovskites quickly drew attention from the scientific community. Given their hybrid nature (organic A part and inorganic B part) and their uncanny electrical behaviour (J-V hysteresis), both chemists (in- and organic) and physicists took interest in these materials. The number of perovskite-related papers went from very few in 2009 to 3,500 in 2018, a rise mirrored (to an even stronger degree) by the steep increase in the number of citations from very few in 2009 up to 160,000 by 2018 (Figure 10). These two metrics highlight the excitement of the scientific community for perovskite PV.

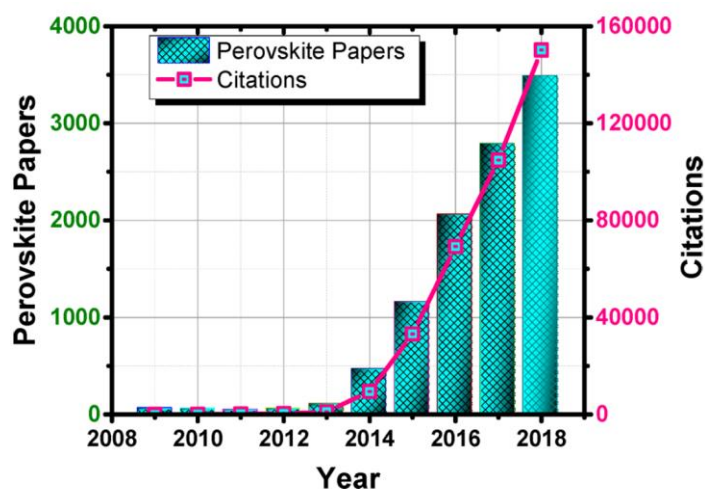


Figure 10. Rise of perovskite research as viewed through the published papers and their citation impact over the 2009–2018 period (Source: Web of Science, Clarivate Analytics March 3, 2019)⁴⁹.

Like for any other PV technology; even though the time lapse was shorter for perovskites; the increase in cell efficiency came with numbers of crucial advances along the way: new chemical compositions, new type of cells and new manufacturing processes.

⁴⁸ NREL efficiency chart (version 2019-08-02)

⁴⁹ De Angelis (2019) ACS Energy Lett., 4, 853–4

i. New perovskite compositions

Nearly half a decade after the ‘simple’ $\text{CH}_3\text{NH}_3\text{PbI}_3$ and $\text{CH}_3\text{NH}_3\text{PbBr}_3$ were used as dyes³⁵ (‘simple’ because A, B and X sites are occupied by single ions), the very first independently certified perovskite solar cell was reported at 14.1%⁵⁰ with a $\text{CH}_3\text{NH}_3\text{PbI}_3$ absorber. Few months later, a new record was set to 16.2%, this time with a mixed halide perovskite $\text{CH}_3\text{NH}_3\text{PbI}_{3-x}\text{Br}_x$ ⁵¹. The subsequent arrival of mixed cation perovskites was a game changer. In 2014, $\text{CH}(\text{NH}_2)^{2+}$ formamidinium cation (FA) was incorporated in the A site at the level of 85%⁵² and then 95%⁵³. In 2016, Saliba *et al.*⁵⁴ even proved the feasibility of incorporating a third cation, simultaneously establishing a new record of 21.1% with a Cs-containing perovskite. Except for the very first one, all reported NREL-certified research perovskite solar cells are based on mixed materials (Figure 11), making it one of the key aspects for the future of this technology.

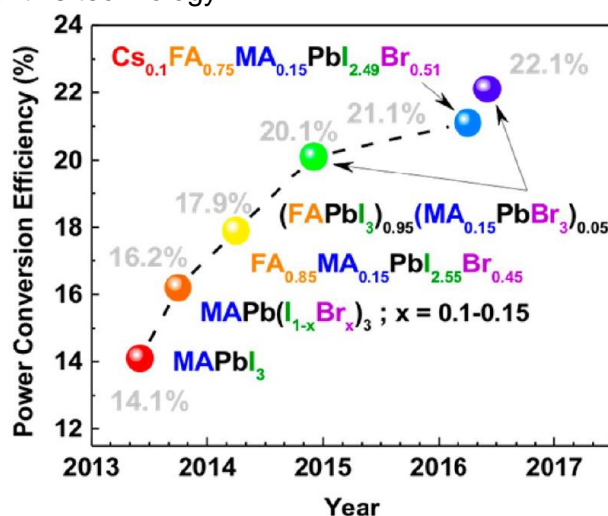


Figure 11. Evolution between 2013 and 2017 of the NREL-certified efficiencies for the best research perovskite solar cells⁵⁵ with the corresponding perovskite compositions.

Considering the 3D lattice defined by the corner-sharing PbX_6 octahedra with A-filled cavities, a relative freedom regarding the A-site cation size is allowed. In 1926, V. M. Goldschmidt rationalized an indicator accounting for the compatibility of ions within the 3D perovskite lattice⁵⁶. Considering a Pb-and-I-based perovskite, it is possible to predict the potential incorporation of a given A-cation into the network depending on the value of the calculated tolerance factor (Figure 12).

⁵⁰ J. Burschka *et al.*, (2013) *Nature*, 499, 316–319

⁵¹ N. J. Jeon *et al.*, (2014) *Nature Materials*, 13, p 897–903

⁵² N. J. Jeon *et al.*, (2015) *Nature*, 517 (7535), p 476-80

⁵³ W. S. Yang *et al.*, (2015) *Science*, 348 (6240) 1234-7

⁵⁴ M. Saliba *et al.*, (2016) *Energy Environ. Sci.*, 9, 1989

⁵⁵ L. K. Ono *et al.*, (2017) *ACS Appl. Mater. Interfaces*, 9, 30197–246

⁵⁶ V. M. Goldschmidt, (1926) *Die Naturwissenschaften*, 21, 477–85

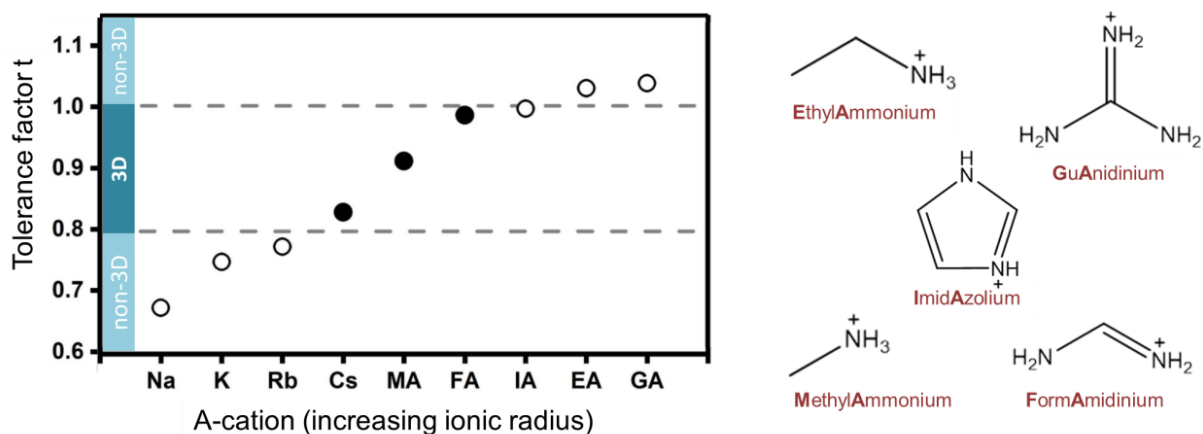


Figure 12. Tolerance factor values for various A cations (structures are shown on the right hand side for MA, FA, IA, EA and GA) and nature of the APbI₃ crystal network (3D or non 3D)⁵⁷.

Reducing mixed compositions to the sole aspect of higher efficiencies would be detrimental; they are also beneficial on other crucial levels. Incorporation of bromide for instance, enables fine tuning of the bandgap (as shown Figure 13 a). Incorporation of formamidinium or Caesium cations has been reported to increase stability of the material (as shown Figure 13 b for Cs⁺). Recently, addition of small amounts of Fluoride⁵⁸ or Imidazolium iodide (C₃N₂H₅)⁵⁹ have been reported to further increase device stability. Both aspects of bandgap tunability and device stability being critical for the industrialization of the technology, mixed compositions unquestionably represent the future of perovskite PV.

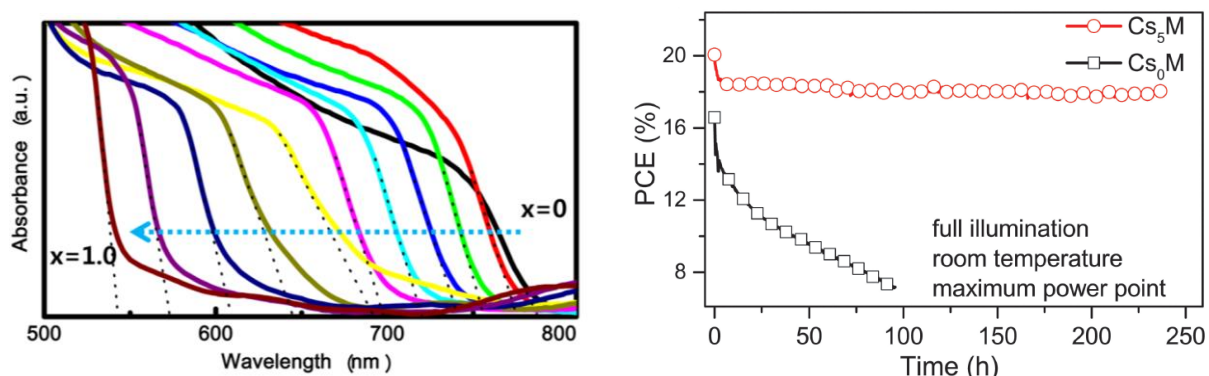


Figure 13. a) UV-vis absorption spectra of FTO/bl-TiO₂/mp-TiO₂/MAPb(I_{1-x}Br_x)₃/Au cells ($x \in [0; 1]$) measured using an integral spheres⁶⁰ and b) Aging of high performance Cs₅M and Cs₀M devices in a N₂ atmosphere (Cs_x(MA_{0.17}FA_{0.83})_{100-x}Pb(I_{0.83}Br_{0.17})₃ perovskite abbreviated as Cs_xM; M for 'mixed')⁵⁴.

ii. New types of cells

Derived from the DSSC technology, the first perovskite cells were very similar to Grätzel's ones⁶¹ with a mesoporous structure and an Electron Transporting Layer (n-type) / perovskite absorber (intrinsic) / Hole Transporting Layer (p-type) (from bottom to top) structure⁴⁶. In 2013 Jeng *et al.*⁶² introduced a fully planar heterojunction structure with a HTL (p) / perovskite absorber (i) / ETL (n) architecture referred to as 'inverted' with regard to the 'direct' one initially developed. Few months later, a direct planar heterojunction cell was

⁵⁷ adapted from M. Saliba *et al.*, (2016) *Science*, 354, 6309, 206-9

⁵⁸ N. Li *et al.*, (2019) *Nature Energy*, 4, 408-15

⁵⁹ M. Salado *et al.*, (2019) *ChemSusChem*, 12, 11

⁶⁰ J. H. Noh *et al.*, (2013) *Nano Lett.*, 13, 4, 1764-69

⁶¹ B. O'Regan and M. Grätzel, (1991) *Nature*, 353, 737-40

⁶² J-Y Jeng *et al.*, (2013) *Adv. Mater.*, 25, 27, 3727-32

reported⁶³. The following year, Wang *et al.*⁶⁴ reported on an inverted mesoscopic cell. Table 1 gathers examples of these four cell types.

	Direct architecture (<i>n-i-p</i>)	Inverted architecture (<i>p-i-n</i>)
Mesoporous structure	<p>Au Spiro-MeOTAD Perovskite mp-TiO₂ bl-TiO₂ FTO</p> <p>[65]</p>	<p>Al BCP PCBM NiO_x/CH₃NH₃PbI₃ Heterojunction sputtered NiO_x ITO</p> <p>[64]</p>
Planar structure	<p>top electrode spiro-OMeTAD perovskite SnO₂ glass & TCO</p> <p>[66]</p>	<p>Al BCP C₆₀ (Acceptor) CH₃NH₃PbI₃ (Donor) PEDOT:PSS ITO</p> <p>[62]</p>

Table 1. Inventory of the different types of perovskite cells (N.B. in the top left figure: “bl” and “mp”-TiO₂ stand for “blocking layer” *i.e.* compact and “mesoporous” respectively).

The use of mesoscopic bottom layers involves a high temperature sintering step (usually 500°C for TiO₂⁴⁶ and 300°C for NiO_x⁶⁷). With the objective of low cost devices, scientists quickly looked into avoiding this energy-consuming step, opening the way to the planar architecture. Owing to the lower active surface (*i.e.* statistically less interface for e⁻/h⁺ pair dissociation), efficiencies of the planar junctions are slightly lower than those of heterojunctions.

Taking a look at the nature of the transporting layers, the direct architecture can be seen as ‘Thin Film PV’-like (with inorganic materials TiO₂ and NiO_x) when the inverted one is closer to Organic PV (with PEDOT:PSS and PCBM). This differentiation echoes with the hybrid organic/inorganic nature of the perovskite material itself; stressing, once again, the rallying character of the perovskite photovoltaics field.

It is important to mention that while TiO₂, NiO_x, spiro-MeOTAD and PEDOT:PSS, PCBM and C₆₀ are the most widely used materials, the library for carrier-selective materials is quite rich (Figure 14) and a dense literature on the subject can be found for both Hole^{68,69,70,71} and Electron^{72,73,74,75} Transporting Materials.

⁶³ M. Liu *et al.*, (2013) *Nature*, 501, 7467, 395-8

⁶⁴ K-C. Wang *et al.*, (2014) *ACS Appl. Mater. Interfaces*, 6, 15, 11851-8

⁶⁵ X. Li *et al.*, (2015) *Nature Chemistry*, 7, 703-11

⁶⁶ M. Saliba *et al.*, (2018) *Chem. Mater.*, 30, 13, 4193-201

⁶⁷ K. C. Wang *et al.*, (2014) *Sc. Reports*, 23, 4, 4756

⁶⁸ Z. Yu and L. Sun, (2015) *Adv. Energy Mater.*, 5, 12, 1500213

⁶⁹ L. Caliò *et al.*, (2016) *Angew. Chem. Int. Ed.*, 55, 14522-45

⁷⁰ P. K. Kung *et al.*, (2018) *Adv. Mater. Interfaces*, 5, 1800882

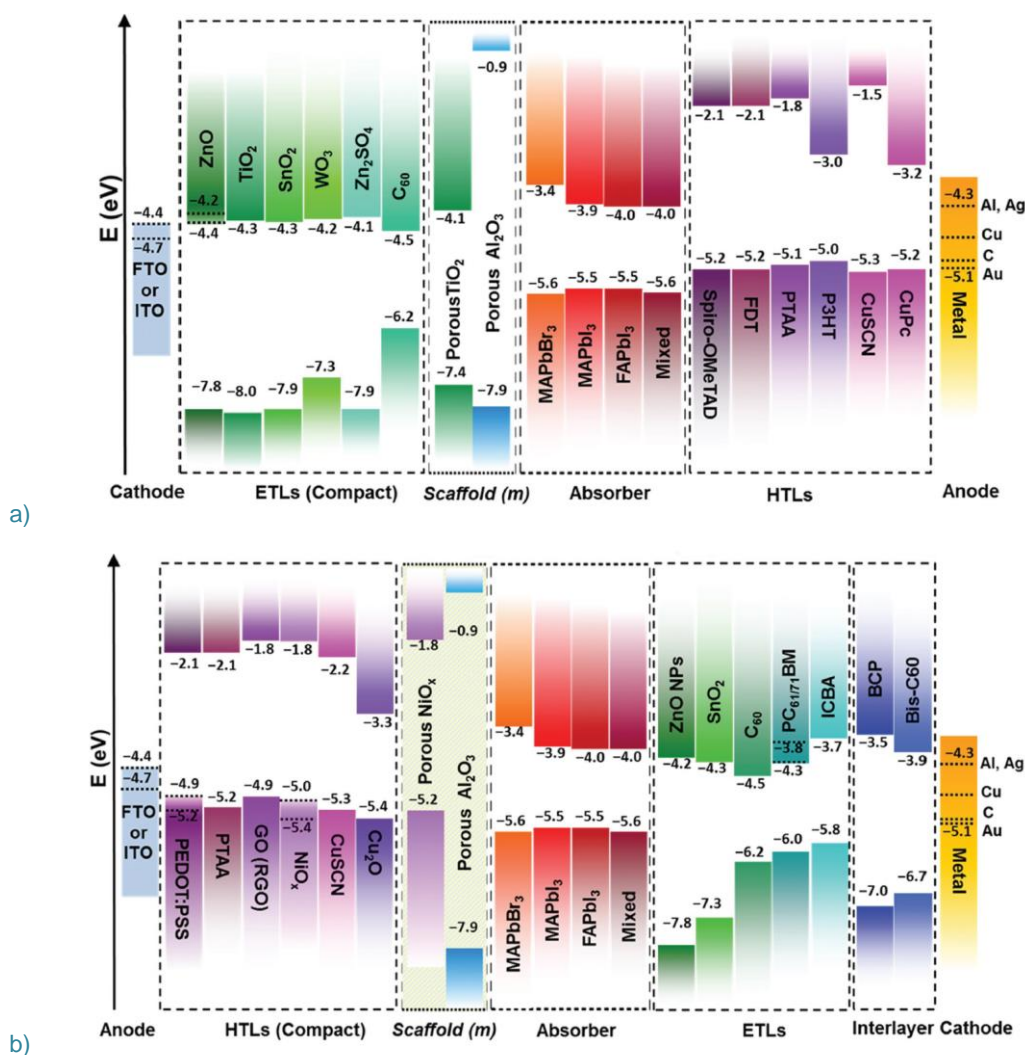


Figure 14. Energy level diagrams for a) n-i-p and b) p-i-n configurations with various Hole and Electron Transporting Layers (H/ETL)⁷⁶.

iii. New manufacturing processes

Among the numerous advantages of perovskites, their ease of process might be one of the most striking. The first perovskites for PV were deposited by the very simple and cheap spincoating technique³⁵: a solution containing $\text{CH}_3\text{NH}_3\text{X}$ and PbX_2 ($\text{X} = \text{I}^-$, Br^-) precursors was spincoated onto a substrate that was then annealed to form the perovskite layer. Solution-based techniques being rather cheap and simple to implement, there has been a lot of development in this field (Figure 15).

⁷¹ J. Urieta-Mora *et al.*, (2018) : Chem. Soc. Rev., 47, 8541-71

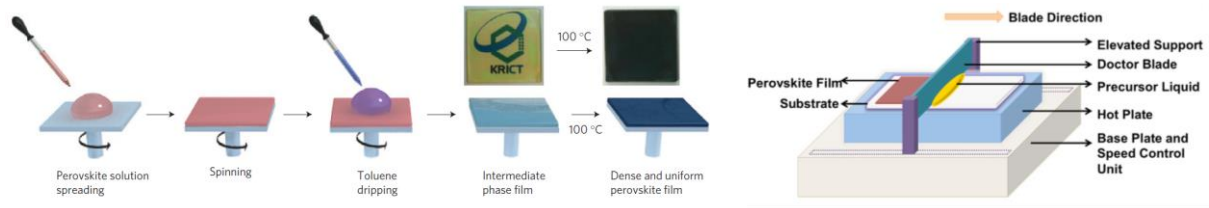
⁷² H. Liu *et al.*, (2016) Nanoscale, 8, 6209-21

⁷³ K. Mahmood *et al.*, (2017) RSC Adv., 7, 17044-62

⁷⁴ J. Lian *et al.*, (2018) Small Methods, 2, 1800082

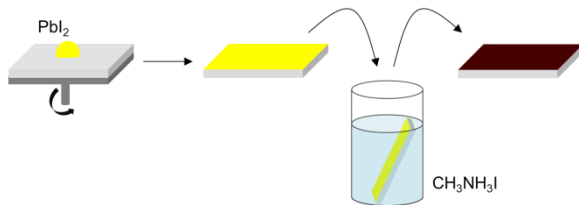
⁷⁵ Y. Chen *et al.*, (2019) J. of Energy Chem., 35, 144-67

⁷⁶ A. Rajagopal *et al.*, (2018) Adv. Mater., 30, 32, 1800455

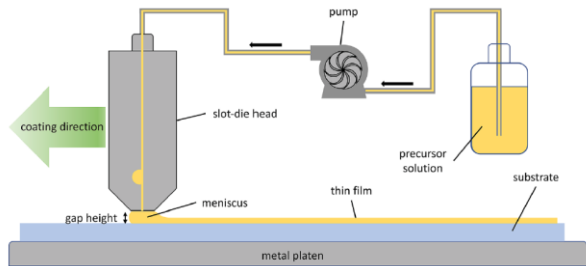


Spincoating with antisolvent treatment⁷⁷

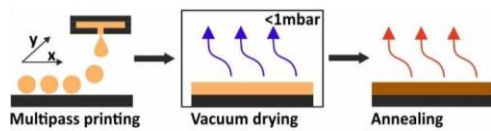
Doctor Blade⁷⁸



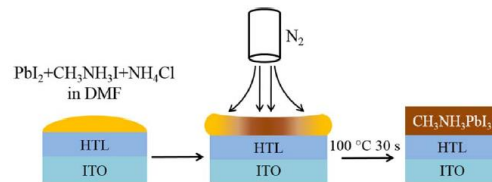
Two-step spincoating/dipping⁷⁹



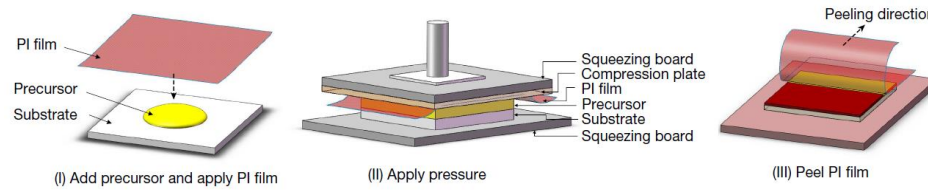
Slot die⁸⁰



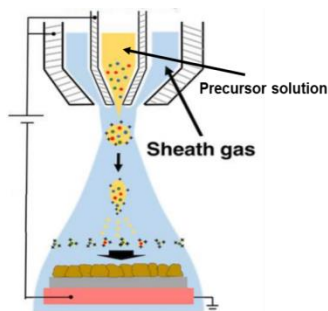
Inkjet printing⁸¹



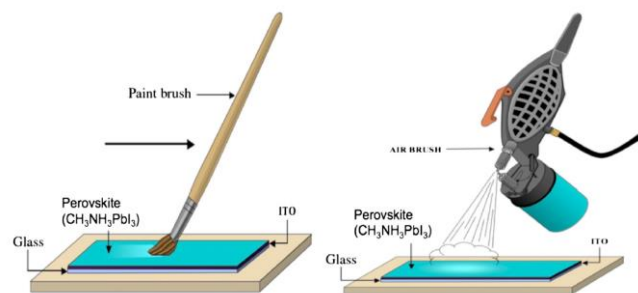
Blowing-assisted drop casting⁸²



Pressure processing method⁸³



Sheath-gas-assisted electrospray⁸⁴



Brush painting and spray coating⁸⁵

Figure 15. Overview of solution-based manufacturing techniques for perovskite thin films.

- ⁷⁷ N. J. Jeon *et al.*, (2014) *Nature Materials*, 13, 897-903
⁷⁸ A. T. Mallajosyula *et al.*, (2016) *Applied Materials Today*, 3, 96-102
⁷⁹ J. Burschka *et al.*, (2013) *Nature*, 499, 316-9
⁸⁰ J. B. Whitaker, (2018) *Sustainable Energy Fuels*, 2, 2442-9
⁸¹ F. Mathies *et al.*, (2016) *J. Mater. Chem. A*, 4, 19207-13
⁸² C. Zuo *et al.*, (2018) *Nano Energy*, 46, 185-92
⁸³ H. Chen *et al.*, (2017) *Nature*, 550, 92-5
⁸⁴ S. Han *et al.*, (2018) *ACS Appl. Mater. Interfaces*, 10, 8, 7281-8
⁸⁵ A. K. Chilvery *et al.*, (2015) *J. of Photonics for Energy*, 5, 053093

Besides the inherent varying parameters of these different techniques (ex. dispensing and coating speeds) there are numerous solution-related varying parameters. Several studies showed the impact of precursor molar ratio⁸⁶, solvent(s)⁸⁷ and aging⁸⁸ of the perovskite solution on the film quality. As such, there are now, for instance, almost as many recipes for spincoating processing as there are of scientists using this method.

While solution-based techniques are relatively easy to master, the large parameter plurality makes them hardly reproducible in between batches. Development of solvent-free methods has thus been undertaken. In 2013 the first vacuum-based perovskite layer for PV applications was fabricated using coevaporation process⁶³. Further developments were made in the field leading to two-steps processes and hybrid evaporation process (Figure 16). A non-exhaustive bibliography on vapor-deposited perovskites, published in 2016, can be found in Ono *et al.*⁸⁹.

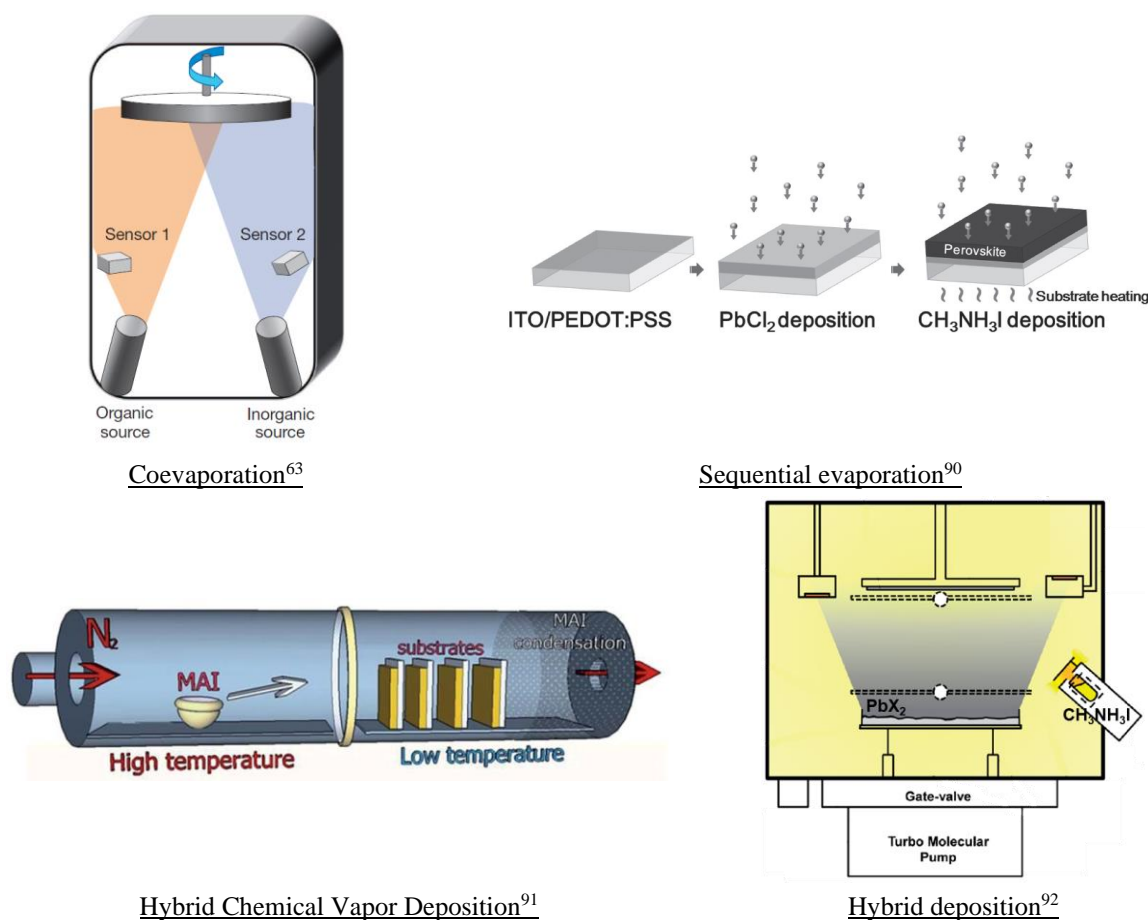


Figure 16. Overview of vacuum-based manufacturing techniques for perovskite thin films.

Due to the volatility of the organic compound during evaporation, control over the perovskite composition is harder to get with regards to the solution process where the molar ratio is controlled from the precursor solution concentration.

⁸⁶ K. Yan *et al.*, (2015) *J. Am. Chem. Soc.*, 137, 4460-8

⁸⁷ X. Cao *et al.*, (2019) *ACS Appl. Mater. Interfaces*, 11, 7639-54

⁸⁸ H. Tsai *et al.*, (2017) *Adv. Energy Mater.* 2017, 7, 1602159

⁸⁹ L. K. Ono *et al.*, (2016) *J. Mater. Chem. A*, 4, 6693-713

⁹⁰ C. W. Chen *et al.*, (2014) *Adv. Mater.*, 26, 38, 6647-52

⁹¹ M. R. Leyden *et al.*, (2014) *J. Mater. Chem. A*, 2, 18742-5

⁹² L. K. Ono *et al.*, (2014) *Energy Environ. Sci.*, 7, 3989-93

Adding to this already quite wide range of processing methods, perovskites thin films can also be fabricated using transfer methods. These latter combine the stoichiometric control of solution-based processes with the homogeneous and larger scale deposition features of vacuum-based processes. The first transfer method was reported in 1999 by Mitzi *et al.*⁹³ that fabricated various perovskites thin films using a single source thermal ablation process. It essentially consists in fabricating a perovskite crystal⁹⁴ or film⁹⁵ from solution based techniques and, using a vacuum reactor, to flash-evaporate it onto the desired substrate (Figure 17). The heating source usually consists of a regular power supply but the use of a laser has also been reported⁹⁶.

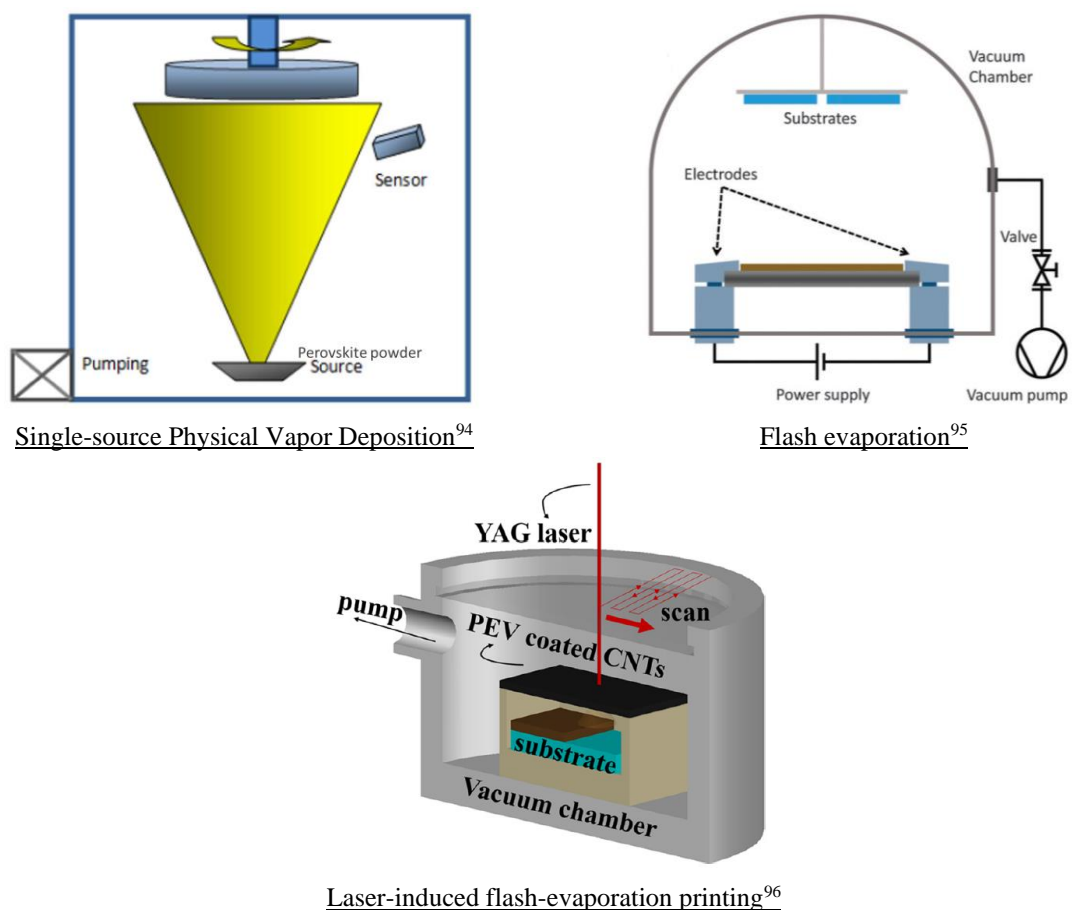


Figure 17. Transfer methods for perovskite thin films.

Over the years vapor-deposited perovskite cells have been challenging solution-processed ones in terms of efficiency, with the symbolic 20% achieved by the end of 2016 (Figure 18). While they require larger and more expensive equipments, they seem nonetheless more suited than solution-based techniques for the industrialization challenge awaiting the perovskite PV technology.

⁹³ D. B. Mitzi *et al.*, (1999) *Chem. Mater.*, 11, 542-4

⁹⁴ P. Fan *et al.*, (2016) *Sc. Reports*, 6, 29910

⁹⁵ G. Longo *et al.*, (2015) *Chem. Comm.*, 51, 7376

⁹⁶ M. Tai *et al.*, (2018) *ACS Appl. Mater. Interfaces*, 10, 26206-12

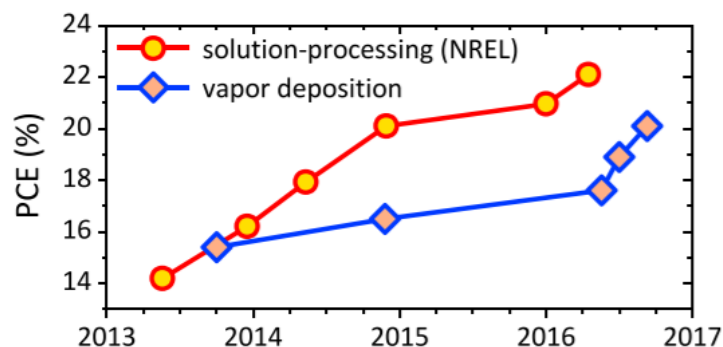


Figure 18. Evolution between 2013 and 2017 of the best research-cell efficiencies for perovskite solar cells obtained by solution processing or vapor deposition⁹⁷.

As a matter of fact, vapor-deposition allows fabrication of homogeneous films, over large area, on any substrate (*i. e.* textured c-Si for tandem applications), with both high repeatability and high reproducibility which makes it very suitable for industry-scale manufacturing. The evaporation technique is, for instance, already widely implemented for OLED (Organic Light Emitting Diodes), with the examples of OLEDON⁹⁸ and Universal Display Corporation⁹⁹ companies. For perovskites, with the future challenge of tandems and particularly the c-Si-based approach, coevaporation seems even more relevant. OXFORD PV Company¹⁰⁰, spin-out from the University of Oxford launched in 2010 by Henry Snaith and Kevin Arthur, spearheads the development on the topic.

In this context, I was asked to implement and develop the coevaporation process for perovskite thin films for large area solar cells using a semi-industrial equipment, starting with the $\text{CH}_3\text{NH}_3\text{PbI}_3$ reference material. In order to better apprehend the working environment, the next section develops all reported works on coevaporated $\text{CH}_3\text{NH}_3\text{PbI}_3$.

IV. 'Simple' $\text{CH}_3\text{NH}_3\text{PbI}_3$ thin films fabrication by coevaporation

The first report for a $\text{CH}_3\text{NH}_3\text{PbI}_3$ thin film by coevaporation can be found in Era *et al.*¹⁰¹ back in 1997. Using a simple dual-source evaporation setting, the authors fabricated various perovskite films starting from RNH_3I and PbI_2 . In this article the mention for $\text{CH}_3\text{NH}_3\text{PbI}_3$ is almost anecdotal and no further description other than a very brief « we succeeded in preparing thin films of the cubic perovskite (CH_3NH_3) PbI_3 » is given.

Almost twenty years later, Liu *et al.*⁶³ integrated for the first time vacuum-processed perovskites into PV devices. They used a dual-source evaporation reactor to fabricate a $\text{CH}_3\text{NH}_3\text{PbI}_{3-x}\text{Cl}_x$ perovskite from the simultaneous evaporation of $\text{CH}_3\text{NH}_3\text{I}$ and PbCl_2 . The fabricated film was of higher homogeneity (flat film with a mean thickness around 330 nm) when compared to a wet-processed spincoated one (undulating film with a thickness ranging from 50 to 410 nm) (Figure 19) and led to better performing PV devices (15.4% vs. 8.6% for a spincoated perovskite film).

⁹⁷ J. Avila *et al.*, (2017) *Joule*, 1, 3, 432-42

⁹⁸ OLEDON

⁹⁹ UDC

¹⁰⁰ OXFORD PV

¹⁰¹ M. Era *et al.*, (1997) *Chem. Mater.*, 9, 1, 8-10

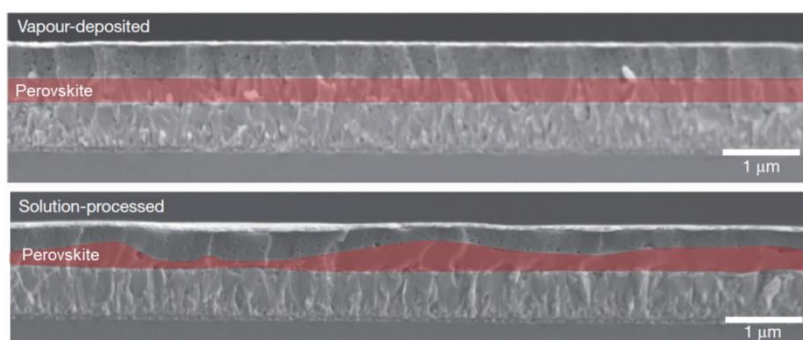


Figure 19. Cross-section SEM images of Glass/FTO/c-TiO₂/CH₃NH₃PbI_{3-x}Cl_x/Spiro-OMeTAD/Ag solar cells constructed from vapour-deposited and solution-processed perovskite films (highlighted in red on the images)¹⁰².

Few months later, at the Instituto de Ciencia Molecular (ICMol), Malinkiewicz *et al.*¹⁰³, reported on the very first evaporated CH₃NH₃PbI₃ for PV applications. The authors noticed that the organic compound exhibited a non-directive evaporation. Upon its heating to 70°C all three quartz sensors of the chamber (one at each evaporation source and one at the substrate holder, Figure 20) gave a signal even though the PbI₂ source was not running. They found themselves unable to calibrate the MAI sensor and had to adapt their process.

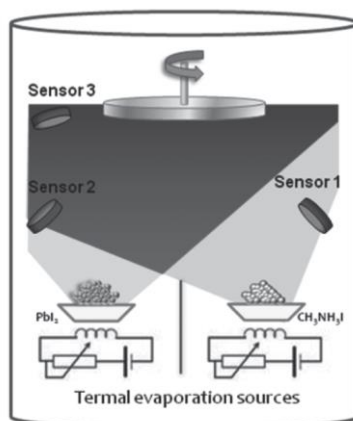


Figure 20. Scheme of the dual evaporation system from ICMol team¹⁰⁸.

They decided to first heat MAI to 70°C, waiting for its quartz sensor reading (sensor 1 on Figure 20) to be stable before heating up PbI₂ and then used this latter rate as the adjusting parameter. They determine the optimum heating temperature for PbI₂ to be 250°C, corresponding to a 0.5 Å/s deposition rate. Integrating these vacuum-processed perovskite layers into PV devices of structure ITO/PEDOT:PSS/polyTPD/perovskite/PCBM/Au they achieved at that time 12% efficiency on a 0.09 cm² device. Since then this procedure has been reported in tens of papers from the ICMol team (Table 2). Optimizing the charge transport layers, efficiencies over 20% have been achieved (on 0.01 cm² cells) with a complex fully evaporated structure¹¹⁴. Outside this team, only very few works on coevaporated CH₃NH₃PbI₃ thin films for PV applications have been reported.

A team from Seoul National University (SNU) developed a MAI-vapor-pressure-based method¹⁰⁵. In their first paper in 2015¹⁰⁴, Kim *et al.* followed ICMol's procedure, heating MAI up to 70°C, to reach a pressure of 2.10⁻⁵ Torr, while PbI₂ was set to a deposition rate of

¹⁰² adapted from reference [63]

¹⁰³ O. Malinkiewicz *et al.*, (2014) *Nature Photonics*, 8, 128-32

¹⁰⁴ B. S. Kim *et al.*, (2015) *Org. Elec.*, 17, 102-6

0.5 Å/s (read on sensor 1, Figure 21). Over 72 samples (within 6 different batches) of ITO/MoO₃/NPB/CH₃NH₃PbI₃/C₆₀/BCP/Al structure with a 0.04 cm² active area, the PCE Gaussian distribution reached its peak between 11 and 12%. Their best device achieved a 13.7% efficiency.

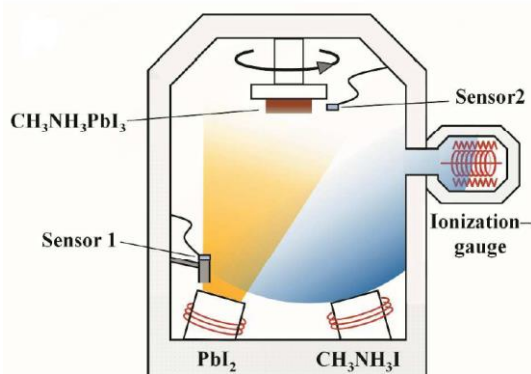


Figure 21. Scheme of the dual evaporation system from SNU team¹⁰⁵.

One year later, in their second paper, SNU's team report their MAI-vapor-pressure-based method¹⁰⁵. They varied the MAI vapor pressure from 0.6 to 8.3.10⁻⁵ Torr in between experiments (the pressure during deposition was kept constant \pm 0.1 Torr by controlling the MAI crucible temperature). They specify in this paper that « a 2 nm thick PbI₂ layer was deposited before heating up the MAI » but no mention of any temperature was made in the overall paper. We expect them to have followed, for this second paper too, the procedure developed at ICMol with the 250°C and 70°C target temperatures for PbI₂ and MAI respectively. In 2015, they had found this MAI temperature to yield a 2.10⁻⁵ Torr vapor pressure. In their second paper where this vapor pressure is quite finely tuned (between 0.6 and 8.3.10⁻⁵ Torr), the authors unfortunately fail to provide any temperature values corresponding to this pressure management.

Another report of coevaporated CH₃NH₃PbI₃ was found in Lin *et al.*¹⁰⁶, with very few details provided. The authors heated the CH₃NH₃I precursor up to a constant 100°C and the PbI₂ temperature was varied between 250 and 280°C yielding an overall deposition rate between 0.3 and 1.1 Å/s (monitored by a single sensor positioned between the two sources). They claim 260°C is the optimal PbI₂ temperature for their evaporation configuration but fail to provide the corresponding deposition rate. Integrating the fabricated films into perovskite devices of structure ITO/PEDOT:PSS/PCDTBT/CH₃NH₃PbI₃/PCBM/LiF/Ag they achieved 16.5% (on 0.2 cm²), a record at that time for a non-oxide perovskite cell.

¹⁰⁵ B. S. Kim *et al.*, (2016) *J. Mater. Chem. A*, 4, 15, 5663-8

¹⁰⁶ Q. Lin *et al.*, (2015) *Nature Photonics*, 9, 106-12

Coevaporation conditions <i>disclosed</i>	Photovoltaic devices		
	Structure (if given, active area in cm²)	PCE (%)	ref.
CH ₃ NH ₃ I 70°C PbI ₂ 250°C; 0.5 Å/s "ICMol procedure"	ITO/PEDOT:PSS/polyTPD/CH ₃ NH ₃ PbI ₃ /PCBM/Au (0.09) (0.98)	12.04 8.27	[103]
	ITO/PEDOT:PSS/polyTPD/CH ₃ NH ₃ PbI ₃ /PCBM/Au (0.06)	12.7	[107]
	ITO/PEDOT:PSS/polyTPD/CH ₃ NH ₃ PbI ₃ /PCBM/3TPYMB/Au (0.065) (0.95)	14.8 10.9	[108]
	ITO/PEDOT:PSS/polyTPD/CH ₃ NH ₃ PbI ₃ /Fullerene/Ba/Au PCBM C ₆₀ (N/A)	15.2 14.7	[109]
	ITO/PEDOT:PSS/polyTPD/CH ₃ NH ₃ PbI ₃ /Fullerene/Ba/Ag PCBM PCBB (N/A)	13.6 13.3	[110]
	ITO/PEDOT:PSS/polyTPD/CH ₃ NH ₃ PbI ₃ /IPH/PDINO/Ag ... /Ba/Ag ... /PFNBr/Ag (N/A)	14.3 13.7 13.9	[111]
	ITO/TaTm:F ₆ -TCNNQ/TaTm/CH ₃ NH ₃ PbI ₃ /C ₆₀ /C ₆₀ :PhIm/Ag (0.01)	15.8	[112]
	ITO/C ₆₀ :PhIm/C ₆₀ /CH ₃ NH ₃ PbI ₃ /TaTm/TaTm:F ₆ -TCNNQ/Au (0.01) (0.1)	18.0 20.3	
	ITO/PEDOT:PSS/polyTPD/CH ₃ NH ₃ PbI ₃ /IPH/PDINO/Ag (0.01)	15.30	[113]
	ITO/MoO ₃ /TBDI/CH ₃ NH ₃ PbI ₃ /IPH/PDINO/Ag (0.01)	14.85	
	ITO/TiO ₂ /C ₆₀ /CH ₃ NH ₃ PbI ₃ /TaTm/TaTm:F ₆ -TCNNQ/Au (0.01)	20.83	[114]
	ITO/MoO ₃ /HTM/CH ₃ NH ₃ PbI ₃ /C ₆₀ /BCP/Ag m-MTDATA TaTm TcTa (N/A)	14.4 16.3 12.2	[115]
	ITO/MoO ₃ /HTM/CH ₃ NH ₃ PbI ₃ /C ₆₀ /BCP/Ag TaTm TPA-2,7-FLTPA-TPA TPA-3,6-FLTPA-TPA (0.01)	15.9 17.1 13.9	[116]

¹⁰⁷ C. Momblona *et al.*, (2014) *APL Mater.*, 2, 8, 081504

¹⁰⁸ O. Malinkiewicz *et al.*, (2014) *Adv. Energy Mater.*, 4, 1400345

¹⁰⁹ G. El-Hajje *et al.*, (2016) *Energy Environ. Sci.*, 9, 2286-94

¹¹⁰ L. Gil-Escrig *et al.*, (2016) *J. Mater. Chem. A*, 4, 3667-72

¹¹¹ L. Gil-Escrig *et al.*, (2016) *Organic Electronics*, 37, 396-401

¹¹² C. Momblona *et al.*, (2016) *Energy Environ. Sci.*, 9, 3456

¹¹³ L. Caliò *et al.*, (2017) *Solar Energy Mater. & Solar Cells*, 163, 237-41

¹¹⁴ D. Pérez del Rey *et al.*, (2018) *J. Phys. Chem. Lett.*, 9, 5, 1041-6

¹¹⁵ B. Dänekamp *et al.*, (2019) *J. Mater. Chem. B*, 7, 523-7

¹¹⁶ H. D. Pham *et al.*, (2019) *J. Mater. Chem. A*, 7, 12507-17

	ITO/C ₆₀ :PhIm/C ₆₀ /CH ₃ NH ₃ PbI ₃ /TaTm/TaTm:F ₆ -TCNNQ/Au (N/A)	18.2	[117]
	TCO/MoO ₃ /TaTm/CH ₃ NH ₃ PbI ₃ /C ₆₀ /BCP/Ag (0.0651)	19.3	[118]
	TCO/TiO ₂ /C ₆₀ /CH ₃ NH ₃ PbI ₃ /TaTm/TPBi/MoO ₃ /Au (0.0651)	18.8	
CH ₃ NH ₃ I vapor pressure of 2.10 ⁻⁵ Torr PbI ₂ 0.5 Å/s	ITO/MoO ₃ /NPB/CH ₃ NH ₃ PbI ₃ /C ₆₀ /BCP/Al (0.04)	13.7	[104]
CH ₃ NH ₃ I vapor pressure of 5.1.10 ⁻⁵ Torr PbI ₂ 0.5 Å/s	ITO/MoO ₃ /NPB/CH ₃ NH ₃ PbI ₃ /C ₆₀ /BCP/Al (0.04)	14.1	[105]
CH ₃ NH ₃ I 100°C PbI ₂ 260°C	ITO/PEDOT:PSS/PCDTBT/CH ₃ NH ₃ PbI ₃ /PCBM/LiF/Ag (0.2)	16.5	[106]
CH ₃ NH ₃ I vapor pressure of 1.23.10 ⁻⁴ mbar PbI ₂ 3 Å/s	FTO/TiO ₂ /CH ₃ NH ₃ PbI ₃ /Spiro-MeOTAD/Au (0.16)	13	[119]
CH ₃ NH ₃ I vapor pressure of 5.10 ⁻⁵ Torr PbI ₂ 0.75 Å/s	FTO/C ₆₀ /CH ₃ NH ₃ PbI ₃ /Spiro-OMeTAD/Au (0.08)	15.7	[120]
CH ₃ NH ₃ I 0.4 Å/s PbI ₂ 0.4 Å/s	FTO/c-TiO ₂ /CH ₃ NH ₃ PbI ₃ /Spiro-OMeTAD/Ag FTO/C ₆₀ /CH ₃ NH ₃ PbI ₃ /Spiro-OMeTAD/Ag FTO/ c-TiO ₂ /PCBM/CH ₃ NH ₃ PbI ₃ /Spiro-OMeTAD/Ag FTO/poly-TPD/CH ₃ NH ₃ PbI ₃ /PCBM/BCP/Ag (0.0919)	15.8 15.4 13.6 12.6	[121]

Table 2. Summary of reported coevaporated CH₃NH₃PbI₃ perovskite thin films for PV applications.

It is worth noting that except two reports for ~ 1 cm² active area cell and two for 0.2 cm², all cells are well below 0.1 cm². Another striking fact is the lack of consistency in the disclosed deposition conditions: no mention of temperature for some papers and no mention of rates for others. It appears clear from this literature review that pressure is a key parameter of the coevaporation process.

With less than 20 papers found on coevaporated CH₃NH₃PbI₃ films for PV applications since 2013, the topic of the present thesis seems rather far from the raging ‘war’ of other perovskites-related subjects.

¹¹⁷ D. Kiermasch *et al.*, (2019) *J. Mater. Chem. A*, 7, 14712-22

¹¹⁸ D. Pérez del Rey *et al.*, (2019) *Chem. Mater.* DOI: 10.1021/acs.chemmater.9b01396

¹¹⁹ J. Teuscher *et al.*, (2015) *ChemSusChem*, 8, 3847-52

¹²⁰ D. Zhao *et al.*, (2016) *Nano Energy*, 19, 88-97

¹²¹ J. B. Patel *et al.*, (2017) *Adv. Electron. Mater.*, 1600470

Conclusion

With the present chapter we have set the scene for this thesis, starting off by introducing the perovskite materials and their broad family, we eventually narrowed down to halide ones. Among their outstanding optoelectronics properties, our interest in the scope of this manuscript lies within photovoltaics. Consequently, we took a step aside to unwind some key aspects of the field: photoconversion process steps, solar cells and their characterization. We finally focused on the multijunction approach since it represents a significant part of the future of photovoltaics.

We then developed the history of halide perovskites photovoltaics, going through the major developments made along its decade of existence. From their very first use as dyes in Grätzel cells in 2009 with an efficiency of 3.8%, halide perovskites now allow 25.2% efficient photoconversion, at the lab-scale. As they became a distinct photovoltaic branch, perovskite solar cells went through few revolutions. First revolution (and maybe the most crucial one): the introduction of mixed compositions. Perovskites went from the very basic $\text{CH}_3\text{NH}_3\text{PbI}_3$ to more complex formulations such as $\text{Cs}_{0.1}(\text{CH}(\text{NH}_2)_2)_{0.75}(\text{CH}_3\text{NH}_3)_{0.15}\text{PbI}_{2.49}\text{Br}_{0.51}$. These latter seem to tackle both the efficiency and stability issues while allowing a fine tuning of the optical properties of the material. Second revolution: the development of new types of device. Perovskites solar cells extended from DSSC-like mesoporous architecture in n-i-p structure toward fully planar architectures and p-i-n structures. Benefiting from their hybrid nature, perovskite have been investigated by both organic and inorganic chemists and physicists, leading to a large variety of solar devices. Third revolution: the explosion of deposition processes. From their initial deposition using basic spincoating method, perovskite thin films can now be obtained by a large variety of techniques, in pure phase (both wet and dry) as well as in mixed phase, as highlighted by the provided overview.

With the increasing interest for perovskites as light absorbers, whether it will be through the single or the multijunction approach, next step of perovskite PV development surely lies within their industrialization. With this objective, I was asked to implement the coevaporation process for perovskite thin films fabrication. The last section of this chapter provided a summary of all reported works on evaporation-based fabrication of the reference perovskite material $\text{CH}_3\text{NH}_3\text{PbI}_3$, setting the scene for the next chapters of this manuscript.

Chapter 2.

Design and engineering of a reactor for perovskite coevaporation.

“If I had nine hours to chop down a tree, I’d spend the first six sharpening my axe.”

A. Lincoln

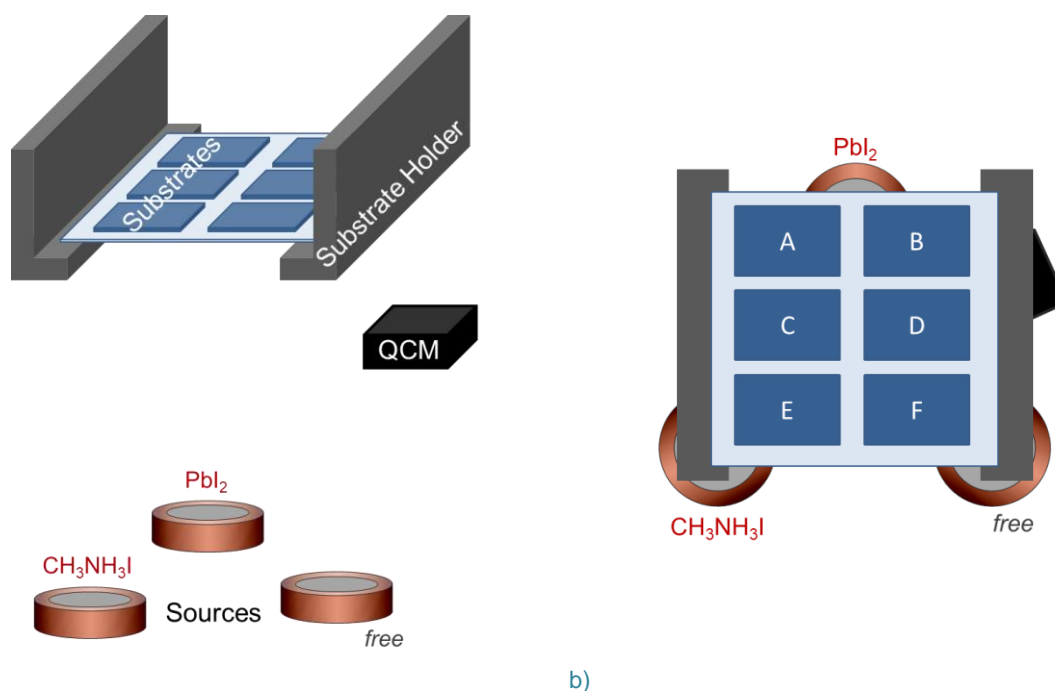
Introduction

Although the first report for dry-processed perovskite thin films goes back almost ten years before the 'perovskite boom' in photovoltaics, for most of the development in that field the wet phase was preferred. Being relatively easy and cheap to implement, solution-based processes are still extensively performed but have the drawback of entailing a high variability, both intra and inter-batches. Given the commercialization challenge that perovskite photovoltaic is facing, interest for vacuum-based techniques has lately been revived. As they combine homogeneous large area with low cost manufacturing, they are expected to hold the key to the future of perovskite solar cells.

In this context I was asked to develop at IPVF and LPICM the coevaporation process for perovskite materials, starting with the reference $\text{CH}_3\text{NH}_3\text{PbI}_3$. With only a few reported papers, most of them coming from the ICMol team, coevaporation of this material appears very challenging, with the organic salt described as complicated to control. My work initially consisted in establishing the feasibility of the coevaporation process using a proof-of-concept reactor. Feedbacks from this latter helped us chose relevant features guiding the design of the new dedicated equipment that was eventually delivered in the second year of this thesis. From then I was in charge of implementing and developing the perovskite coevaporation process using this dedicated reactor.

I. Coevaporation process for perovskites using a proof-of-concept reactor

Initial developments were carried out using a reactor from RIBER company. The system, initially designed for ozone treatment, was 'recycled' to deposit perovskites as a proof of concept. The reactor is equipped with three sources, a single Quartz Crystal Microbalance (QCM) sensor and a stationary substrate holder suited for 6 substrates of 17x25 mm² dimension. Schematic views of the reactor are given Figure 22 (see Table 3 page 42 for more details).



a) **Figure 22.** Schematic side (a) and top (b) views of the interior of the RIBER reactor set up with its three sources, its QCM sensor and the stationary substrate holder with the six samples.

With the purpose of perovskite coevaporation, we started with the methylammonium lead triiodide ($\text{CH}_3\text{NH}_3\text{PbI}_3$ or MAPbI_3) reference material synthesized from PbI_2 and $\text{CH}_3\text{NH}_3\text{I}$ (or MAI), each loaded in a source of the reactor as shown Figure 22.

Since the purpose of this reactor was the proof of concept only few results will be disclosed in the following sections, going from initial results setting the ground for the design of the next reactor (I.i.) to results assessing the feasibility of the process (I.ii.).

i. Initial developments and identification of missing features

Upon exploring the MAI heating behaviour, which is expected to be complicated based on the previously reported studies (see Table 2), we noticed that the chamber pressure increased, gaining about one order of magnitude from its initial value upon heating of the organic salt (Figure 23).

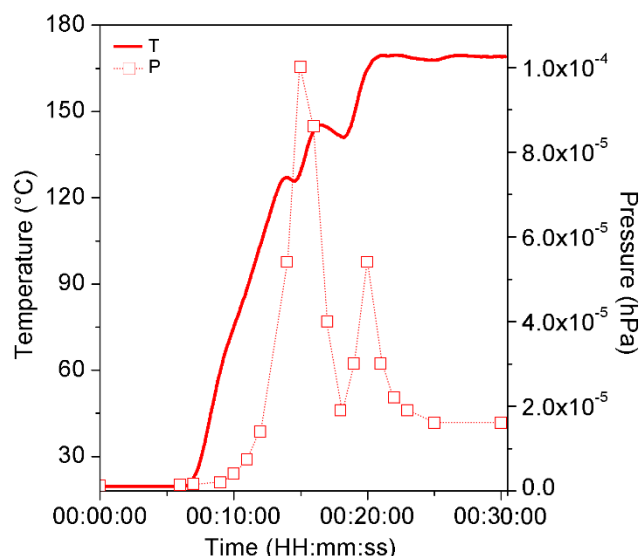


Figure 23. Temperature (solid line) and pressure plots (dotted line with symbols) for MAI heating.

This pressure boost, that doesn't occur with PbI_2 evaporation, shows the volatility of the methylammonium iodide compound. Accordingly, we anticipate the organic material to be difficult to control, possibly evaporating as a 'cloud' filling the entire reactor volume during the process. From the rate plot displayed Figure 24a, we see that the MAI deposition rate keeps increasing while the temperature is constant; compared to PbI_2 for which the rate is constant when the temperature is stable (Figure 24b). This trend supports our hypothesis of dynamic MAI vapour cloud swirling in the chamber during the process, inducing a variable rate response.

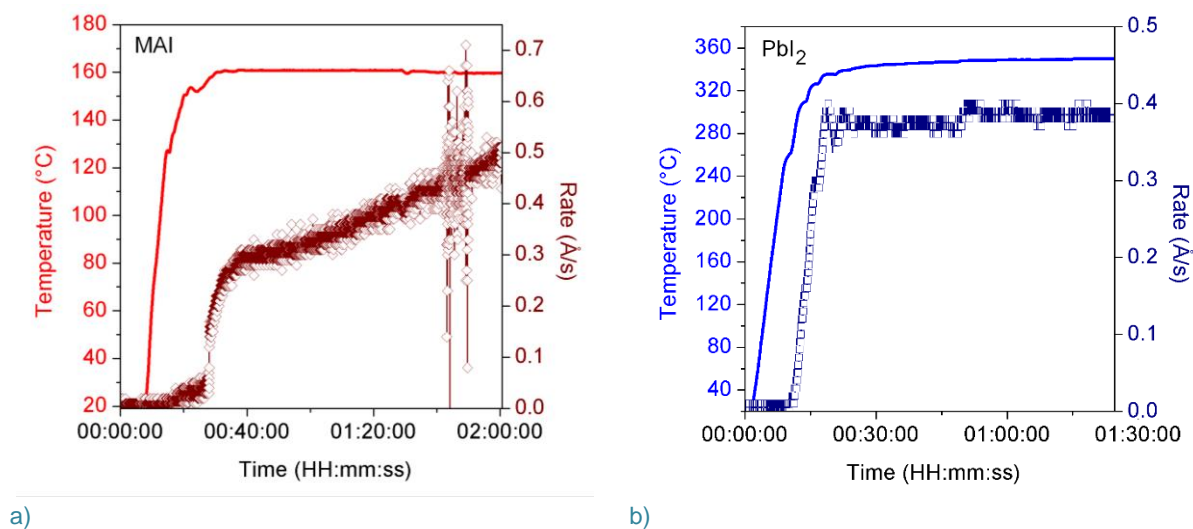


Figure 24. Temperature (solid line) and deposition rate (solid line with symbols) plots for single-compound evaporation processes of a) MAI and b) PbI_2 .

From this early realization, we expect the MAI behaviour and the chamber pressure to be closely linked. Unfortunately we found ourselves unable to accurately monitor the pressure on this reactor as it can only be read on the vacuum pump box and is not monitored from the software interface. In order to better understand the MAI temperature correlation with pressure we would include in the new reactor specifications the precise and direct live monitoring of the pressure from the software.

The observation of MAI deposition on the back of samples and all over the chamber walls further supported our hypothesis of an organic cloud filling the entire reactor volume. From our different experiments we roughly estimated a temperature of 40°C to trigger the pressure increase (Figure 23) and thus, in our opinion, the evaporation of MAI. In addition to the vapour arising from the MAI source heating (intended), we would potentially also have MAI redepositing from the walls (far from intended). Given the high temperature of the PbI_2 source (>200°C) and the sources/walls closeness we suspect the source heating to radiate toward the walls causing the release of the MAI deposited during the previous experiments.

Being intrinsically linked to the MAI compound, this vapour cannot be suppressed and kicks off as soon as 40°C is reached. While we cannot avoid it, we can counter it by depositing an initial layer of PbI_2 that would be converted into perovskite following a vapour-assisted process, previously reported for perovskites¹²², as the MAI cloud occurs. Following this idea, we then adapted our process by dephasing PbI_2 and MAI heatings (that were previously simultaneously started as shown Figure 25a) and integrating a step where few nanometres of PbI_2 are deposited while the organic source is still at room temperature (RT), *i. e.* below the 40°C triggering temperature (T_{trig}) (Figure 25b).

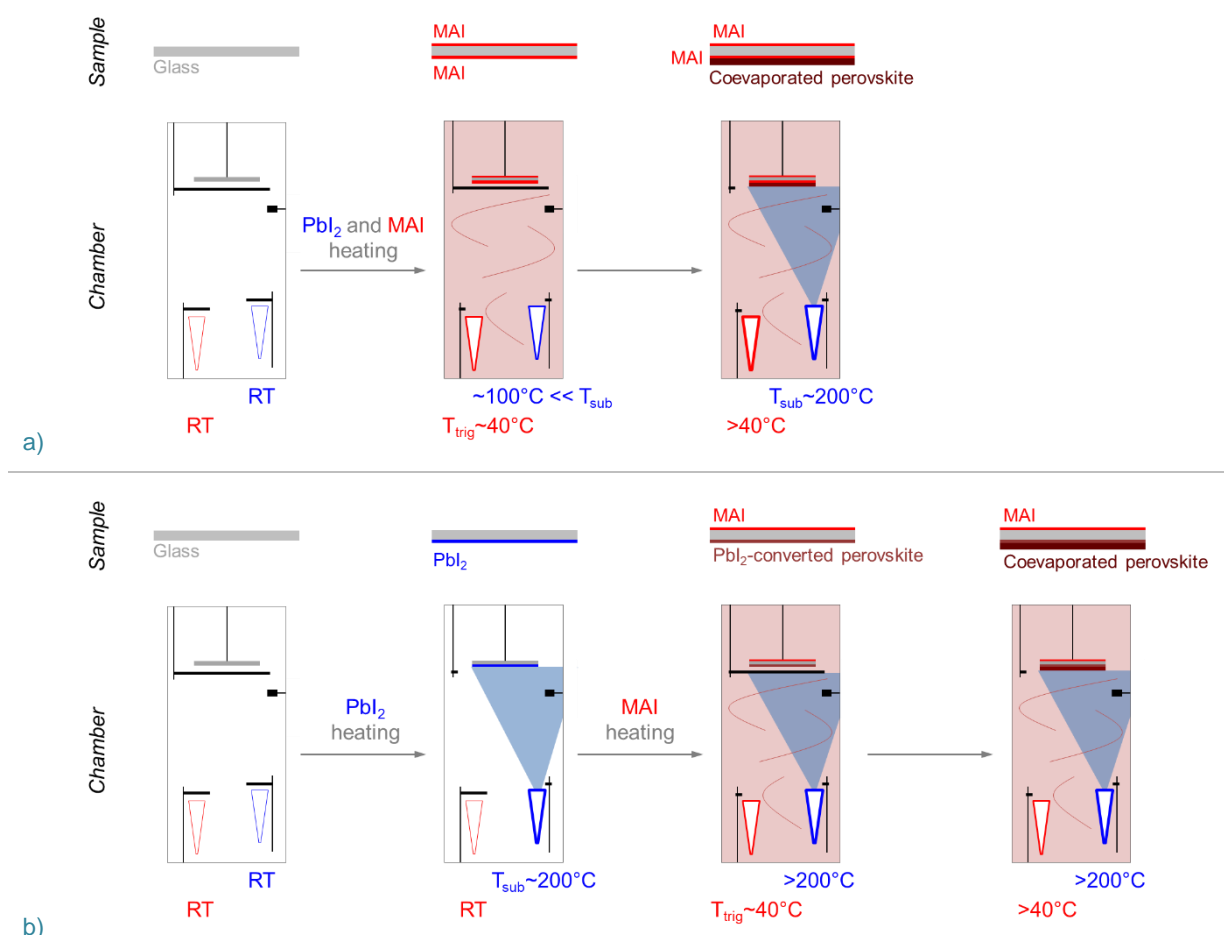


Figure 25. a) Initial heating process: MAI and PbI_2 are heated from the same starting point, causing some parasitic MAI to deposit on both sides of the samples as 40°C is reached that will remain when coevaporation is performed and b) Updated heating process: PbI_2 is first heated, few nm are deposited as its sublimation temperature is reached ($T_{\text{sub}} \sim 200^\circ\text{C}$) while MAI is still at room temperature (RT), then MAI is heated and the initial PbI_2 is converted into perovskite as the organic vapour appears followed by the deposition of coevaporated perovskite.

¹²² Q. Chen *et al.*, (2014) *J. Am. Chem. Soc.*, 136, 2, 622-5

While this updated process does prevent the deposition of parasitic MAI originating from the source heating, it hardly prevents the parasitic MAI coming from the walls (PbI₂ sublimation temperature of 200°C being surely high enough to activate the release of MAI off the walls). This MAI release seems hardly avoidable as it would involve a thorough cleaning of the reactor by hand before every experiment. This cannot be reasonably done as it would tremendously increase the workload (and the risk due to Pb exposure) to properly clean the reactor as well as the down time between experiments. Increasing the source-to-walls distance could be a viable alternative, worth implementing on the next equipment.

Further into our developments, we identified two supplementary features missing from the present reactor that we deem relevant to implement on the new equipment: the presence of one QCM per source and the rotation of the substrate holder.

As shown Figure 22, this proof-of-concept reactor is equipped with a single QCM sensor, making it impossible to follow each material deposition rate throughout a multi-source coevaporation process. To bypass this matter we have decided to work in three phases: settings, coevaporation and checking. In the initial setting phase, by alternatively shutting the two sources (MAI source shutter closed when PbI₂ source one is open and vice versa), it is possible; although tedious; to follow and adjust each deposition rate. During the coevaporation phase, the two sources are opened and what is monitored by the microbalance (given its location) is the PbI₂+MAI deposition rate, estimated to be the 'perovskite' deposition rate. Once the coevaporation is over, we proceed similarly to the initial phase (shutting one source while looking at the other) to check the end-of-process deposition rates of the two materials (so called 'checking phase'). An example of deposition rate plot is shown Figure 26 to illustrate the different phases.

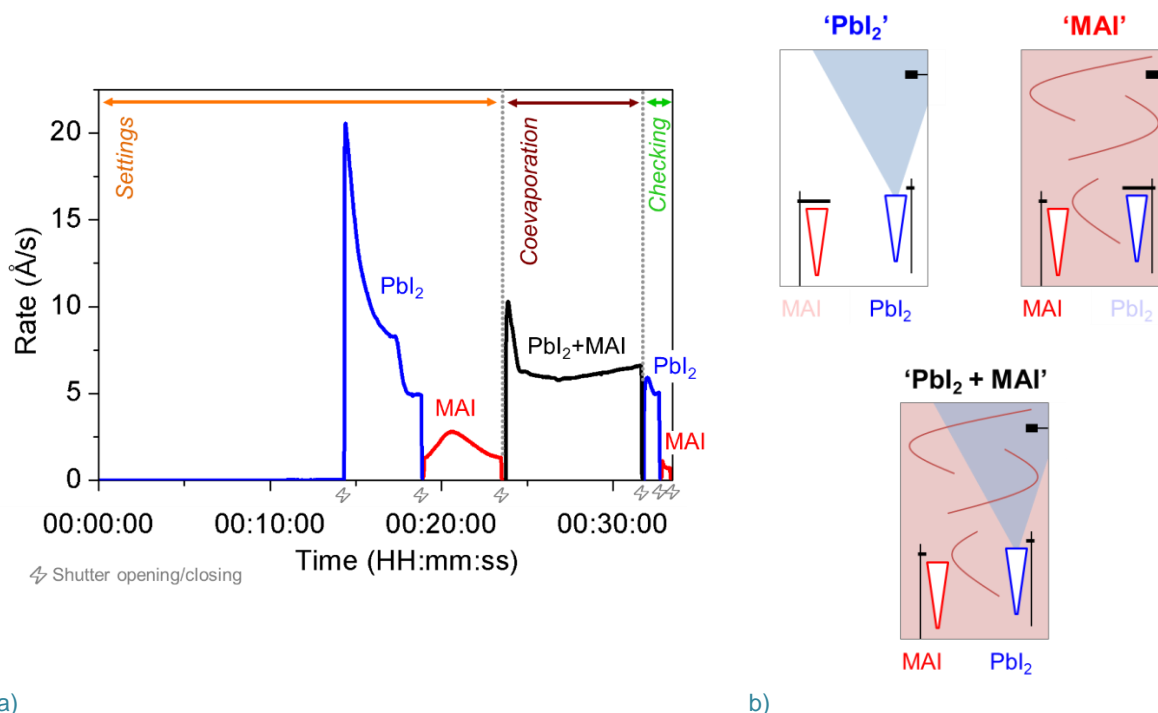


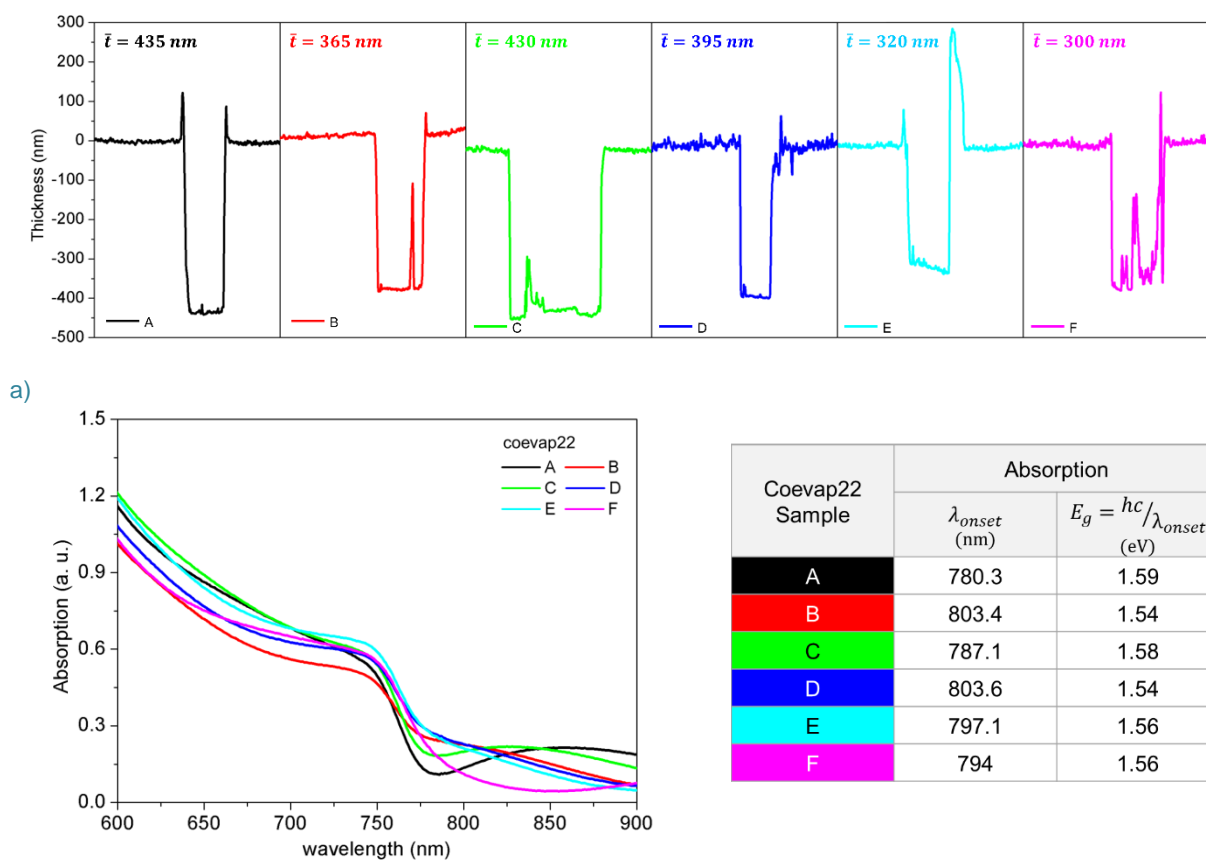
Figure 26. a) Deposition rate plot for a full process showing the settings, coevaporation and checking phases and b) corresponding shutter status for PbI₂, MAI and PbI₂+MAI QCM sensor reading.

Since it is not possible to monitor the precursors (PbI₂ and MAI) instant deposition rates, any temperature adjustment made during the coevaporation phase is done blindly.

Indeed, the user has no way to assess the impact of a temperature increase on the corresponding deposition rate but can only see the impact on the overall PbI₂+MAI QCM sensor reading. It is thus very difficult to be sure that although two batches of samples are deposited with the same PbI₂+MAI ‘perovskite’ rate, that they do indeed have the same PbI₂ and MAI instant rates (*i. e.* the same composition). Consequently, we integrate in the new design the presence of one QCM sensor per source to get a more accurate reading of each material deposition rate.

Following our initial investigations, we foresee that the organic salt will behave erratically, its evaporation cloud swirling inside the reactor during the coevaporation process as it does for single-compound evaporation. With the technical impossibility to rotate the substrate holder during the process on this reactor, we expect this phenomenon to impair the homogeneity of the deposition as well as, potentially, the composition of the films.

Indeed, as shown Figure 27 for one experiment (*i. e.* 6 samples as shown Figure 22), we do see a variability both in the film thickness which ranges from 300 to 435 nm (Figure 29a) and in composition with an onset absorption wavelength varying from 780 to almost 804 nm. From the profilometry measurements one can also notice a difference in film roughness comparing sample C to D, the latter exhibiting a noisier signal for the non-scratched part of the profile. The thickness inhomogeneity can also be seen from the absorption spectra, with low energy absorption tail (from 800 nm) originating from interference effect due to thick films for samples A and C.



b) **Figure 27.** a) Profilometry plots with corresponding mean thickness (\bar{t}); b) absorption spectra and c) corresponding onset wavelength (determined from the spectra with a linear regression) and calculated bandgap E_g (using Planck-Einstein equation) for all six Glass/perovskite samples of coevaporation #22.

We would include in the new reactor design a substrate holder rotating feature, hoping that it would soften (if not fully counter) the variability induced by the MAI vapour swirling dynamics.

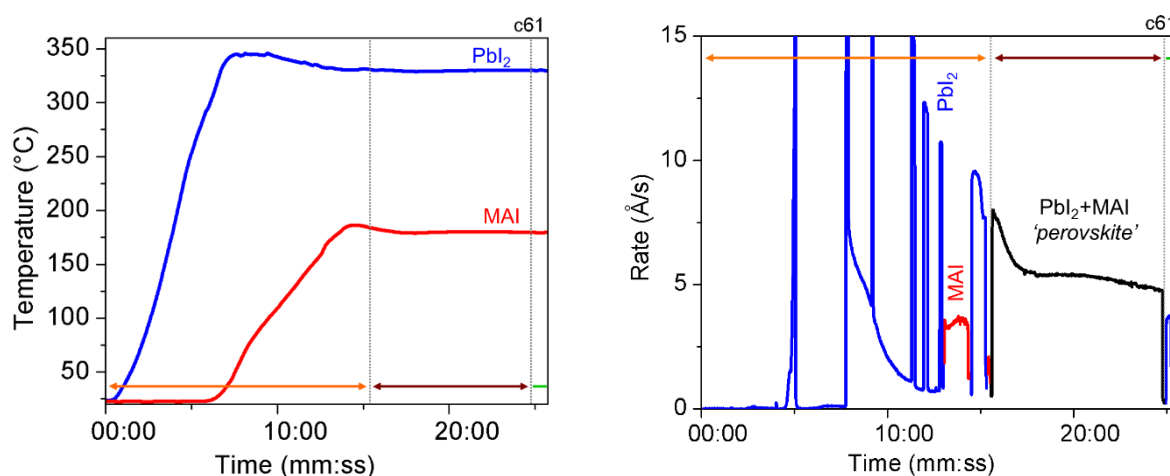
With the aim of further mitigating the impact of the MAI swirling vapour, we also include in the new reactor design the presence of a screening shield (with a shutter opening) between the sources and the substrate holder. Doing so, we hope that the MAI cloud will be restrained to the lower part of the chamber, less parasitizing the deposition on the samples (located in the upper part of the chamber).

Despite the missing features of this proof-of-concept reactor, we were nonetheless able to perform experiments, fabricating thin films, preparing perovskite solar cells and achieving very encouraging results.

ii. Proof-of-concept assessment results

The aim of this reactor being the proof of concept this section will provide a rapid overview of the work conducted, giving only few major results. The equipment features (or lack thereof) preventing us from accurately getting a handle on the coevaporation process, the conditions determined can only be considered as ‘relatively’ optimized.

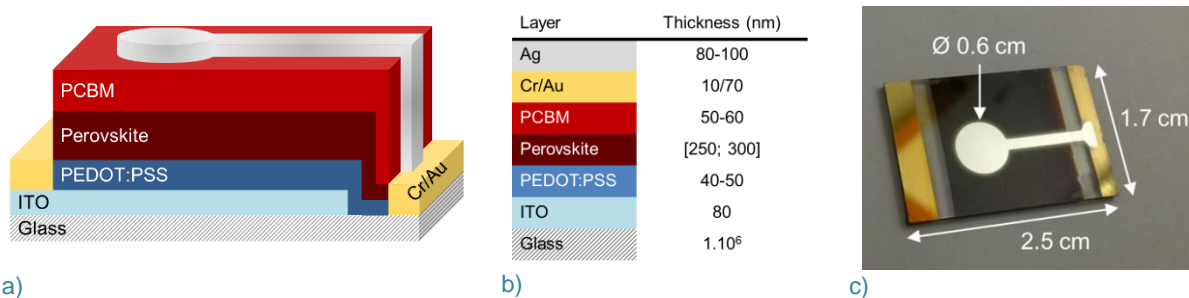
A typical coevaporation process is shown here after with the temperature profiles (Figure 28a) showing MAI heating delayed from PbI_2 's and the rate profile (Figure 28b) showing the different phases of settings, coevaporation and checking.



a) **Figure 28.** a) Temperature profiles for PbI_2 and MAI (respectively blue and red solid lines) and b) Deposition rate profile with PbI_2 (blue) and MAI (red) settings (up to 15 minutes into the process), coevaporation (between 15 and 25 minutes) and final checking step.

As can be seen from the rate plot, setting the deposition rate of the two precursors takes about 15 minutes and is followed by 10 minutes of coevaporation and finally few minutes to check each precursor final rates. Overall the process, as we developed it with this reactor, lasts less than half an hour with deposition rates of $\sim 2 \text{ \AA/s}$ for MAI, $\sim 6 \text{ \AA/s}$ for PbI_2 and $\sim 5 \text{ \AA/s}$ for ‘perovskite’.

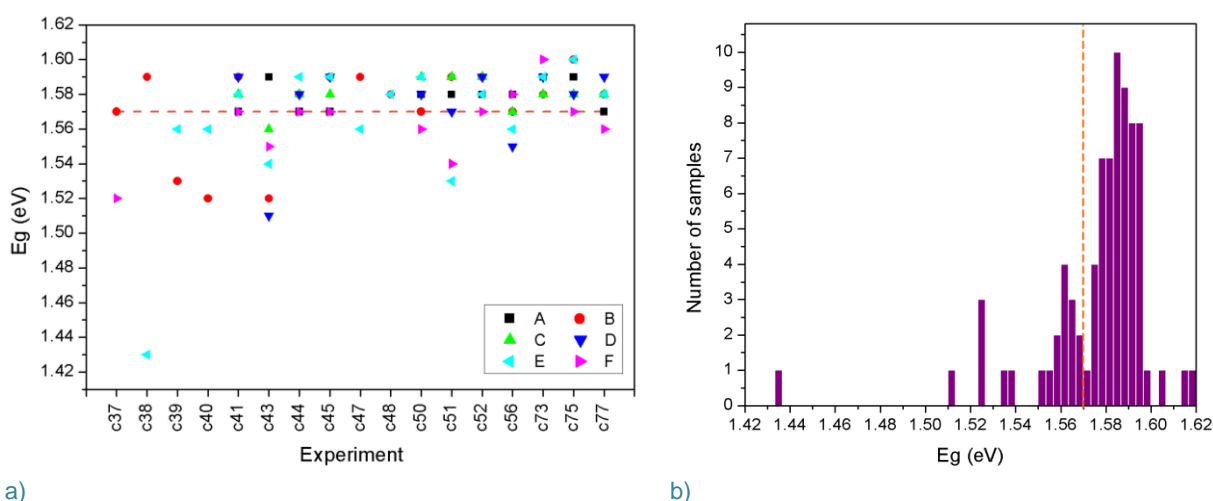
Coevaporated films were either deposited on Glass only substrates or integrated into PV devices of structure: Glass/ITO/PEDOT:PSS/Perovskite/PCBM/Ag with an active area of 0.28 cm^2 (Figure 29) (fabrication steps are detailed in the Annexes/section 0/pages A-C).



a) b) c) **Figure 29.** Perovskite solar cell: a) layers stack, b) corresponding thicknesses and c) picture of a sample.

In six months of exploitation of this proof-of-concept reactor, approximately one hundred experiments were conducted. Due to the lack of features of the present reactor we found ourselves unable to accurately follow and apprehend the coevaporation process, thus hardly confident to make any clear sense of the experiments. First, we know the MAI vapour to be of great impact on the process, but we are unable to assess it due to the lack of accurate pressure monitoring. Second, with the presence of a single QCM sensor, we are unable to follow each precursor instant rate during the process (only the ‘perovskite’ one) which prevents us from following the precursor deposition rates ratio that we suspect to be of great importance for the material composition. Despite these two issues, some statistics for the conducted experiments will be quickly discussed in the following paragraphs.

Focusing on the bandgap values (E_g) shown Figure 30a (calculated from absorption spectroscopy measurement), one can notice a difference between samples of a same experiment. Although a small part of this intra-batch variability can originate from the linear regression calculation, the main part is, in our mind, linked to the stationary status of the sample holder. E_g being intrinsically linked to the material, variation in its value can *in extenso* mean a variation in the material composition. Interestingly, one also notices a difference in amplitude of this intra-batch variability between experiments. Considering, for example, experiments c43 and c52: the amplitude is very different, E_g values ranging from 1.51 to 1.59 eV for c43 and from 1.55 to 1.58 eV for c52. Very likely this lack of consistency between experiments finds its roots in the non reproducible and parasitic MAI vapour cloud.



a) b) **Figure 30.** Statistics for Glass/perovskite samples: bandgap values (E_g) calculated from UV-visible absorption spectroscopy measurements using Planck-Einstein equation (absorption threshold wavelength was determined by a linear regression from the spectra). The dashed line at 1.57 eV stands for the $\text{CH}_3\text{NH}_3\text{PbI}_3$ reference bandgap value calculated accordingly from the spectra of a wet-processed film.

As for the E_g distribution (Figure 30b) it reaches a peak slightly above the ± 1.57 eV characteristic of the $\text{CH}_3\text{NH}_3\text{PbI}_3$ composition (determined from a wet-processed film). More than half of our samples have a calculated E_g between 1.58 and 1.60 eV. All calculated points are more or less concentrated around the 1.57 eV target value. Although we are not perfectly at a $\text{CH}_3\text{NH}_3\text{PbI}_3$ -composition, we are relatively close to it.

Considering the PV performances (Figure 31a), we find a similar intra-batch variability, no consistency between the six samples of a same experiment. Part of this latter very likely originates from the intrinsically inhomogeneous solution process used to deposit the lower and upper layers (respectively PEDOT:PSS and PCBM) of the devices. Unfortunately, at that time we failed to prepare fully wet-processed devices alongside the evaporated-perovskite ones, which would have allowed us to address this aspect. Considering all the experiments the amplitude of this variability is not consistent between them, with PCE values ranging from 5.37 to 8.99% for c61 when they only go from 1.02 to 2.23% for c64. In our opinion, this inter-batch variability finds its main origin in the non-repeatability of the coevaporation process itself. Unfortunately we are unable to assess it for sure.

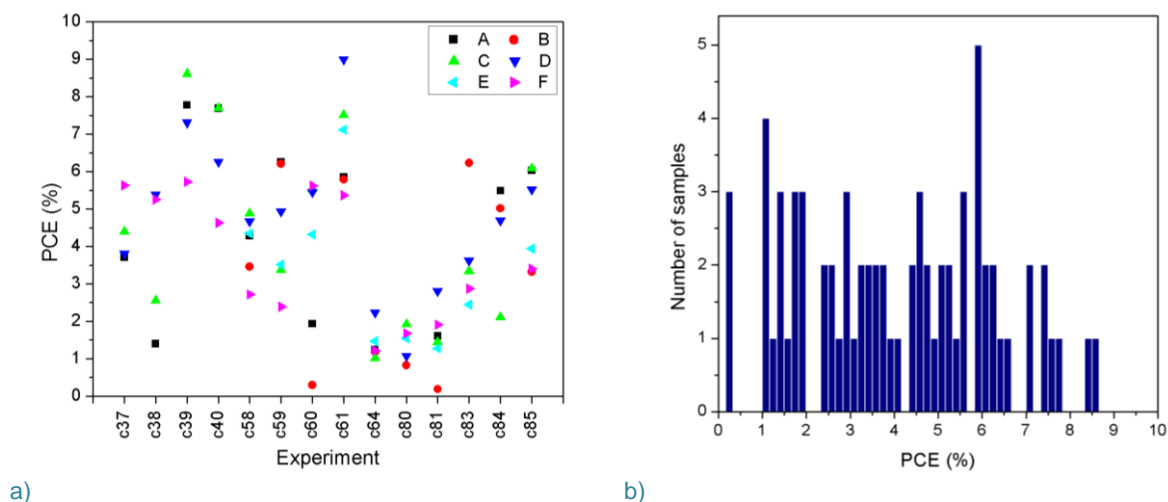


Figure 31. Statistics for Glass/ITO/PEDOT:PSS/Perovskite/PCBM/Ag solar cells (active area is 0.28 cm^2): PhotoConversion Efficiency (PCE) values.

As far as the PCE distribution goes (Figure 31b), we have a mean efficiency around 4% and a record of almost 9% (experiment c61, sample D). Regrettably, the number of samples is too low to be statistically significant, nonetheless few conclusions can be drawn from these results. Given their centred location, with respects to the two sources (Figure 22b), we expect samples in positions C and D to exhibit the most balanced composition (*i. e.* no excess of any of the two precursors), leading to the best material quality and thus potentially the highest efficiencies. From the PCE statistics displayed Figure 31a we find no such correlation between the sample position and the efficiency, echoing with the absence of correlation between E_g values and positions (Figure 30). Once again, the stationary status of the sample holder surely takes part in this issue.

Focusing on the two ‘worst-performing’ batches (c64 and c80, with a mean PCE $< 2\%$) and taking a closer look at the process, one can notice that the deposition rates throughout the coevaporation were consistent with each other, which is logical, but, surprisingly, also consistent with the deposition rate of the best performing batch (c61) (Figure 32).

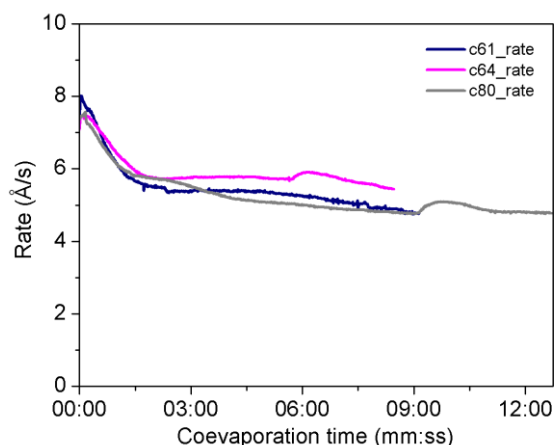


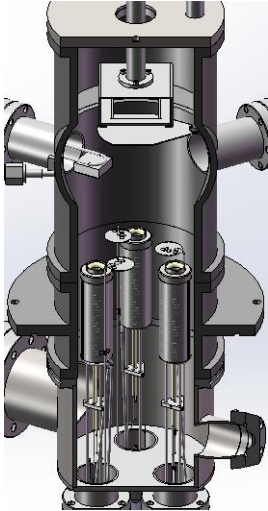
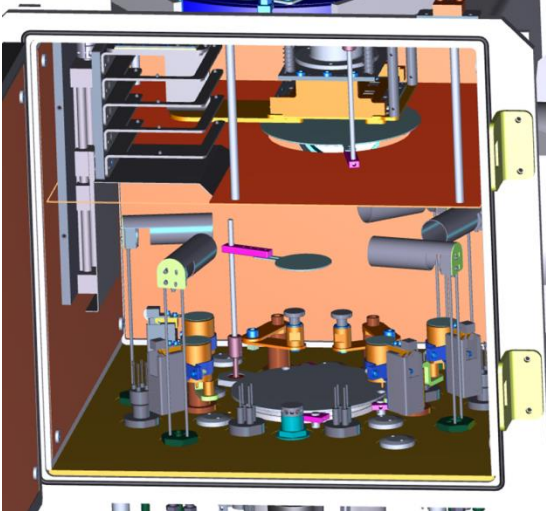
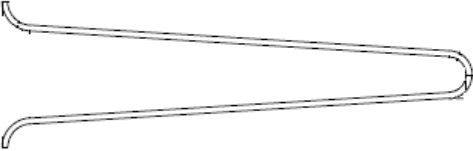
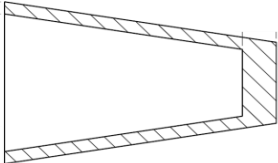
Figure 32. Deposition rate plots for experiments 61, 64 and 80 (only plotted for the coevaporation time range).

Lacking the possibility to know the precursors instant rates during the coevaporation (only the ‘perovskite’ $\text{PbI}_2 + \text{MAI}$ combined rate) we are unable to know the value of the MAI to PbI_2 instant rates ratio for each of these different experiment and thus correlate the material composition to the PV performances. Unfortunately, these three experiments consisted of only solar cell samples; no absorption-dedicated samples were included, we are thus unable to highlight a potential difference in composition that could explain the difference in PV efficiencies.

At that point we feel like the limits of our thinking have been reached as we are operating a system that does not provide us enough insights on our process, we are not confident going further into the results’ interpretation.

Based on these initial results, we consider this reactor’s purpose of proof-of-concept to be fulfilled. Even though we found ourselves lacking some key understandings, we were able to get a first handle on the coevaporation process, achieved encouraging results and we made some crucial discoveries that will drive our future work. In the sake of effectiveness, as the new equipment was delivered to the lab we solely focused our attention on it, neglecting this proof-of-concept reactor.

II. Comparison of the specifically designed reactor with the proof-of-concept one

Proof-of-concept reactor	Perovskite coevaporation-designed reactor
<p style="text-align: center;">RIBER</p>  <p style="text-align: center;">Glovebox integrated</p>	<p style="text-align: center;">M BRAUN</p>  <p style="text-align: center;">Glovebox integrated</p>
<u>Dimensions</u>	
$V = 9 \text{ dm}^3$ $(\varnothing 15 \text{ cm} \times h 51 \text{ cm})$	$V = 125 \text{ dm}^3$ $(l 50 \text{ cm} \times w 50 \text{ cm} \times h 50 \text{ cm})$
<u>Sources</u>	
3 for organic/inorganic materials	4 for organic/inorganic materials + 1 for Metal (high temperature)
<u>Crucible</u>	
	

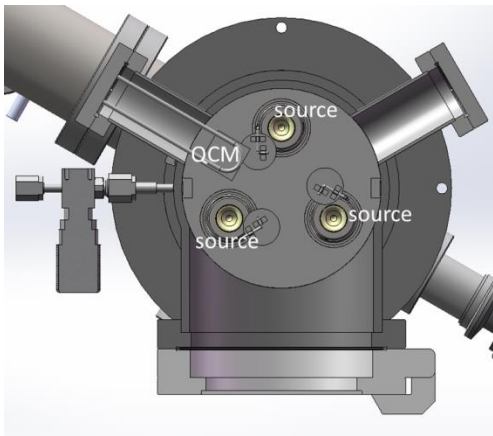
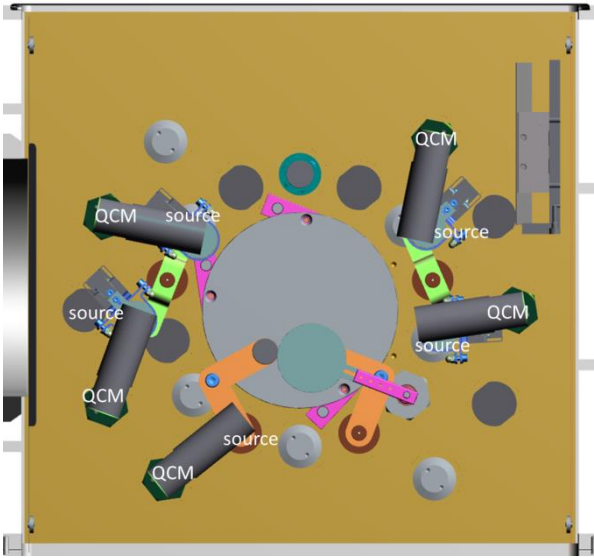
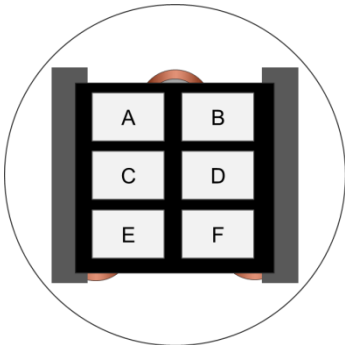
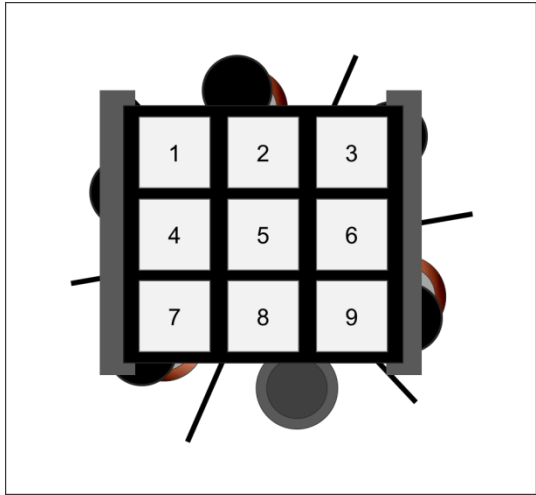
Quartz Crystal Microbalance (QCM)			
<p>1</p>  <p>Distance from crucible: 9 cm</p>	<p>5 (1/source)</p>  <p>Distance from crucible: ~12 cm</p>		
Sample Holder			
<p>Stationary 6 samples of 17x25 cm² Distance from crucible: 29 cm</p> 	<p>Rotating and heating 9 samples of 25x25 cm² Distance from crucible: 17 cm</p> 		
Monitoring			
<p>Temperature for each source Deposition rate on the QCM sensor Thickness</p>	<table border="0" style="width: 100%;"> <tr> <td style="width: 50%; vertical-align: top;"> <p>Temperature Deposition rate Thickness Chamber pressure</p> </td> <td style="width: 50%; vertical-align: middle; text-align: center;"> <p>for each source</p> </td> </tr> </table>	<p>Temperature Deposition rate Thickness Chamber pressure</p>	<p>for each source</p>
<p>Temperature Deposition rate Thickness Chamber pressure</p>	<p>for each source</p>		

Table 3. Comparative table of the two perovskite reactors features.

III. Implementation of the new reactor designed for perovskite coevaporation

The new reactor purchased by IPVF was delivered to the LPICM laboratory in March 2017 (at that time IPVF lab facilities were not yet ready). Waiting for some corrective actions from MBRAUN, the equipment was ready to be used by mid-June. The site acceptance tests (SAT) were done by mid-July and the equipment was then available for exploitation. In January 2019, the equipment was moved from LPICM to the IPVF building. At the time of writing, the equipment is still in standby due to issues on the reactor pumping system.

Since the equipment was purchased in the framework of this thesis, first step of its implementation consisted in running the site acceptance tests to check that the reactor fulfilled all desired features.

i. Site Acceptance Tests

The Site Acceptance Tests (SAT), mandatory upon acquisition of any new system to insure the specifications are met, were established between LPICM, IPVF and MBRAUN. Several items were to check including some features on the glovebox and on the pumping system that will not be disclosed here. Relevant items definition is given Table 4 and corresponding check tests are here after detailed.

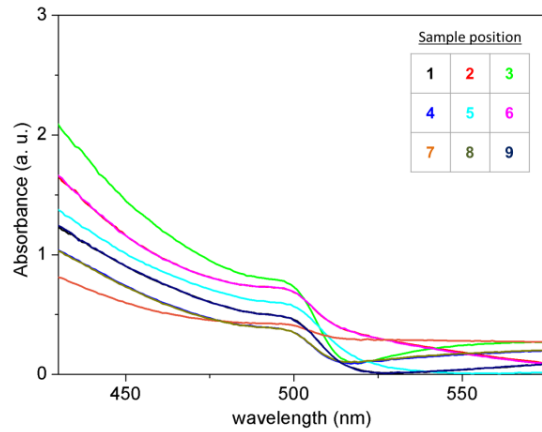
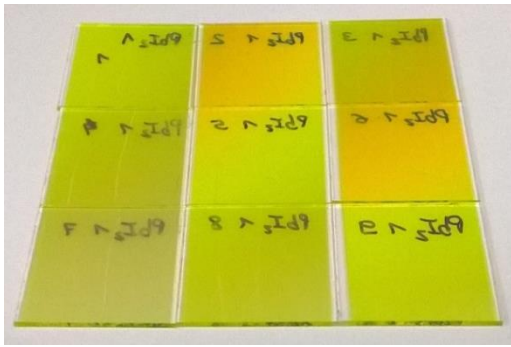
Definition	Specificity	Comments
<u>Substrate Holder rotation:</u> Thickness uniformity over 5 samples (1 center + 4 corners)	$< \pm 5\%$	Thickness measurements using profilometer
<u>Deposition:</u> of PbI_2 (300 nm thick) of organic material (100 nm thick) of metal (50-100 nm thick)	0 to 0.5 nm/s	Deposition tests and thickness measurements using profilometer or SEM

Table 4. Site Acceptance Tests definition.

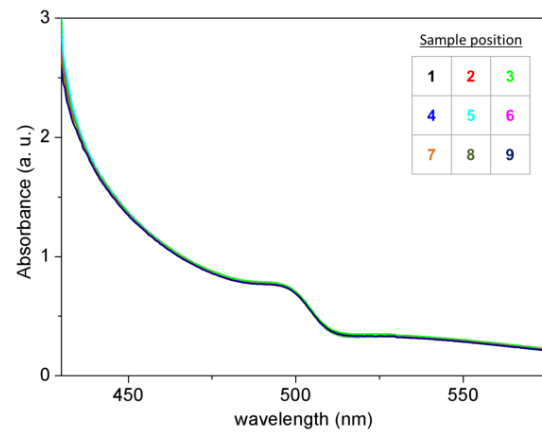
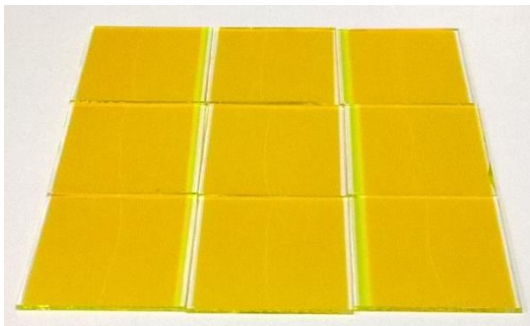
a. Substrate Holder rotation SAT tests

Given the erratic behaviour of the organic compound, foreseen from the RIBER reactor feedback, the substrate holder rotation tests were conducted using PbI_2 as the evaporated material since it behaves more conventionally, *i. e.* with a directive evaporation cone. Two sets of PbI_2 films (nine samples each time) were fabricated without and with substrate holder rotation during the evaporation process.

When the rotation feature is not used, a difference in thickness can already be seen by the naked eye (picture Figure 33a) and is further assessed from the absorption spectra that exhibit a clear thickness effect. On the other hand, when the rotation is used, all nine plots perfectly overlay (spectra Figure 33b).



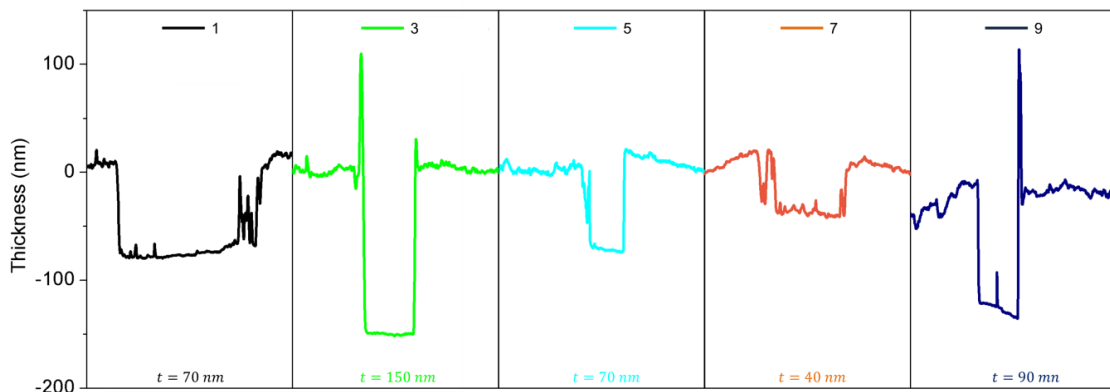
a) no rotation



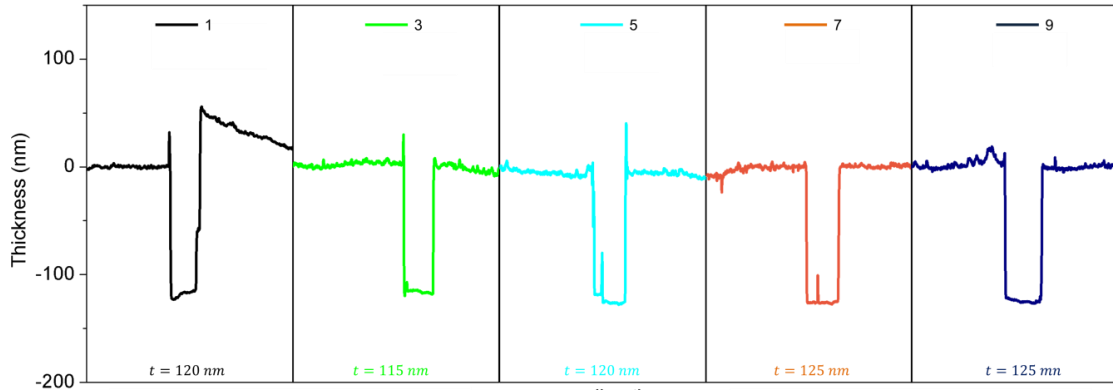
b) with rotation

Figure 33. Deposition of PbI_2 films on glass without (a) and with (b) rotation of the substrate holder: pictures of the nine samples (left) and corresponding absorption spectrum (right).

The thicknesses were measured using a stylus profilometer. For each set of films, five samples (centred (position 5) and cornered ones (positions 1, 3, 7 and 9)) were scratched and measured. Profile plots along with the mean thicknesses are given Figure 34 for each rotation status: OFF (a) and ON (b).



a) no rotation



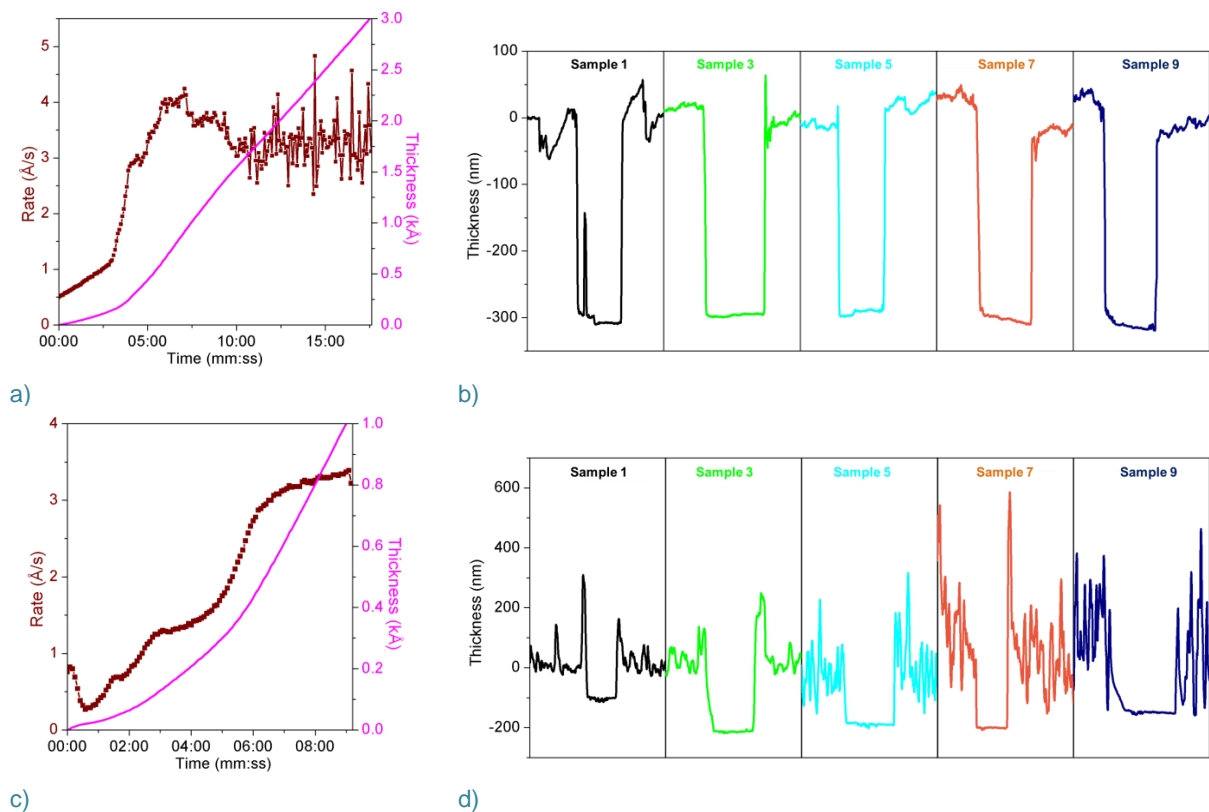
b) with rotation

Figure 34. Profilometry profiles and corresponding thicknesses (t) of five samples Glass/PbI₂ without (a) and with (b) rotation of the substrate holder.

Thicknesses range from 40 to 150 nm without rotation and from 115 to 125 nm with rotation. Given the precision of the profilometer, we estimated the thickness homogeneity criterion, if not of 5% but of 8.7%, to be nonetheless fulfilled.

b. Deposition SAT tests

For each compound (PbI₂, organic and metal) the material was heated to a random temperature and then adjusted so that the rate doesn't go above the 0.5 nm/s limit defined in Table 4). Each time, nine samples were prepared and following section III.i.a. results, the substrate holder was rotated during the different experiments. The sensor-read thickness and deposition rates process outputs as well as measured thickness profiles of five samples are plotted for each material and gathered Figure 35.



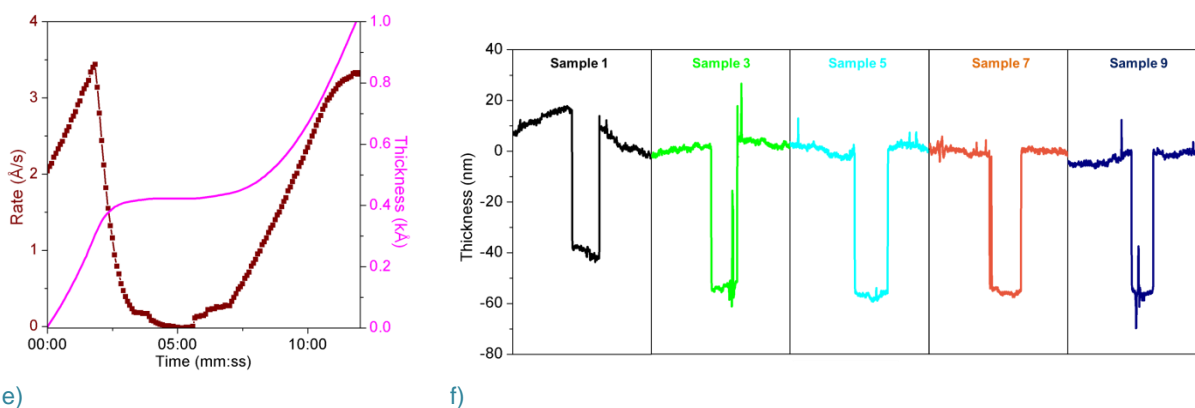


Figure 35. Evaporation process outputs: deposition rate (dark red line with symbols, left scale) and QCM-read thickness (pink solid line, right scale) (a, c, e) and measured thicknesses of five glass samples (b, d and f) for PbI_2 (a, b), organic $\text{CH}_3\text{NH}_3\text{I}$ (c, d) and silver metal (e, f).

For PbI_2 and Ag, that have a classical directive evaporation, the thickness measurements show a good homogeneity between the five selected samples upon rotation of the holder during deposition (Figure 35b and f). Even though the rotation feature was used, the erratic behaviour of the organic salt $\text{CH}_3\text{NH}_3\text{I}$ (reported in the literature by other groups and shown by our group in I.i.) could not be mitigated, resulting in thicknesses varying between 100 and 200 nm (Figure 35d). Comparing the thickness profiles one can notice the difference in film roughness between MAI and PbI_2 (or Ag). The organic film profile (on each side of the scratching fingerprint) is very noisy compared to the inorganic and metallic ones, confirming the swirling nature of the MAI evaporation. Since the organic material is, inherently, hardly controllable, we consider the SAT deposition criteria to be satisfied and will investigate further its behaviour later in the manuscript.

Once all the acceptance tests satisfied, we proceeded with some initial developments starting with single compound evaporations to assess the behaviour of the precursors in this new reactor, hoping to get deeper insights with regard to the RIBER development thanks to the added features.

ii. Transfer knowledge between equipments

As we started implementing the coevaporation process on the new equipment, we wanted to follow the routine developed on the previous reactor, *i. e.* high heating rates of 50 and 20°C/min for PbI_2 and MAI respectively. Due to a safety interlock on the new reactor sources, the heating rate could not exceed 20°C/min, we then had to adapt our process.

Taking advantage of this restraint, we decided to run a study on the influence of the heating rate. We performed single-compound evaporation of PbI_2 at three heating rates: 20, 10 and 8°C/min with target temperatures around 300°C and single-compound evaporation of MAI at five heating rates: 20, 15, 10, 5 and 2°C/min with a target temperature of 120°C. The results are shown Figure 36.

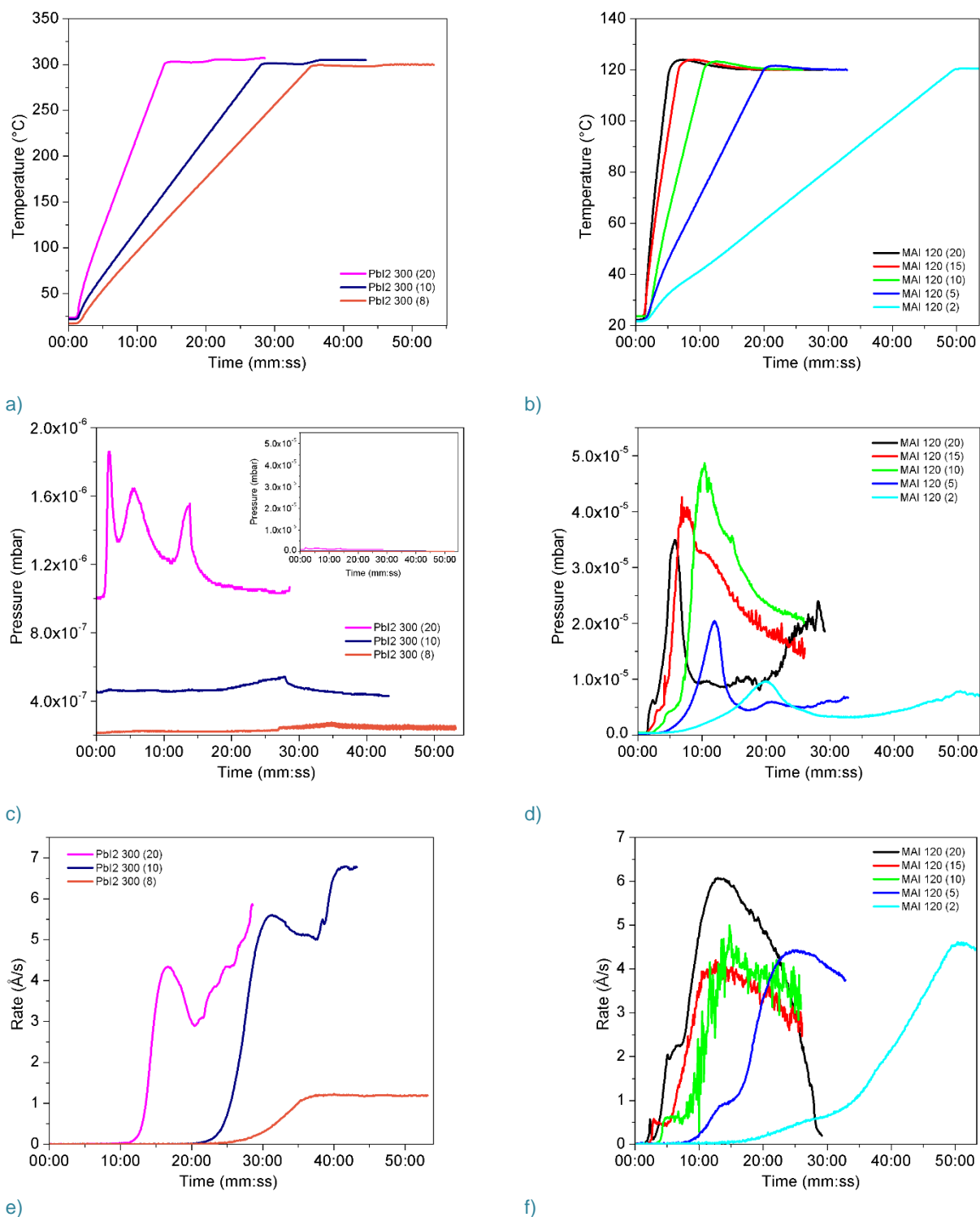


Figure 36. Influence of the heating rate: temperature (a, b), pressure (c, d) and deposition rate (e, f) plots for PbI₂ heating rates of 20, 10 and 8°C/min with target temperatures ~300°C (a, c, e) and MAI heating rates of 20, 15, 10, 5 and 2°C/min with a target temperature of 120°C (b, d, f). Insert in c) shows the PbI₂ pressure plot scaled to the MAI pressure plot (d). N.B. each experiment is a single-compound evaporation.

Considering the PbI₂ pressure plots (Figure 36c), although the 20°C/min plot shows stronger oscillations than the 10 and 8°C/min plots, these oscillations turn out to be insignificant considering their amplitude (from 9.10^{-7} mbar to $1.9.10^{-6}$ mbar). Scaling the PbI₂ plots to the MAI ones (insert Figure 36c) clearly shows the flatness of PbI₂ pressure profiles (whatever the heating rate) with respect to the MAI profiles.

While all MAI pressure profiles (Figure 36d) follow the same trend (from the initial value P_i the pressure increases up to a peak value P_{peak} before stabilizing down to a pressure $P > P_i$), interestingly the amplitude of the pressure increase seems to depend on the heating rate. For the three highest heating rates, the peak pressure value is higher 3.5×10^{-5} mbar when it is below 2.10^{-5} mbar for the two lowest (Figure 37a). What is also worth mentioning is the shift in the peak-pressure temperature with the heating rate, going from 120°C for the three highest heating rates down to 60°C for the $2^\circ\text{C}/\text{min}$ plot (T at P_{peak} in Figure 37b).

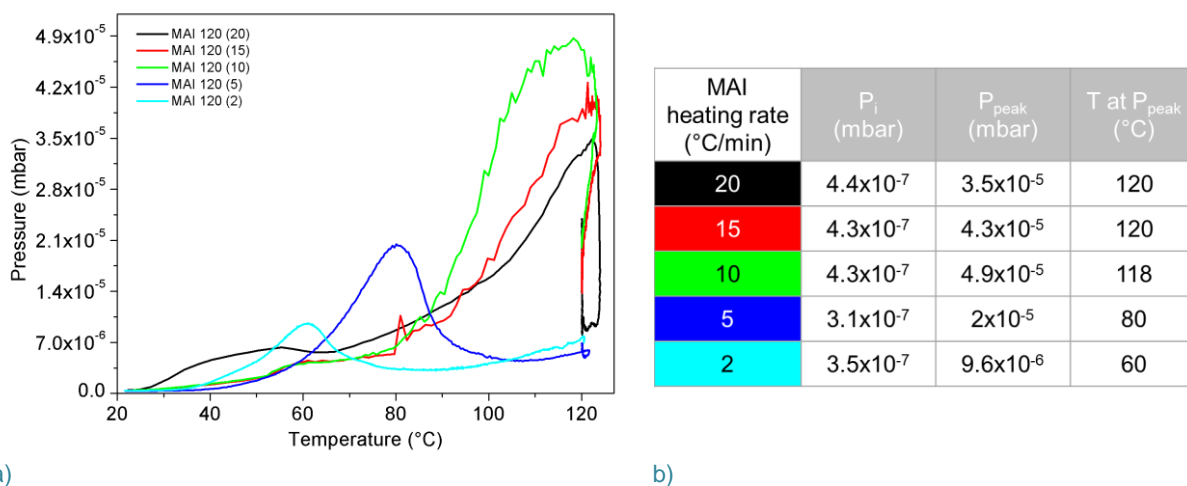


Figure 37. a) Evolution of the pressure with the temperature for all five MAI heating rates and b) Values of initial and peak pressure values (respectively P_i and P_{peak}) and the corresponding temperature (T at P_{peak}) for the five different MAI heating rates.

These results show that decreasing the MAI heating rate limits the pressure increase; potentially mitigating the organic swirling cloud effect which would suggest a better control of the MAI evaporation with low heating rates.

Considering the deposition rate plots for MAI (Figure 36f), no clear difference is seen between the five experiments while we would have expected very different response from the three highest heating rates with respect to the two lowest (as seen with the pressure), potentially with higher deposition rates and/or more oscillating profiles (due to the parasitic swirling MAI cloud). This inconsistency between the pressure trend and the deposition rate still puzzles us to this day.

As far as PbI_2 goes, while the 20 and $10^\circ\text{C}/\text{min}$ plots show the same trend, there is, quite surprisingly, a very strong difference between the 10 and $8^\circ\text{C}/\text{min}$ profiles (Figure 36e). The two highest heating rates yield a rather similar deposition rate profile with a peak value as the target temperature is reached, followed by a decrease. The $8^\circ\text{C}/\text{min}$ heating rate on the other hand leads to a profile where the deposition rate is stable from $\sim 35:00$ until the end of the process 20 minutes later. It is worth mentioning that, for the 20 and $10^\circ\text{C}/\text{min}$ experiments, a second increase in deposition rate occurs as the temperature is slightly increased to 307 and 305°C respectively (at $2^\circ\text{C}/\text{min}$). A slight increase in temperature was also applied during the $8^\circ\text{C}/\text{min}$ experiment (to 300°C at $2^\circ\text{C}/\text{min}$) but interestingly enough it did not disturb the deposition rate.

This study suggests that low heating rates allow a better control of the PbI_2 deposition rate while mitigating the parasitic MAI cloud. We then decided to work with heating rates

below 10°C/min for Pbl₂ and below 5°C/min for MAI with the new reactor, when we were using 50 and 20°C/min on the previous one.

iii. Single compound depositions

a. Single evaporation of Pbl₂

For the single evaporation of lead iodide, several experiments were ran with the same inputs *i. e.* a target temperature of 220°C with a heating slope of 10°C/min. The process parameters plots (temperature, pressure and deposition rate) are shown Figure 38.

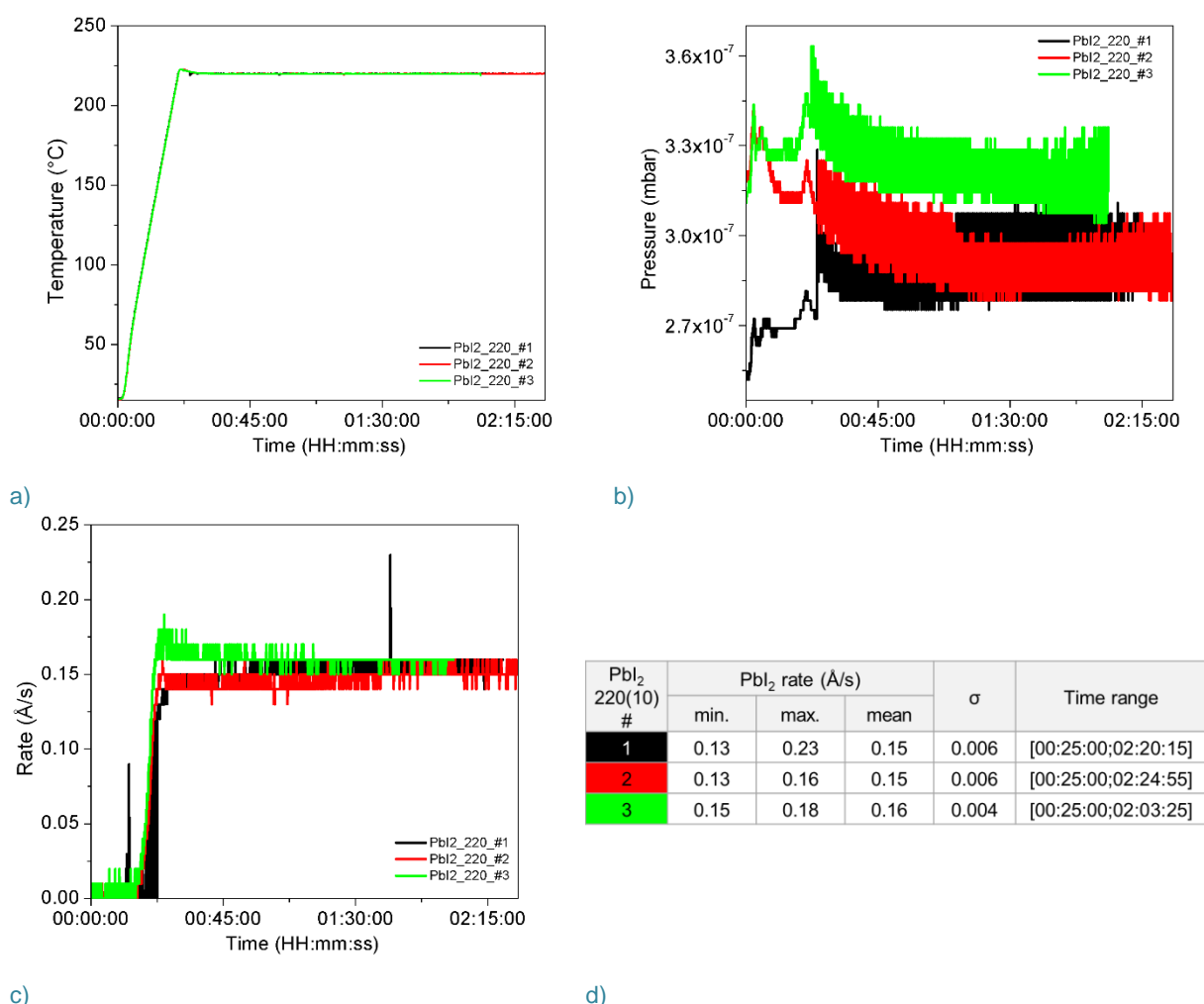


Figure 38. Process parameters for three Pbl₂ single compound evaporation experiments: a) temperature; b) chamber pressure; c) deposition rate and d) rate statistics (σ is the standard deviation).

Upon heating Pbl₂ up to 220°C, the chamber pressure remains close to the initial value and relatively constant, between 2.8 and 3.3.10⁻⁷ mbar. As the target temperature is reached, the Pbl₂ deposition rate hits a value of 0.15 Å/s. During the 2 hours of process, this value remains steady with a standard deviation well below 0.01.

All three experiments where Pbl₂ was heated to 220°C at 10°C/min lead to a mean stabilized rate of 0.15 Å/s, showing a good repeatability of the process.

b. Single evaporation of CH₃NH₃I

For the single evaporation of organic methylammonium triiodide (CH₃NH₃I or MAI), ten experiments were ran with the same inputs *i. e.* a target temperature of 60°C with a

heating slope of 4°C/min. The output parameters plots (measured temperature, pressure and deposition rate) are shown Figure 39.

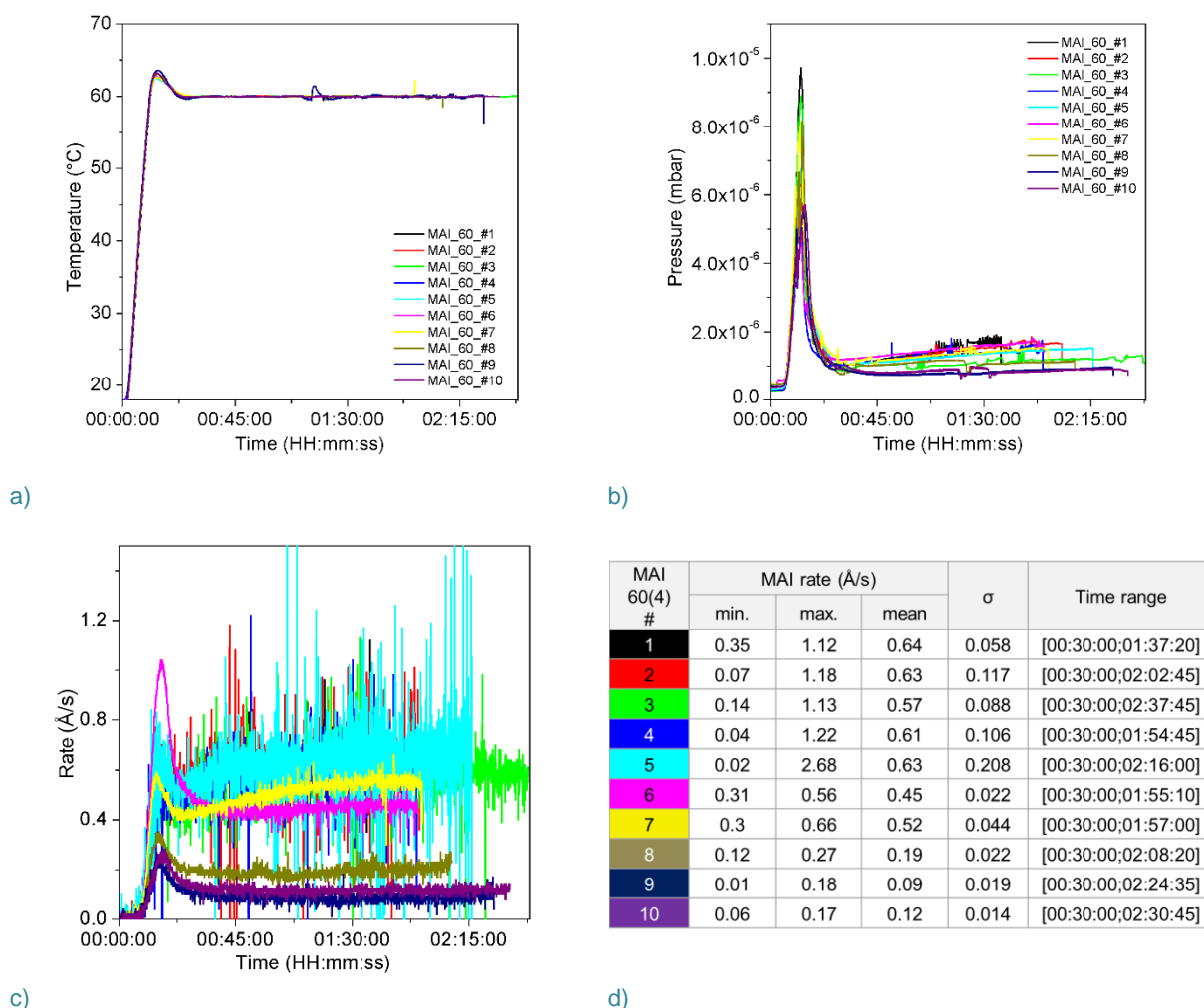


Figure 39. Process parameters for ten MAI single compound evaporation experiments: a) temperature; b) chamber pressure; c) deposition rate and d) rate statistics (σ is the standard deviation).

Regarding the chamber pressure, the trend upon MAI evaporation is very different from the one for PbI_2 where the pressure was stable and close to the initial value. Upon heating of the organic material, the chamber pressure quickly increases to reach a peak value as the temperature peaks, before going down as the temperature stabilizes at 60°C. This sharp increase in pressure shows the volatility of the organic methylammonium iodide material, as previously noticed with the proof-of-concept reactor. The stabilized working pressure (reached after 30 minutes into the process) is slightly higher than the initial one. To compare the MAI pressure behaviour with the one from PbI_2 evaporation, four points of interest are considered: initial, maximum, at $t_0+30\text{min}$ and final. The corresponding profiles are shown Figure 40 for all MAI and PbI_2 experiments.

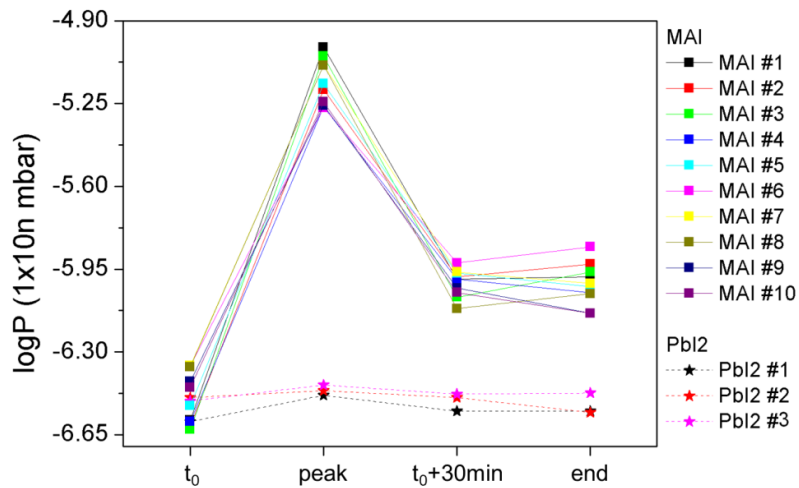


Figure 40. Comparison of pressure trends between MAI (solid line with squares) and Pbl₂ (dotted line with stars) single compound evaporations for four points of interest: P_i at t₀, P_{peak}, 30 minutes into the process (t₀+30min) and final pressure value at the end of the deposition process.

Considering Pbl₂, all four points of interest are more or less in the same range, yielding a flat pressure profile. Considering MAI, the pressure profile shows an increase of approximately one order of magnitude from the initial pressure before stabilization to a working pressure higher than the t₀ value.

Even though the temperature inputs are identical for all ten MAI experiments (60°C target with a 4°C/min slope) the deposition rate outputs are very different ranging from 0.64 Å/s for MAI #1 to five times less for MAI #10 (table d) Figure 39). It is worth noting that the difference in noise in the rate profiles (plot c) is due to the QCM sensor lifetime. For experiments #1 to #5, the QCM lifetime went down from 94.5 to 90.8%, the membrane was then changed for a new one (99.2% initial lifetime for experiment MAI #6) that went down to 97.6% by the end of experiment MAI #10. Regardless of this aspect, deposition rates are not consistent between experiments as shown by the factor 3 difference in the mean deposition rates between experiments MAI #6 and #10 for instance (Figure 41).

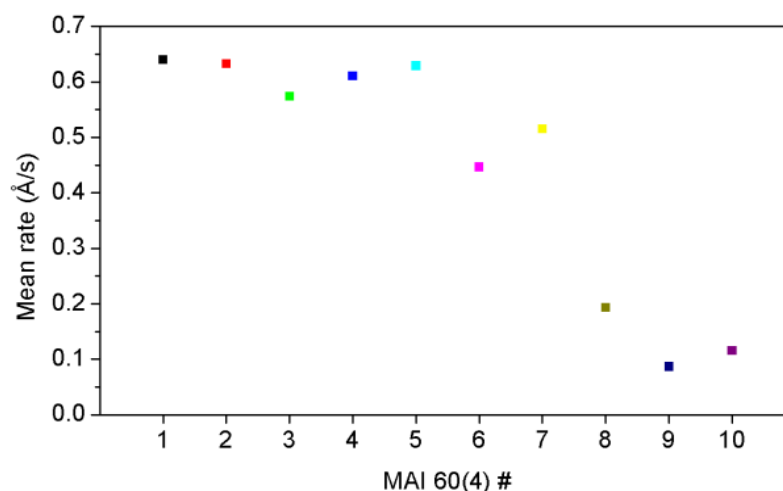


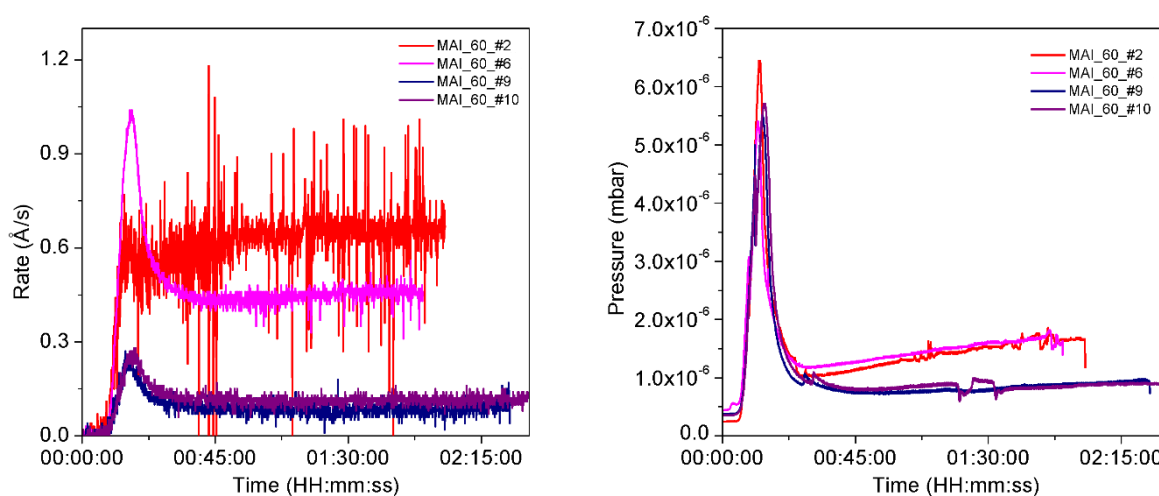
Figure 41. Mean rate values for all ten MAI single-compound evaporations (data from Figure 39d table).

In terms of standard deviation, given the lower QCM lifetime (thus the higher signal noise), experiments #1 to #5 exhibit higher σ values (around 0.1) than experiment #6 to #10 (below 0.05). Compared to Pbl₂, for which values were well below 0.01 (table Figure 39d),

standard deviations for MAI range from 0.014 to 0.208 stressing once again the erratic nature of the organic salt evaporation.

At this point, we have showed that the evaporation of the organic salt is slightly less stable than the one for PbI_2 and that it is poorly reproducible between experiments, even though the input parameters (target temperature and heating rate) are identical. We tried to correlate the deposition rate dispersal with any quantifiable parameter.

All ten experiments follow the same temperature trend, with a stabilized temperature of 60°C (Figure 39a), the difference in deposition rate thusly does not originate from there. The only remaining monitored parameter being the pressure we took a closer look at it. Focusing on two sets of experiments (one where the two deposition rates are almost identical: MAI #9 and #10, and one where they are different: MAI #2 and #6) we compared both the deposition rates and pressure plots (Figure 42).



a) b)
Figure 42. a) Deposition rates and b) pressure plots for the two sets of experiments considered.

Considering the set of experiments with comparable deposition rates (#9 and #10), their pressure plots nicely overlay, potentially showing that pressure and deposition rate are correlated. Yet, the second set of experiment (with different rates, respectively 0.63 and 0.45 \AA/s for #2 and #6), also shows overlying pressure profiles. At this point, we find ourselves unable to explain the difference in deposition rate response.

Thanks to the automatic and accurate pressure monitoring on this designed reactor we were able to assess more precisely the temperature triggering the pressure increase occurring upon MAI heating. On the proof-of-concept RIBER reactor, we found a value around 40°C . With the fine and accurate pressure monitoring featured on this new reactor, we were able to refine this triggering value around 35°C as shown Figure 43.

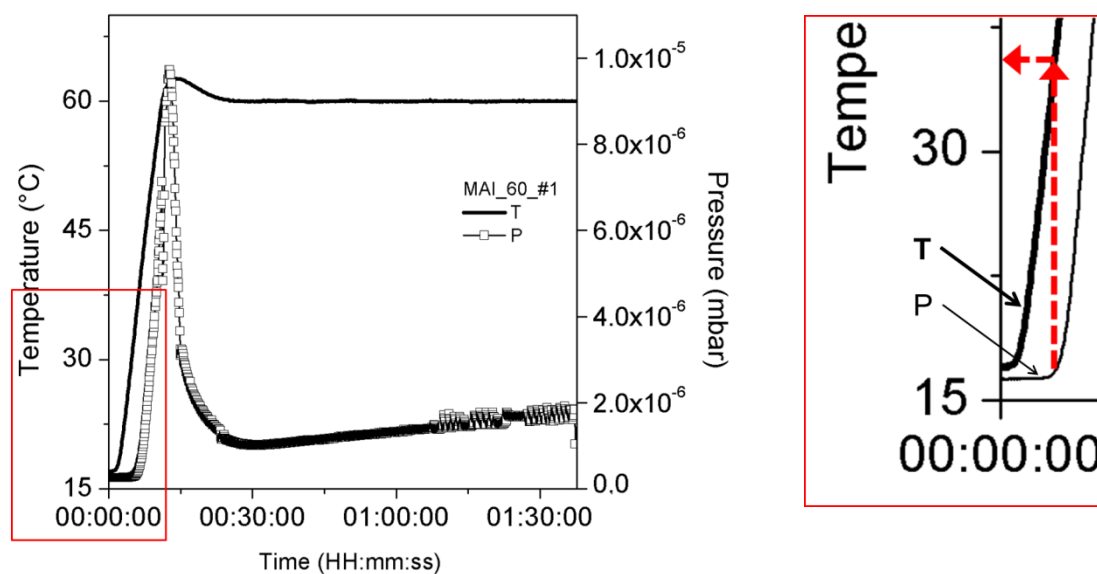


Figure 43. Process plots for MAI single evaporation #1 correlating the temperature and pressure increase (insert shows a zoom of the starting region).

This section's findings are in good agreement with the previous work of Malinkiewicz *et al.*¹⁰⁸ where they pinpointed the difficulty to control the organic salt evaporation. From its behaviour in single-compound evaporation, we expect the MAI to react accordingly in a coevaporation process, potentially perturbing the stable response of PbI_2 .

iv. Toward coevaporation

With the previous section we have shown that the pure evaporation of PbI_2 seems reproducible with a stable deposition rate during process (around 0.15 \AA/s for a target temperature of 220°C) and found the organic compound MAI evaporation to be relatively stable during one experiment but poorly reproducible between experiments. Before jumping into optimizing the coevaporation process itself, we ran few experiments where starting from a single evaporation of PbI_2 we then added MAI, to apprehend its influence on the process, leaning toward pseudo coevaporation conditions.

From the start PbI_2 is heated up to a 220°C target temperature with a 10°C/min slope. After more than an hour of process where only the inorganic material is evaporating, the organic MAI is heated up to a 80°C target temperature with a 4°C/min slope. The output parameters (PbI_2 and MAI temperatures, chamber pressure and PbI_2 deposition rate) for three experiments are shown Figure 44 along with the PbI_2 rate statistics). Given the two working regimes (PbI_2 only and $\text{PbI}_2 + \text{MAI}$), rate statistics are calculated for two time ranges: from t_0 to MAI starting point (t_{MAI}) (PbI_2 only regime) and from t_{MAI} to the end ($\text{PbI}_2 + \text{MAI}$ regime).

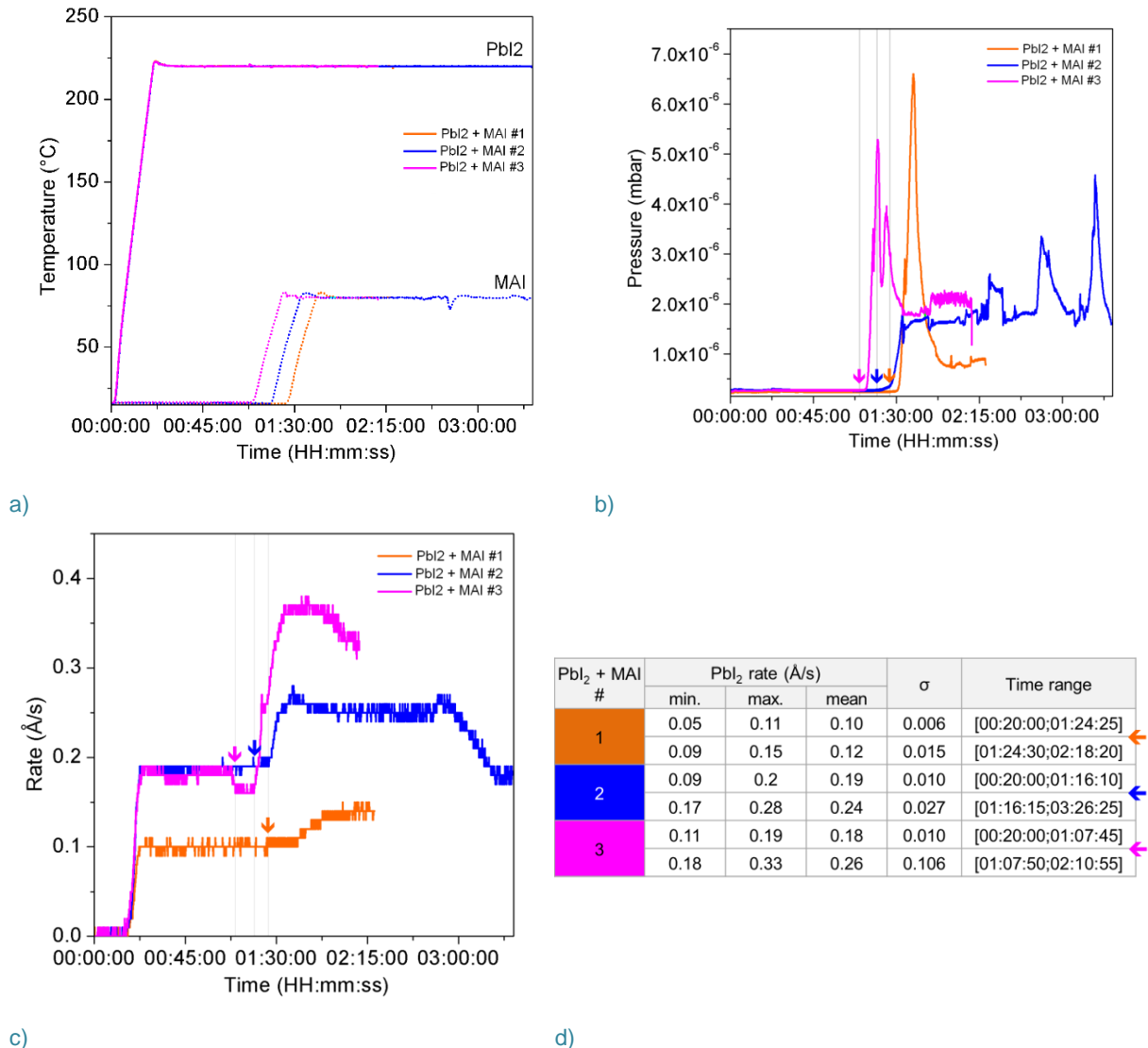


Figure 44. Process parameters for three Pbl₂ evaporation experiments where MAI heating is activated during the process (↓ shows the starting point): a) temperatures; b) chamber pressure; c) Pbl₂ deposition rate and d) rate statistics (σ is the standard deviation and ← shows the starting point of the MAI heating).

From the Pbl₂ rate plots we clearly see the impact of MAI. When Pbl₂ is alone, its behaviour is similar to the results from Figure 38c and d, *i. e.* a stable rate with σ values below 0.01. Even though the target temperature is identical to the Pbl₂ only study (220°C) the rates obtained here are slightly different from the 0.15 Å/s previously reached (Figure 38c) with 0.10 Å/s for coevaporation #1 and 0.20 Å/s for #2 and #3. Few minutes after starting MAI heating the Pbl₂ rate increases.

Regarding the pressure, the three coevaporations plots are a perfect sequence of the Pbl₂ only and MAI only pressure plots (respectively Figure 38 b) and Figure 39 b)) with a flat pressure profile for the time range where only Pbl₂ is heated and the characteristic pressure increase of one decade when the MAI heating is activated. Given the two working regimes of the discussed experiments (Pbl₂ only and Pbl₂ + MAI) the pressure trend is followed in seven points of interest: initial, peak in Pbl₂ only regime, t₀+30min, t_{MAI}, peak in Pbl₂ + MAI regime, t_{MAI}+30min and final. The resulting profiles are shown Figure 45.

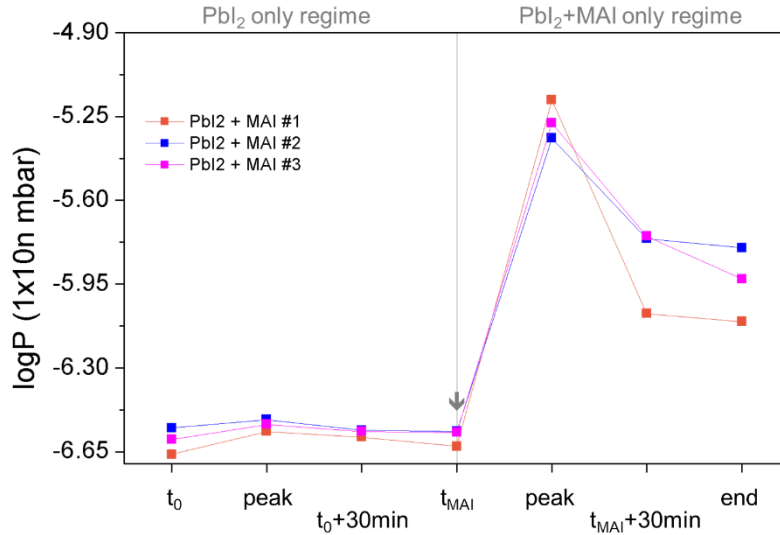


Figure 45. Pressure trends for Pbl₂+MAI experiments for seven points of interest: initial (t_0), peak, t_0+30 minutes in the Pbl₂ only regime and t_{MAI} , peak, $t_{\text{MAI}}+30$ minutes and end in the Pbl₂+MAI regime (the arrow ↓ shows the starting point of MAI heating).

The profiles are consistent with the ones from Figure 40 with a flat profile in the Pbl₂ only regime and the MAI-characteristic peak in pressure in the Pbl₂ + MAI regime.

After these first, relatively raw, trials of pseudo coevaporation we found ourselves actively questioning the process reported by the ICMol team in which they first heat the MAI up to 70°C, wait for the sensor reading to stabilize and then heated the Pbl₂ up to 250°C. Indeed, we have shown that despite an identical target temperature, MAI deposition rate varies throughout experiments. We have also highlighted that the presence of MAI alongside Pbl₂ disrupts this latter deposition rate and that this behaviour is not reproducible between experiments, with a factor three difference eventually occurring.

Conclusion

This thesis was the first on the topic of evaporated perovskites at both IPVF and LPICM levels. As such I had to prove the feasibility of the process using a non-purposely-designed reactor while taking part to the definition of requirement specifications for the next equipment. I was later on in charge of implementing this specially designed reactor.

As we developed the coevaporation of PbI_2 and $\text{CH}_3\text{NH}_3\text{I}$ using the proof-of-concept reactor we found ourselves facing a lack of functionalities, with only one QCM sensor and no accurate pressure monitoring. These latter being process-specific, *i. e.* induced by the aforementioned materials and their coevaporation, this feedback allowed us to finely tune the design of the next (dedicated) reactor. Despite this lack of features, that prevented us from accurately controlling it, we were able to get a grasp on the process. As reported in the literature, we found the behaviour of organic compound $\text{CH}_3\text{NH}_3\text{I}$ to be quite unusual. We noticed a substantial increase in the chamber pressure upon heating of the compound that we attributed to a cloud of MAI filling the reactor in a swirling manner. We adapted our process accordingly and integrated a PbI_2 -only deposition step (prior to the coevaporation) to counter the potentially parasitic effect of the organic cloud. Within six months of use, we managed to control, to a relative degree, the coevaporation of PbI_2 and MAI and achieved very encouraging results with efficiencies around 5-6% in perovskite photovoltaic devices.

Once the new reactor was delivered and could be used, we first performed the qualifications tests (mandatory for any new equipment acquisition) and then studied the perovskite precursors behaviour in single-compound evaporation. We have found PbI_2 to behave classically, with a deposition rate stable throughout one experiment and reproducible between experiments of same process conditions. We have found MAI to behave more erratically with a deposition rate stable throughout one experiment but far from reproducible between experiments of same process conditions. We were able to confirm our insight that MAI behaviour and pressure are closely related, yet it requires further study to be better assessed. These initial developments allowed us to get accustomed to the new reactor's features and corroborate their relevance, paving the way for the next chapter where the specifically designed reactor will be extensively used for perovskite coevaporation purposes.

Chapter 3.

Fabrication of perovskite thin films using coevaporation.

“It doesn’t matter how beautiful your theory is, it doesn’t matter how smart you are.
If it doesn’t agree with experiment, it’s wrong.”

R. P. Feynman

Introduction

In the framework of this thesis I was asked to develop the coevaporation process to fabricate $\text{CH}_3\text{NH}_3\text{PbI}_3$ perovskite thin films for solar cells applications. Working on a proof-of-concept reactor we were able to get a first handle on the process and designed a reactor more suited for perovskite coevaporation purposes. With the initial developments on this second reactor, we tamed its new features and were able to deepen our understanding of the precursors behaviour. We were able to direct ourselves toward good process conditions.

The present chapter is dedicated to the development of the coevaporation process using this second, specifically designed, reactor. The first part of this chapter will focus on presenting the obtained results while the second part will be built around discussions on these latter. Based on our initial developments with single compound evaporations and the first pseudo-coevaporation trials, we expect actual coevaporation process to be complicated to control. As we were developing things from scratch, we tried to establish the process repeatability; fabricating films we would then characterize to direct our investigations toward the good deposition parameters.

It is worth recalling that, at the time of writing, due to an issue on its pumping system the MBRAUN reactor is still in standby in IPVF laboratory clean room facilities (since January). We are unable to know if the behaviours reported in the following part (obtained when the reactor was located in LPICM) will be found again once the reactor finally starts off in its new location.

I. Coevaporation process for perovskite thin films

Before jumping into anything it must be specified that all experiments were carried out following a temperature-controlled process: the target temperature and heating rate are entered by the user from the software interface and are the process inputs. Although the present MBRAUN reactor also offers a rate control mode (*i. e.* the temperature is automatically managed to meet the target deposition rate input) we did not use it as it implies the simultaneous opening of both source shutters (MAI and PbI_2), which does not fit with our developed procedure. As explained in the previous chapter, our procedure includes the deposition of an initial thin layer of PbI_2 (while the MAI source is at room temperature and its shutter closed) to prevent the deposition of a parasitic initial layer of MAI on the samples.

As seen with the few previous attempts of pseudo-coevaporation (chapter **2.III.iv** page 53), we expect the repeatability to be poor between experiments following the same procedure. Indeed, we have uncovered the parasitizing effect of MAI heating on the (otherwise stable when alone) PbI_2 deposition rate and its lack of consistency between experiments. As we started performing actual coevaporations, we made the choice to run campaigns of experiments in which we would follow the same procedure (temperature-driven) for a significant number of experiments. From there, we would study the output parameters (pressure and deposition rates) to assess their consistency between experiments and thus the repeatability of the process. Various material characterizations (absorption spectroscopy, SEM, I-V,...) were performed on the fabricated films, in the hope of correlating process parameters with material properties.

i. Focus on the process repeatability

In order to assess the process repeatability, we ran a few campaigns where a statistically significant number of experiments were performed following the same heating procedure (*i. e.* target temperatures, heating rates and MAI heating timing):

- **Study 1:** PbI_2 to 290°C target temperature at 8°C/min heating rate and then MAI to 92°C target temperature at 4°C/min heating rate.
- **Study 2:** PbI_2 to 220°C target temperature at 10°C/min heating rate then to 250°C at 4°C/min as MAI is set to ~60°C target temperature at 4°C/min heating rate.
- **Study 3:** PbI_2 to 220°C target temperature at 10°C/min heating rate then to 250°C at 4°C/min as MAI is set to 80°C target temperature at 4°C/min heating rate.

For each study, at least ten experiments were performed. In the sake of repeatability, for each experiment, starting from an empty crucible, the same amount of fresh material, coming from the same powder batch, was loaded. The source locations (see Table 3 page 42 in Chapter 2) as well as the substrate holder rotation speed were kept constant.

It is important to stress again that the focus is here on the process outputs, not the material properties (these latter will be discussed further into the manuscript), as such the following sections will disclosed only process parameters (temperatures, chamber pressure and deposition rates) for each of the studies.

a. Study 1: PbI_2 290°C (8°C/min) and MAI 92°C (4°C/min)

This first study follows a routine close to the one previously used on the proof-of-concept reactor with both high temperatures and high deposition rates. Process plots for the different monitored parameters (temperatures, chamber pressure and deposition rates) are shown Figure 46 a to d. All ten experiments followed the exact same timing, as can be seen from the perfect overlay of all temperatures plots in Figure 46a.

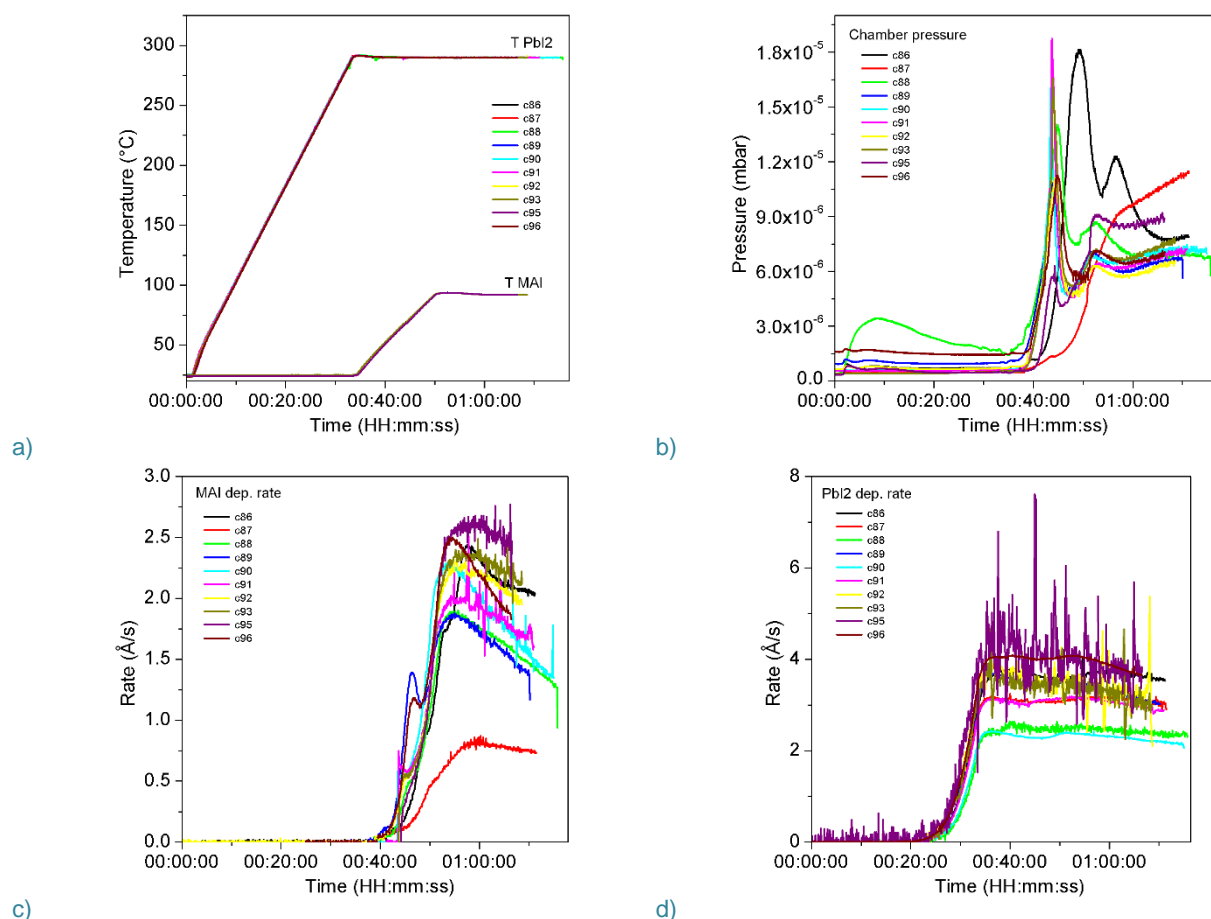


Figure 46. Process plots: a) Temperatures, b) Pressure, c) MAI deposition rate and d) PbI_2 deposition rate for experiments c86 to c96 for which the procedure was to heat PbI_2 to 290°C at 8°C/min from t_0 and then at t_0+35 min MAI was heated to 92°C with a 4°C/min heating rate.

Although the heating rates and target temperatures are perfectly identical between experiments, the pressure profiles (Figure 46b) are relatively different from one another. They follow more or less the same trend with a peak pressure and a stabilization to a pressure higher than the initial one. Both the amplitude of this pressure increase and the stabilization values are not consistent between experiments. Experiment c86 goes from 6×10^{-7} mbar to a peak pressure of 1.8×10^{-5} mbar before stabilizing around 9×10^{-6} mbar when experiment c92 goes from 6.4×10^{-7} mbar to a peak pressure of 1.1×10^{-5} mbar before stabilizing around 6×10^{-6} mbar.

Comparing the two compounds, one can notice a difference in profile between MAI and PbI_2 deposition rates: the organic salt response has a bell shape for most of the experiments (Figure 46c) while the lead-based compound remains relatively steady once a stabilized value is reached (Figure 46d).

Focusing on the quite unusual MAI deposition rate value of experiment c87 (red plot in Figure 46c), we find a corresponding pressure profile continuously increasing. As we would have expected an increasing pressure value to translate into an accordingly increasing deposition rate, we are unable to explain this behaviour. In fact, while c87's pressure profile is the highest, reaching 1.2×10^{-5} mbar by the end, the corresponding MAI deposition rate is the lowest of the present study, with 0.74 \AA/s in average.

From the rate statistics (Figure 47), we can see that the two precursors' responses are hardly consistent between experiments. Mean deposition rates (over the temperature-stable regime) going from 0.7 to 2.5 \AA/s for MAI and from 2.3 to 3.9 \AA/s for PbI_2 .

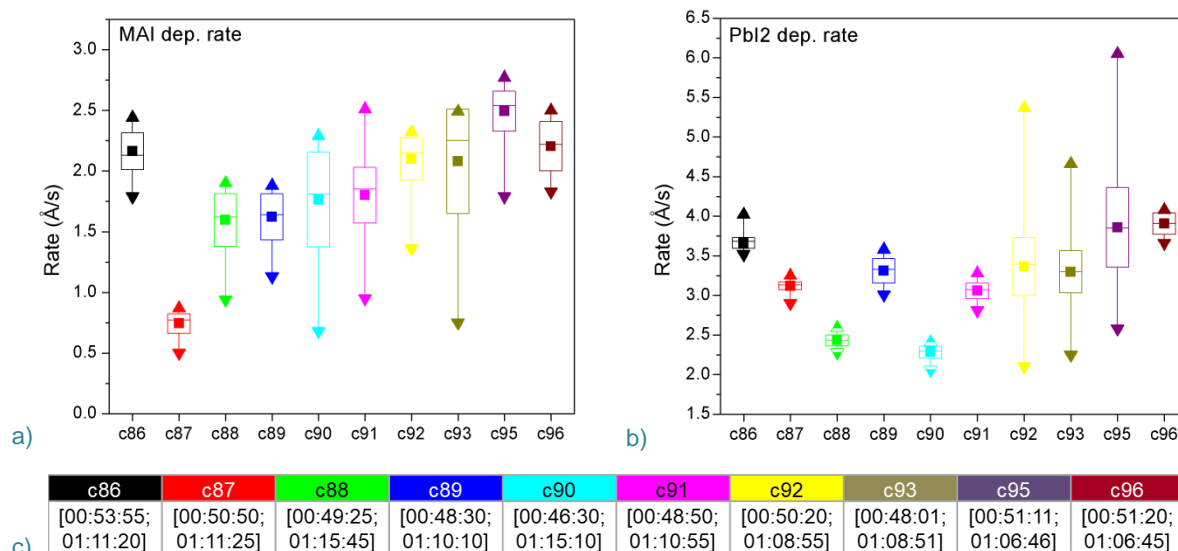


Figure 47. a) MAI and b) PbI_2 rate statistics for the different experiments of Study 1: \blacktriangle , \blacktriangledown , \blacksquare stand for the maximum, minimum and mean values, the box amplitude represents $2 \times \sigma$ (with σ the standard deviation) and the median value is materialized by the horizontal line in the box; and c) temperature-stable time range for statistics calculations.

b. Study 2: PbI_2 220°C ($10^\circ\text{C}/\text{min}$) then 250°C ($4^\circ\text{C}/\text{min}$) and MAI 60°C ($4^\circ\text{C}/\text{min}$)

In this second study we targeted lower temperatures both for MAI and PbI_2 as we were hoping to avoid any bell-shaped MAI deposition rate and to get a more reproducible PbI_2 deposition rate. Process plots for the different monitored parameters (temperatures, chamber pressure and deposition rates) are plotted Figure 48 (a to d). For this study, we were less rigorous on the timing as highlighted by the slight time delay of the temperature plots in between the different experiments in Figure 48a, but we kept the PbI_2/MAI heating timing consistent for each experiment.

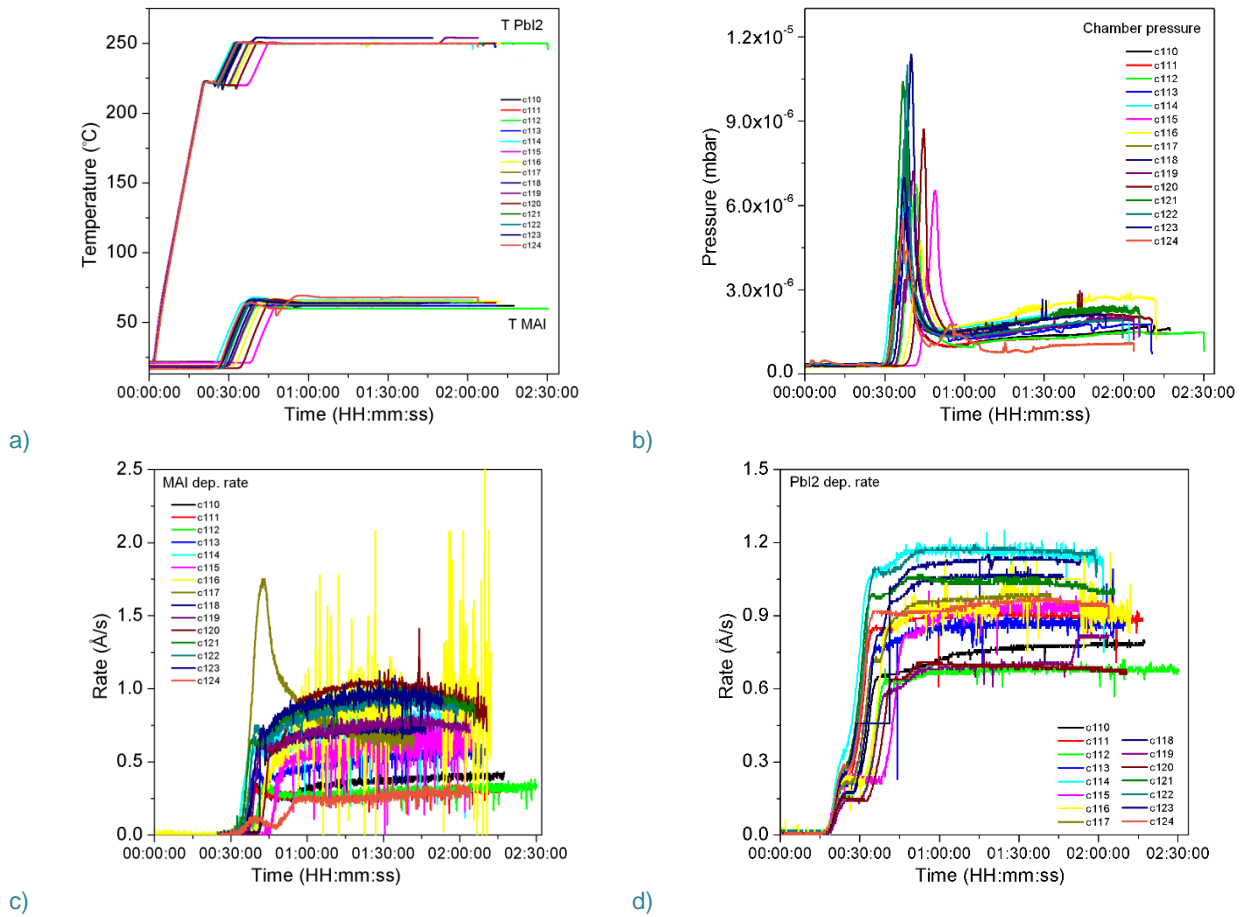


Figure 48. Process plots: a) Temperatures, b) Pressure, c) MAI deposition rate and d) Pbl₂ deposition rate for experiments c126 to c136 for which the procedure was to heat Pbl₂ to 220°C at 10°C/min from t_0 and then 250°C at 4°C/min while MAI was heated to 60°C with a 4°C/min heating rate from $t_0 \pm 30$ min.

Several differences can be found with the previous study. The pressure profiles (Figure 48b) now all follow the same trend, with a sharp increase as the 60°C target temperature is achieved, and their stabilization pressures are both more consistent and lower than for the previous study. In fact, they are now all below 3×10^{-6} mbar when they were between 6×10^{-6} mbar and 1.2×10^{-5} mbar in the case of the 92°C target temperature of Study 1. Also, the MAI deposition rate profiles are no more bell-shaped and the deposition rate remains relatively stable over an hour.

As for the previous study, although the temperatures and heating rates are consistent between experiments, neither of the deposition rates (MAI or Pbl₂) are consistent between experiments with a factor three difference between the lowest and highest MAI mean deposition rates (0.26 Å/s lowest value for c124 and 0.95 Å/s highest value for c120, Figure 49a) and almost a factor two for Pbl₂ (0.68 Å/s for c112 vs 1.15 Å/s for c114, Figure 49b).

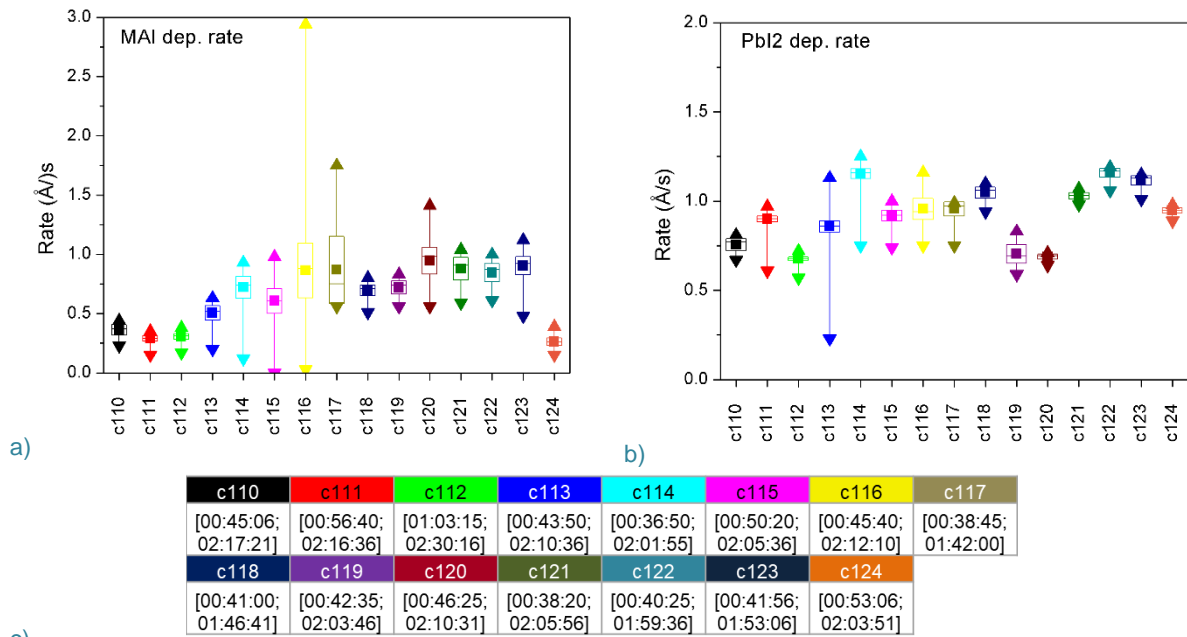
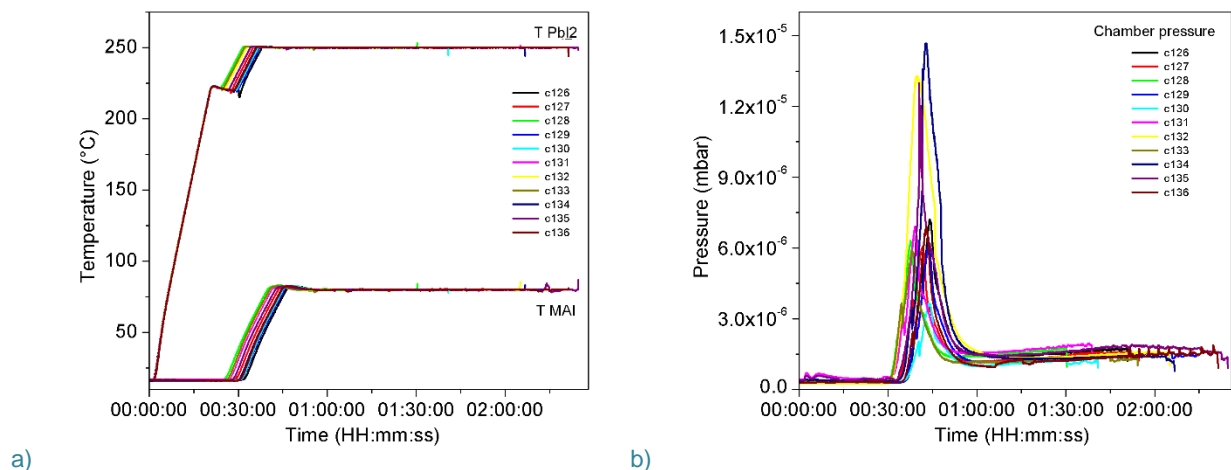
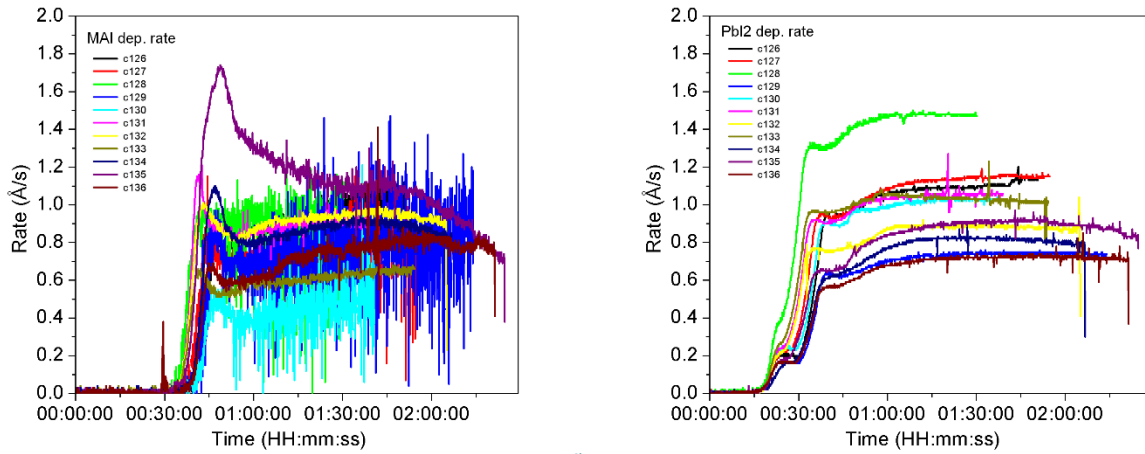


Figure 49. a) MAI and b) Pbl₂ rate statistics for the different experiments of Study 2: ▲, ▼, ■ stand for the maximum, minimum and mean values, the box amplitude represents 2 × σ (with σ the standard deviation) and the median value is materialized by the horizontal line in the box; and c) time range for statistics calculations.

c. Study 3: Pbl₂ 220°C (10°C/min) then 250°C (4°C/min) and MAI 80°C (4°C/min)

With the two first studies we have highlighted the difference in MAI behaviour between a 92°C and a 60°C target temperature. Both the pressure and deposition rates were more stable for the lower value. With this third study, we wanted to keep this stability gain while decreasing the processing time by choosing a 80°C MAI target temperature. The Pbl₂ heating conditions were kept constant from the previous study (*i. e.* 220°C at 10°C/min then 250°C at 4°C/min). Process plots for the different monitored parameters (temperatures, chamber pressure and deposition rates) are plotted Figure 50 a to d.

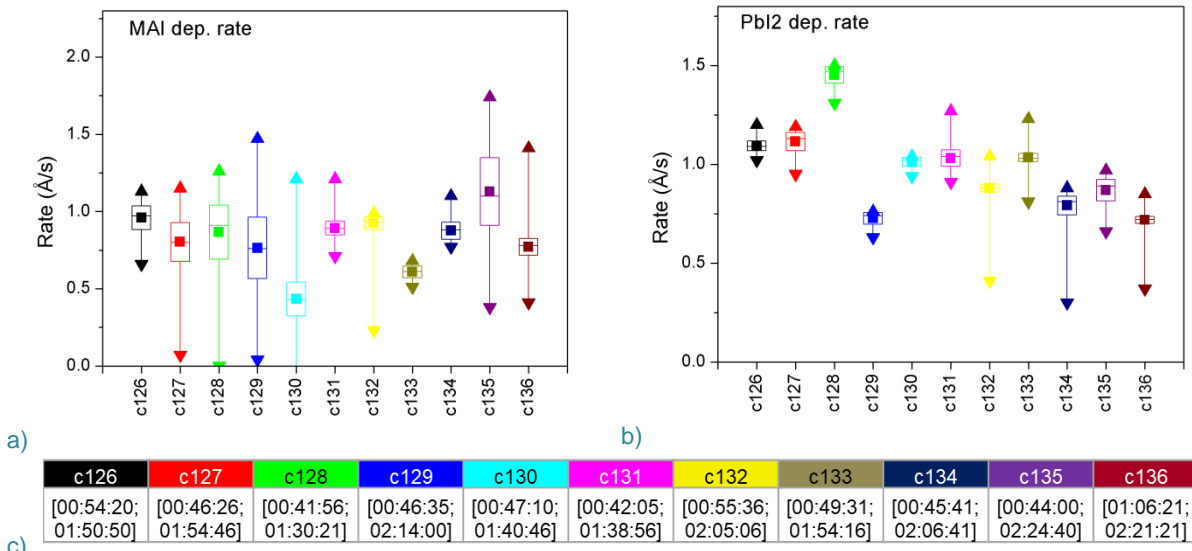




c) d)
Figure 50. Process plots: a) Temperatures, b) Pressure, c) MAI deposition rate and d) PbI₂ deposition rate for experiments c126 to c136 for which the procedure followed was to heat PbI₂ to 220°C at 10°C/min from t₀ and then 250°C at 4°C/min while MAI was heated to 80°C with a 4°C/min heating rate from t₀±30min.

For this third study, the pressure profiles follow the same trend as the previous study: with a sharp increase as the target temperature is reached followed by a stabilization to values below 3x10⁻⁶ mbar. The peak pressures are slightly higher, compared to the previous 60°C study, with values of 1.5x10⁻⁵ mbar reached.

Similarly to the previous study, although the temperatures and heating rates are identical between experiments, neither of the deposition rates (MAI or PbI₂) are consistent throughout this study. There is a factor 3 difference between the highest and lowest deposition rates (mean values) for MAI (1.13 Å/s for c135 vs 0.44 Å/s for c130) and a factor 2 in the case of PbI₂ (0.72 Å/s for c136 and 1.45 Å/s for c128) (Figure 51).



a) b) c)
Figure 51. a) MAI and b) PbI₂ rate statistics for the different experiments of Study 3: ▲, ▼, ■ stand for the maximum, minimum and mean values, the box amplitude represents 2 × σ (with σ the standard deviation) and the median value is materialized by the horizontal line in the box; and c) time range for statistics calculations.

d. Overall comparison of the three studies

The three studies are now compared to each other, with a focus on the deposition rates (Figure 52).

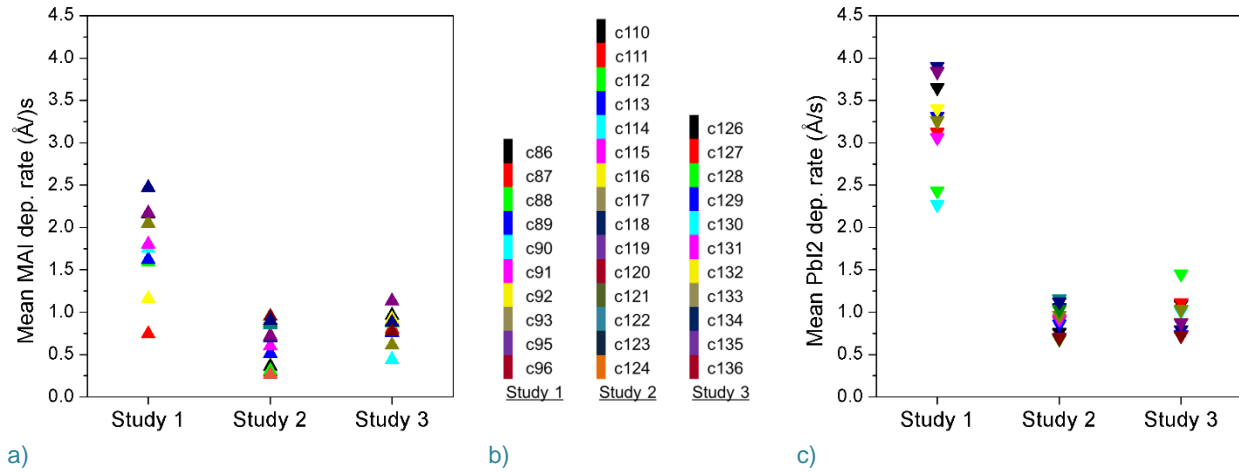


Figure 52. Mean deposition rates of each experiments of the different studies: a) for MAI and c) for Pbl₂. The color code for each study experiments is shown again in b).

These plots clearly highlight the differences in the deposition rates between the three studies. First, considering the inter-experiment variability: although there is still a non-consistency between the mean deposition rates outputs, its amplitude is smaller for the two last studies than for the first one where the mean deposition rates values are broadly spread (from 0.7 to 2.5 Å/s for MAI and from 2.2 to 4 Å/s for Pbl₂). Then, focusing on the deposition rates values themselves: for the first study, where the two precursors are heated to high temperatures (290°C and 92°C for Pbl₂ and MAI respectively), the mean deposition rates are higher than for the two lower-temperatures studies, with a factor three difference for Pbl₂ (± 3 Å/s for study 1 vs ± 1 Å/s for studies 2 and 3, Figure 52c). Interestingly, we identify no clear impact of increasing MAI target temperature from 60°C to 80°C on the deposition rates, these latter being rather consistent between studies 2 and 3.

It is interesting to notice that no correlation between the MAI and Pbl₂ responses could be found, for any of the three studies. Indeed, the lowest MAI deposition rate does not correspond to the lowest Pbl₂ deposition rate and the same goes for the respective highest deposition rates. This is quite surprising since we have shown, with the pseudo-coevaporations tests from the previous chapter, that MAI heating rises Pbl₂ deposition rate. From there, one would have thought that the greater the MAI deposition rate, the greater the Pbl₂ deposition rate would be, yet we do not see such correlation here.

It is also worth noting that, contrary to what we could have expected, we do not identify a clear trend in the evolution of the deposition rates between experiments. As aforementioned, we fear that the MAI covering the chamber walls (Figure 53) would become more and more parasitic as the number of experiments increases (as the amount on the walls would increase accordingly), yet no evidence of such tendency was found throughout the different studies.



Figure 53. Picture of the inside of the reactor (lower part, below the screening shield) highlighting the presence of a white MAI veil covering all the surfaces.

As this point, we find ourselves puzzled by these different tendencies (or lack thereof). In our mind, the parasitic behaviour of MAI is the only explanation for the process variability, yet we fail to clearly assess it with the present results.

With this focus on the process repeatability we have shown that despite being consistent in our inputs (target temperatures and heating rates), the output responses unfortunately lack of consistency. We were able to mitigate, to a relative extent, the amplitude of this non-consistency by decreasing both the PbI_2 and MAI temperatures, yet we couldn't entirely avoid it. We have reached an impasse and find ourselves unable to exactly pinpoint the origins of the inter-experiment variability.

Fortunately, these studies were not ran for the sole purpose of studying the parameter outputs, for each of these experiments samples were loaded into the reactor and thin films were fabricated. Let us now direct our focus toward the properties of these latter.

ii. Focus on the material properties

As we were in the developing phase, to save materials and time, we mostly worked with Glass/perovskite samples and only very rarely prepared full photovoltaic devices. The present section will disclose the results of the different material characterizations performed on the fabricated thin films. The Glass/perovskite samples were consistently studied by absorption spectroscopy and occasionally by Scanning Electron Microscopy (SEM) when the PV devices were studied by I-V characteristics measurements.

a. Absorption spectroscopy results for coevaporated perovskite thin films

Starting off with the Glass/perovskite samples, Figure 54 indexes all bandgap values, calculated from the absorption spectra using Planck-Einstein equation [7]:

$$E = \frac{hc}{\lambda} \quad [7]$$

where λ is the absorption threshold wavelength, determined from the spectra using a linear regression.

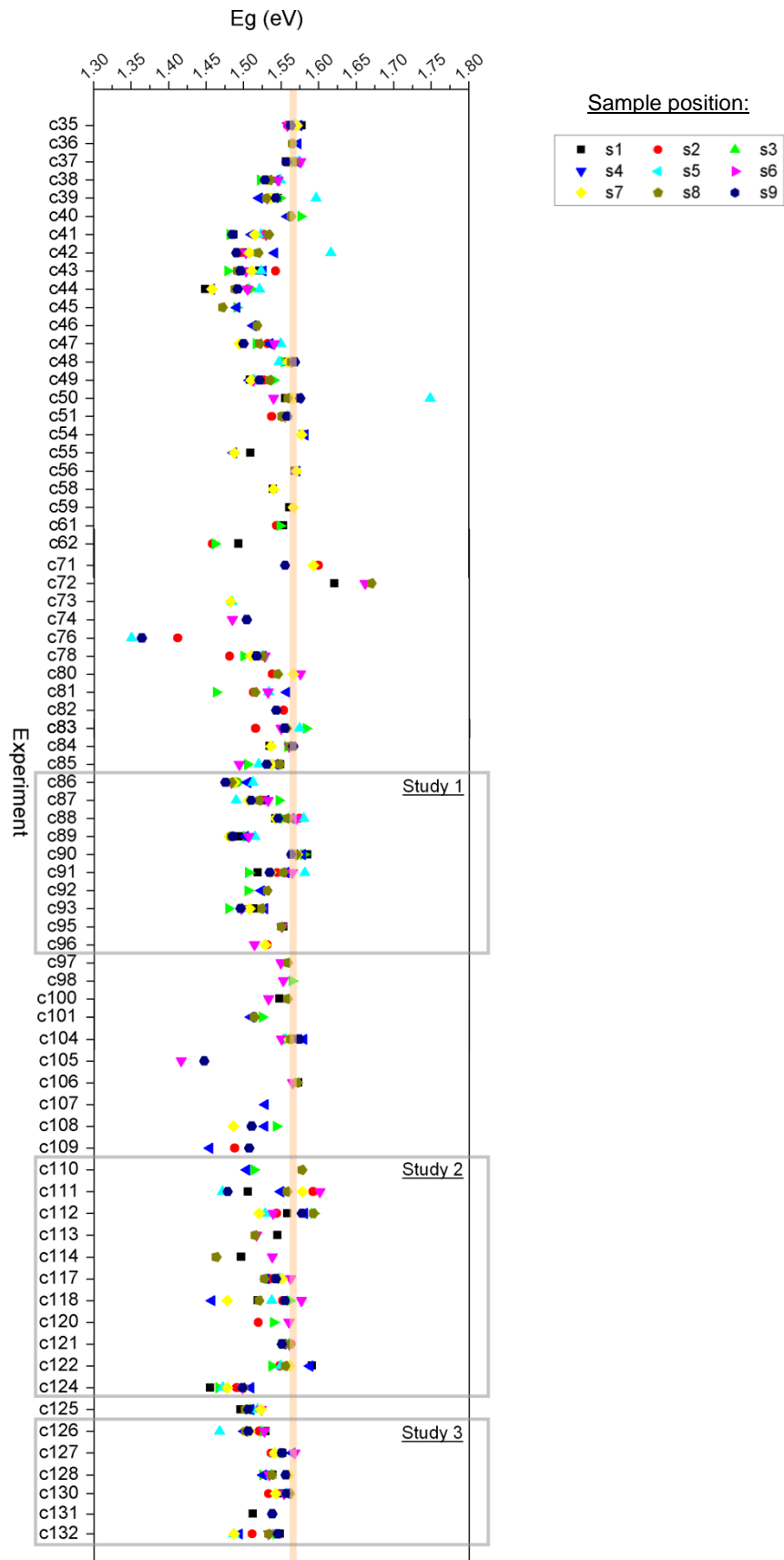


Figure 54. Bandgap (E_g) values calculated from absorption UV-visible spectroscopy measurements using Planck-Einstein equation ([7]) for all Glass/perovskite samples. The orange line at ± 1.57 eV stands for the $\text{CH}_3\text{NH}_3\text{PbI}_3$ reference bandgap value calculated accordingly from the spectra of wet-processed films. The three studies from the previous section are framed.

This representation of all calculated E_g values nicely highlights both the intra- and inter-batch variabilities. The corresponding value distribution (plotted Figure 55) does not follow a normal law: as two peaks can be seen; the first one being around 1.52 eV and the second one closer to 1.58 eV. With most of the values being between 1.5 and 1.60 eV, we are not so far from the target $\text{CH}_3\text{NH}_3\text{PbI}_3$ composition; although we are slightly off ($E_g < 1.5$ eV for instance) for a non-negligible number of samples.

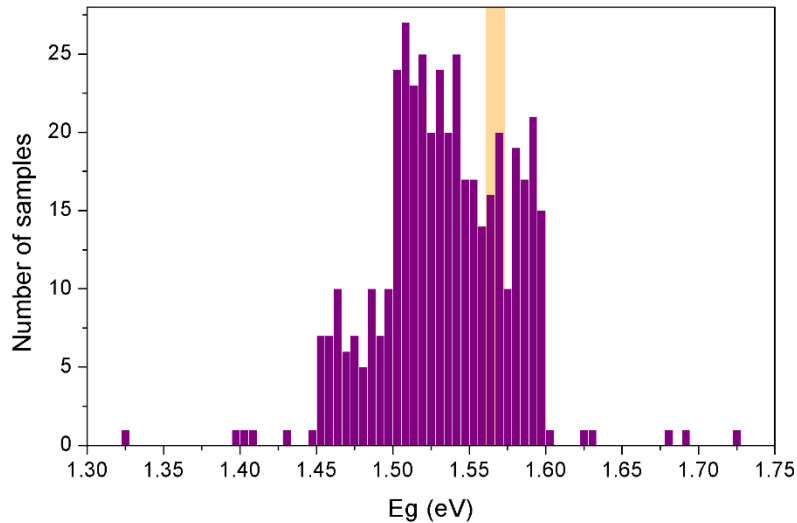
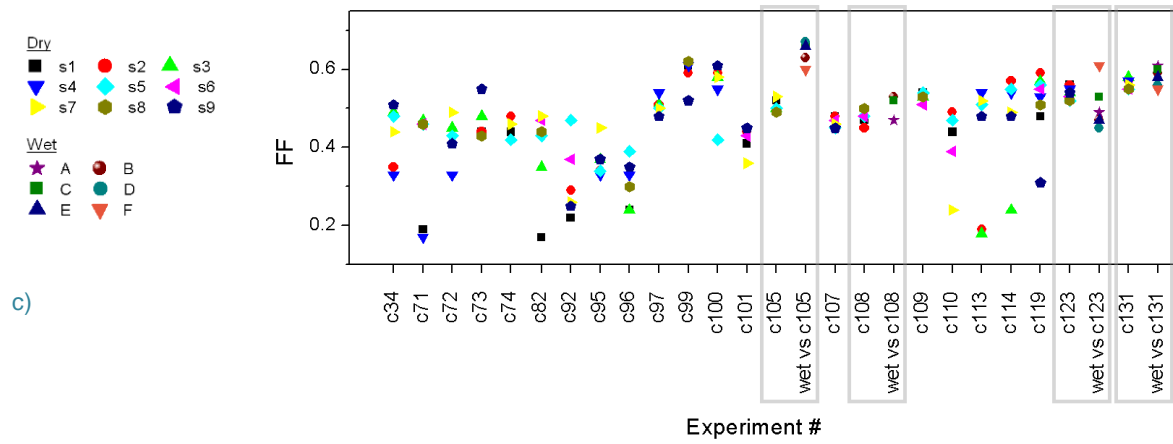
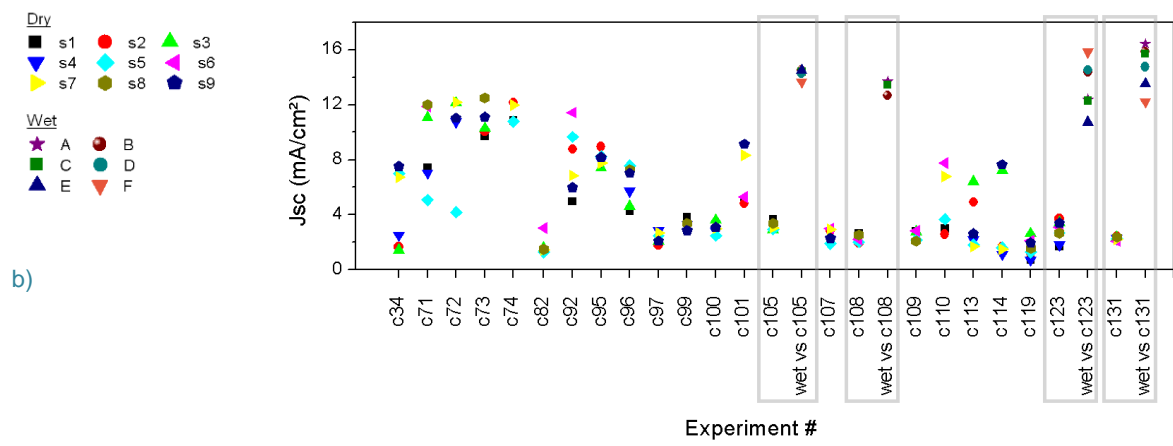
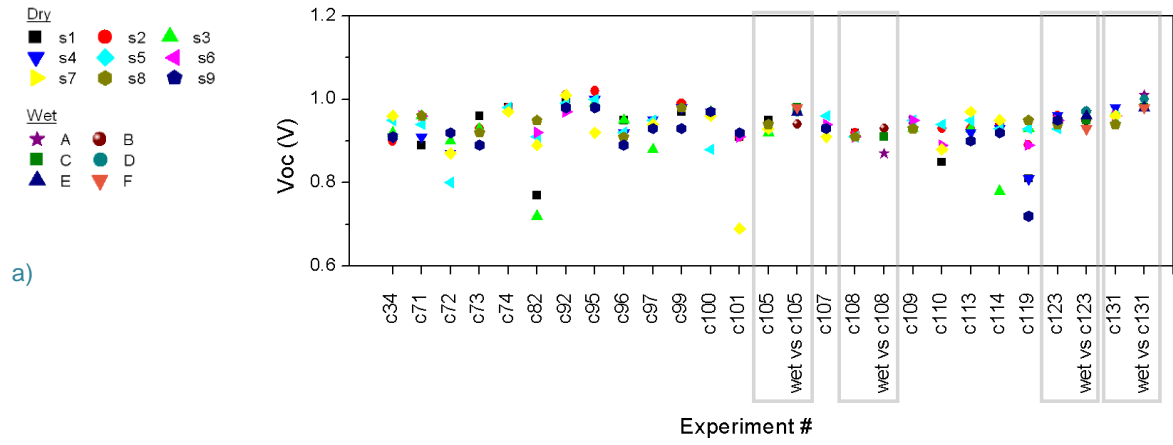


Figure 55. Distribution of Figure 54's E_g results. The orange line at ± 1.57 eV stands for the $\text{CH}_3\text{NH}_3\text{PbI}_3$ reference bandgap value calculated from the spectra of wet-processed films.

Given the non-consistency of the process, we found no clear correlation between the deposition conditions and the absorption spectroscopy results.

b. I-V characteristics results for coevaporated perovskite based solar cells

For I-V measurements, Glass/ITO/PEDOT:PSS/Perovskite/PCBM/Ag samples with a 0.28 cm^2 active area were fabricated (fabrication steps are detailed in Annexes, pages A to C). For few experiments, PV devices where the perovskite layer is wet-processed were prepared alongside the dry-processed ones, as a comparison. These fully wet-processed Glass/ITO/PEDOT:PSS/ $\text{CH}_3\text{NH}_3\text{PbI}_3$ /PCBM/Ag samples are part of LPICM baseline. Values of each PV parameters (V_{oc} , J_{sc} , FF and PCE) for all the fabricated perovskite solar cells are plotted in Figure 56.



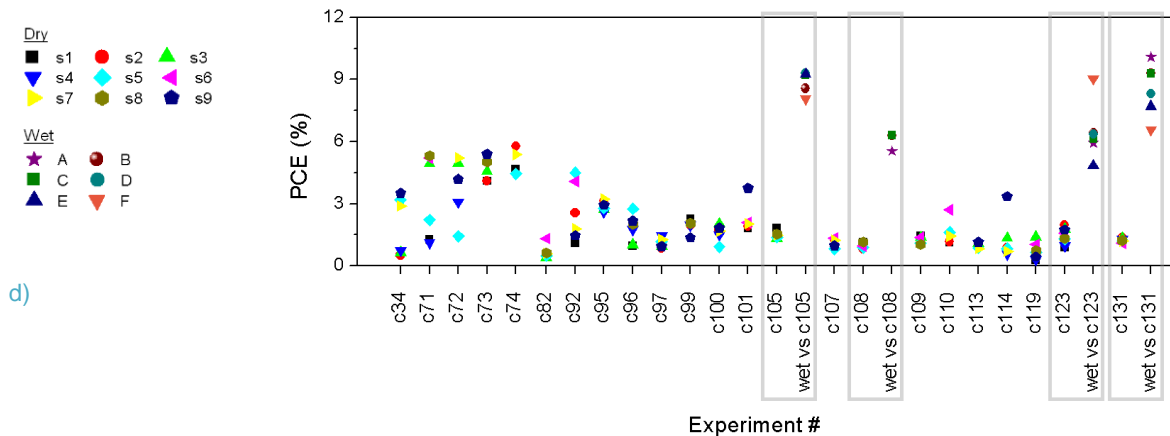
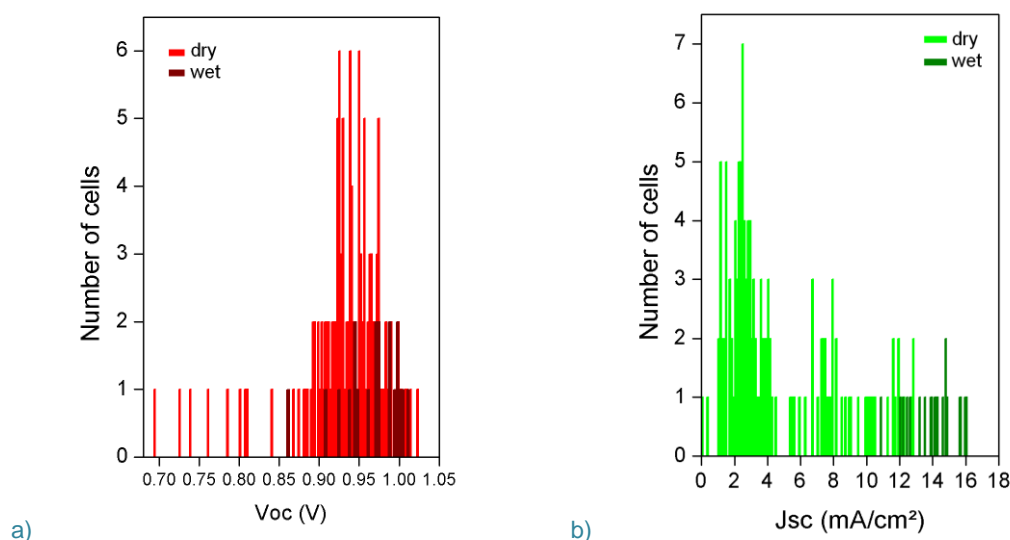


Figure 56. I-V characteristics values: a) Open circuit voltage (V_{oc}); b) Short-circuit current density (J_{sc}); c) Fill factor (FF) and d) Photoconversion efficiency (PCE) for all Glass/ITO/PEDOT:PSS/perovskite/PCBM/Ag solar cell fabricated ($s=0.28 \text{ cm}^2$). For experiments c105, c108, c123 and c131: fully wet-processed perovskite cells were prepared alongside as references (reported here as “wet vs experiment#”). These dry/wet comparisons are framed on each graphs.

From the absorption statistics (Figure 54) we have seen that the fabricated materials were not far from the $\text{CH}_3\text{NH}_3\text{PbI}_3$ target composition, yet the performances in solar cells are poor, with over 80% of dry-perovskite based cells below 3% photoconversion efficiency (Figure 56d). Taking a closer look at the other PV parameters, one can notice that the V_{oc} values are in good agreement with the usual values for the reference $\text{CH}_3\text{NH}_3\text{PbI}_3$ perovskite around 0.95 V but the J_{sc} and FF are on the other hand very low, resulting logically in low PCE. Even though these values are off, it is interesting to mention that they seem to be less distributed than for the wet-perovskite devices. This shows a higher homogeneity throughout the samples of a same batch in favour of the dry process with respect to the wet one, which is a good point for the industrialization stake.

To make more sense of these values, it appears more relevant to consider their distribution, while underlining the difference between wet- and dry-perovskite based devices results (Figure 57).



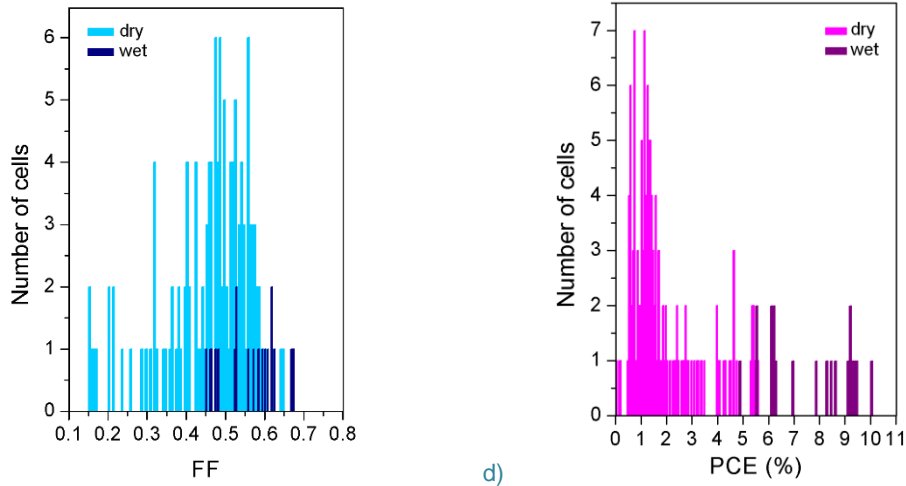
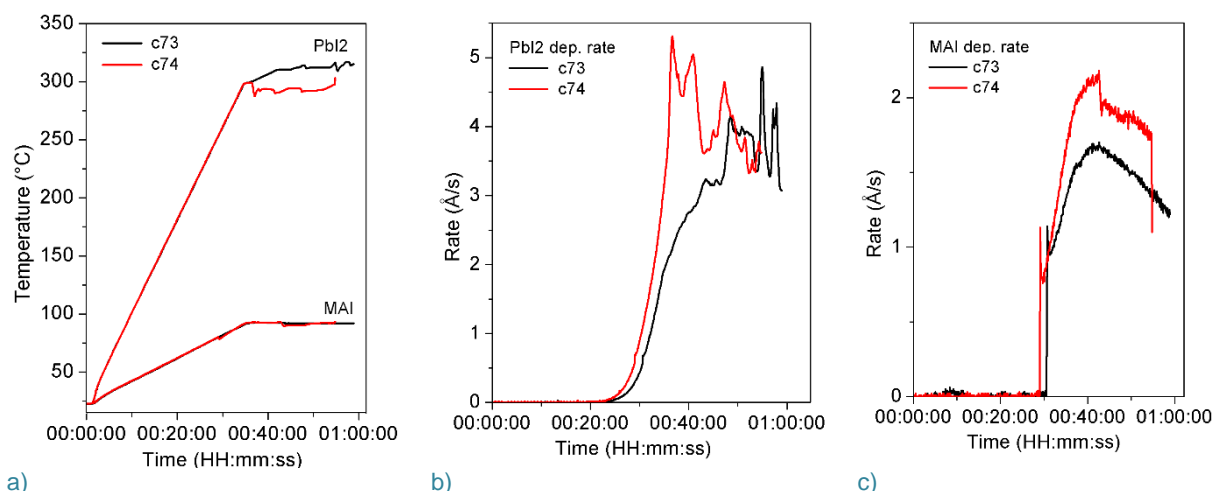


Figure 57. Distribution of Figure 56's results: a) V_{oc} ; b) J_{sc} ; c) FF and d) PCE values, only for coevaporated perovskite layers

With these distributions, we can clearly see, between dry- and wet-perovskites, a good consistency for the V_{oc} values (Figure 57a), a relative consistency for the FF values (Figure 57c) but a very poor consistency for the J_{sc} values (Figure 57b). In fact, the wet J_{sc} values are ~8 points higher than the dry ones. Despite the good V_{oc} consistency, this J_{sc} difference is so strong that it is passed on to the PCE (Figure 57d) where over 90% of dry-perovskite based devices are less than 3% efficient when all wet ones are between 5 and 10%.

From these results, the J_{sc} and FF values are clearly identified as problematic. While it could also be an issue of material (composition or quality), we rather suspect an interface issue to be at stake. One could think that the wet/dry/wet (PEDOT:PSS/perovskite/PCBM) sequence can be problematic, particularly the lower wet/dry interface (PEDOT:PSS/perovskite) but it seems very unlikely given that the poly-TPD/perovskite/PCBM (wet/dry/wet) sequence has been widely (and successfully) reported^{103, 107-111, 113}. One could then think it could be an issue of materials. While the dry-perovskite/PCBM interface has been widely reported; it is, to our knowledge; the first report of a PEDOT:PSS/dry-perovskite interface.

Focusing on the good efficiencies from experiments c73 and c74, one notices that these were high deposition rates experiments. Accordingly, deposition rates were poorly stable throughout the process (Figure 58), with a bell-shaped profile for the MAI. As such, we are hardly able to know the composition of the material deposited. It is also expected to be impossible to reproduce these experiments.



a) b) c)
Figure 58. Process plots for experiments c73 (black lines) and c74 (red lines): a) temperatures; b) Pbl₂ deposition rates and c) MAI deposition rates.

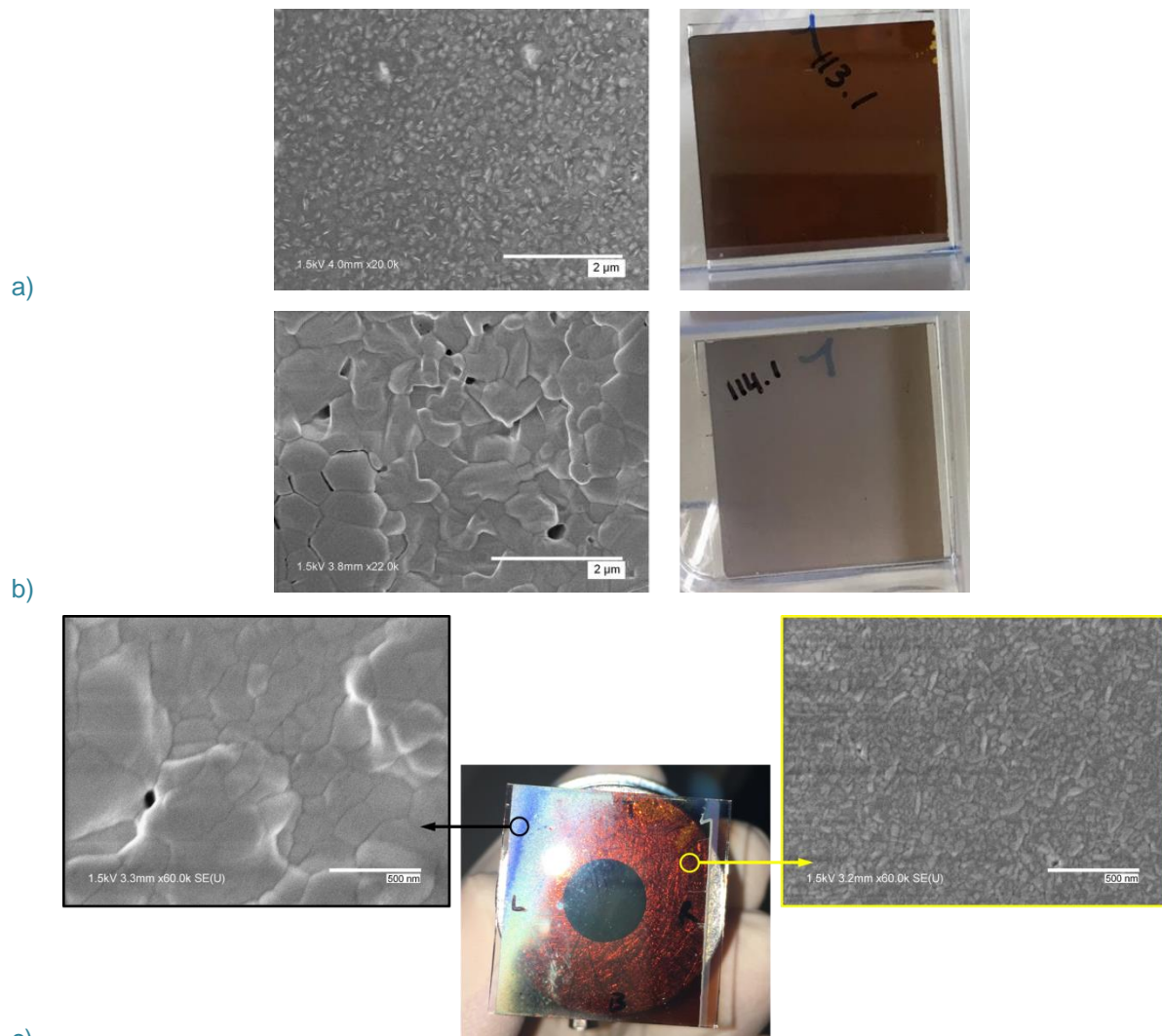
Despite the lack of consistency in the deposition conditions for these two experiments, we notice that the E_g values for the measured samples of both these experiments are around 1.49 eV, slightly off from the target 1.57 eV value for a CH₃NH₃PbI₃ composition. Yet, due to the intra-batch variability (seen for all experiments) we do not feel confident claiming that the good PV-performing samples had a composition consistent with the absorption-measured samples.

Correlating these PV performances to the repeatability studies, it appears that the gain in stability and repeatability (to a relative extent) on the process level appears to have been made at the expense of the material quality.

Considering poorly PV performing batches (c82, c95 and c113 among others), we notice that the absorption measured samples show E_g values closer to the target composition (~ 1.55 eV). At this point, we are unable to find any logical relationship between E_g values and PV performances.

c. Scanning Electron Microscopy analysis of coevaporated perovskite thin films

While running our repeatability studies we noticed the appearance of a white veil on some samples that gave them a milky aspect, with respect to their usual bright aspect. Using SEM we investigated the impact of this veil on the material structure. The results are shown in Figure 59.



c)
Figure 59. SEM image and pictures of a) fully bright sample (s1 from c113); b) fully 'milky' sample (c1 from c114) and c) both bright and 'milky' sample (s3 from c117) (on SEM images the scale bar is 2 μm on a and b and 500 nm on c).

From these SEM images we see a clear difference in the material structure, with small rice-like grains for the bright-looking films and big grain domains (1 μm wide for some) for 'milky'-looking films.

Given the striking difference in the material structure, one could think that the white aspect of the films could be optically induced. Recording absorption spectroscopy, we have shown a difference in the absorption feature too (Figure 60).

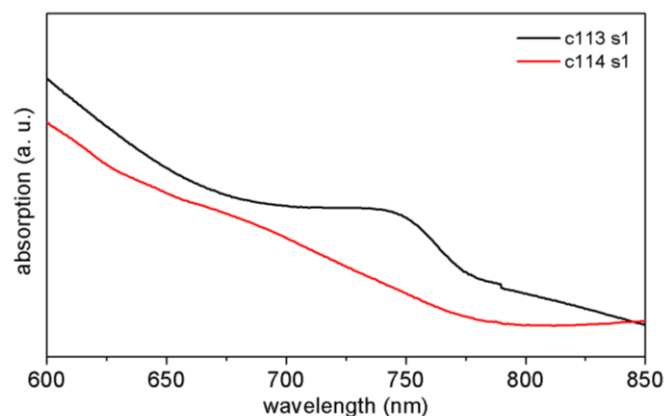


Figure 60. Absorption spectra of a bright-looking sample (c113 s1, black plot) and a milky-looking one (c114 s1, red plot).

Bright sample from c113 shows the characteristic perovskite absorption with an onset wavelength around 800 nm (black plot Figure 60) when milky sample from c114 shows a diffuse absorption feature (red plot Figure 60). From this difference, one can reasonably conclude that the white aspect of the films is not only optically induced but originates from the presence of an actual white layer. Given the materials loaded in the reactor (white MAI and yellow PbI_2) and the presence of MAI all over the chamber, we can assume that this white layer is MAI. We found no conclusive process-related explanation (pressure, MAI/ PbI_2 deposition rates) for this difference in composition. Our hypothesis is that upon cooling of the chamber after the process, parasitic MAI deposits on the samples.

The presence of this white veil was neither homogeneous nor reproducible: for some experiments, all nine samples were covered (some fully (c114 samples in Figure 61), others only partly (Figure 59c)) and for others only some samples of the batch were covered (c113 samples in Figure 61). No correlation was found between the veil presence and the sample position.

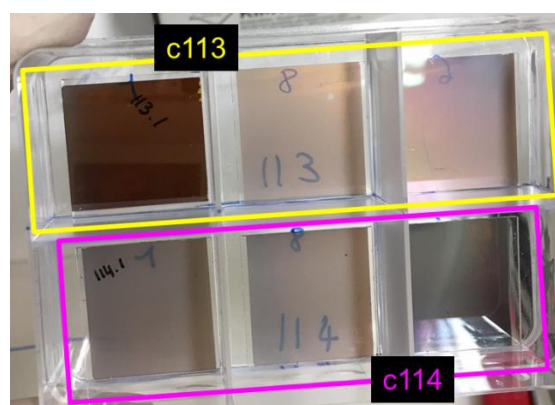


Figure 61. Picture of samples showing both bright and 'milky' samples for c113 when all three samples of c114 were 'milky'.

At this point, we have shown the difficulty of managing and understanding the coevaporation process of MAI and PbI_2 . We spent quite some time trying to understand the reactor response, trying to get repeatability between our experiments. We deemed best to focus mostly on Glass/perovskite samples and prepared only few batches of solar cells. As we did not really know what would be the material deposited given our repeatability issues, we wanted to save time and materials by focusing on simple samples and not complex solar

cell stacks. Failing to get repeatability in the process, we nonetheless managed to mitigate the inter-batch variability, to a relative extent. The large number of samples fabricated did not allow to identify any clear link between deposition conditions and material properties.

II. Open discussions

Writing this manuscript we realized that some choices (made as we started working on this reactor) were maybe not the best ones. The present section will address some of these choices through open discussions, while providing ideas for future developments.

i. Process-related aspects

With our different studies, we managed to get stable deposition rates during process, working with low heating rates and temperatures, but unfortunately failing to get a good repeatability between experiments. As we were unable to be reproducible using the temperature control mode, next step would be to switch to the rate control mode. Using a rate-driven process would ensure this output repeatability we are lacking for the moment and would allow us to run studies where we would vary the materials deposition rates, their ratio and the deposited thickness. Building a design of experiments we would then be able to determine the good deposition conditions.

Switching to a rate control mode would require a slight adjustment of the process. As aforementioned, rate control mode implies the simultaneous opening of all active source shutters. Given our PbI_2 initial deposition step, performed while the MAI source is cold and its shutter closed, we would either need to work in two regimes (a first temperature-driven regime where only PbI_2 source is heated to its sublimation temperature for the few nanometres deposition and a second rate-driven regime where both MAI and PbI_2 sources are active for coevaporation) or work with a two-step rate-driven regime (during the first phase MAI rate target would be zero while PbI_2 rate target would be non-zero for the few nanometres deposition and in the second phase MAI rate would be set to the target value for coevaporation).

From the results presented in this chapter, we were unable to correlate the process conditions (MAI and PbI_2 deposition rates) to the material properties. We have shown that the MAI vapor cloud disturbs the PbI_2 sensor reading. We then expect the PbI_2 -sensor signal to correspond in fact to a ' $\text{PbI}_2 + \Delta\text{MAI}$ ' deposition rate. Given the presence of a directing tube on the sensor (Figure 53) and the swirling nature of the MAI cloud, we hardly expect the MAI part interfering in the QCM read to be neither constant nor reproducible. It would be interesting to put one QCM sensor at the sample position and see how its reading correlates to the PbI_2 one.

ii. Material-related aspects

We are fully aware that we are missing some key insights on the material characterization level. The choice was made to focus on understanding the reactor, to be able to prepare samples in a reproducible way rather than fully characterize a batch of samples we could only fabricate once. From the pitfalls of the current approach, we have identified several relevant characterizations that would provide us with useful information.

To investigate further the white parasitic layer (that we suspect to be MAI) we would perform Energy Dispersive X-ray Spectroscopy (EDX) or UV Photoelectron Spectroscopy to confirm the nature of the layer.

Assuming that the low J_{sc} values are linked to the material, we could perform Time-Resolved PhotoLuminescence (TRPL) measurements to assess the carrier lifetime. Assuming that the low J_{sc} values are linked to an interface issue, it would be interesting to integrate a polyTPD layer to our current stack structure (between PEDOT:PSS and perovskite) to see if this improves in any way the performances.

With the objective of commercialization, next steps would include going from 25x25 mm samples to a 10x10 cm. Going one step further toward commercialization, we would eventually go for fully dry-processed solar cells, removing all solution-process steps.

As it can be guessed from its constant mention throughout this chapter (and the previous one), MAI vapor is an important issue. Given the objective of fabricating $CH_3NH_3PbI_3$ by coevaporation, we have until now only used MAI and PbI_2 , it would be interesting to switch to other precursors (thus other perovskite composition) that would potentially be less problematic than MAI, for instance formamidinium iodide $CH(NH_2)_2I$ or CsI. Despite the slight disinterest of the community for it (as it is poorly stable and not the best performing absorber), the reference $CH_3NH_3PbI_3$ perovskite is yet still not fully understood. It is the most basic perovskite material, which makes it very relevant for fundamental studies.

Keeping the $CH_3NH_3PbI_3$ composition and thus the MAI precursor, we would need to mitigate its parasitic effect. One way would be to clean the reactor between each experiment. Besides being tedious it is also far from safe as it would imply a direct contact with hazardous materials like PbI_2 . Although it would complicate the set up, we could implement an *in situ* cleaning, as it is widely performed for in the field of Silicon with plasma. Another, less constraining, approach would be to succeed in turning the cloud-like evaporation behaviour of MAI into something directive (like PbI_2). Given the high volatility of MAI (we have shown that the pressure starts increasing as soon as a 35°C temperature is reached) one idea would be to work in a cooled environment. As we started working on the reactor, MBRAUN Company along with its partner CreaPhys announced the launching of an updated version of their equipment with a cooling system integrated into the chamber walls¹²³. Unfortunately, no upgrade of our equipment was possible. We could try to implement a similar set up by inserting inside the chamber a water distribution system. A less heavy alteration could be to adapt a cone on the MAI source that would physically constraint its evaporation and would limit the chamber contamination.

Finding the right balance between samples fabrication and characterization surely holds the key to better understand both the process and the material.

¹²³ PEROVap system (patent pending)

Conclusion

In the present chapter we have presented the development of the coevaporation process to fabricate $\text{CH}_3\text{NH}_3\text{PbI}_3$ starting from $\text{CH}_3\text{NH}_3\text{I}$ (MAI) and PbI_2 powder precursors using the previously designed reactor. Starting from scratch we performed experiments in a repeatable manner building studies where we would follow an identical procedure for several experiments. We were quite puzzled by the non-repeatability in the output parameters we first obtained. We managed to mitigate to a certain extent this variability by adjusting our input parameters to lower temperatures but were not able to entirely suppress it. Logically, this poor process repeatability translated into an inter-experiment variability.

Despite the lack of process repeatability, we have performed a significant number of experiments and fabricated perovskite films for various characterization purposes: absorption spectroscopy, SEM and even I-V measurements. Considering all these experiments we stumbled upon several issues. First, adding to the inter-experiment variability, we have shown an intra-experiment variability; with material properties varying throughout one batch of samples. Then, we have found all our PV devices to have good V_{oc} while having very low J_{sc} , resulting overall in low efficiencies. Finally, we faced the non-predictable and non-reproducible presence of a parasitic white veil on our samples.

We eventually took a step aside from all these results and provided ideas to better control the process and better know our material. These ideas would eventually be implemented as the reactor starts again in its new location in IPVF.

Chapter 4.

Nanoscale characterisation of perovskite films using Synchrotron-based technique.

“The average user of Synchrotron Radiation is not so much concerned about the complex equipment behind the concrete wall which separates the experimental area from the storage ring itself. What the user is aware of is that the source of radiation can easily become a master rather than a servant and the enthusiastic experimenter can be confronted by frustrating periods of down time just at the moment when the measurements are on the verge of success. (...) Nevertheless, judging by the increasing number of users of Synchrotron Radiation and the quality of the work they are producing the scientific advantages outweigh the irritations and difficulties.”

P. J. Duke

“Synchrotron Radiation and the Submicron world:
selected activities at the Daresbury Laboratory, UK.”
in *Examining the submicron world*

Introduction

In the course of this thesis, our team conducted three Synchrotron beamtimes on a Scanning Transmission X-ray Microscopy technique at SOLEIL facility in the Paris region. While two of them were focused on wet-processed perovskite PV devices, one beamtime was dedicated to the study of dry-processed ones. With the aim of better understanding the evaporated perovskite material, we found it relevant to benefit from one of these synchrotron campaigns to build a study around the comparison of wet- and dry-processed perovskite films.

As a spectromicroscopy technique, Scanning Transmission X-ray Microscopy (STXM) combines X-ray microscopy imaging with X-ray Absorption Spectroscopy. Given the nature and complexity of perovskite layers, studying them with a low damage (soft X-rays) and high resolution (35 nm) technique such as STXM seems a reasonable choice. The spectral aspect of the technique was expected to be useful to determine the actual composition of our evaporated perovskite material with respect to the wet one as well as potentially pointing out difference in chemical environment depending on the deposition method.

By now, the reader masters the two topics of perovskites and their vacuum deposition (as they were thoroughly developed in the two previous chapters) but Synchrotron-based STXM might be a mystery. As the first thesis in our team including Synchrotron measurements, the present chapter will take the reader through the basic principles of X-rays interaction with matter (with a focus on X-ray Absorption Spectroscopy), background and history of Synchrotron facilities and the application in Scanning Transmission X-ray Microscopy before stepping into the study conducted and unveiling the results.

I. X-ray radiation¹²⁴

X-rays were discovered in 1895 by Wilhelm Conrad Röntgen, a German physicist, using a Crookes-Hittorf tube powered by a Ruhmkorff coil and a barium platinocyanide-painted paper screen. He noticed that when set almost two meters away from the fully covered tube the screen fluoresced in the distinctive [Pt(CN)₄Ba, H₂O]'s green. No rays were visible between the tube and the screen. Röntgen concluded that some invisible-to-the-naked-eye rays were passing through the covering cardboard and air to reach and excite the painted screen. He published only three papers on his discovery^{125,126,127} when no less than a thousand papers were published on the topic in the year 1896 alone. Röntgen was awarded in 1901 the very first Nobel Prize in Physics “in recognition of the extraordinary services he has rendered by the discovery of the remarkable rays subsequently named after him”¹²⁸.

Very promptly the medical community took a strong interest in these new rays. In 1896, Frost and Austin used X-rays as a diagnostic tool¹²⁹ (marking the beginning of medical imaging) and Dr Grubbé succeeded in treating breast cancer with X-rays¹³⁰ (marking the beginning of radiotherapy). Dangers of these rays were pointed out very early by Dr Gage and confirmed by Becquerel and the Curie couple, respectively discovering and conceptualizing radioactivity (shared Nobel Prize in 1903). In the following years, fear grew stronger, slowing things down a bit for X-rays in science. The 1910s marked the revival of the interest with several milestone discoveries. In 1912 Von Laue, Nobel Prize in 1914 “for his discovery of the diffraction of X-rays by crystals”, proved the electromagnetic nature of these radiations. In 1913, Bragg father and son, shared Nobel Prize in 1915 “for their services in the analysis of crystal structure by means of X-rays”, formulated the law to determine a crystal structure. Overall, there are over 20 Nobel Prizes (Chemistry, Physics and Medicine) based on X-ray work.

Given their small wavelengths (high energy) and unique interaction with matter, X-rays are very powerful probes to study both structural and chemical properties of a large variety of samples at the nanoscale. Their interaction with matter can result in emission, scattering, reflection or absorption¹³¹, the latter being our focus in the present chapter.

¹²⁴ J. J. Samuelli 'The discovery of X-rays by Röntgen', [bibnum library](#)

¹²⁵ W. C. Röntgen “Über eine neue Art von Strahlen” (1895) Sitzungsberichten der Würzburger Physik.-medic. Gesellschaft, English translation in [Nature](#)

¹²⁶ W. C. Röntgen “Über eine neue Art von Strahlen 2” (1896)

¹²⁷ W. C. Röntgen “Weitere Beobachtungen über die Eigenschaften der X Strahlen” (1897) Sitzungsberichten der Akademie der Wissenschaften zu Berlin

¹²⁸ [nobelprize.org](#)

¹²⁹ 'Inventions: Diagnostic X-rays' from [Darmouth.edu](#)

¹³⁰ E. H. Grubbé, (1933) *Radiology*, 21, 156-62

¹³¹ B. L. Henke *et al.*, (1993) *Atomic Data and Nuclear Data Tables*, 54, 2, 181-342

II. X-ray Absorption Spectroscopy^{132 133 134}

X-ray Absorption Spectroscopy (XAS) is the study of the energy dependency of the absorption coefficient of a material, in the X-ray range. This technique can provide insights on the structural, electronic and magnetic properties of a specimen.

Considering an incident ray of I_0 intensity absorbed by a sample of thickness t , the transmitted intensity I_t follows the Beer-Lambert law:

$$I_t = I_0 e^{-\mu(E)t} \quad [8]$$

where $\mu(E)$ is the absorption coefficient of an atom that varies as a function of energy as follows:

$$\mu(E) \sim \frac{dZ^4}{mE^3} \quad [9]$$

with d , Z and m being respectively the density, atomic number and mass. Following this equation, as energy increases, absorption coefficient should decrease. However, for particular energy values, a steep increase in $\mu(E)$ can occur. The energy of this so called 'absorption edge' corresponds to a transition between particular electronic levels. In the case of X-ray absorption, the energy is high enough (100 eV to 100 keV) that affected levels, for many elements, are core ones.

When X-rays strike an atom, an electron from the core shell is promoted to a higher energy level, leaving behind a very unstable core hole (10^{-15} s lifetime¹³⁵). This core hole will be quickly filled by a higher-level electron, resulting in an energy release via non-radiative Auger electron emission or X-ray fluorescence. As depicted Figure 62, the X-ray generated photoelectron can go to an unoccupied bound level (process '1') or into free levels, *i.e.* the vacuum (process '2') (Figure 62).

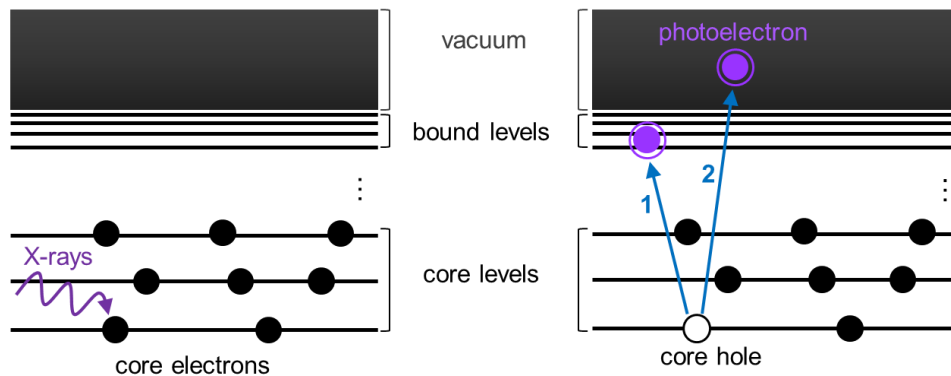


Figure 62. X-ray absorption processes¹³⁶.

Following Bohr's model, absorption edges are named after the initial level of the transition. As such, the K-edge represents the transition from the $n=1$ level (1s orbital),

¹³² Y. Joly and S. Grenier, 'Theory of X-ray absorption near edge structure' in *X-Ray Absorption and X-Ray Emission Spectroscopy: Theory and Applications*, J. A. Van Bokhoven and C. Lamberti (2006).

¹³³ C. S. Schnohr and M. C. Ridgway, 'Introduction to X-ray absorption spectroscopy' in *X-ray absorption spectroscopy of semi-conductors*, C. S. Schnohr and M. C. Ridgway (2015).

¹³⁴ X-ray Spectroscopy Chemistry LibreTexts

¹³⁵ O. Björneholm *et al.*, (1997) Phys. Rev. Lett. 79, 17, 3150-3

¹³⁶ adapted from Ref. 133

L-edges the transition from the $n=2$ level (2s and 2p orbitals for L_1 and $L_{2,3}$) and M-edges the transitions from $n=3$ level (3s, 3p and 3d orbitals for M_1 , $M_{2,3}$ and $M_{4,5}$).

Depending on the value of the energy of the incident X-rays (E), different subsets of XAS can be defined (Figure 63): when E matches the binding energy of a core electron (E_0) it corresponds to the edge; when E is in the range of $[E_0; E_0 + 50 \text{ eV}]$ it corresponds to the X-ray Absorption Near-Edge Structure (XANES, or NEXAFS for Near-Edge X-ray Absorption Fine Structure) and when E exceeds E_0 by more than 50 eV it corresponds to the Extended X-ray Absorption Fine Structure (EXAFS) region.

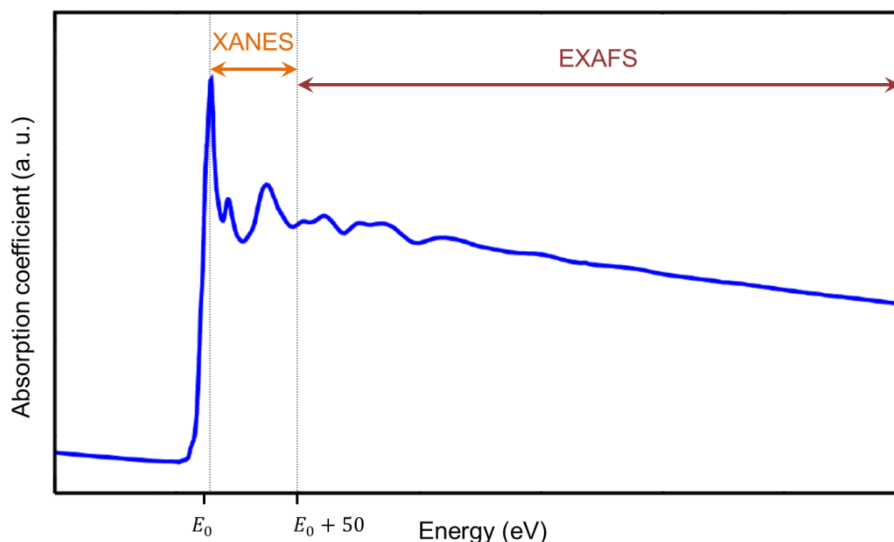


Figure 63. Example of XAS spectra with the XANES and EXAFS subregions¹³⁷.

If the edge energy is characteristic of the absorbing atom itself, XANES and EXAFS subregions give insights on its surroundings. In the XANES region, the photoelectron has enough kinetic energy ($E_c = E - E_0$) to reach the vacuum but not enough to be completely free from the parent atom. It will encounter multiple scattering with the surrounding non-absorbing atoms. In the EXAFS region, the photoelectron is so energetic that it will encounter non-elastic scattering with a surrounding atom and then be emitted.

Laboratory scale equipment for X-ray Absorption Spectroscopy; such as Bruker XRD equipment¹³⁸; use tubes (usually with Cu or Mo targets) as X-ray sources. It has the advantages of being cheap and easy to implement but the quality of the obtained X-ray is relatively poor. As shown Figure 64, these laboratory sources are more than four orders of magnitude less brilliant than storage rings Synchrotron sources.

¹³⁷ adapted from M. Newville, (2014) Reviews in Mineralogy and Geochemistry, 78, 1

¹³⁸ XRD Bruker

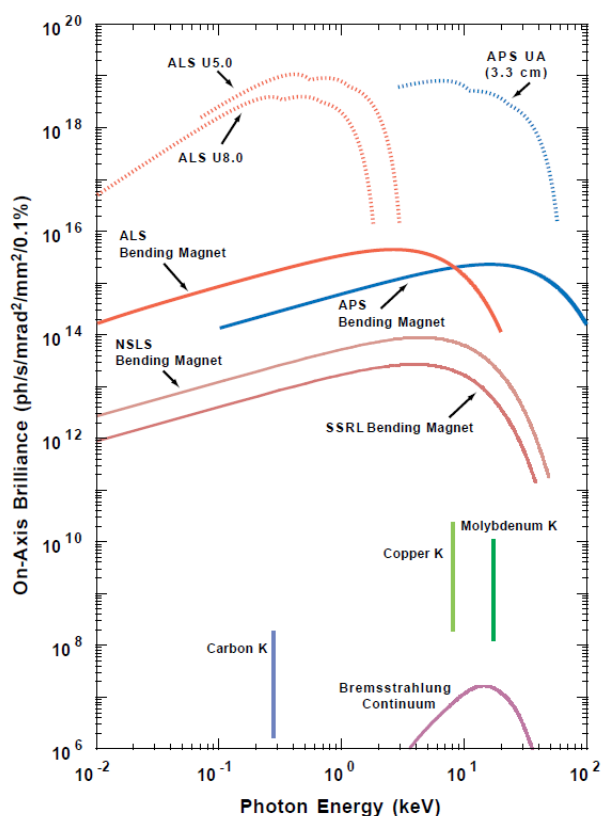


Figure 64. Comparison of laboratory sources (Copper and Molybdenum) and storage rings Synchrotron sources (ALS: Advanced Light Source, APS: Advanced Photon Source, NSLS: National Synchrotron Light Source and SSRL: Stanford Synchrotron Radiation Lightsource)¹³⁹.

Synchrotron lightsources unique features of energy tunability and high brilliance are very relevant to study multi-elemental composition materials such as perovskites.

III. Synchrotron lightsource^{140 141 142}

A Synchrotron lightsource is a type of particle accelerator that turns relativistic electrons into very bright light with a continuous spectrum: the so called 'Synchrotron radiation'. The working principle relies on one unique simple physical phenomenon (simplified Maxwell-Lorentz theory): when diverted, a moving electron will release energy.

i. Synchrotron radiation^{143 144 145 146 147}

The Synchrotron Radiation (SR) corresponds to a specific type of electromagnetic radiation emitted by radially accelerated particles. It can be naturally or artificially generated (Figure 65). The Crab Nebula is one of the most known examples of natural state SR. What

¹³⁹ J. R. Helliwell, (1998) *Nature Structural Biology*,5, 614-7

¹⁴⁰ [Diamond light source education resources](#)

¹⁴¹ [Canadian light source education resources](#)

¹⁴² [ESRF light source education resources](#)

¹⁴³ A. L. Robinson, 'History of Synchrotron Radiation' from *X-ray Data Booklet*

¹⁴⁴ [Lightsources.org resources](#)

¹⁴⁵ M. N. Piancastelli 'Intro to SR and FEL spectroscopy' for EUSpec Winter School on core levels 2016

¹⁴⁶ F. Baudelet (2014) 'Les origines du rayonnement synchrotron' in *Histoire de la recherche contemporaine Rayonnement Synchrotron: de Frascati à SOLEIL (1963-2013)*

¹⁴⁷ F. Méot 'An introduction to particule accelerators' (2009)

is considered to be the first artificial generation of SR, was seen at General Electric's 70-MeV betatron¹⁴⁸ in 1947.

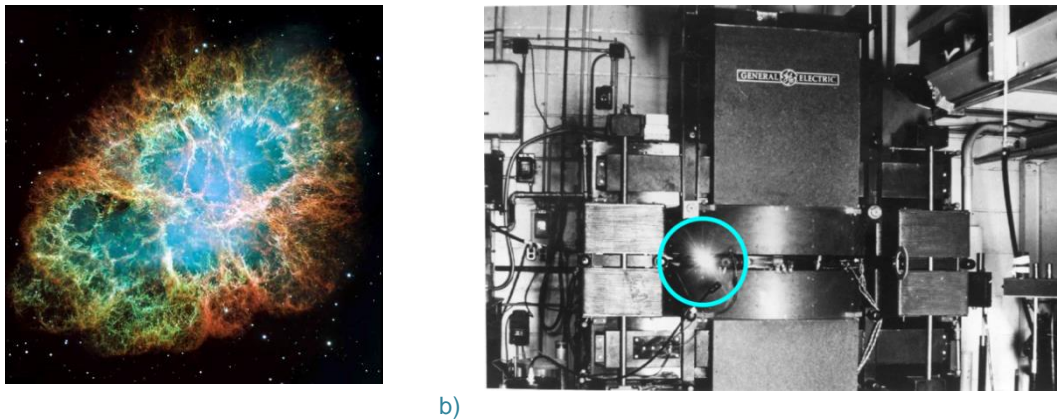


Figure 65. a) Composite image from NASA¹⁴⁹ of the Crab Nebula exhibiting natural state SR (central bluish light) and b) First artificially generated visible SR at General Electric in 1947¹⁵⁰ seen through the transparent vacuum chamber wall (circled out on the image).

Compared to a cyclotron in which particles are accelerated using an electric field, a betatron is a magnetic-field-driven particle accelerator. In 1994, Iwanenko and Pomeranchuk calculated the maximal working energy of these instruments to be of 0.5 GeV following the 'values [*then*] being in use'¹⁵¹. This limitation was due to the radiative energy loss occurring at high energies in a betatron. The two scientists were in fact just pointing out the SR phenomena (already fully theorized by Liénard in 1898¹⁵²). At the time, this radiation; considered as hindering since it was weakening the energy of the accelerated particles; was not at the heart of high-energy physicists' work. Fortunately enough, scientists like John Paul Blewett persisted and investigated further into this radiative energy loss phenomenon. The Canadian scientist was in fact the first to quantitatively measure SR in 1946¹⁵³ but, unfortunately, the vacuum chamber of the 100-MeV betatron used at that time was opaque, preventing any concrete observation. This latter came a year after with the direct observation by Elder *et al.*¹⁴⁸ of a visible light radiation: the Synchrotron Radiation.

This discovery gave credit to Liénard, Iwanenko, Pomeranchuk and Blewett's work and paved the way for the development of new particle accelerators: the Synchrotron lightsource facilities.

ii. Synchrotron facility

The Synchrotron electrons, once generated in the electron gun and extracted from it, need to be accelerated. The first accelerating step takes place in the linear accelerator (LINAC), a 16-metre-long tunnel (for SOLEIL) where small magnetic fields are successively generated. At the end of the LINAC, electron energy is of 100 MeV (for SOLEIL). The second accelerating step occurs in the Booster, a racetrack-like tunnel that brings the electrons to their operating energy using Radio Frequency cavities. In the case of SOLEIL facility, this

¹⁴⁸ F.R. Elder *et al.*, (1947) *Phys. Rev.*, 71, 11, 829-30

¹⁴⁹ NASA, ESA, J. Hester, A. Loll (ASU) [NASA image gallery](#)

¹⁵⁰ image adapted from J. P. Blewett, (1998) *J. Synchrotron Rad.* (1998), 5, 135-139

¹⁵¹ D. Iwanenko and I. Pomeranchuk, (1944) *Phys. Rev.* 65, 343

¹⁵² A. Liénard, (1898) *L'éclairage électrique*, 16-21

¹⁵³ John P. Blewett, (1946) *Phys. Rev.*, 69, 87

operating value is of 2.75 GeV. Once this energy is reached, the electrons are injected in the storage ring where they will travel at 99.999998% of the speed of light for several hours.

The storage “ring” is in fact made of a series of alternating straight and curved sections. In the straight sections, electrons evolve in a linear trajectory and go through focusing magnets to maintain the most ideal path. In the curved sections, electrons encounter bending magnets that divert their path and cause energy release in the form of light: the synchrotron radiation. To get a brilliant beam, insertion devices are used. These undulators consist of an array of small magnets in which the different emitted radiations overlap, resulting in a more focused and intense beam.

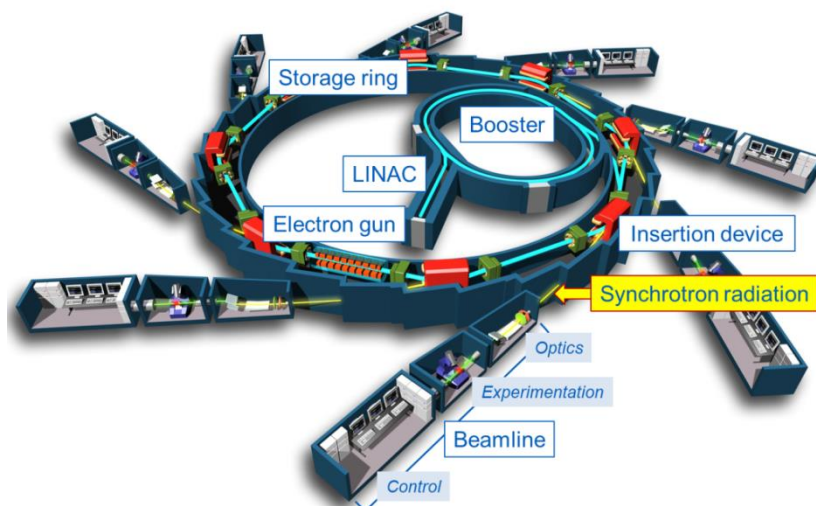


Figure 66. Structure of a Synchrotron facility¹⁵⁴.

Emitted light then travel to the beamline where it will be used. The beamlines are distributed all around the storage ring. In the case of SOLEIL, there are 29 operating beamlines out of the 43 spots available. Each of these laboratories is composed of the same three hatches: optics, experimentation and control (see Figure 66). In the optics hatch, the raw synchrotron beam is tuned using different sets of mirrors, slits and a monochromator to fit the beamline needs. At SOLEIL, most of the beamlines cover X-ray (hard and soft) and UV ranges, yet few beamlines also operate in the visible and IR ranges (Table 5). The experimentation hatch is where the specific beamline technique is implemented. Finally, the control hatch is where scientists (from the beamline or occasional users) operate their measurements and process the data.

	IR	Vacuum UV / UV / Visible	Soft X-rays < 1,5 keV	Hard X-rays > 8 keV
	AILES, SMIS	ANTARES, CASSIOPÉE, DESIRS, DISCO, METROLOGIE, PLÉIADES	ANTARES, CASSIOPÉE, DEIMOS, HERMES, METROLOGIE, SEXTANTS, PLÉIADES, TEMPO	ANATOMIX, CRISTAL, DIFFABS, GALAXIES, MARS, METROLOGIE, NANOSCOPIUM, ODE, PROXIMA-1, PROXIMA-2A, PSICHÉ, PUMA, ROCK, SAMBA, SIRIUS, SIXS, SWING
			1 to 10 keV	
			ANATOMIX, DEIMOS, DIFFABS, GALAXIES, HERMES, LUCIA, MÉTROLOGIE, ODE, ROCK, SAMBA, SIRIUS, SIXS	

Table 5. SOLEIL beamlines by energy range¹⁵⁵

¹⁵⁴ adapted from SOLEIL education resources

¹⁵⁵ SOLEIL beamlines

Among the different techniques available at SOLEIL synchrotron, we found Scanning Transmission X-ray Microscopy (STXM) to be highly suitable to study perovskite materials. Indeed, its soft X-ray regime covers edges for C, N, Pb and I elements, its high resolution (30 nm) enables the study of a material with nanoscale inhomogeneities and its feature of chemical mapping can provide insight on the composition of both grain and corresponding boundaries.

At SOLEIL, STXM technique is available on the High Efficiency and Resolution beamline for X-ray Microscopy and Electron Spectroscopy (HERMES). Implemented in 2015¹⁵⁶, this beamline currently operates in the soft X-ray regime from 70 eV to 1.5 keV (to be extended soon to 2.5 keV) covering, among others, M-edges of rare earth elements (157 eV for Y M_{4,5}), K-edges of light elements such as C, N, and O (respectively at 284, 401 and 532 eV) and L-edges of transition metals (872 eV for Ni L₂)¹⁵⁷. HERMES beamline is equipped with two endstations: X-ray PhotoEmitted Electron Microscopy and Scanning Transmission X-ray Microscopy.

IV. Scanning Transmission X-ray Microscopy¹⁵⁸

Scanning Transmission X-ray Microscopy is a XAS technique in transmission mode: the absorption coefficient is directly monitored by measuring the intensity of the transmitted light with respect to the intensity of the incident beam. The basic working principle of this photon-in/photon-out technique is the following: a tunable X-ray beam is shine onto a sample that is scanned and the transmitted light is recorded by a detector.

i. History and development^{159 160}

Although the first idea for a scanning X-ray microscope can be found as early as 1953 with the work of Howard Pattee¹⁶¹, the first instrument was only implemented twenty years later by Horowitz and Howell¹⁶² at the Cambridge Electron Accelerator. They performed the first transmission and fluorescence measurements on aluminium and silicon samples, in ambient conditions. The beam was at that time collimated to a micron size using a simple pinhole.

In the 70s, Niemann *et al.* developed the first Zone Plate based microscopes, first using a laboratory source¹⁶³ and then using Synchrotron Radiation¹⁶⁴. At the Deutsches Elektronen-Synchrotron they succeeded in resolving a 0.5 μm distance showing the promising potential of Synchrotron Radiation for zone plate based STXM. Ten years later, a 75-nm resolution was reported by Rarback *et al.*¹⁶⁵.

¹⁵⁶ R. Belkhou *et al.*, (2015) *J. Synchrotron Rad.*, 22, 968-979

¹⁵⁷ [HERMES beamline - SOLEIL](#)

¹⁵⁸ A. P. Hitchcock *et al.*, (2002), *J. Biomater Sci. Polymer Edn*, 13, 8, 919-37

¹⁵⁹ J. Kirz and C. Jacobsen, (2009) *J. of Physics: Conference series*, 186, 012001

¹⁶⁰ G. Schmid, M. Obst, J. Wu and A. Hitchcock '3D chemical imaging of nanoscale biological, environmental and synthetic materials by Soft X-ray STXM spectrotomography' in *X-ray and Neutron Techniques for Nanomaterials Characterization*, C. S. S. R. Kumar (2016)

¹⁶¹ H. H. Pattee, (1953) *J. of the Opt. Soc. of America*, 43, 1, 61-2

¹⁶² P. Horowitz and J A Howell, (1972) *Science*, 178, 4061, 608-11

¹⁶³ B. Niemann *et al.*, (1974) *Optics Comm.*, 12, 2, 160-3

¹⁶⁴ B. Niemann *et al.*, (1976) *Appl. Optics*, 15, 8, 1883-4

¹⁶⁵ H. Rarback *et al.*, (1988) *Rev. of Sc. Inst.*, 59, 1, 52

For over 20 years most of the progress on STXM technique were achieved at NSLS (National Synchrotron Light Source) by Rarback^{166,167,168}, Kirz^{169,170,171} and Jacobsen^{172,173}. The development in 2003 at ALS (Advanced Light Source) of an interferometer integrated STXM instrument¹⁷⁴; that would later on be commercialized by Bruker¹⁷⁵; was a game changer. By 2015, there were in fact 20 operating STXM implemented all around the world, HERMES being among the most recent (Table 6).

Facility	Name	City	Country	E-range (eV)	1st image	Status
ALS	7.0.1	Berkeley	USA	100–1200	1995	Ended 2001
ALS	5.3.2.2	Berkeley	USA	250–750	2001	Operating
ALS	11.0.2	Berkeley	USA	100–2000	2002	Operating
ALS	5.3.2.1	Berkeley	USA	250–2500	2011	Operating
Australian SR		Melbourne	Australia	100–2000	2014	Commissioning
Bessy -II	old-STXM	Berlin	Germany	250–600	2004	Ended 2011
Bessy-II	MAXYMUS	Berlin	Germany	250–1500	2008	Operating
CLS	10ID1	Saskatoon	Canada	130–2500	2006	Operating
CLS	10ID1	Saskatoon	Canada	130–2500	2015	Commissioning
Diamond	I08	Harwell	UK	250–2500	2015	Construction
Elettra	Twin-mic	Trieste	Italy	250–2000	2002	Operating
UVSOR	BL4U	Okazaki	Japan	50–800	2013	Operating
NSLS	X1A	Upton	USA	250–1000	1989	Ended 2000
NSLS	X1A	Upton	USA	250–1000	1998	Ended 2011
NSLS	X1A	Upton	USA	250–1000	2004	Ended 2011
NSRRC	BL09A1	Hinschu	Taiwan	60–1500	2017	Construction
PLS	nanoscopy	Pohang	Korea	100–2000	2014	Construction
PF	Various BL	Tsukuba	Japan	100–8000	2013	Operating
SLS	PolLux	Villigen	Switzerland	250–750	2006	Operating
SLS	NanoXAS	Villigen	Switzerland	270–1800	2009	Operating
Soleil	Hermes	Saint-Aubin	France	250–1500	2015	Construction
SSRF	SXS	Shanghai	China	200–2000	2011	Operating
SSRL	13-1	Stanford	USA	250–1000	2010	Operating

Table 6. STXM at synchrotron light sources (data from 2015)¹⁷⁶.

Over the last two decades, STXM has drowned increasing interest from the community: from less than ten per year until the 90s, there were no less than 110 papers published last year on the subject, over two times more than the other common soft X-ray microscopes combined (Figure 67).

¹⁶⁶ H. Rarback, J. Kenney, J. Kirz and X. Xie 'Scanning Soft X-ray Microscopy: First Tests with Synchrotron Radiation' in *Scanned Image Microscopy*, E. Ash (1980)

¹⁶⁷ H. Rarback *et al.*, (1986) Nucl. Inst. and Methods in Phys. Res., 246, 159-62

¹⁶⁸ H. Rarback *et al.*, (1990) Nucl. Inst. and Methods in Phys. Res., 291, 54-9

¹⁶⁹ J. Kirz, (1988) Nucl. Inst. and Methods in Phys. Res., 266, 293-5

¹⁷⁰ J. Kirz *et al.*, (1990) Physica Scripta, 31, 12-7

¹⁷¹ J. Kirz *et al.*, (1992) Rev. of Sc. Inst., 63, 1, 557

¹⁷² C. Jacobsen *et al.*, (1986) Photochem. and Photobio., 44, 3, 421-3

¹⁷³ C. Jacobsen *et al.*, (2000) J. of Microscopy, 197, 173-84

¹⁷⁴ A. L. D. Kilcoyne *et al.*, (2003) J. Synchrotron Rad., 10, 125-36

¹⁷⁵ Bruker ASC STXM

¹⁷⁶ A. P. Hitchcock, (2015) J. of Elec. Spectro. and Related Phenom., 200, 49-63

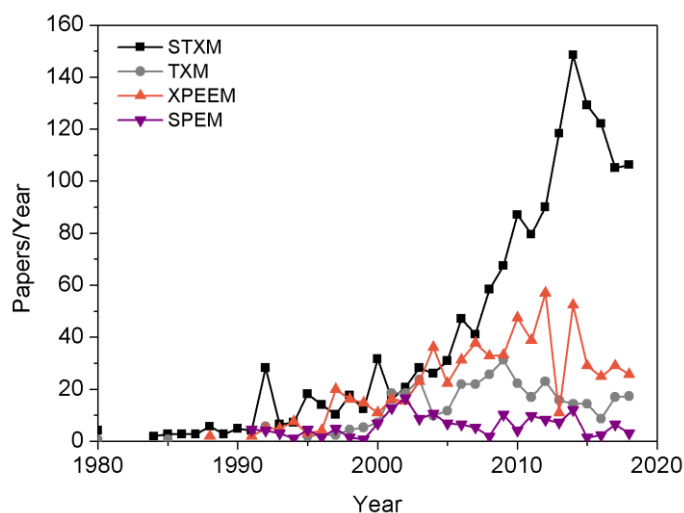


Figure 67. Overview of the number of papers per year between 1980 and 2018 for the four common types of soft X-ray microscopes (Scanning Transmission X-ray Microscopy, full field Transmission X-ray Microscopy, X-ray PhotoEmission Electron Microscopy and Scanning PhotoElectron Microscopy)¹⁷⁷.

This dominance of STXM over the other types of soft X-ray microscopes can be explained by its combined features of high spatial resolution and chemical sensitivity. Spatial resolutions below 50 nm are now routinely achieved in STXM^{178,179}. Additional detection techniques implemented simultaneously along with photon detection and flexibility in sample environments are few of the aspects that has helped STXM dominate over other types of microscopies. As shown Figure 68, STXM spectrum displays much more fine structures compared to a more classical EELS (Electron Energy Loss Spectroscopy) spectrum.

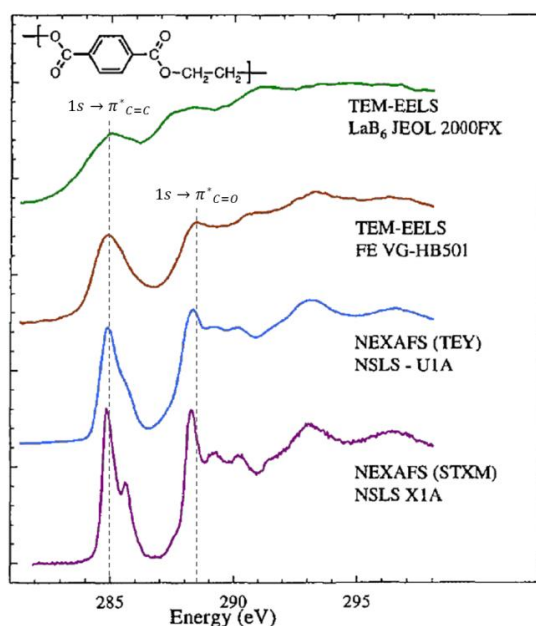


Figure 68. C 1s spectra of PET (polyethylene terephthalate) from Electron Energy Loss Spectroscopy (EELS) with two different sources (LaB₆ filament or a Field Emission Gun) and from XAS spectroscopy in Total Electron Yield (TEY) or Transmission (STXM) mode¹⁸⁰.

¹⁷⁷ adapted from A. P. Hitchcock's Bibliography of Soft X-ray Microscopy

¹⁷⁸ T. H. Yoon et al., (2004) Langmuir, 20, 24, 10361–6

¹⁷⁹ H. Bluhm et al., (2006) J. of Elec. Spectro. and Related Phenom., 150, 86-104

¹⁸⁰ adapted from H. Ade and S. Urquhart, 'NEXAFS spectroscopy and microscopy of natural and synthetic polymers' in Chemical Applications of Synchrotron Radiation, T.-K. Sham (2002)

As a spectromicroscopy technique STXM can allow a direct correlation between the sample morphology and its chemical composition, making it very powerful and suitable for complex analysis.

ii. STXM instrumentation

The general outline of a Scanning Transmission X-ray Microscope and a picture of the HERMES set up are shown Figure 69. The incident beam, focused using a set of optics, is shine onto the sample and the transmitted beam is recorded by a detector.

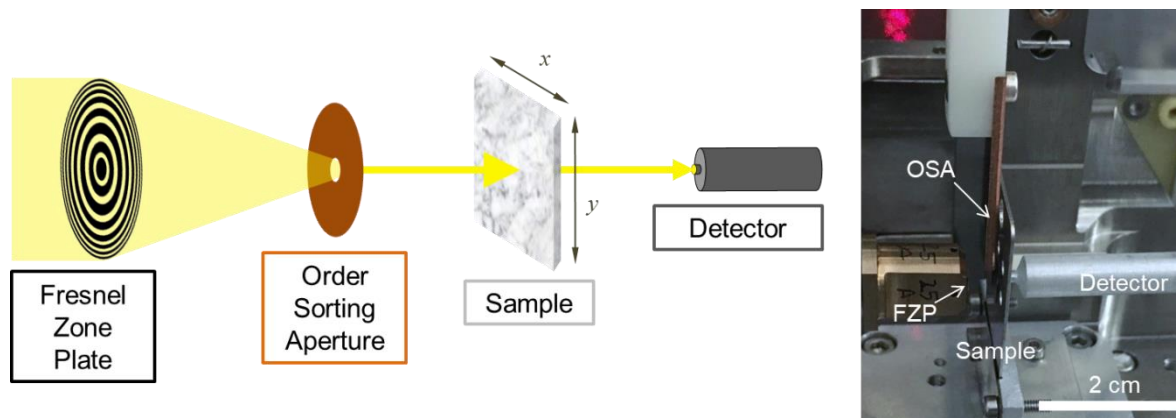


Figure 69. Scanning Transmission X-ray Microscope: schematic outline and picture of the HERMES set up.

In an STXM, the beam is focused using a diffractive device called a Fresnel Zone Plate (FZP) which consists of an array of concentric Gold rings deposited on a transparent Silicon Nitride membrane¹⁸¹ (Figure 70). The transparent zones are spaced such as the diffracted beams constructively interfere at the same focal point. The resolution of the STXM is defined by the spot size at this particular point. Optimizing the optical resolution of the microscope then implies a fine design of the zone plate. Typical resolutions are about 25 nm but spot sizes as low as 7 nm have also been reported¹⁸².

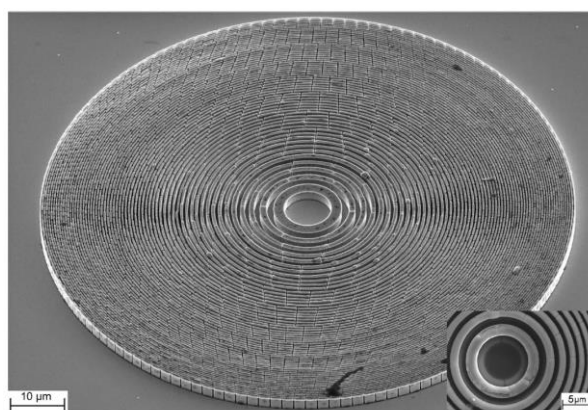


Figure 70. SEM image of a Fresnel zone plate¹⁸³.

To operate as a focusing lens, a FZP has to be used in the first order. To filter higher-order diffracted beams (and prevent dispersive radiations) an exit aperture called the Order Sorting Aperture (OSA) is conveniently placed between the FZP and the first order focal point where

¹⁸¹ x-ray-optics.de

¹⁸² B. Rösner *et al.*, (2018) *Microsc. Microanal.*, 24 (S2) 272-3

¹⁸³ I. Mohacsi *et al.*, (2016) *Optics Letters*, 41, 2, 281-4

the sample is placed. To protect the sample from unfocused incident beams, a central opaque stop is integrated into the FZP design.

STXM technique is not very sample-compelling. Studied samples can consist of coated silicon nitride membranes, cross-sections lamella or even wet cells¹⁸⁴. Only requirements are sufficient X-ray absorption (30% transmission) and vacuum compatibility. Operating in the soft X-ray region makes STXM a very suitable technique for the study of soft materials such as polymers and biological specimens when compared to electron microscopes. Indeed, in 1997 Rightor *et al.* studied Poly(Ethylene Terephthalate) by EELS and STXM and they reported a beam damage two times less important for the latter one¹⁸⁵. The study of polymers using STXM is extensively investigated by Adam P. Hitchcock and his team at ALS (USA) and CLS (Canada) light sources^{186,187}.

Transmitted X-ray detectors in STXM can be of various types: fluorescence¹⁸⁸, Charge-Coupled-Device¹⁸⁹ or photomultiplier¹⁹⁰. On HERMES STXM, transmitted photons are detected using a photomultiplier tube.

While the OSA and detector are fixed during measurements, the FZP moves in z upon spectral scanning and the sample moves in (x; y) upon spatial scanning. As to have a spatial coherence between the images and keep the resolution constant, the sample and zone plate positions (respectively (x; y) and z) during measurements are monitored by an interferometer.

iii. STXM measurements

One of the strong features of STXM is that it combines imaging with spectral analysis. As a comparison, XPS (X-ray Photoelectron Spectroscopy) only provides spectral analysis and SEM (Scanning Electron Microscopy) only imaging. This dual character makes STXM a very powerful technique to study chemically complex materials with nanoscale inhomogeneities.

a. Data acquisition

STXM data consist of scans and depending on the type of information sought, the scan type varies: spatial only, spectral only or spatial and spectral. For spatial imaging only purpose, scans are single images where the beam energy is constant. For spectral analysis (beam energy varies), scans can have different spatial dimensionalities from 0 to 2 (Table 7.).

¹⁸⁴ J. R. Lawrence *et al.*, (2003) *Appl Environ Microbiol.*, 69, 9, 5543–54

¹⁸⁵ E. G. Rightor *et al.*, (1997) *J. Phys. Chem. B*, 101, 1950-60

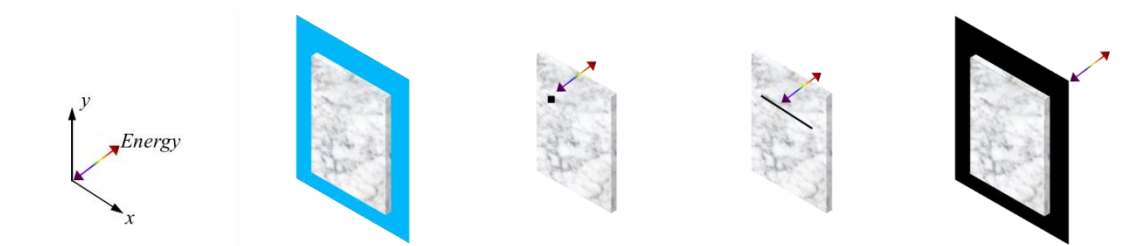
¹⁸⁶ Hitchcock group publications 'Polymers and polymer model studies'

¹⁸⁷ A. P. Hitchcock 'Bibliography of Soft X-ray Microscopy' S.I. from H. Ade and A. P. Hitchcock, (2008) *Polymer*, 49, 643-75

¹⁸⁸ R. Barrett *et al.*, (2000) *AIP Conf. Proc.*, 507, 458

¹⁸⁹ A. Gianoncelli *et al.*, (2006) *Appl. Phys. Lett.*, 89, 251117

¹⁹⁰ C. Jacobsen *et al.*, (1993) *J. of Microscopy*, 172, 2, 121-9



Spectral dimension	0	1	1	1
Spatial dimension	2	0	1	2
Scan name	Image	Point	Line	Stack
Spatial analysis	✓	✗	✗	✓
Spectral analysis	✗	✓	✓	✓

Table 7. STXM scan types.

Each sample scan type has its own usefulness. Image scans are roughly performed during the initial steps to locate the sample and then the area of interest but they can also be carried out for high resolution imaging. Stack scans are the most exhaustive of the scan types as they combine imaging along with spectral analysis (3D data). Depending on the range and resolution (both spatial and spectral), acquisition of stack scans can take from a few minutes to 2 to 3 hours or even 5 hours and generate 2 Mo files.

Whatever the scan type, each of these is very rich of information and must be processed to extract meaningful results.

b. Data processing

In order to be quantitative, raw acquired data need to be first converted from transmitted intensity into absorbance, also widely referred to as 'Optical Density' (OD). From the raw data, OD is calculated as follow:

$$OD = \log \frac{I_0}{I_t} \quad [10]$$

where I_0 and I_t are respectively the incident and transmitted recorded beam intensities.

From Beer-Lambert law, OD is then correlated to the absorption coefficient $\mu(E)$ by

$$OD = \mu(E)\rho t \quad [11]$$

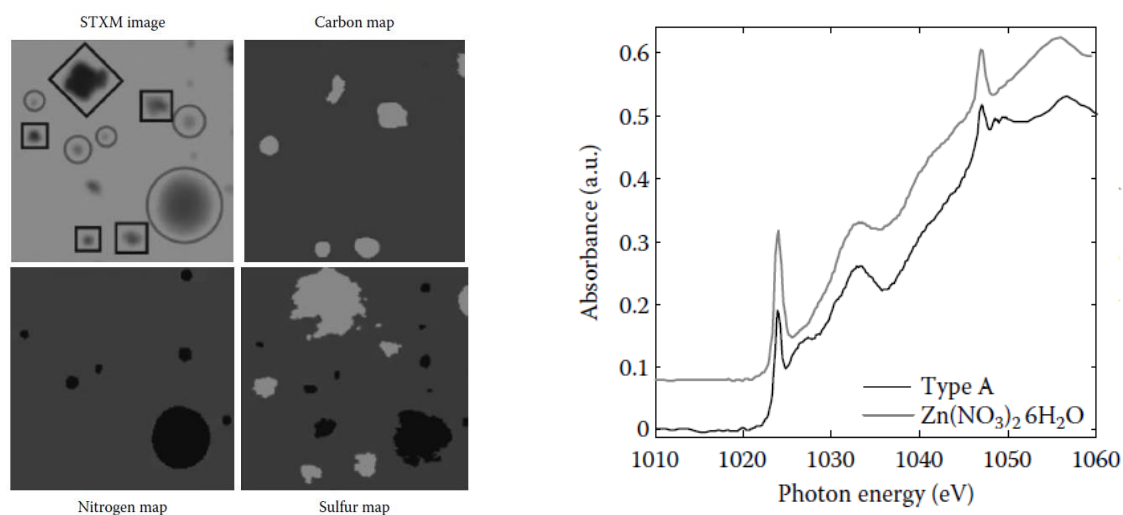
where ρ and t are the material density and the sample thickness respectively.

This first step of OD conversion is performed whatever the type of scans.

For stack scans, an extra pre-processing step is needed. Repeated (x ; y) motions can cause heating of the sample holder piezo motors, this energy is mechanically released and induces a shift between the images of the sequence. Although this drift is mitigated by the interferometer monitoring, it is still there and can increase with the image size, resolution and spectral range. In order to correct this offset between the sequence images, they have to be aligned before any further analysis.

OD and alignment steps can be carried out using specific tools in STXM data analysis software such as aXis2000¹⁹¹ or MANTiS¹⁹². Following these pre-processing steps, the data are ready to be analysed.

There are a large variety of ways to analyse STXM data depending on the intended results (chemical mapping, spectral analysis, ...). The three most widely used approaches are: a) ratio between at- and pre-edge images; b) linear decomposition combined with reference spectra and c) cluster analysis. A more detailed description can be found in Schmid *et al.*¹⁹³. Results from these processing can be chemical mapping and/or XAS spectra (Figure 71).



a) **Figure 71.** a) single-energy (290.8 eV) STXM image ($12 \times 12 \mu\text{m}^2$) of externally mixed sea salt/ $\text{CH}_3\text{SO}_3^-/\text{SO}_4^{2-}$ (squares) and $\text{H}_2\text{SO}_4/(\text{NH}_4)_2\text{SO}_4$ (circles) particle residuals and principal component maps at the C K-edge, N K-edge and S L-edge and b) Zn L-edge NEXAFS spectra for ambient particle of type A and $\text{Zn}(\text{NO}_3)_2 \cdot 6\text{H}_2\text{O}$ standard.¹⁹⁴

While a substantial number of STXM studies have been carried out on organic films^{195,196,197,198,199,200,201,202,203} to our knowledge very few have been led on hybrid perovskite ones.

¹⁹¹ [aXis2000 \(Analysis of X-ray Images and Spectra\)](#) is a software developed by Adam Hitchcock at Mc Master University (Canada)

¹⁹² [MANTiS \(Multivariate ANalysis Tool for Spectromicroscopy\)](#)

¹⁹³ [G. Schmid, M. Obst, J. Wu and A. Hitchcock, '3D Chemical Imaging of Nanoscale Biological, Environmental, and Synthetic Materials by Soft X-Ray STXM Spectrotomography' In *X-ray and Neutron Techniques for Nanomaterials Characterization*, C. Kumar \(2016\)](#)

¹⁹⁴ [R. C. Moffet, A. T. Tivanski and M. K. Gilles, 'Scanning Transmission X-ray Microscopy: Applications in Atmospheric Aerosol Research' in *Fundamentals and Applications in Aerosol Spectroscopy*, R. Signorell and J. P. Reid \(2010\)](#)

¹⁹⁵ [C. R. Mc Neill *et al.*, \(2006\) Nano Lett., 6, 6, 1202-6](#)

¹⁹⁶ [C. R. Mc Neill *et al.*, \(2008\) Nanotechnology, 19, 424015](#)

¹⁹⁷ [C. Hub *et al.*, \(2010\) J. Mater. Chem., 20, 4884-4887](#)

¹⁹⁸ [S. Swaraj *et al.*, \(2010\) Nano Lett., 10, 8, 2863-9](#)

¹⁹⁹ [W. Zhang *et al.*, \(2011\) Polym. Adv. Technol., 22, 65-71](#)

²⁰⁰ [S. Pack *et al.*, \(2012\) Polymer 53, 4787-99](#)

²⁰¹ [B. A. Collins and H. Ade, \(2012\) J. of Elec. Spectro. and Related Phenom., 185, 5-7, 119-28](#)

²⁰² [J. Dhar *et al.*, \(2015\) J. Phys. Chem. B, 119 \(34\), 11307-16](#)

²⁰³ [Q. Arnoux *et al.*, \(2017\) Nano Research, 5, 2771-82](#)

V. Synchrotron-based studies of perovskite films

The literature survey we conducted on the topic of (Lead trihalide) perovskite films and synchrotron-based techniques led to about a dozen of articles with only two STXM studies (highlighted in bold in Table 8) and neither of those on dry-processed perovskites.

(Lead trihalide) Perovskite	Deposition method	Synchrotron <i>Beamline</i>	Technique	Ref.
CH ₃ NH ₃ PbI ₃	Wet 1-step spincoating	SSRF <i>BL14B1</i>	GIXRD	[204]
CH ₃ NH ₃ PbI ₃	Wet 1-step spincoating	SSRF <i>BL14B</i>	XRD	[205]
CH ₃ NH ₃ PbI ₃ (Cl)	Wet 1-step spincoating	SSRF <i>BL14W1</i>	XRF	[206]
CH ₃ NH ₃ PbI ₃	Wet 2-step spincoating/dipping	SLAC SSRL <i>NA</i>	XRD	[207]
CH ₃ NH ₃ PbI ₃	Wet 1-step spincoating	SSRF <i>BL14B</i>	XRD	[208]
CH ₃ NH ₃ PbI ₃	Wet 1-step spincoating	PAL <i>PLS-II 9 A U-SAXS</i> <i>4D PES</i>	2D-GIWAXD HR-XPS	[209]
Cs _{0.05} MA _{0.16} FA _{0.79} Pb(I _{0.83} Br _{0.17}) ₃	Wet 1-step spincoating	SLAC SSRL <i>BL11-3</i>	GIXRD	[210]
CH ₃ NH ₃ PbI ₃ (Cl)	Wet 1-step spincoating	SLAC SSRL <i>BL11-3</i> <i>BL4-1</i>	GIXRD XRF	[211]
CH ₃ NH ₃ PbI ₃	Wet Spray	SLAC SSRL <i>BL11-3</i>	WAXS	[212]
CH ₃ NH ₃ PbI ₃ (FAD) _{1.0} (MABr) _{0.2} (PbI ₂) _{1.1} (PbBr ₂) _{0.20} Cs _{0.5} (MA _{0.17} FA _{0.83}) _{0.95} Pb(I _{0.83} Br _{0.17}) ₃	Wet 1-step spincoating	ESRF <i>XMaS</i>	GI-WAXS	[213]
CH ₃ NH ₃ PbI ₃	Wet 1-step spincoating	NSRL <i>BL11U</i>	SRPES XPS	[214]
CH ₃ NH ₃ PbI ₃	Wet 2-step spincoating/dipping	UVSOR <i>BL4U</i>	STXM	[215]
CH ₃ NH ₃ PbI ₃ C ₆ H ₅ (CH ₂) ₂ NH ₃ I/PbI ₂	Wet Vapor Assisted 2-step spincoating/vapor	UVSOR <i>BL4U</i>	STXM	[216]

Table 8. Overview of Synchrotron-based study of perovskite films (GI-XRD: Grazing Incidence X-ray Diffraction; GI-WAXD: Grazing-Incidence Wide-Angle X-ray Diffraction; XPS: X-ray Photoelectron Spectroscopy; XRF: X-ray Fluorescence; WAXS: Wide Angle X-ray Scattering; GI-WAXS: Grazing Incidence Wide Angle X-ray Scattering; SRPES: Synchrotron Radiation PhotoEmission Spectroscopy).

²⁰⁴ H. Li *et al.*, (2016) *Nanomater. Nanotechnol.*, 2016, 6, 24

²⁰⁵ J. Zhao *et al.*, (2016) *Sc. Rep.*, 6, 21976

²⁰⁶ J. A. McLeod *et al.*, (2016) *Nanoscale*, 8, 6361-8

²⁰⁷ L. T. Schelhas *et al.*, (2016) *ACS Energy Letters*, 1, 5, 1007-12

²⁰⁸ G. Ji *et al.*, (2016) *Appl. Surf. Sc.*, 393, 417-21

²⁰⁹ N. K. Kim *et al.*, (2017) *Sc. Rep.*, 7, 4645

²¹⁰ N. Rolston *et al.*, (2018) *Adv. Energy Mater.*, 1802139

²¹¹ K. H. Stone *et al.*, (2018) *Nature Comm.*, 9, 3458

²¹² F. Hilt *et al.*, (2018) *Energy Environ. Sci.*, 11, 2102-13

²¹³ M. Alsari *et al.*, (2018) *Energy Environ. Sci.*, 11, 383

²¹⁴ X. Li *et al.*, (2019), *Chinese J. of Chem. Phys.*, DOI:10.1063/1674-0068/cjcp1808189

²¹⁵ M. W. Lin *et al.*, (2016) *Adv. Mater. Interfaces*, 3, 1600135

²¹⁶ M. H. Li *et al.*, (2018) *Adv. Mater.*, 30, 1801401

The first STXM study of perovskites published in 2016 by Lin *et al.*²¹⁵ studied SiN/NiO_{nc}/PbI₂ microaggregates before and after MAI treatment (PbI₂ is expected to be converted into perovskite upon exposure to MAI) using NEXAFS spectroscopy at the O and Pb-edges. They found proof that a redox reaction occurred at the NiO_{nc}/PbI₂ interface leading to the formation of a PbO compound. This compound when exposed to MAI will turn into a MAPbI_{3-2δ}O_δ that proved to be beneficial for the hole collection at the interface with NiO.

In 2018, Li *et al.*²¹⁶ studied low-vapor assisted solution process perovskite coated on a TiO₂ mesoporous layer. They used NEXAFS at the C K-edge to investigate the dynamic of the partial integration of PEA⁺ (PhenylEthylAmmonium) into the PbI₂ network (PEAI/PbI₂ ratio of 0.05). In the absence of MAI vapor, the PEA⁺ intercalates itself into the PbI₂ network to form a material close to the 2D perovskite with PEAI/PbI₂ = 2. In the presence of MAI vapor, the PEA⁺ intercalates into the pre-formed perovskite network to form a material closer to the 3D MAPbI₃ perovskite.

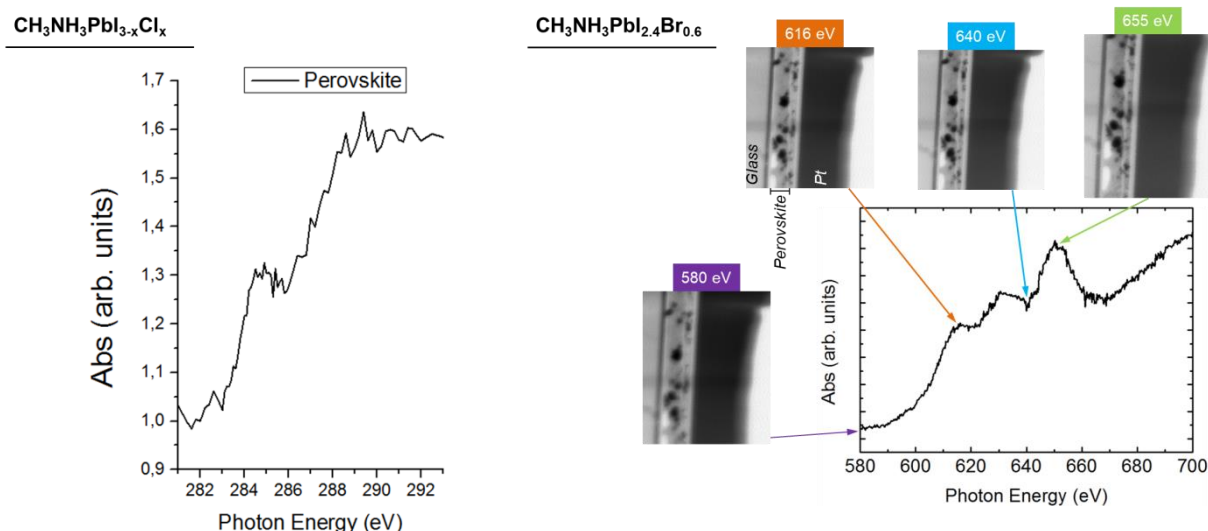
Besides these two papers, we found no other report of STXM study on perovskite materials. To this point, it is important to take a step aside to develop the history of our perovskite team with STXM.

VI. LPICM perovskite team STXM studies

When our team submitted its first proposal in 2016 to study cross-sections of full perovskite PV devices, we had no clear idea what to expect from these measurements, being the first to run such study (if it was done by the past, we found no report of it in our literature survey). Following the acceptance of our proposal by SOLEIL's peer reviewing committee, we conducted our first beamtime in December 2016. Besides, being our first time in a Synchrotron, it was also a premiere for the HERMES team to work on perovskite materials. As such, the first beamtime was very exploratory. On our side we were learning about the technique, with the goal of being the most independent possible, and on the HERMES team side, they were apprehending the material and its complexity (both on the chemical and structural levels).

During this first beamtime we studied cross-sections of Glass/ITO/PEDOT:PSS/Perovskite/PCBM/Ag stacks with three perovskite compositions: CH₃NH₃PbI₃, CH₃NH₃PbI_{3-x}Cl_x and CH₃NH₃PbI_{2.4}Br_{0.6}. We went back and forth between the two spectral regions of [280; 310] and [620; 700] eV thought to be of interest due to the C K-edge at 284 eV, I M_{4,5}-edge at 620 eV and Pb N_{2,3}-edge at 644 eV²¹⁷. Figure 72 shows few results from this beamtime: a spectrum where the characteristic C K-edge can be seen for the Cl-perovskite (a) and a Pb and I spectrum along with nicely resolved images showing grains in the Br-perovskite layer (b).

²¹⁷ From <http://www.eels.info/atlas/lead>



a) **Figure 72.** Example of results from our first STXM beamtime: a) perovskite spectrum at the C K-edge for the $\text{CH}_3\text{NH}_3\text{PbI}_{3-x}\text{Cl}_x$ composition and b) perovskite spectrum at the Pb and I edges with few images for energies of interest (before (580 and 640 eV) and at-edges (616 and 655 eV)) for the $\text{CH}_3\text{NH}_3\text{PbI}_{2.4}\text{Br}_{0.6}$ composition.

The three peaks in the [580; 700] eV spectrum (Figure 72b) are surprising as we would have expected a single peak from Iodine at 620 eV and a discrete Pb-related component due to its $\text{N}_{2,3}$ -edge at 644 eV. Assuming the peak at 616 eV on Figure 72b corresponds to I $\text{M}_{4,5}$ -edge (implying a -4 eV shift with the expected energy of 620 eV that can be explained by the line configuration) we were unable to explain the two extra peaks at 630 and 655 eV (that would correspond to 634 and 659 eV corrected from the eV shift). The Pb $\text{N}_{2,3}$ -edge we were expecting to see would have turned out at 640 eV given the shift, yet there is no absorption feature at that energy in the spectrum. Some weeks after our beamtime, we performed extra experiments on KI, PbCl_2 and PbI_2 films (deposited full plate on SiN membranes) trying to decipher this triple-peak feature.

Comparing pure Iodine/no Lead (KI), pure Lead/no Iodine (PbCl_2) and mix Iodine/Lead (PbI_2) reference materials we were hoping to attribute the extra peaks from the first beamtime results. OD spectra for each of the three compounds are shown here after in Figure 73 in the [620; 700] eV range.

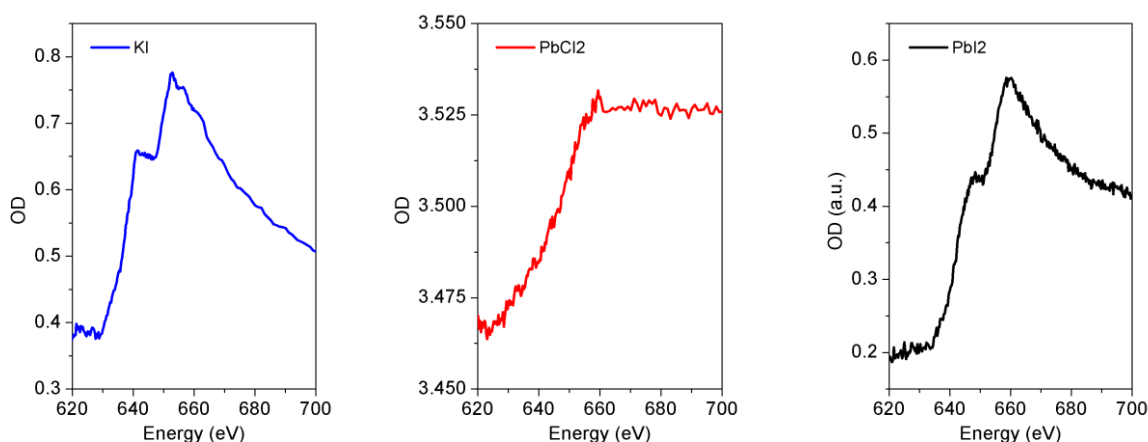


Figure 73. OD spectra for KI (blue), PbCl_2 (red) and PbI_2 (black) reference materials in the [620; 700] eV energy range.

When comparing PbI_2 (Pb and I containing compound, black plot) to KI and PbCl_2 (respectively I- and Pb-only compounds, blue and red plots), one can see that PbI_2 and KI spectra perfectly match in shape (Figure 73). While PbCl_2 spectrum is relatively flat in the studied range (amplitude of 0.006 in OD), KI and PbI_2 both show the same double-peaked sharp absorption feature. While we are to this day unable to explain the double-peak absorption seen in KI and PbI_2 , these results led us to assume that all features from Figure 72b were very likely only I-related and not Pb-related.

Besides being unable to better understand some of our data (for example Figure 72b spectrum), we were not even able to properly compare the different perovskite compositions ($\text{CH}_3\text{NH}_3\text{PbI}_3$, $\text{CH}_3\text{NH}_3\text{PbI}_{3-x}\text{Cl}_x$ and $\text{CH}_3\text{NH}_3\text{PbI}_{2.4}\text{Br}_{0.6}$) due to a lack of consistency in our measurements. We had very nice high resolution images for one composition (Figure 72b images) or very nicely resolved spectra for another (Figure 72a spectrum) but not both for any of the three compositions. We also had spectra with different energy resolution, making it difficult to properly compare them. Even if we were not able to draw any clear conclusion from this first beamtime, the results we achieved were very encouraging and drove us to submit a second proposal to continue our investigations.

We were eventually granted with a second beamtime that fitted well in the timeline of the coevaporation process development; we then seized this opportunity to build a study around the comparison of wet- and dry-processed perovskite films. At that time we had tamed the STXM technique to a relative degree (at least enough to operate it quite autonomously) but we were still not expert enough to choose the most suitable acquisition parameters. Nonetheless, this time, we adjusted our measurement procedure so that it would be consistent (*i. e.* same energy range, same spatial and spectral resolution, etc...) to allow a fair comparison between our samples. We also adapted our sample structure with respect to the first beamtime. At the time, the omnipresence of Carbon in the layers surrounding the perovskite (PEDOT:PSS and PCBM) complicated the layer assignment. Thus for this second beamtime, we simplified our structure by removing the PCBM (and therefore Ag) layer(s), while maintaining the perovskite growth conditions by keeping the PEDOT:PSS lower layer. The following section details the study from sample preparation, STXM measurements and obtained results, all the way down to our interpretation of these latter with the purpose of assessing the homogeneity difference between variously processed perovskite films.

VII. Homogeneity of wet- and dry-perovskite films assessed by Synchrotron STXM

Our study aims at comparing dry-processed perovskite films with wet- ones. As we have already foreseen from basic SEM images, the two methods do not yield the same film quality, in favour of the dry method. Samples studied by STXM consisted of cross-sections of semi-PV-device stacks of structure: Glass/ITO/PEDOT:PSS/Perovskite where the methylammonium lead triiodide ($\text{CH}_3\text{NH}_3\text{PbI}_3$) perovskite was either wet- or dry-processed. The following section details the preparation steps from bulk samples to STXM-ready cross-sections.

i. Samples preparation

The Glass/ITO/PEDOT:PSS samples were prepared following the procedure described in section A of the Annexes. The wet-processed perovskite was deposited using spincoating technique from an equimolar solution of $\text{MAI}:\text{PbI}_2$ in a GBL-DMSO mix using a

toluene anti-solvent treatment. The dry-processed perovskite was deposited by coevaporation from MAI and PbI_2 powders heated at 95°C and 295°C respectively. The thickness of the obtained active layers is between 250 and 300 nm. In order to perform Scanning Transmission X-ray Microscopy, cross sections lamellas have been prepared²¹⁸ using the Focus Ion Beam (FIB) technique on these bulk samples.

Before transferring the sample within the FIB dual beam microscope chamber (Scios DualBeam) a thin layer of carbon (C) is applied by hand (using a writing pen) in order to avoid any electron and ionic beam charge effects that might appear during the preparation. At first, the area of interest is selected and a $2/2/20\ \mu\text{m}$ Platinum (Pt) protective layer is deposited to protect the chosen area from excessive ion damage. Secondly, the selected area is isolated using the energetic Gallium ion beam. Once the area is isolated, the milling process begins using high current ion beam and then as the lamella becomes thin (down to $0.8\text{-}1\ \mu\text{m}$) the ion beam current is decreased (Figure 74).

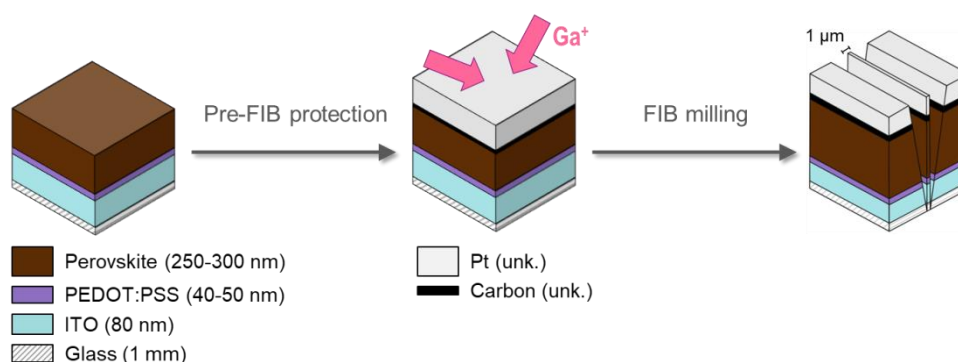


Figure 74. FIB milling initial steps: pre-beam exposition protection with Carbon and Pt, Ga^+ ion beam exposition and first rough milling step down to $1\ \mu\text{m}$ thickness (thickness of the different layers is given in bracket, Pt and Carbon thicknesses are unknown (unk.)).

The lamella is then removed from the substrate with a micro manipulator and transferred onto a TEM sample grid. A second milling process using very low ion beam current is then performed to bring the lamella thickness down to $150\text{-}200\ \text{nm}$ (Figure 75).

²¹⁸ by Dr. Ileana Florea (LPICM, Ecole Polytechnique/CNRS)

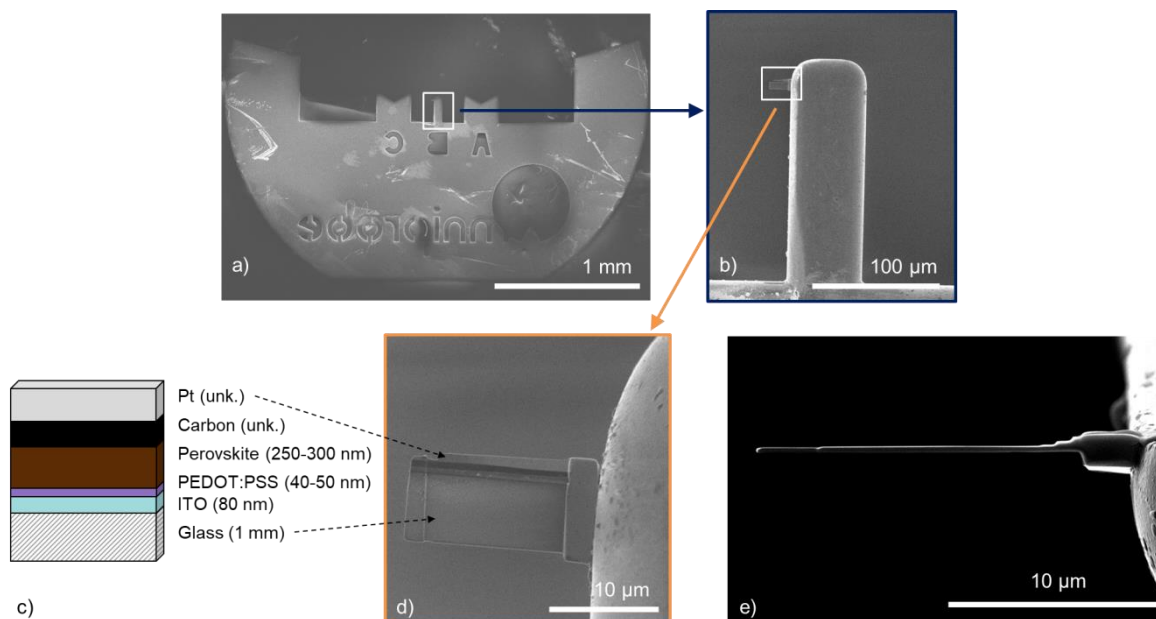


Figure 75. a) SEM image of the TEM grid, b) SEM image of the grid's finger B with the lamella, c) scheme of the lamella stack (with thicknesses), d) zoomed SEM image of the lamella and e) TEM image side view of the lamella.

The sample is removed from the FIB chamber and stored under neutral atmosphere. TEM grids with milled slices are then transferred into a N₂-filled glovebox to be mounted on the STXM sample holder before being brought to SOLEIL for STXM measurements.

ii. STXM Measurements

The present section will take the reader through the process of our STXM measurements from data acquisition down to data processing. It is important to mention that the following measurements represent only one day of Synchrotron beamtime. The STXM set up, with the FIB-prepared lamella in position, is shown once again as a reminder in Figure 76.

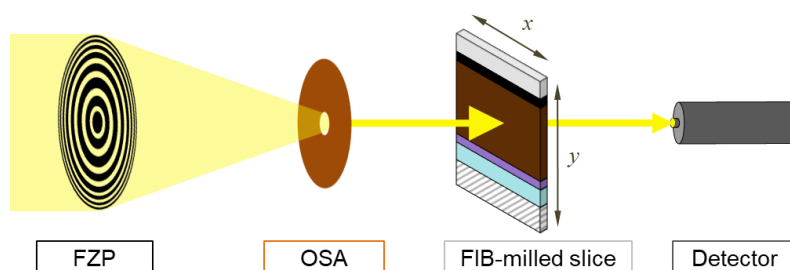


Figure 76. STXM set up with the FIB-prepared cross-section slice of perovskite semi-PV-device implemented (slice layers from bottom to top: Glass/ITO/PEDOT:PSS/Perovskite/C/Pt).

a. Data acquisition

During the first beamtime, we lacked consistency in our measurements that prevented us from properly comparing our different samples. For this second beamtime we followed a unique measurement procedure for both our samples. Given their wholeness, we chose to perform only stack scans. As aforementioned, these scans are very rich of information as they contain both imaging and spectral data, yet they are highly time-consuming. We then had to find a trade-off between the energy range and the spectral and spatial definition to fit this study in one day of measurement.

From simulations of the different elements composing the perovskite (C, H, N, Pb and I) shown Figure 77, we determined [240; 700] eV to be a suitable range. From the first beamtime feedbacks, we knew we had to broaden the investigated spectral window aiming for the Pb $N_{4,5}$ -edge at 413 eV we hoped to be more relevant than the $N_{2,3}$ one we failed to see. Yet as we went into this second beamtime we did not know really where the differences between our samples (if there would be any) would occur, we then decided to cover a large spectral range, including perovskite-composing elements absorption features from C K-edge at 284 eV up to the I $M_{4,5}$ one at 620 eV.

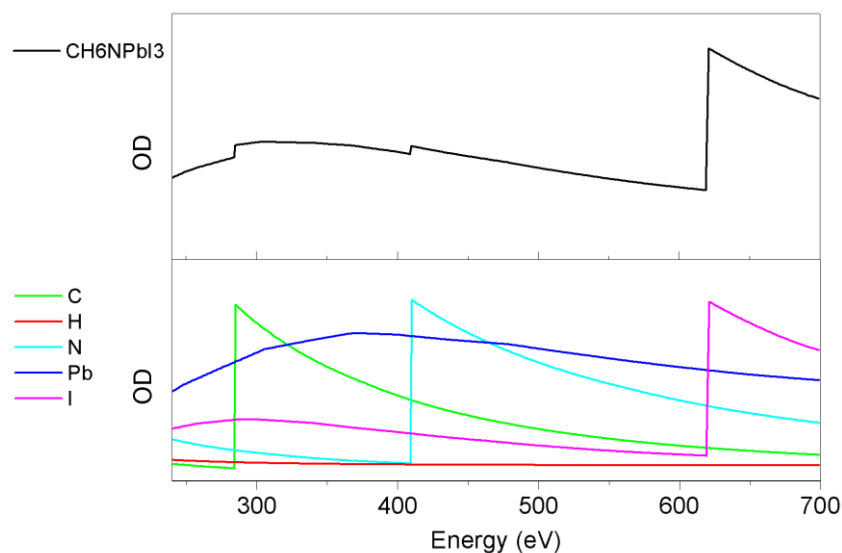


Figure 77. Simulations for a $\text{CH}_3\text{NH}_3\text{PbI}_3$ formula (black plot, top) and the different perovskite elements (C, H, N, Pb and I) (coloured plots, bottom).

As we had only one day to run this study, we had to make some adjustments on the spectral definition (both on the energy range and eV step). As such the 520 to 615 eV region was not included in the stack definition since no perovskite-related element had any edge in this range and including it would have increased the acquisition time of the stacks far too consequently. We then proceeded by running two stacks: one from 240 to 520 eV and the second from 615 to 700 eV. We also defined varying eV step depending on the spectral regions. For energy ranges where peaks were expected (for example [281; 290] eV with the C K-edge at 284 eV), we defined fine eV step to get highly defined spectra. For energy ranges where no relevant peaks were expected ([291; 390] eV) the definition was lowered (*i. e.* the eV step was increased). Eventually we followed the stack definition showed in Table 9. Acquisition times were about 4 hours for the [240; 520] eV stack and 1 hour for the [515; 700] eV stack.

Energy range (eV)	Step (eV)
[240 ; 280]	5
[281 ; 290]	1
[291 ; 390]	8.25
[395 ; 415]	1
[420 ; 520]	5
[615 ; 650]	1
[651 ; 700]	4.9

Table 9. Stack definition parameters.

We recorded images of $7 \times 1.8 \mu\text{m}^2$ ($x \times y$) dimension with a $0.030 \mu\text{m}$ step in each direction. Examples of raw images are shown in Figure 78 for the two samples.

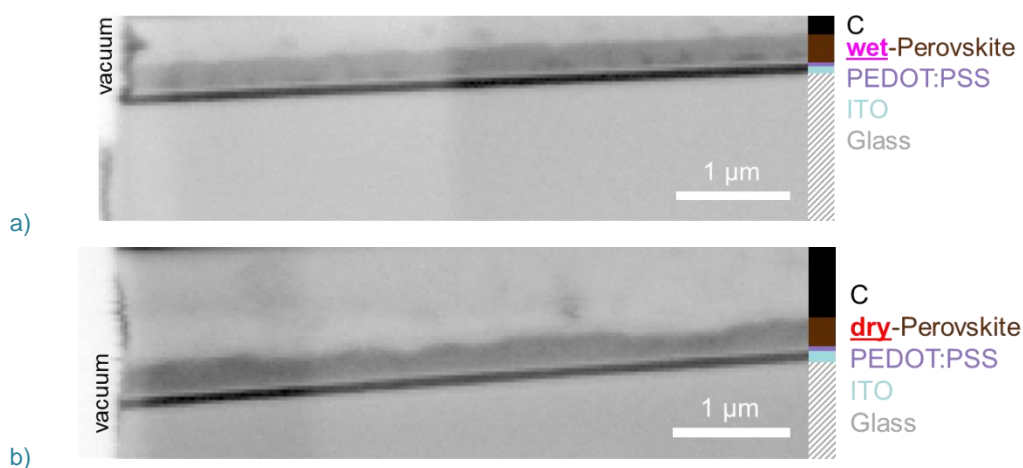


Figure 78. Examples of raw STXM images at 490 eV for the a) wet- and b) dry-processed perovskite samples (reminder: what is shown here is just one out of the 116 images of each stack scan).

From these raw images one can already notice a difference between wet- and dry-processed films, as wet perovskite lower interface with PEDOT:PSS shows small dark aggregates we don't see for the dry perovskite. Yet, before being able to draw any meaningful conclusion these raw data need to be processed. The processing procedure followed, detailed in the next section, starts with the mandatory pre-processing steps that lead to useable data; that can then be variously post-processed depending on the pursued purpose.

b. Data pre-processing

As a first step the two stacks ([240; 520] and [615; 700] eV) were appended together to get a [240; 700] eV stack (easier to process) that was then aligned (to correct the shift from drifting) and converted to Optical Density using the vacuum part of the images (see Figure 78) as I_0 . Figure 79 schematically represents these pre-processing steps. In our case, the images were also cropped to get rid of some of the glass and carbon parts to decrease the size of the file and thus facilitate later processing.

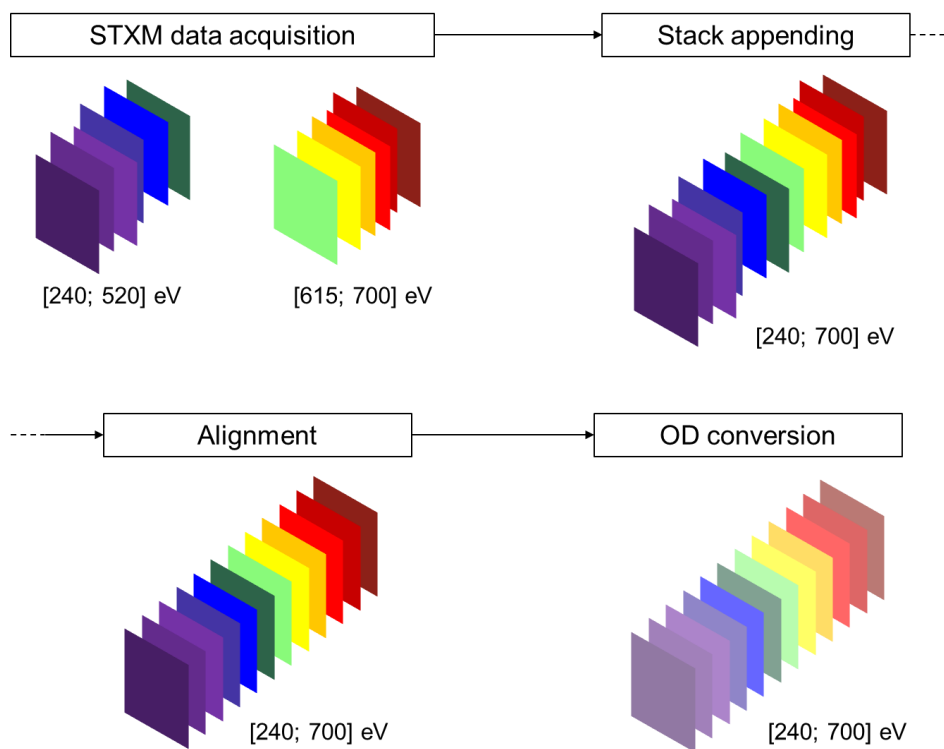


Figure 79. Pre-processing steps (*N.B. colors do not match the beam energy*).

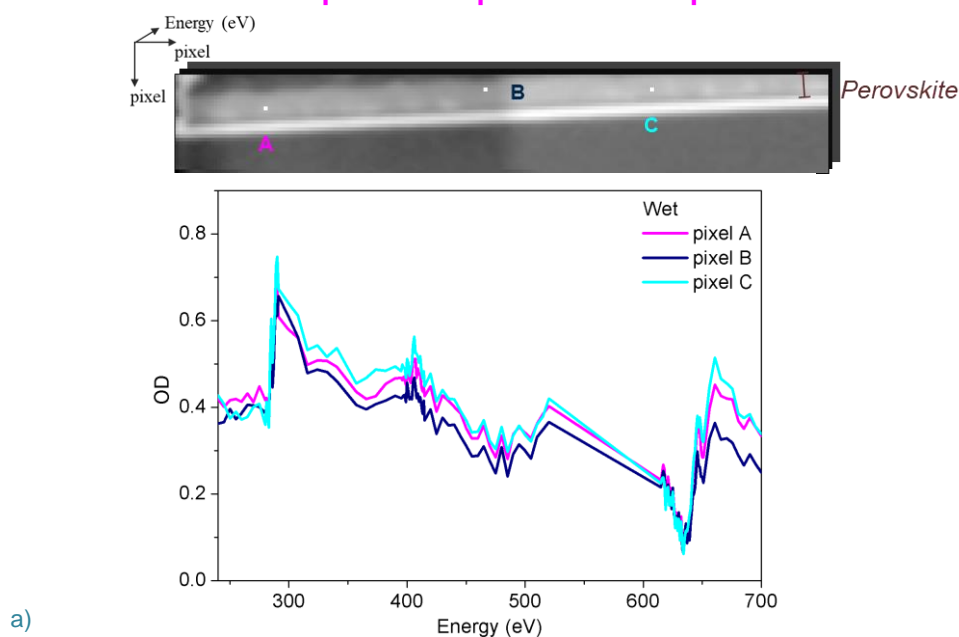
Examples of accordingly pre-processed images are shown in Figure 80.



Figure 80. Examples of aligned, ODed and cropped STXM images at 490 eV for the a) wet- and b) dry-processed perovskite samples (reminder: what is shown here is just one out of the 116 images of each stack scan).

From these pre-processed data, it is then possible to plot absorption spectra for pixels of interest, in our case: pixels in the perovskite layer, as illustrated in Figure 81.

Wet-processed perovskite sample



Dry-processed perovskite sample

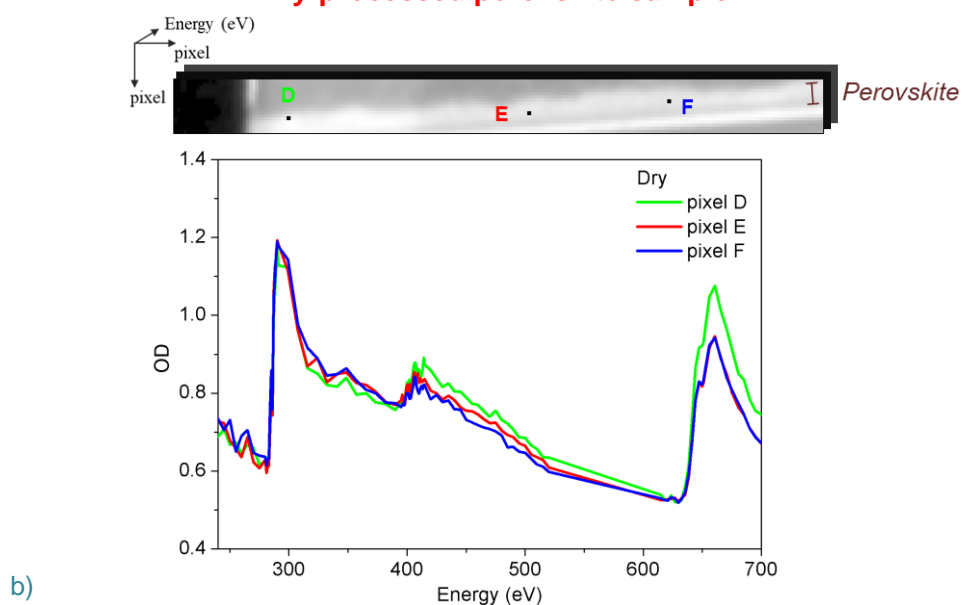


Figure 81. OD cropped image at 490 eV with few selected pixels and corresponding OD spectra (reminder: the 520 to 615 eV range was not covered in our measurements, thus the linear section in the spectra) for a) wet- and b) dry-processed perovskite sample.

Now that the stacks are pre-processed, they can be further analysed to serve our purpose of homogeneity assessment through post-processing steps. It is important to mention that although the pre-processing steps (*i. e.* from raw data Figure 78 to aligned ODED cropped data Figure 80) were carried out during the beamtime, the post-processing steps that follow were carried out post-beamtime.

Given the very occasional nature of a beamtime, its short duration and dynamics, data are usually recorded and partially processed (enough to direct the next measurements but not entirely) during the measurement time and then further processed after the

beamtime. Operating without any processing means blindly performing a lot of measurements and hope that the processed data will eventually make sense, coming down to sound results. Extensively processing the data leads to important downtime where the beam is not used, users don't take advantage of their beamtime to the fullest. Running a 'good' beamtime is a question of finding the right balance between recording and processing the data.

iii. Post-processing methodology

As we conducted the post-processing steps after the beamtime, we had to make the best of the available data; as we could not record complementary ones. We realized post-beamtime that our measurements were maybe still not the best and most representative; that we might have overlooked some aspects in our measurements but at least we knew we could properly compare our two samples as we made sure, for this study, to be consistent in our measurement procedure. We then had to find a metric to base our comparison on.

Confronting our data to the simulations (Figure 77), we estimated the monitoring of the Pb and I features to be relevant. As our study was the first of its kind we had to develop our own post-processing methodology. In close collaboration with the HERMES beamline team, we eventually settled down for a Pb/I ratio figure of merit. This ratio was calculated using two methods (so called Fitting and Integration) that will now be described.

a. Fitting method

The Fitting method consists in fitting a simulated OD spectrum with the measured one. Simulated OD spectra are obtained from the energy-dependent equation of OD. As aforementioned (page 93), the optical density is linked to the absorption coefficient through:

$$OD = \mu(E)\rho t \quad [11]$$

with $\mu(E)$ the absorption coefficient that can be defined as:

$$\mu(E) = \frac{N_A}{MW} \sum_i z_i \sigma_{a_i} \quad [12]$$

where N_A is the Avogadro number, MW the molecular weight, z_i the atomic coefficients of the chemical element i and σ_{a_i} the atomic photoabsorption cross-sections.

The latter can be expressed as:

$$\sigma_{a_i} = 2r_0 \lambda f_{2_i}(E) \quad [13]$$

with r_0 the electron radius, λ the wavelength and $f_{2_i}(E)$ the energy-dependant atomic scattering factor.

The energy dependency is clearly displayed by developing the wavelength given by the Planck-Einstein equation:

$$\lambda = \frac{hc}{E} \quad [14]$$

Combining equations [11], [12], [13] and [14] provides the complete energy-dependent expression of the optical density:

$$OD = \frac{N_A}{MW} 2r_0 \frac{hc}{E} \rho t \sum_i z_i f_{2_i}(E) \quad [15]$$

For a $(CH_3NH_3)_{z_{CH_3NH_3}}Pb_{z_{Pb}}I_{z_I}$ formula, the OD equation [15] becomes:

$$OD = \frac{N_A}{(32z_{CH_3NH_3} + 126.9z_I + 207.2z_{Pb})} 2r_0 \frac{hc}{E} \rho t \times [z_{CH_3NH_3}(f_{2_C} + 6f_{2_H} + f_{2_N}) + z_I f_{2_I} + z_{Pb} f_{2_{Pb}}] \quad [16]$$

After seeing no difference between the fitting results when its value was either 0.1, 0.5, 0.8 or 1, the organic part coefficient $z_{CH_3NH_3}$ was arbitrarily set to 1; leading to the following OD equation for a $CH_3NH_3Pb_{z_{Pb}}I_{z_I}$ formula:

$$OD = \frac{N_A}{(32 + 126.9z_I + 207.2z_{Pb})} 2r_0 \frac{hc}{E} \rho t [(f_{2_C} + 6f_{2_H} + f_{2_N}) + z_I f_{2_I} + z_{Pb} f_{2_{Pb}}] \quad [17]$$

Atomic coefficients z_{Pb} and z_I are used as fitting parameters to fit the simulated OD spectrum that follows equation [17] with the measured one. The fitting is carried out using the least squares method. An example of fit between measured and simulated spectra is shown Figure 82.

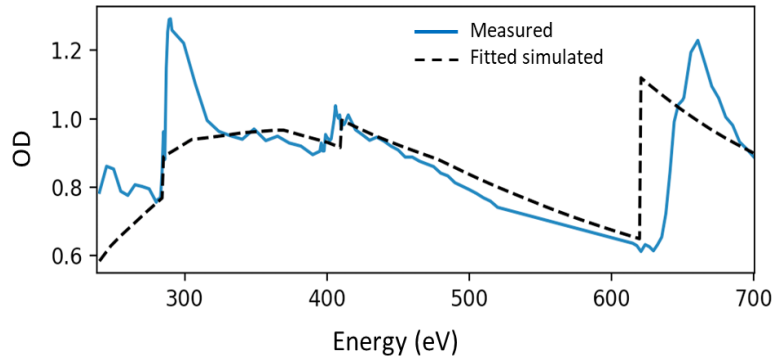


Figure 82. Example of fitting of a simulated OD spectrum (dashed black line) with a measured one (solid blue line).

The Fitting ratio was then calculated as the following numerical ratio:

$$\left(\frac{Pb}{I}\right)_{Fit} = \frac{z_{Pb}}{z_I} \quad [18]$$

where z_{Pb} and z_I are the Pb and I atomic coefficients in equation [17] of the fitted simulated spectrum (dashed black line in Figure 82).

The validity of this fitting method was assessed using PbI_2 a pure and stable compound with a known density. The measured spectrum from a 75 nm thick PbI_2 film deposited on a SiN membrane was compared to various simulated spectra of $Pb_{z_{Pb}}I_{z_I}$ formula with a 75 nm thickness and a 6.16 g/cm³ density. The general equation for these simulated spectra is given by equation [19] and the simulated spectra are shown in Figure 83.

$$OD = \frac{N_A}{(126.9z_I + 207.2z_{Pb})} 2r_0 \frac{hc}{E} \rho t [z_I f_{2_I} + z_{Pb} f_{2_{Pb}}] \quad [19]$$

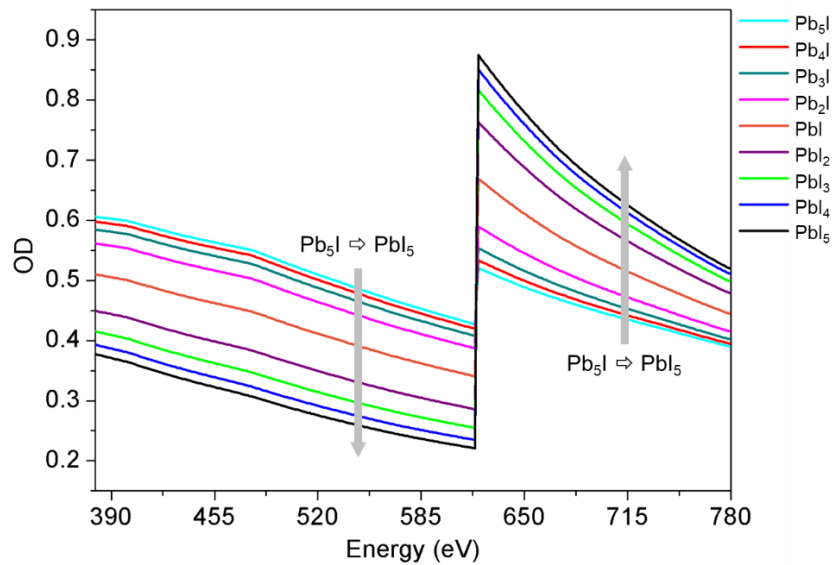


Figure 83. Simulated spectra for various Pb_xI_y formulas going from Pb_5I (light blue plot) to PbI_5 (black plot).

We have found the simulated spectrum for $z_{Pb} = 1$ and $z_I = 2$ i. e. PbI_2 to fit with the measured spectrum as shown in Figure 84.

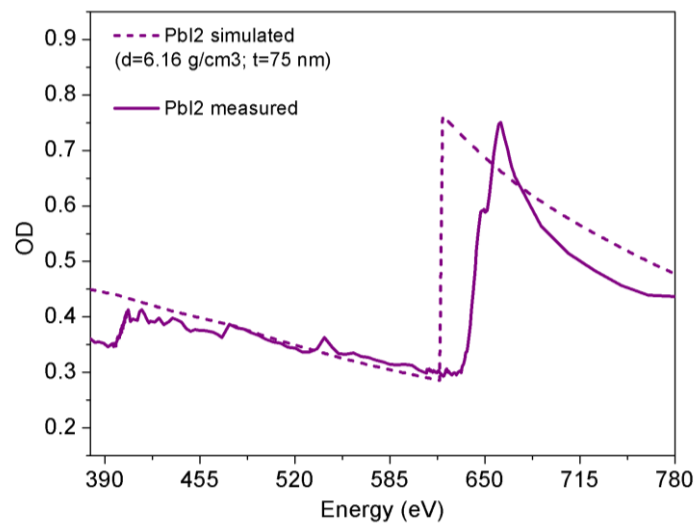


Figure 84. Comparison between the measured spectrum for a 75 nm thick PbI_2 film (solid line) with the simulated spectrum for a PbI_2 formula ($z_{Pb} = 1$ and $z_I = 2$) with a density of 6.16 g/cm^3 and a thickness of 75 nm (dashed line).

The measured spectrum for a PbI_2 film matches the simulated spectrum for a PbI_2 formula ($z_{Pb} = 1$ and $z_I = 2$), establishing the righteousness of the fitting calculation method.

It is worth mentioning that the two spectra cannot perfectly match given the fine structures in the measured spectrum (for example the small peaks around 400, 480 and 550 eV) and the shift between the two absorption maxima (at 620 eV for simulated and 660 eV for measured) that are linked to experimental factors (respectively Nitrogen contamination and beamline settings) that cannot be accounted for in the simulations.

b. Integration method

We confronted the Fitting method to a second one, more empiric, so called Integration. It consisted in calculating the Pb/I ratio as the graphical ratio of the two corresponding spectrum parts. Confronting our data (Figure 81 pixel OD spectra) to simulations (Figure 77) and previous experiments (Figure 73), we postulated that from 240 to 632 eV the absorption was mostly Pb-related and that from 632.5 to 700 eV the absorption was I-related (Figure 85).

It is important to note that with this assumption we are neglecting the fine features of C and N as well as the discrete contribution of Iodine at low energies (that can be seen in Figure 77 simulations) in the Pb-defined region. We are making intentionally the following approximation:

$$Pb + \Delta C + \Delta N + \Delta I = Pb \quad [20]$$

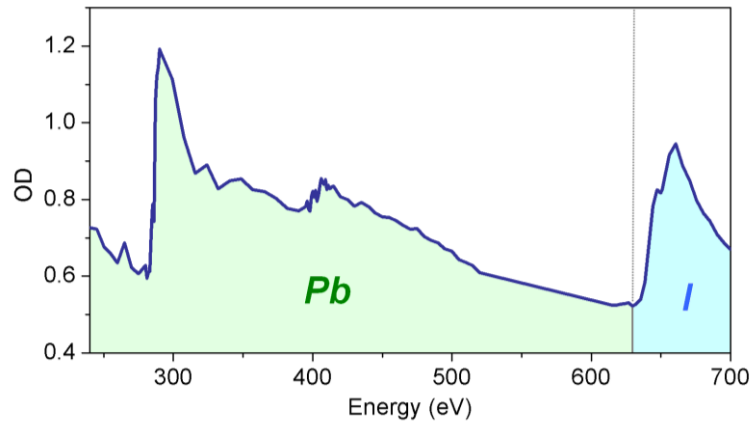


Figure 85. Example of pixel spectrum with the integration areas as we have defined them: Pb region from 240 to 632 eV and I region from 632.5 to 700 eV.

The Pb/I Integration ratio is then calculated as:

$$\left(\frac{Pb}{I}\right)_f = \frac{\int_{240}^{632} OD}{\int_{632.5}^{700} OD} \quad [21]$$

with $\int_{240}^{632} OD$ and $\int_{632.5}^{700} OD$ the integration areas shown Figure 85.

iv. Ratio calculations results

Both Fitting and Integration methods were carried out using Python²¹⁹ for each pixel of both the wet- and dry-perovskite stacks as depicted in Figure 86.

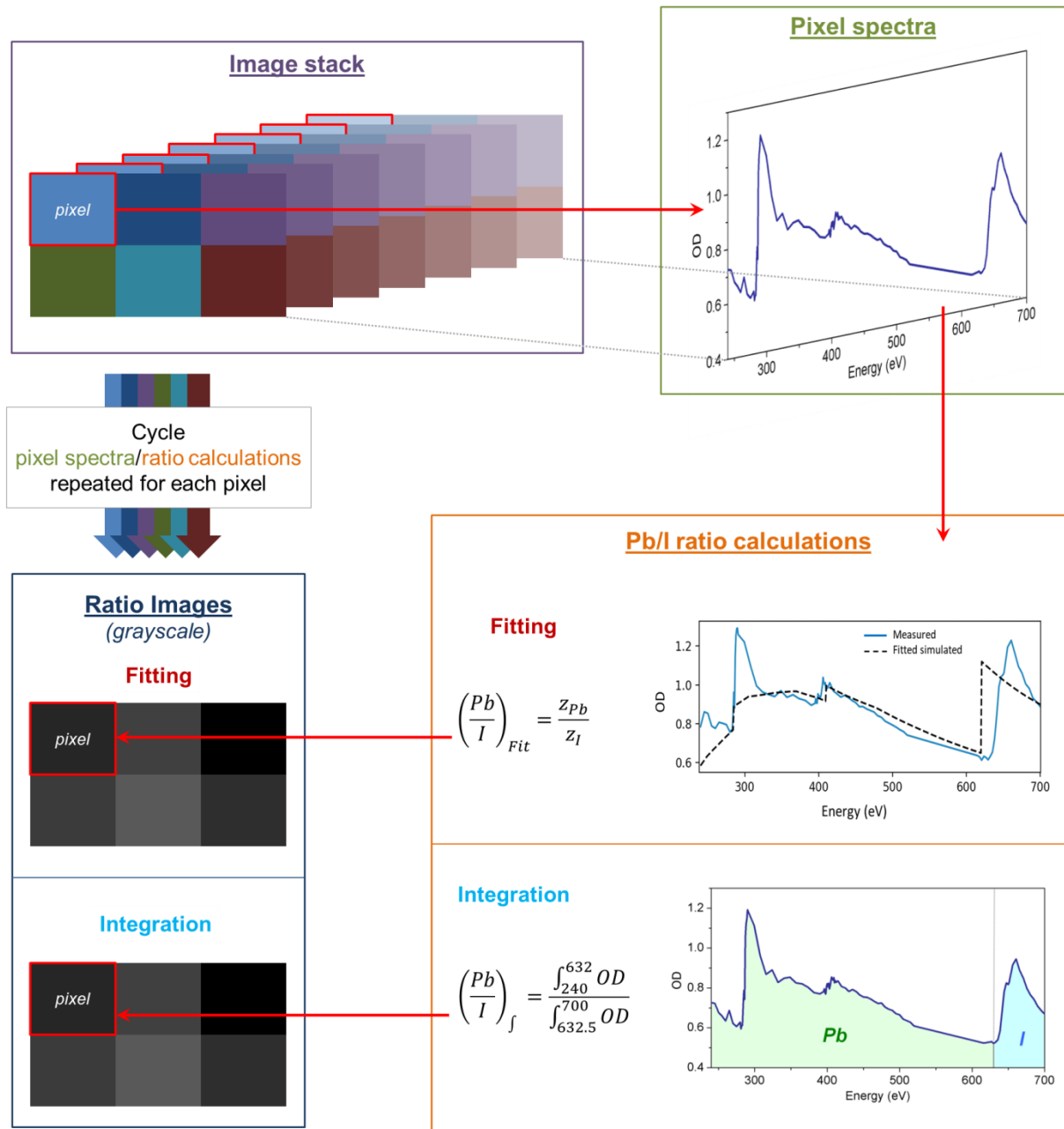


Figure 86. Data processing overflow for Pb/I ratio calculations.

²¹⁹ Code by Dr. Sufal Swaraj beamline scientist on HERMES.

The ratio images resulting from the two ratio calculation are shown in Figure 87 for both samples.

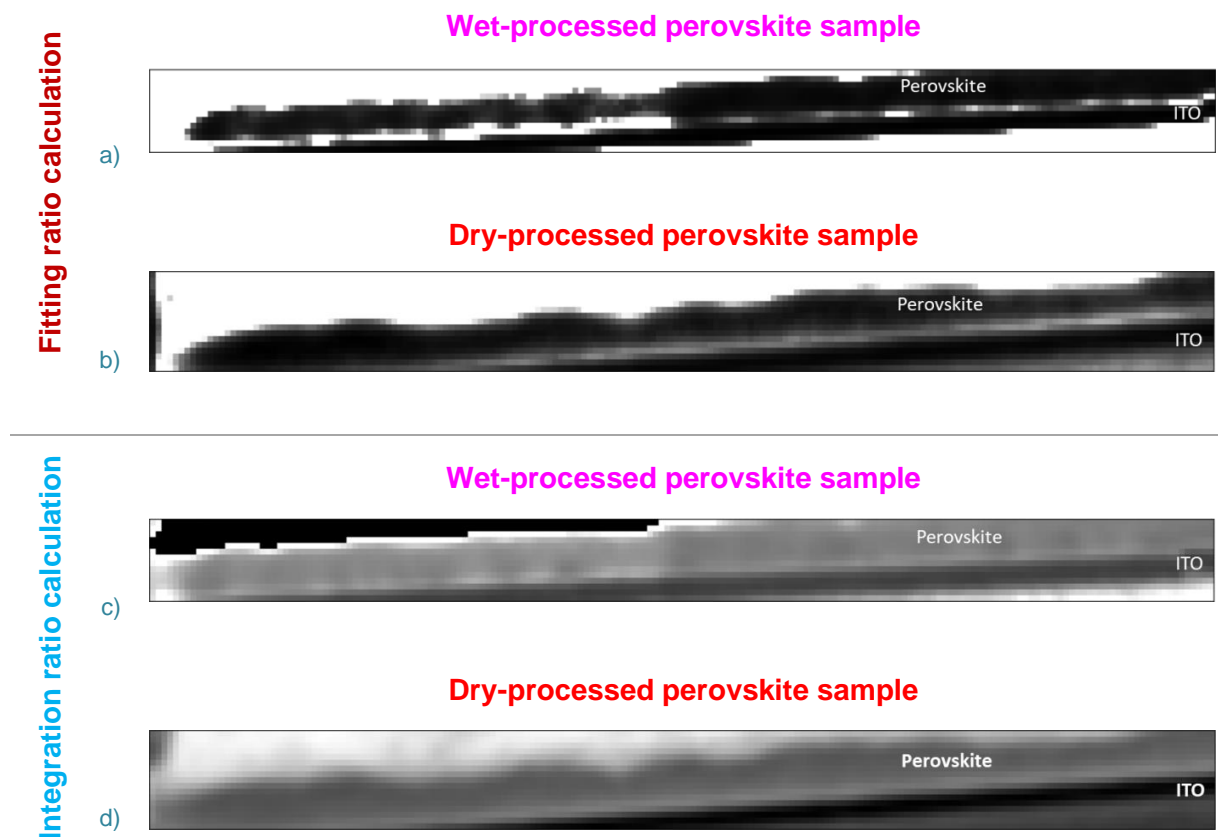
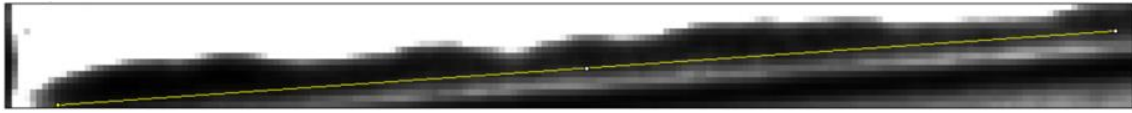


Figure 87. Ratio images results (grayscale) for a) wet- and b) dry-processed perovskites with Integration ratio calculation and c) wet- and d) dry-processed perovskites with Fitting ratio integration (for clarity, only the perovskite and ITO layers are tagged on the images).

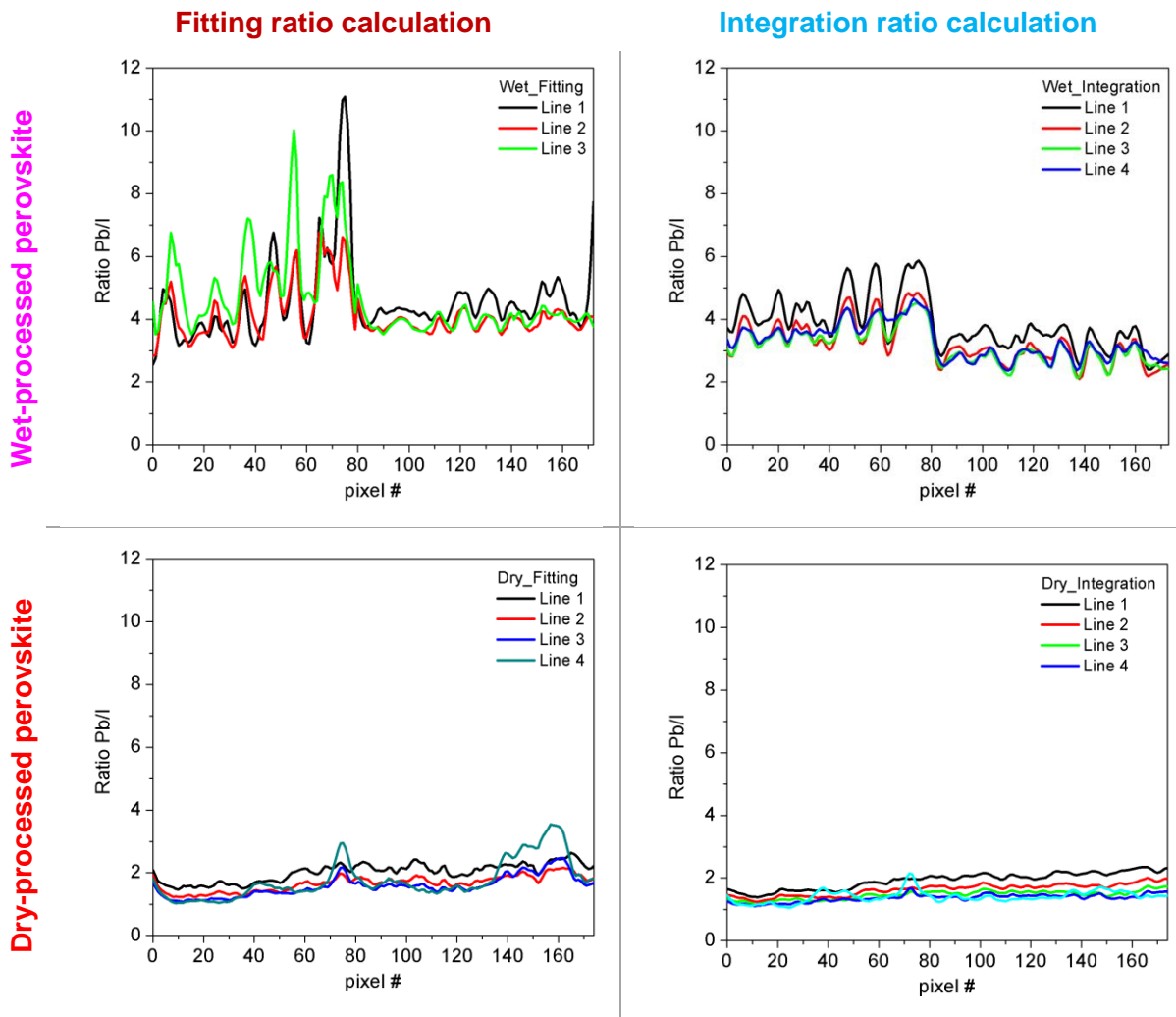
From these images, we used a processing software (Fiji²²⁰) to analyse our data, studying the evolution of the calculated Pb/I ratio in the perovskite layers.

As an initial approach, we defined lines across the perovskite layer of the different images (an example of line definition is shown in Figure 88a) and plotted the corresponding profiles (Figure 88b graphs).

²²⁰ Fiji (former ImageJ)



a)

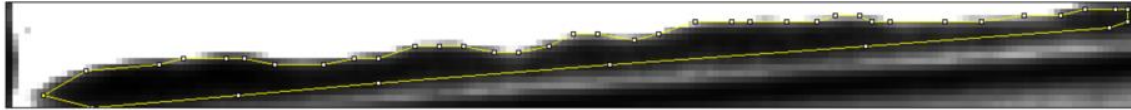


b)

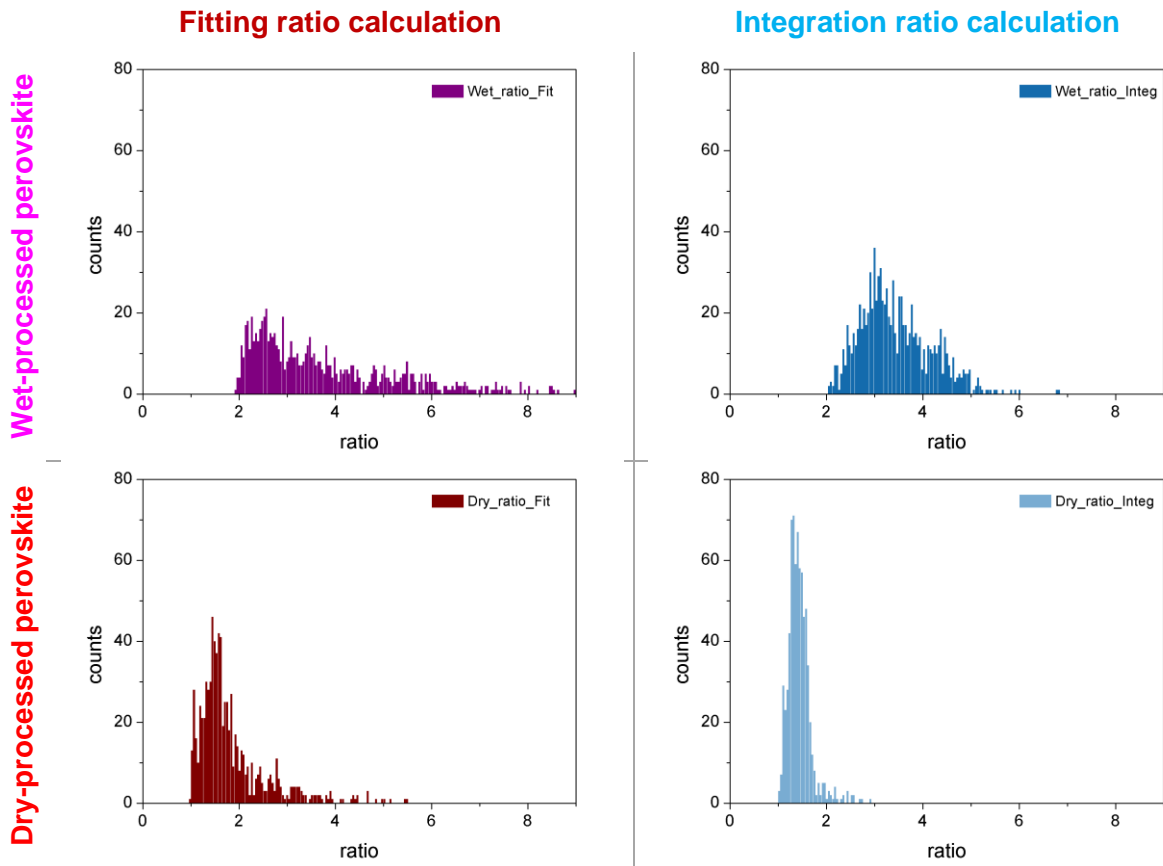
Figure 88. Profile lines: a) example of line definition across the perovskite layer for one ratio image and b) corresponding profiles for the four different ratio images (two perovskites -Wet and Dry- with two ratio calculations -Fitting and Integration-).

The two calculation paths (Fitting and Integration) yield the same kind of ratio profiles: rather smooth with a mean value close to 1.5 for the dry perovskite and bumpier with a mean value around 3 for the wet perovskite. Our ratio calculations seem consistent with each other, both in amplitude and values.

Given the tilt of the layers on the images, we were unable to plot a more statistically relevant number of lines (while keeping the same number of pixels). We then decided to consider the perovskite layer in its wholeness and plot histogram of the ratio distribution. An example of the perovskite layer selection is shown in Figure 89a and the four corresponding histograms are shown in Figure 89b.



a)



b)

Figure 89. Ratio distribution: a) example of region selection and b) corresponding histograms for the four different ratio images (two perovskites with two ratio calculations).

The distribution results are consistent with the profile lines analysis (Figure 88): the distribution is sharper for the dry perovskite and localized around a ratio value of 1.5 when it is wider with a value closer to 3 for the wet perovskite, whatever the ratio calculation path. Once again our two calculation methods (Fitting and Integration) are consistent with each other.

Given the agreement between the two statistical analysis (line and distribution), we can conclude; with a relative confidence; that our results are trustworthy.

Focusing on the results themselves, we can draw several conclusions. First, considering a qualitative analysis of the results: whatever the calculation path and the statistical analysis, ratio values are more distributed for the wet-processed perovskite (noisier profile and wider distribution) than for the dry-processed one (flatter profile and narrower distribution). This finding shows a higher homogeneity of the dry-processed perovskite film with respect to the wet-processed, based on the Pb/I ratio figure of merit we have defined here. Focusing on a quantitative analysis of the results: the Pb/I ratio values being lower for the dry perovskite would mean that either the Pb content is lower or the I content is higher with respect to the wet perovskite. While we do not see any reason why the Pb content would be impacted by the deposition method, it seems highly likely that the I content would

be. Given the potential MAI parasitic redeposition suspected from the work detailed in the previous two chapters during the coevaporation process, it is possible that the I content is higher for the dry sample. It is also possible that the I content is lower for the wet sample as it is now widely acknowledged that $\text{CH}_3\text{NH}_3\text{PbI}_3$ degradation mechanism releases I^{221} . The degradation of the material is highly plausible given its poor stability and the time delay (inherent to the FIB milling step) between deposition and STXM measurement. At the time, we found ourselves unable to clearly validate any of these two hypotheses without supplementary experiments. Although we can hardly get rid of the excess of I for the dry-processed perovskite (unless the reactor is thoroughly cleaned before deposition), we could moderate the Iodine loss in wet-processed perovskite by studying fresher samples, getting rid of the time delay induced by the FIB preparation.

Although our method seems robust (the two calculations leading to consistent results) it suffers several weaknesses. To this point it seems important to take the time to discuss once again these latter (already dispensed throughout the previous paragraphs).

v. Open discussion

Considering the Fitting approach, as shown with the PbI_2 (Figure 84), simulated and measured spectra will never perfectly fit. Small absorption features coming from experimental factors (beamline settings, Nitrogen contamination, etc...) cannot be accounted for in simulations, this induces a difference that might distort the fitting.

Considering the Integration approach, it is even more contentious than the Fitting one. First, in our stack definition we neglected almost 100 eV (520 to 615 eV) of the spectral range. Absorption in this range was approximated to be linear while it might have shown fine structures. Also, as we have specified we made quite an approximation overlooking the C, N and I contributions in the Pb region from 240 to 632 eV (equation [20]).

In spite of these weaknesses, that certainly calls our method into question; we were at least consistent in both our data acquisition and data analysis between our two samples, which allow us to be reasonably confident in the presented study and its outcomes.

²²¹ M. Shirayama *et al.*, (2016) *J. of Applied Physics*, 119, 115501

Conclusion

The current chapter aimed at presenting a Synchrotron-based X-ray Absorption Spectroscopy technique used for the first time, in our team, to study perovskite films. After an overview on the topic of X-rays, their interaction with matter, an introduction to Synchrotron radiation lightsource, we focused on the particular technique of Scanning Transmission X-ray Microscopy. We then step into the heart of our STXM/perovskites studies with a focus on the comparative investigation of wet- and dry-processed perovskite films.

The study we conducted was quite unique, as it involved the comparison of two deposition techniques (one still scarcely used) of an emerging material using a large instrument based spectromicroscopy technique. With the goal of assessing the homogeneity differences between wet- and dry-phase depositions of perovskite films we have developed a whole new methodology to analyse our STXM data. We chose as a figure of merit the Pb/I ratio for our comparison. Confronting two calculation methods (one based on simulations and one more empirical) we have shown a higher homogeneity of this Pb/I ratio in favour of the dry-processed perovskite film. As we are aware of the weaknesses of our method, we would need further investigations to strengthen it. Expanding the spectral range down to 180 and up to 800 eV to properly cover respectively the Pb and I contributions would allow for a more righteous integration calculation.

In the present study we favoured a rough statistical analysis of the perovskite layer in its wholeness; future work could focus on finer analysis, distinguishing regions in the perovskite, such as its core, the interface with a lower layer and the one with an upper layer. As it is widely acknowledge that interfaces are crucial in a perovskite device, this could unveil structural differences one could link to differences in PV performances. Given the difficulty we faced with our Pb and I monitoring, future work could focus on less intertwined features such as Carbon and Nitrogen. Studying different perovskite compositions would then be highly relevant. For example pure methylammonium, pure formamidinium and mixed methylammonium/formamidinium compositions would exhibit different absorption features as the N atom configuration varies from $\text{CH}_3\text{NH}_3\text{I}$ to $\text{CH}(\text{NH}_2)_2\text{I}$.

With the two beamtimes mentioned in the present chapter, we have set the groundwork for future studies. We know that we must be very consistent in our different measurements (both during one beamtime and in between beamtimes), we have started deciphering the different contributions but are aware that we need to build a library of reference spectra. All these initial results are very encouraging and have opened the way for a PhD thesis between the LPICM and HERMES beamline that will start in autumn 2019. Given the novelty of the perovskite material, the richness of the STXM technique and the very few reported papers on the topic, the scope for future studies is quite broad and they are expected to be of great impact for the scientific community as to better understand the nanoscale organization of the material as well as its behaviour.

Conclusion and Perspectives

Within this document we have presented the development of the coevaporation process for the fabrication of perovskite thin films for photovoltaic applications. The major findings are here after summarized and future work ideas are proposed.

As this thesis started, the coevaporation of perovskites had never been undertaken neither in IPVF nor LPICM. As such, we first had to assess the feasibility of the process. Using a proof-of-concept reactor we got a first handle on the coevaporation of PbI_2 and $\text{CH}_3\text{NH}_3\text{I}$ (MAI). We were quickly confronted to the unusual evaporation behaviour of the organic precursor that was far from directive, filling the chamber volume and parasitizing the PbI_2 evaporation. Lacking some features on the reactor we were unable to fully grasp the impact of this erratic evaporation of MAI. Despite this issue, encouraging results were obtained that validated the feasibility of the perovskite coevaporation process.

From the pitfalls of the proof-of-concept reactor, we designed hand in hand with the manufacturer a second reactor, dedicated to the coevaporation of perovskites, integrating new relevant features. Following its implementation, we thoroughly studied the behaviour of each of the precursors. The added features of the reactor provided us with useful insights that allowed us to mitigate to a certain extent the impact of the organic salt. Following these single-compound evaporation studies, we eventually started to perform coevaporation. Facing both intra- and inter-batch variability we found ourselves unable to draw any clear conclusion and not knowing where to go from there.

Stepping aside from these practical issues, we had the opportunity to investigate our dry-processed material using a Synchrotron-based spectromicroscopy technique. Building a study around wet- and dry-processed films, we wanted to assess the suspected homogeneity difference between these two phases. Monitoring the Pb to I ratio throughout the two materials we found a clear difference in favour of the dry-deposition method.

Regarding the coevaporation process, as the second reactor was moved from LPICM to IPVF, we are unable to know whether the issues we reported in the present manuscript will be found again. In the event they are, we could resort to an alteration of the reactor to implement a cooling system; that is believed to eradicate the MAI parasitic behaviour. If this latter cannot be suppressed by any practical upgrade, we would eventually switch to other organic precursors.

The Synchrotron study of wet and dry perovskite materials would need a more statistically significant number of samples, to consolidate the initial findings. To further investigate the Pb/I ratio and validate (or invalidate) our findings, it would be worth studying variously aged wet perovskite samples. Given the weaknesses of the method presently used (Pb/I ratio figure of merit) due to the difficulty to clearly untangle the Pb and I contributions, another approach could consist in focusing the interest on the Nitrogen region with various perovskite compositions. Future works could also include investigating the material response (both spectroscopically and microscopically) to an electrical bias with the hope of showing in situ ionic migration.

List of references

- 1 [Internation Energy Agency 2018 World Energy Outlook report](#)
- 2 [Merckgroup.com](#)
- 3 [Heliatek.com](#)
- 4 [Asca.com](#)
- 5 [OxfordPV.com / news 14 Nov. 2016](#)
- 6 [OxfordPV.com / news 3rd July 2019](#)
- 7 [Sauletech.com](#)
- 8 [Skanska.pl](#)
- 9 [M. F. M. Zwinke, E. Knittle and R. Jeanloz, \(1987\) Science 235, 668](#)
- 10 [F. Nestola *et al.*, \(2018\) Nature, 555, 237-41](#)
- 11 [Is *et al.*, \(1999\) Catalysis Today, 47, 73-82](#)
- 12 [H. Huang *et al.*, \(2019\) Diamond & Related Materials, 91, 199-206](#)
- 13 [Q. Wang and L. Ma, \(2019\) New J. Chem., 43, 2974-80](#)
- 14 [adapted from N. Louvain's thesis manuscript « Relations Structures-Propriétés dans des matériaux hybrides multifonctionnels : Investigations structurales et théoriques. » \(2008\) <tel-00450691>](#)
- 15 [Wikipedia](#)
- 16 [Earth-Building Bridgmanite; Caltech \(2014\)](#)
- 17 [L. An and H. Onishi, \(2015\) ACS Catal., 5, 3196-206](#)
- 18 [T. Ishihara, \(1994\) J. of Luminescence, 60 & 61, 269-74](#)
- 19 [D. B. Mitzi *et al.*, \(1994\) Nature, 369, 467-9](#)
- 20 [F. Hao *et al.*, \(2014\) Nat. Photon., 8, 489-94](#)
- 21 [B-W. Park *et al.*, \(2015\) Adv. Mater., 27, 6806-13](#)
- 22 [G. Stoumpos *et al.*, \(2015\) J. Am. Chem. Soc., 137, 21, 6804-19](#)
- 23 [S. Lee *et al.*, \(2018\) 227, 311-4](#)
- 24 [N. Ito *et al.*, \(2018\) J. Phys. Chem. Lett., 97, 1682-8](#)
- 25 [A. Leblanc *et al.*, \(2017\) Angew. Chem. Int. Ed., 56, 16067-72](#)
- 26 [C. K. Møller, \(1958\) Nature, 182, 1436](#)
- 27 [D. Weber, \(1978\) Zeitschrift für Naturforschung B, 33, 8, 862-5](#)
- 28 [D. Weber, \(1978\) Zeitschrift für Naturforschung B, 33, 12, 1443-5](#)
- 29 [D. B. Mitzi 'Synthesis, Structure, and Properties of Organic-Inorganic Perovskites and Related Materials' in *Progress in Inorganic Chemistry*, K. D. Karlin \(1999\)](#)
- 30 [Y. H. Kim *et al.*, \(2015\) Adv. Mater., 27, 1248](#)
- 31 [W. Yu *et al.*, \(2018\) Nature Communications, 9, 354](#)
- 32 [M. Grätzel, \(2014\) Nature Materials, 13, 838-42](#)
- 33 [O. Almora *et al.*, Rev. Cub. Fís. \(2017\), 34, 1, 58-68](#)
- 34 [H. Cho *et al.*, \(2015\) Science, 4, 350, 6265, 1222-5](#)
- 35 [A. Kojima *et al.*, \(2009\) J. Am. Chem. Soc., 131, 17, 6050-1](#)
- 36 [E. Becquerel, \(1839\) Comptes rendus des séances de l'Académie des sciences, 9, 561](#)
- 37 [W. Shockley and H. J. Queisser, \(1961\) J. Appl. Phys. 32, 510](#)
- 38 [S.H. Moon *et al.*, \(2015\) Sci. Rep. 5, 8970](#)
- 39 [S. Lu *et al.*, \(2017\) Sc. China Chem., 60, 4, 460-71](#)
- 40 [P. Colter *et al.*, \(2018\) Crystals, 8, 445](#)
- 41 [M. Yamaguchi *et al.*, \(2018\) J. Phys. D: Appl. Phys., 51, 133002](#)
- 42 [adapted from I. Etxebarria *et al.*, \(2014\) Solar Energy Materials & Solar Cells, 130, 495-504](#)
- 43 [Franhofer Photovoltaics Report, March 2019](#)
- 44 [T. Todorov *et al.*, \(2016\) Mol. Syst. Des. Eng., 1, 370-6](#)
- 46 [H-S. Kim *et al.*, \(2012\) Sci Rep, 2, 591](#)
- 47 [Sciences' top 10 breakthroughs 2013](#)

48 [NREL efficiency chart \(version 2019-08-02\)](#)
49 [De Angelis \(2019\) ACS Energy Lett., 4, 853–4](#)
50 [J. Burschka *et al.*, \(2013\) Nature, 499, 316–319](#)
51 [N. J. Jeon *et al.*, \(2014\) Nature Materials, 13, p 897–903](#)
52 [N. J. Jeon *et al.*, \(2015\) Nature, 517 \(7535\), p 476-80](#)
53 [W. S. Yang *et al.*, \(2015\) Science, 348 \(6240\) 1234-7](#)
54 [M. Saliba *et al.*, \(2016\) Energy Environ. Sci., 9, 1989](#)
55 [L. K. Ono *et al.*, \(2017\) ACS Appl. Mater. Interfaces, 9, 30197–246](#)
56 [V. M. Goldschmidt, \(1926\) Die Naturwissenschaften, 21, 477–85](#)
57 [M. Saliba *et al.*, \(2016\) Science, 354, 6309, 206-9](#)
58 [N. Li *et al.*, \(2019\) Nature Energy, 4, 408-15](#)
59 [M. Salado *et al.*, \(2019\) ChemSusChem, 12, 11](#)
60 [J. H. Noh *et al.*, \(2013\) Nano Lett., 13, 4, 1764–69](#)
61 [B. O'Regan and M. Grätzel, \(1991\) Nature, 353, 737-40](#)
62 [J-Y Jeng *et al.*, \(2013\) Adv. Mater., 25, 27, 3727-32](#)
63 [M. Liu *et al.*, \(2013\) Nature, 501, 7467, 395-8](#)
64 [K-C. Wang *et al.*, \(2014\) ACS Appl. Mater. Interfaces, 6, 15, 11851-8](#)
65 [X. Li *et al.*, \(2015\) Nature Chemistry, 7, 703–11](#)
66 [M. Saliba *et al.*, \(2018\) Chem. Mater., 30, 13, 4193–201](#)
67 [K. C. Wang *et al.*, \(2014\) Sc. Reports, 23, 4, 4756](#)
68 [Z. Yu and L. Sun, \(2015\) Adv. Energy Mater., 5, 12, 1500213](#)
69 [L. Calìo *et al.*, \(2016\) Angew. Chem. Int. Ed., 55, 14522-45](#)
70 [P. K. Kung *et al.*, \(2018\) Adv. Mater. Interfaces, 5, 1800882](#)
71 [J. Urieta-Mora *et al.*, \(2018\) : Chem. Soc. Rev., 47, 8541-71](#)
72 [H. Liu *et al.*, \(2016\) Nanoscale, 8, 6209-21](#)
73 [K. Mahmood *et al.*, \(2017\) RSC Adv., 7, 17044-62](#)
74 [J. Lian *et al.*, \(2018\) Small Methods, 2, 1800082](#)
75 [Y. Chen *et al.*, \(2019\) J. of Energy Chem., 35, 144-67](#)
76 [A. Rajagopal *et al.*, \(2018\) Adv. Mater., 30, 32, 1800455](#)
77 [N. J. Jeon *et al.*, \(2014\) Nature Materials, 13, 897-903](#)
78 [A. T. Mallajosyula *et al.*, \(2016\) Applied MaterialsToday, 3, 96-102](#)
79 [J. Burschka *et al.*, \(2013\) Nature, 499, 316-9](#)
80 [J. B. Whitaker, \(2018\) Sustainable Energy Fuels, 2, 2442-9](#)
81 [F. Mathies *et al.*, \(2016\) J. Mater. Chem. A, 4, 19207-13](#)
82 [C. Zuo *et al.*, \(2018\) Nano Energy, 46, 185-92](#)
83 [H. Chen *et al.*, \(2017\) Nature, 550, 92-5](#)
84 [S. Han *et al.*, \(2018\) ACS Appl. Mater. Interfaces, 10, 8, 7281-8](#)
85 [A. K. Chilvery *et al.*, \(2015\) J. of Photonics for Energy, 5, 053093](#)
86 [K. Yan *et al.*, \(2015\) J. Am. Chem. Soc., 137, 4460-8](#)
87 [X. Cao *et al.*, \(2019\) ACS Appl. Mater. Interfaces, 11, 7639-54](#)
88 [H. Tsai *et al.*, \(2017\) Adv. Energy Mater. 2017, 7, 1602159](#)
89 [L. K. Ono *et al.*, \(2016\) J. Mater. Chem. A, 4, 6693-713](#)
90 [C. W. Chen *et al.*, \(2014\) Adv. Mater., 26, 38, 6647-52](#)
91 [M. R. Leyden *et al.*, \(2014\) J. Mater. Chem. A, 2, 18742-5](#)
92 [L. K. Ono *et al.*, \(2014\) Energy Environ. Sci., 7, 3989-93](#)
93 [D. B. Mitzi *et al.*, \(1999\) Chem. Mater., 11, 542-4](#)
94 [P. Fan *et al.*, \(2016\) Sc. Reports, 6, 29910](#)
95 [G. Longo *et al.*, \(2015\) Chem. Comm., 51, 7376](#)
96 [M. Tai *et al.*, \(2018\) ACS Appl. Mater. Interfaces, 10, 26206-12](#)
97 [J. Avila *et al.*, \(2017\) Joule, 1, 3, 432-42](#)
98 [OLEDON](#)
99 [UDC](#)
100 [OXFORD PV](#)
101 [M. Era *et al.*, \(1997\) Chem. Mater., 9, 1, 8-10](#)

103 [O. Malinkiewicz et al., \(2014\) Nature Photonics, 8, 128-32](#)
104 [B. S. Kim et al., \(2015\) Org. Elec., 17, 102-6](#)
105 [B. S. Kim et al., \(2016\) J. Mater. Chem. A, 4, 15, 5663-8](#)
106 [Q. Lin et al., \(2015\) Nature Photonics, 9, 106-12](#)
107 [C. Momblona et al., \(2014\) APL Mater., 2, 8, 081504](#)
108 [O. Malinkiewicz et al., \(2014\) Adv. Energy Mater., 4, 1400345](#)
109 [G. El-Hajje et al., \(2016\) Energy Environ. Sci., 9, 2286-94](#)
110 [L. Gil-Escrig et al., \(2016\) J. Mater. Chem. A, 4, 3667-72](#)
111 [L. Gil-Escrig et al., \(2016\) Organic Electronics, 37, 396-401](#)
112 [C. Momblona et al., \(2016\) Energy Environ. Sci., 9, 3456](#)
113 [L. Calìo et al., \(2017\) Solar Energy Mater. & Solar Cells, 163, 237-41](#)
114 [D. Pérez del Rey et al., \(2018\) J. Phys. Chem. Lett., 9, 5, 1041-6](#)
115 [B. Dänekamp et al., \(2019\) J. Mater. Chem. B, 7, 523-7](#)
116 [H. D. Pham et al., \(2019\) J. Mater. Chem. A, 7, 12507-17](#)
117 [D. Kiermasch et al., \(2019\) J. Mater. Chem. A, 7, 14712-22](#)
118 [D. Pérez del Rey et al., \(2019\) Chem. Mater. DOI: 10.1021/acs.chemmater.9b01396](#)
119 [J. Teuscher et al., \(2015\) ChemSusChem, 8, 3847-52](#)
120 [D. Zhao et al., \(2016\) Nano Energy, 19, 88-97](#)
121 [J. B. Patel et al., \(2017\) Adv. Electron. Mater., 1600470](#)
122 [Q. Chen et al., \(2014\) J. Am. Chem. Soc., 136, 2, 622-5](#)
123 [PEROvap system \(patent pending\)](#)
124 [J. J. Samueli 'The discovery of X-rays by Röntgen', bibnum library](#)
125 [W. C. Röntgen "Über eine neue Art von Strahlen" \(1895\) Sitzungsberichten der Würzburger Physik.-medic. Gesellschaft, English translation in Nature](#)
126 [W. C. Röntgen "Über eine neue Art von Strahlen 2" \(1896\)](#)
127 [W. C. Röntgen "Weitere Beobachtungen über die Eigenschaften der X Strahlen" \(1897\) Sitzungsberichten der Akademie der Wissenschaften zu Berlin](#)
128 [nobelprize.org](#)
129 ['Inventions: Diagnostic X-rays' from Darmouth.edu](#)
130 [E. H. Grubbé, \(1933\) Radiology, 21, 156-62](#)
131 [B. L. Henke et al., \(1993\) Atomic Data and Nuclear Data Tables, 54, 2, 181-342](#)
132 [Y. Joly and S. Grenier, 'Theory of X-ray absorption near edge structure' in X-Ray Absorption and X-Ray Emission Spectroscopy: Theory and Applications, J. A. Van Bokhoven and C. Lamberti \(2006\)](#)
133 [C. S. Schnorr and M. C. Ridgway, 'Introduction to X-ray absorption spectroscopy' in X-ray absorption spectroscopy of semi-conductors, C. S. Schnorr and M. C. Ridgway \(2015\)](#)
134 [X-ray Spectroscopy Chemistry LibreTexts](#)
135 [O. Björneholm et al., \(1997\) Phys. Rev. Lett. 79, 17, 3150-3](#)

137 [M. Newville, \(2014\) Reviews in Mineralogy and Geochemistry, 78, 1](#)
138 [XRD Bruker](#)
139 [J. R. Helliwell, \(1998\) Nature Structural Biology, 5, 614-7](#)
140 [Diamond light source education resources](#)
141 [Canadian light source education resources](#)
142 [ESRF light source education resources](#)
143 [A. L. Robinson, 'History of Synchrotron Radiation' from X-ray Data Booklet](#)
144 [Lightsources.org resources](#)
145 [M. N. Piancastelli 'Intro to SR and FEL spectroscopy' for EUSpec Winter School on core levels 2016](#)
146 [F. Baudalet \(2014\) 'Les origines du rayonnement synchrotron' in Histoire de la recherche contemporaine Rayonnement Synchrotron: de Frascati à SOLEIL \(1963-2013\)](#)
147 [F. Méot 'An introduction to particule accelerators' \(2009\)](#)
148 [F.R. Elder et al., \(1947\) Phys. Rev., 71, 11, 829-30](#)

149 [NASA, ESA, J. Hester, A. Loll \(ASU\) NASA image gallery](#)
 150 [J. P. Blewett, \(1998\) J. Synchrotron Rad. \(1998\). 5, 135-139](#)
 151 [D. Iwanenko and I. Pomeranchuk, \(1944\) Phys. Rev. 65, 343](#)
 152 [A. Liénard, \(1898\) L'éclairage électrique, 16-21](#)
 153 [John P. Blewett, \(1946\) Phys. Rev., 69, 87](#)
 154 [SOLEIL education resources](#)
 155 [SOLEIL beamlines](#)
 156 [R. Belkhou *et al.*, \(2015\) J. Synchrotron Rad., 22, 968-979](#)
 157 [HERMES beamline - SOLEIL](#)
 158 [A. P. Hitchcock *et al.*, \(2002\), J. Biomater Sci. Polymer Edn, 13, 8, 919-37](#)
 159 [J. Kirz and C. Jacobsen, \(2009\) J. of Physics: Conference series, 186, 012001](#)
 160 [G. Schmid, M. Obst, J. Wu and A. Hitchcock '3D chemical imaging of nanoscale biological, environmental and synthetic materials by Soft X-ray STXM spectrotomography' in *X-ray and Neutron Techniques for Nanomaterials Characterization*, C. S. S. R. Kumar \(2016\)](#)
 161 [H. H. Pattee, \(1953\) J. of the Opt. Soc. of America, 43, 1, 61-2](#)
 162 [P. Horowitz and J A Howell, \(1972\) Science, 178, 4061, 608-11](#)
 163 [B. Niemann *et al.*, \(1974\) Optics Comm., 12, 2, 160-3](#)
 164 [B. Niemann *et al.*, \(1976\) Appl. Optics, 15, 8, 1883-4](#)
 165 [H. Rarback *et al.*, \(1988\) Rev. of Sc. Inst., 59, 1, 52](#)
 166 [H. Rarback, J. Kenney, J. Kirz and X. Xie 'Scanning Soft X-ray Microscopy: First Tests with Synchrotron Radiation' in *Scanned Image Microscopy*, E. Ash \(1980\)](#)
 167 [H. Rarback *et al.*, \(1986\) Nucl. Inst. and Methods in Phys. Res., 246, 159-62](#)
 168 [H. Rarback *et al.*, \(1990\) Nucl. Inst. and Methods in Phys. Res., 291, 54-9](#)
 169 [J. Kirz, \(1988\) Nucl. Inst. and Methods in Phys. Res., 266, 293-5](#)
 170 [J. Kirz *et al.*, \(1990\) Physica Scripta, 31, 12-7](#)
 171 [J. Kirz *et al.*, \(1992\) Rev. of Sc. Inst., 63, 1, 557](#)
 172 [C. Jacobsen *et al.*, \(1986\) Photochem. and Photobio., 44, 3, 421-3](#)
 173 [C. Jacobsen *et al.*, \(2000\) J. of Microscopy, 197, 173-84](#)
 174 [A. L. D. Kilcoyne *et al.*, \(2003\) J. Synchrotron Rad., 10, 125-36](#)
 175 [Bruker ASC STXM](#)
 176 [A. P. Hitchcock, \(2015\) J. of Elec. Spectro. and Related Phenom., 200, 49-63](#)
 177 [A. P. Hitchcock's Bibliography of Soft X-ray Microscopy](#)
 178 [T. H. Yoon *et al.*, \(2004\) Langmuir, 20, 24, 10361-6](#)
 179 [H. Bluhm *et al.*, \(2006\) J. of Elec. Spectro. and Related Phenom., 150, 86-104](#)
 180 [H. Ade and S. Urquhart, 'NEXAFS spectroscopy and microscopy of natural and synthetic polymers' in *Chemical Applications of Synchrotron Radiation*, T.-K. Sham \(2002\)](#)
 181 [x-ray-optics.de](#)
 182 [B. Rösner *et al.*, \(2018\) Microsc. Microanal., 24 \(S2\) 272-3](#)
 183 [I. Mohacsi *et al.*, \(2016\) Optics Letters, 41, 2, 281-4](#)
 184 [J. R. Lawrence *et al.*, \(2003\) Appl Environ Microbiol., 69, 9, 5543-54](#)
 185 [E. G. Rightor *et al.*, \(1997\) J. Phys. Chem. B, 101, 1950-60](#)
 186 [Hitchcock group publications 'Polymers and polymer model studies'](#)
 187 [A. P. Hitchcock 'Bibliography of Soft X-ray Microscopy' S.I. from H. Ade and A. P. Hitchcock, \(2008\) Polymer, 49, 643-75](#)
 188 [R. Barrett *et al.*, \(2000\) AIP Conf. Proc., 507, 458](#)
 189 [A. Gianoncelli *et al.*, \(2006\) Appl. Phys. Lett., 89, 251117](#)
 190 [C. Jacobsen *et al.*, \(1993\) J. of Microscopy, 172, 2, 121-9](#)
 191 [aXis2000 \(Analysis of X-ray Images and Spectra\)](#)
 192 [MANTiS \(Multivariate ANalysis Tool for Spectromicroscopy\)](#)
 193 [G. Schmid, M. Obst, J. Wu and A. Hitchcock, '3D Chemical Imaging of Nanoscale Biological, Environmental, and Synthetic Materials by Soft X-Ray STXM Spectrotomography' In *X-ray and Neutron Techniques for Nanomaterials Characterization*, C. Kumar \(2016\)](#)

- 194 R. C. Moffet, A. T. Tivanski and M. K. Gilles, 'Scanning Transmission X-ray Microscopy: Applications in Atmospheric Aerosol Research' in *Fundamentals and Applications in Aerosol Spectroscopy*, R. Signorell and J. P. Reid (2010)
- 195 C. R. Mc Neill *et al.*, (2006) *Nano Lett.*, 6, 6, 1202-6
- 196 C. R. Mc Neill *et al.*, (2008) *Nanotechnology*, 19, 424015
- 197 C. Hub *et al.*, (2010) *J. Mater. Chem.*, 20, 4884-4887
- 198 S. Swaraj *et al.*, (2010) *Nano Lett.*, 10, 8, 2863-9
- 199 W. Zhang *et al.*, (2011) *Polym. Adv. Technol.*, 22, 65-71
- 200 S. Pack *et al.*, (2012) *Polymer* 53, 4787-99
- 201 B. A. Collins and H. Ade, (2012) *J. of Elec. Spectro. and Related Phenom.*, 185, 5-7, 119-28
- 202 J. Dhar *et al.*, (2015) *J. Phys. Chem. B*, 119 (34), 11307-16
- 203 Q. Arnoux *et al.*, (2017) *Nano Research*, 5, 2771-82
- 204 H. Li *et al.*, (2016) *Nanomater. Nanotechnol.*, 2016, 6, 24
- 205 J. Zhao *et al.*, (2016) *Sc. Rep.*, 6, 21976
- 206 J. A. McLeod *et al.*, (2016) *Nanoscale*, 8, 6361-8
- 207 L. T. Schelhas *et al.*, (2016) *ACS Energy Letters*, 1, 5, 1007-12
- 208 G. Ji *et al.*, (2016) *Appl. Surf. Sc.*, 393, 417-21
- 209 N. K. Kim *et al.*, (2017) *Sc. Rep.*, 7, 4645
- 210 N. Rolston *et al.*, (2018) *Adv. Energy Mater.*, 1802139
- 211 K. H. Stone *et al.*, (2018) *Nature Comm.*, 9, 3458
- 212 F. Hilt *et al.*, (2018) *Energy Environ. Sci.*, 11, 2102-13
- 213 M. Alsari *et al.*, (2018) *Energy Environ. Sci.*, 11, 383
- 214 X. Li *et al.*, (2019), *Chinese J. of Chem. Phys.*, DOI:10.1063/1674-0068/cjcp1808189
- 215 M. W. Lin *et al.*, (2016) *Adv. Mater. Interfaces*, 3, 1600135
- 216 M. H. Li *et al.*, (2018) *Adv. Mater.*, 30, 1801401
- 217 <http://www.eels.info/atlas/lead>
- 220 Fiji (former ImageJ)
- 221 M. Shirayama *et al.*, (2016) *J. of Applied Physics*, 119, 115501

Annexes

Fabrication of perovskite solar cells at LPICM

ITO coated glass substrates (from Xin Yan Tech.) are patterned using chlorhydric acid (HCl) and zinc powder (Zn) to remove ITO over one third of the sample surface to create the two poles of the device (Figure 90b). Following this etching step the samples are cleaned in the following sequence of ultrasonic baths:

- Water + detergent (15 min)
- Clear water (15 min) x3
- Acetone (15 min)
- Isopropan-2-ol (15 min)

Etched samples are then transferred into a vacuum chamber where Cr (10 nm) and Au (70 nm) contacts are deposited by Physical Vapor Deposition (PVD) (Figure 90c). Following this, the substrates are ready for experiments.

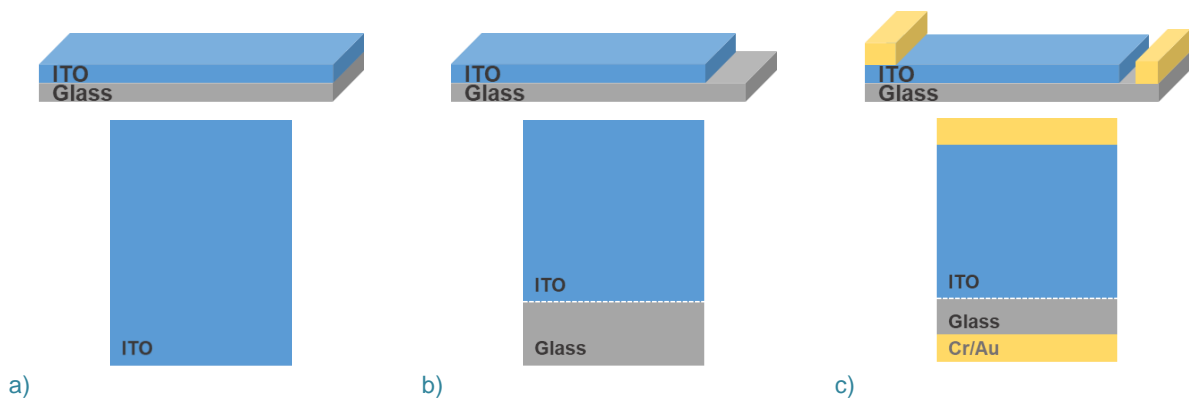


Figure 90. Substrate preparation steps from a) the full plate ITO glass coated; b) to the etched and c) Cr/Au contacted substrate (side and top views of the sample stack).

The patterned and contacted ITO samples are cleaned in ultrasonic baths of acetone and isopropanol and then treated by UV-ozone for 15 minutes. A PEDOT:PSS hole transport layer (approximately 50 nm thick) is then deposited via spin-coating process (4500 rpm spinning rate for 40 seconds) and annealed at 120 °C for 20 minutes. The Cr/Au contacts are cleaned using a cotton tip dipped in water before annealing.

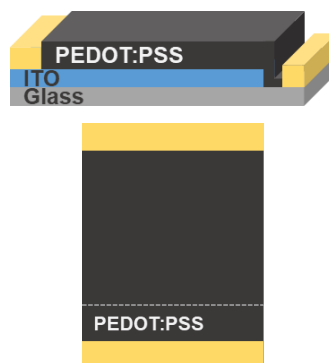


Figure 91. PEDOT:PSS deposition (side and top views of the sample stack).

For the wet-processed perovskite films:

A mix of PbI_2 and $\text{CH}_3\text{NH}_3\text{I}$ (1:1 molar ratio) was solubilized in a mix of γ -Butyrolactone and DiMethyl SulfOxide (GBL-DMSO, 8:2, v/v)²²² with a concentration of 1.23 M. The solution is stirred for 1h at 70°C in N_2 conditions before deposition. The filtered perovskite solution is then spincoated on the PEDOT:PSS layer at 2500 rpm for 30 seconds. An anti-solvent treatment⁷⁷ is performed by dropping 0.5 mL of toluene 5 seconds before the end of the spinning. Samples are then annealed for 1 minute at 70°C and 5 minutes at 100°C in N_2 conditions. The Cr/Au contacts are cleaned using a cotton tip dipped in N,N-DiMethylFormamide (DMF) after annealing while the substrate is still hot to prevent any DMF diffusion.

For the dry-processed perovskite films:

- Using the proof-of-concept reactor from RIBER Company:

PbI_2 bids and MAI powder are loaded in their respective sources (Table 3). The Glass/ITO/PEDOT:PSS samples are loaded in the substrate holder and the reactor chamber is then evacuated to $\sim 4.10^{-6}$ hPa. Coevaporation conditions are disclosed in Chapter 2 section I page 32. Following the perovskite deposition, the samples are transferred to a hot plate where they are annealed for at least 15 minutes at 90°C. The Cr/Au contacts are cleaned using a cotton tip dipped in N,N-DiMethylFormamide (DMF) after annealing while the substrate is still hot to prevent any DMF diffusion.

- Using the designed reactor from MBRAUN Company:

PbI_2 bids and MAI powder are loaded in their respective sources, in the amount of 0.70 and 0.5 g respectively before each experiment. The Glass/ITO/PEDOT:PSS samples are loaded in the substrate holder and the reactor chamber is then evacuated to $\sim 5.10^{-7}$ mbar. Heating rates and temperature targets are extensively disclosed in the manuscript. The substrate holder is rotated to a speed of 250 rpm during both the deposition of the PbI_2 initial layer and the coevaporation. Following the perovskite deposition, the samples are transferred to a hot plate where they are annealed for at least 15 minutes to 90°C. The Cr/Au contacts are cleaned using a cotton tip dipped in N,N-DiMethylFormamide (DMF) after annealing while the substrate is still hot to prevent any DMF diffusion.

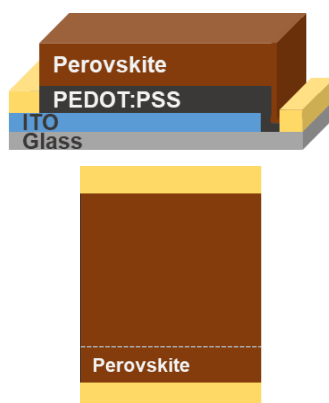


Figure 92. Perovskite deposition (side and top views of the sample stack).

²²² Recipe adapted from [S. Ghanavi's master thesis](#)

A solution of 40 mg/mL of PCBM in ChloroBenzene (CB) is then spincoated on top of the perovskite layer (2000 rpm for 30 seconds). The samples are then annealed 3 minutes at 90°C. The Cr/Au contacts are cleaned using a cotton tip dipped in CB.



Figure 93. PCBM deposition (side and top views of the sample stack).

The solar stack is completed by the deposition using PVD of a silver top electrode through a shadow mask defining a 0.28 cm² area.



Figure 94. Ag top electrode deposition (side and top views of the sample stack).

Résumé en français

Elaboration de films de perovskites hybrides par coévaporation pour des applications photovoltaïques.

Les pérovskites hybrides célèbrent cette année leurs 10e anniversaire dans le domaine du photovoltaïque. Bien que la grande majorité des films de pérovskites sont obtenus par la méthode d'enduction centrifuge, celle-ci ne permet pas l'obtention de films homogènes, sur grandes surfaces et de façon répétable. Etant donné l'enjeu industriel qui attend les pérovskites et l'intérêt croissant pour les structures tandems Silicium/Pérovskite, les méthodes sans solvant semblent plus adaptées. Publiée pour la première fois en 2013, la synthèse par coévaporation des pérovskites semble constituer une solution commercialement viable. Elle est pour le moment encore peu étudiée car nécessitant des équipements plus coûteux que les procédés en voie liquide.

La présente thèse vise à mettre en place et développer la technique de coévaporation pour la fabrication de films de pérovskites hybrides pour des applications en cellules solaires grandes surfaces.

Afin d'évaluer la faisabilité du procédé, nous avons commencé notre travail avec un réacteur de démonstration, ce qui nous a permis d'appréhender la réponse à la sublimation des deux précurseurs. Nous avons très vite identifié le comportement du sel organique $\text{CH}_3\text{NH}_3\text{I}$ comme étant problématique car difficilement contrôlable, s'évaporant sous forme de « nuage ». En six mois d'exploitation de ce réacteur nous avons fabriqué des films de pérovskites ayant permis d'atteindre des rendements de 9% en cellules solaires, malheureusement avec une mauvaise répétabilité. A cause d'un manque de fonctionnalités sur l'équipement, nous nous sommes trouvés dans l'incapacité d'aller plus en profondeur dans la compréhension du procédé. Grâce à nos différents retours d'expérience avec ce réacteur de démonstration nous avons pu concevoir, en étroite collaboration avec l'équipementier, un réacteur semi-industriel dédié à la fabrication de films de perovskites par coévaporation.

Suite à la mise en place de ce nouvel équipement, plus optimisé pour la coévaporation de perovskites, et aux tests de qualification obligatoires nous avons pu nous focaliser sur la problématique de répétabilité de nos expériences en essayant de limiter l'impact parasite du nuage organique. En diminuant les températures de chauffage ($^{\circ}\text{C}$) et les rampes associées ($^{\circ}\text{C}/\text{min}$) nous avons pu augmenter la stabilité des vitesses de dépôt des précurseurs et améliorer, dans une moindre mesure, la répétabilité de nos expériences.

Avec l'amélioration de la stabilité et de la répétabilité du procédé, nous avons pu nous intéresser à la caractérisation des matériaux obtenus. Bien que les efficacités atteintes en cellules solaires avec des perovskites coévaporées fussent moindres que pour des perovskites par enduction centrifuge, nous soupçonnions une meilleure homogénéité en faveur du procédé voie sèche. Les matériaux ont été étudiés par quelques techniques de base telles que la microscopie électronique à balayage et la spectroscopie d'absorption UV-visible, mais aussi à l'aide d'une technique plus complexe de spectromicroscopie : la

microscopie à rayons X à balayage et transmission (STXM en anglais). Une étude comparative de films perovskites voie liquide et voie sèche par cette technique a été menée par cette technique Synchrotron. Nous avons étudié les films sur une large gamme d'énergie (240 ; 700 eV) afin de couvrir les pics d'absorption des différents éléments chimiques composant le matériau (C, N, Pb et I). En se fixant le rapport Pb/I comme facteur comparatif et en confrontant deux méthodes de calcul de ce dernier, nous avons montré une meilleure homogénéité de ce rapport et donc *in fine* de la composition du matériau en faveur de la voie sèche par rapport à la voie liquide.

Titre : Elaboration de films de perovskites hybrides par coévaporation pour des applications photovoltaïques.

Mots clés : perovskite – dispositifs photovoltaïques – procédé sous vide – Synchrotron

Résumé : Les pérovskites hybrides célèbrent cette année leurs 10^e anniversaire dans le domaine du photovoltaïque. Bien que la grande majorité des films de pérovskites sont obtenus par la méthode d'enduction centrifuge, celle-ci ne permet pas l'obtention de films homogènes, sur grandes surfaces et de façon répétable. Etant donné l'enjeu industriel qui attend les pérovskites et l'intérêt croissant pour les structures tandems Silicium/Pérovskite, les méthodes sans solvant semblent plus adaptées.

Publiée pour la première fois en 2013, la synthèse par coévaporation des pérovskites semble constituer une solution commercialement viable, elle est pour le moment encore étudiée par peu de groupes car nécessitant des équipements plus coûteux. La présente thèse vise à mettre en place et développer la technique de coévaporation pour la fabrication de films de pérovskites hybrides pour des applications en cellules solaires.

Afin d'évaluer la faisabilité du procédé, nous avons commencé notre travail sur un réacteur de démonstration, ce qui nous a permis d'appréhender la réponse des précurseurs.

En six mois d'utilisation, nous avons fabriqué des cellules solaires à 9% d'efficacité, malheureusement avec une faible répétabilité (que nous expliquons en partie par le caractère aléatoire de l'évaporation du composé organique $\text{CH}_3\text{NH}_3\text{I}$).

Grâce aux différents retours d'expérience avec le réacteur de démonstration nous avons pu concevoir un réacteur semi-industriel dédié à la fabrication de films de perovskites par coévaporation. Suite à sa mise en place, nous nous sommes focalisés sur la problématique de la répétabilité dans nos expériences en essayant de diminuer l'impact du nuage organique. Bien que les efficacités atteintes en cellules solaires pour des films coévaporés fussent moindres que pour des films déposés par la technique classique d'enduction centrifuge, nous soupçonnions néanmoins une meilleure homogénéité des films obtenus par voie sèche.

Nous avons ainsi intégré à cette thèse une étude comparative voie liquide/voie sèche par le biais d'une technique de spectromicroscopie rayons X en Synchrotron.

Title: Development of coevaporated hybrid perovskite thin films for solar cells applications.

Keywords : perovskite – photovoltaic devices – vacuum process – Synchrotron

Abstract: Hybrid perovskites celebrate this year their 10-year anniversary in the photovoltaic field. While most of the reported works on perovskite thin films are based on the basic wet-process spincoating technique, this latter hardly allows large scale, homogeneous and reproducible deposition. With the future challenge of industrialization and the increasing interest for the Silicon/Perovskite tandem approach, solvent-free methods appear more suitable.

Reported for the first time in 2013, coevaporation stands as a viable option for perovskites industrial future. The technique is still scarcely studied compared to wet-based techniques, requiring more expensive set ups. In the present thesis, we implemented and developed the coevaporation process to fabricate perovskite thin films for solar cells applications.

Starting off on a proof-of-concept reactor to assess the feasibility of the technique, we got accustomed to the perovskite precursors behaviour.

In six months of use, we were able to obtain perovskite films leading to 9% efficient photovoltaic devices, unfortunately with a poor repeatability that we think to be partially due to the cloud vapour behaviour of $\text{CH}_3\text{NH}_3\text{I}$.

From this feedback we then designed, hand in hand with the manufacturer, a dedicated semi-industrial equipment for perovskite coevaporation. Following its implementation, we then focused on establishing the repeatability of the method, trying to mitigate the parasitic effect of the organic compound. Even though the efficiencies in solar cells were still slightly lower for coevaporated perovskites, with respect to classical spincoated ones, we expected the material homogeneity to be in favour of the vacuum-based process.

We then eventually integrated to this thesis a comparative study between wet- and dry-processed perovskite films using a Synchrotron-based X-ray spectromicroscopy technique.

